

*Enhanced chromodynamic multi-component lattice boltzmann method for drop and vesicle modelling*

SPENDLOVE, James

Available from the Sheffield Hallam University Research Archive (SHURA) at:

<http://shura.shu.ac.uk/30032/>

## A Sheffield Hallam University thesis

This thesis is protected by copyright which belongs to the author.

The content must not be changed in any way or sold commercially in any format or medium without the formal permission of the author.

When referring to this work, full bibliographic details including the author, title, awarding institution and date of the thesis must be given.

Please visit <http://shura.shu.ac.uk/30032/> and <http://shura.shu.ac.uk/information.html> for further details about copyright and re-use permissions.

# **Enhanced Chromodynamic Multi-Component Lattice Boltzmann Method for Drop and Vesicle Modelling**

James Spendlove

A thesis submitted in partial fulfilment of the requirements of

Sheffield Hallam University

for the degree of Doctor of Philosophy

December 2021

# Candidate Declaration

I hereby declare that:

1. I have not been enrolled for another award of the University, or other academic or professional organisation, whilst undertaking my research degree.
2. None of the material contained in the thesis has been used in any other submission for an academic award.
3. I am aware of and understand the University's policy on plagiarism and certify that this thesis is my own work. The use of all published or other sources of material consulted have been properly and fully acknowledged.
4. The work undertaken towards the thesis has been conducted in accordance with the SHU Principles of Integrity in Research and the SHU Research Ethics Policy.
5. The word count of the thesis is 52,069.

Name	James Spendlove
Award	PhD
Date of Submission	December 2021
Faculty	Materials Engineering Research Institute (MERI)
Director(s) of Studies	Dr Xu Xu

# Acknowledgements

I have been extremely lucky to have had an amazing supervisory team, who all have been invaluable to my PhD and an inspiration throughout. I would like to thank my director of studies Xu Xu for her constant support and encouragement —I could not have asked for a better DoS. I doubt my understanding of lattice Boltzmann (LB) would be nearly as good without the dedication of Ian Halliday, who I spent many an hour with filling up whiteboards with mathematical analysis and long conversations about LB theory. I would also like to thank Torsten Schenkel who always provided a valuable point of view, with many of his insights leading to more interesting questions. Overall, I feel extremely privileged to have been guided by such a team.

I will forever be grateful to my family and friends, who have supported and encouraged me throughout my studies and provided a source of inspiration. My wonderful girlfriend Phoebe Marriott deserves a special mention for her patience and support during the late nights and weekends spent finishing papers or preparing for presentations. Who without, I'm sure this process would have been much harder, and my motivation lower.

Finally, I would like to thank again Ian Halliday for suggesting I apply for the PhD, and Xu Xu for her joint support in the application process. Thank you to the Materials Engineering Research Institute (MERI) for providing the graduate teaching associate scholarship, alongside a great environment to work in. In addition, thank you to both Dr Lyuba Albou and Professor Andrew Masters for agreeing to examine my PhD.



# Advanced Studies

A list of notable publications and presentations relating to the work presented here in this thesis, conducted throughout this PhD.

## Publications

Work from the following publications produced during this PhD contribute to the content of this thesis as follows: (i) forms the basis of Chapter 3, (ii) & (iii) form the basis of Chapter 4, and (iv) the basis of Chapter 5. All papers are freely and legally available online at this time of writing, and permission has been gained from the publishers to reuse content from these publications within this thesis, with appropriate referencing.

- (i) K. Burgin, J. Spendlove, X. Xu and I. Halliday (2019). Kinematics of chromodynamic multicomponent lattice Boltzmann simulation with a large density contrast. *Physical Review E*, 100 (4), 043310.
- (ii) J. Spendlove, X. Xu, T. Schenkel, M. Seaton and I. Halliday (2020). Chromodynamic multi-component lattice Boltzmann equation scheme for axial symmetry. *Journal of Physics. A: Math. Theor.* 53 145001.
- (iii) J. Spendlove, X. Xu, O. J. Halliday, T. Schenkel and I. Halliday (2020). Chromodynamic multi-relaxation time lattice Boltzmann scheme for fluids with density difference. *Physical Review E*, 102, 013309.
- (iv) J. Spendlove, X. Xu, T. Schenkel, M. Seaton, I. Halliday and J. Gunn (2021). Three-dimensional single framework multi-component lattice Boltzmann equation method for vesicle hydrodynamics. *Physics of Fluids*, 33 (7), 077110.

## Presentations

- Computational Collaboration Project No. 5 (CCP5) DL\_Software Workshop (2018) - Poster: "Kinematics of Chromodynamic Multi-Component Lattice Boltzmann Method"

- Polymers Nanocomposites Modelling Research Centre (PNMRC) (2019) - Presentation: "Kinematics of Chromodynamic Multi-Component Lattice Boltzmann Simulation with a Large Density Contrast"
- Computational Collaboration Project No. 5 (CCP5) Summer School (2019) - Poster: "Lattice Boltzmann Schemes for Simulating Multi-Component Flows With Large Density Contrasts"
- Materials Engineering Research Institute (MERI) Research Symposium (2019) - Short-Presentation: "Lattice Boltzmann Method (LBM) for Simulating Multi-Component Flows"
- Industry and Innovation Research Institute (I2Ri) Winter Poster Event (2020) (Visual Impact prize winner) - Poster: "Multi-Component Chromodynamic Lattice Boltzmann Method for Simulating Red Blood Cells"
- Materials Engineering Research Institute (MERI) Research Symposium (2021) - Presentation: "A Transparent Approach to Modelling RBCs: Using Chromodynamic Lattice Boltzmann Method (LBM)"
- 30<sup>th</sup> International Conference on Discrete Simulation and Fluid Dynamics (DSFD) (2021) - Presentation: "Modelling Fluid Filled Vesicles Using Chromodynamic Multi-Component Lattice Boltzmann Method"

# Abstract

Multi-component fluid flows are frequently seen in both nature and industry, such as gas-liquid flows (air-water) and liquid-liquid flows (oil-water). The accurate simulation of such fluid flows requires models to: (i) solve the governing fluid dynamics equations; (ii) reproduce known boundary behaviour at the free surface between the fluids; (iii) embed known surface physics representative of that of the target fluid object, i.e., surface tension when simulating drops. Here, meso-scale modelling techniques offer attractive options for simulating such flows, where due to working at a smaller scale than macro-scale approaches, one can investigate more detailed interactions and phenomena, whilst also recovering the continuum fluid dynamics equations.

The development of the lattice Boltzmann method (LBM), a bottom-up kinetic scale Navier-Stokes solver, furnishes the ability to model such macro-scale properties whilst allowing for the inclusion of meso-scale physics. The chromodynamic multi-component extension of this (cMCLBM) treats the fluids as separate species, with a diffused interfacial region (*de facto* surface), where discrete immersed interface forces can be applied to embed known physics of the fluid object. Theoretically, such a modelling approach should be capable of simulating a range of fluid objects, for example: liquid drops, vesicles (erythrocytes), and capsules, by manipulating the treatment of the interface.

This work explores extensions to the cMCLBM, with a final objective of modelling vesicles (tailored towards erythrocytes) using this essential approach. Before this, however, it is sensible to confirm the fundamental foundations of the model, i.e., the model's kinematics and dynamics. As such, work first focuses on the simulation of less complex fluid objects (drops), investigating the utility of the model when applied to fluid flows with a density contrast, where stability is strained. Here, the kinematics and dynamics of the model are assessed in detail through both mathematical analysis and simulation data, to quantify its compliance with known continuum hydrodynamic conditions such as: mutual impenetrability, the no-slip condition, and stress balance across the interface. Following the enhanced understanding of the cMCLBM gained from this work, the simulation of vesicles is targeted. The primary outcome of this work is the development of a single framework approach to modelling vesicle hydrodynamics, with promising possibilities for future applications within haemorheology and microfluidics.

# Contents

<b>List of Figures</b>	<b>ix</b>
<b>List of Tables</b>	<b>xi</b>
<b>List of Abbreviations</b>	<b>xii</b>
<b>1 Introduction</b>	<b>1</b>
1.1 Background and Motivation . . . . .	1
1.2 Aims and Contribution of this Work . . . . .	3
1.3 Thesis Outline . . . . .	4
<b>2 Background in Hydrodynamics and Simulation Techniques</b>	<b>5</b>
2.1 Introduction . . . . .	5
2.2 Hydrodynamics . . . . .	9
2.2.1 Governing Equations . . . . .	9
2.2.2 Boundary Conditions . . . . .	12
2.2.3 Non-Dimensional Quantities . . . . .	16
2.3 Lattice Boltzmann Equation Simulation . . . . .	18
2.3.1 Development and Fundamentals . . . . .	18
2.3.2 Collision Operators . . . . .	21
2.3.3 Multi-Component Lattice Boltzmann . . . . .	26
2.3.4 Boundary Conditions . . . . .	34
2.4 Simulation of fluids using LBM . . . . .	37
2.5 Concluding Remarks . . . . .	39
<b>3 Kinematics and Dynamics of Chromodynamic Multi-Component Lattice Boltzmann Equation Simulation</b>	<b>41</b>
3.1 Introduction . . . . .	41
3.2 Methodology . . . . .	45
3.2.1 Isothermal cMCLBM for Binary Fluid Flows with a Density Contrast . . . . .	45
3.2.2 Extension to Many-Component Fluid Flows . . . . .	47
3.3 Analysis . . . . .	49
3.3.1 Dynamics . . . . .	50

3.3.2	Kinematics . . . . .	57
3.3.3	Dynamics and Kinematics Coupling . . . . .	64
3.4	Results . . . . .	65
3.4.1	Spurious Current . . . . .	65
3.4.2	Kinematical Condition . . . . .	69
3.5	Concluding Remarks . . . . .	75
<b>4</b>	<b>Extended cMCLBM for the Simulation of Drops within Stokes Flow</b>	<b>78</b>
4.1	Introduction . . . . .	78
4.2	MRT Two-dimensional System . . . . .	79
4.2.1	Introduction . . . . .	79
4.2.2	Extension of Methodology . . . . .	81
4.2.3	Results . . . . .	87
4.3	Pseudo Three-dimensional System . . . . .	97
4.3.1	Introduction . . . . .	97
4.3.2	Extension of Methodology . . . . .	98
4.3.3	Results . . . . .	105
4.4	Concluding Remarks . . . . .	118
<b>5</b>	<b>The Simulation of Fluid-Filled Vesicles using cMCLBM</b>	<b>122</b>
5.1	Background and Motivation . . . . .	123
5.1.1	Vesicle Physics . . . . .	123
5.1.2	Existing Methods . . . . .	125
5.1.3	Chromodynamic MCLBM approach . . . . .	127
5.2	Extension of Methodology . . . . .	130
5.2.1	Immersed Boundary Force . . . . .	130
5.2.2	Force Characterisation . . . . .	138
5.2.3	Computation of Membrane Forces . . . . .	141
5.2.4	Multiple Vesicles . . . . .	147
5.3	Results . . . . .	148
5.3.1	Steady State Equilibrium Data . . . . .	150
5.3.2	Dynamics . . . . .	159
5.3.3	Simulation of Multiple Vesicles . . . . .	165
5.4	Concluding Remarks . . . . .	169
<b>6</b>	<b>Conclusions and Future Work</b>	<b>174</b>
6.1	Conclusions . . . . .	174
6.2	Future Work . . . . .	177
6.2.1	Extension to the Simulation of Many Immiscible Fluids . . . . .	177
6.2.2	Modular cMCLBM . . . . .	179
6.2.3	Applications . . . . .	181

## Appendices

<b>A</b>	<b>Multi-Relaxation Time Chromodynamic Lattice Boltzmann Method</b>	<b>183</b>
A.1	Dynamics . . . . .	183
A.1.1	Dynamics: 2D MRT cMCLBM for fluids with a large density contrast . . . . .	183
A.1.2	Dynamics: Pseudo 3D MRT cMCLBM for fluids with a large density contrast . . . . .	186
A.2	Analytical Solutions . . . . .	188
A.2.1	Transient uni-directional multi-component flow with transverse density stratification . . . . .	188
A.2.2	Numerical solution of steady, pressure-driven flow with density stratification . . . . .	194
<b>B</b>	<b>Simulation of Vesicles</b>	<b>196</b>
B.1	Computation of vesicle surface principal curvatures . . . . .	196
	<b>References</b>	<b>201</b>

# List of Figures

2.1	Length and time scales used in the modelling of materials and fluid flows . . . . .	7
2.2	Schematic of an immiscible drop submerged in a background fluid . .	13
2.3	Lattice structures: D2Q9 & D3Q19 . . . . .	19
2.4	Schematic of the streaming & collision process in LBM . . . . .	20
2.5	Periodic boundary condition . . . . .	35
2.6	Bounce back boundary condition . . . . .	36
2.7	Mid-link bounce back boundary condition . . . . .	36
2.8	Slip (specular reflection) boundary condition . . . . .	37
2.9	C Code flow chart . . . . .	38
3.1	Neumann's triangle - triple contact . . . . .	48
3.2	Schematic of the kinematics analysis flow geometry . . . . .	58
3.3	BGK microcurrent - mean curvature fixed . . . . .	68
3.4	BGK Microcurrent - mean curvature calculated . . . . .	68
3.5	Advecting fluid perpendicular to the flat interface test . . . . .	71
3.6	Advecting fluid perpendicular to the flat interface - unstable result . .	72
3.7	Advecting fluid perpendicular to the flat interface - Error and stability relation. . . . .	73
3.8	Schematic of fluid pushed parallel to the flat interface. . . . .	74
4.1	MRT microcurrent - mean curvature fixed . . . . .	88
4.2	MRT microcurrent - mean curvature calculated . . . . .	88
4.3	Schematic: pressure driven flow with density stratification . . . . .	90
4.4	Data: pressure driven flow with density stratification . . . . .	91
4.5	Schematic: sheared stratified fluids with flat interface . . . . .	92
4.6	Data: sheared stratified fluids with flat interface . . . . .	93
4.7	Schematic: sheared stratified fluids with curved interface . . . . .	95
4.8	Data: sheared stratified fluids with curved interface . . . . .	96
4.9	Schematic of system reduction from three to two-dimensions. . . . .	100
4.10	Numerical integration of Eq. (4.51) needed to calculate $u_x$ . . . . .	104
4.11	Phase-field freezing approach . . . . .	109
4.12	Comparison of the drops internal velocity field against an analytical solution at $\Lambda = 1$ . . . . .	111

## List of Figures

4.13	Comparison of the drop fluid velocity components against an analytical solution for flow pushed past an effectively tethered spherical drop . .	112
4.14	Simulation data of flow past a spherical liquid drop at varying density ratios . . . . .	113
4.15	Meridional section showing velocity and pressure field for flow past a deforming liquid drop. . . . .	114
4.16	Meridional section showing deformation of a liquid drop overtime in low Reynolds number flow . . . . .	115
4.17	Comparison of deformed drop profile in low Reynolds number flow against theoretical data . . . . .	117
5.1	Schematic of the structure of a RBC membrane [150] . . . . .	125
5.2	Fluid-interface-fluid schematic . . . . .	129
5.3	Surface manifold differential geometry . . . . .	132
5.4	Deflation of spherical vesicle . . . . .	136
5.5	Surface Curvature Frames . . . . .	143
5.6	Effect of varying deflation on vesicle shape . . . . .	152
5.7	Grid resolution effects on bicuspid vesicle profile . . . . .	156
5.8	Comparison of bicuspid vesicle profile against the parametric expression given in [183] . . . . .	157
5.9	Time evolution of the eigenvalues of the inertia tensor for a prolate and torus vesicle . . . . .	159
5.10	Wheeler test . . . . .	161
5.11	Vesicle flow profile when exposed to a strong shear resulting in a deformation index of 29%. . . . .	163
5.12	Shear recovery of a bicuspid vesicle - eigenvalues . . . . .	164
5.13	Drop spreading test . . . . .	166
5.14	Vesicle-Vesicle pseudo-ballistic impact . . . . .	168
5.15	Vesicle-Vesicle sedimentation test . . . . .	169
6.1	Four vesicle sedimentation test . . . . .	178
6.2	<i>Modular</i> cMCLBM for the simulation of liquid drops, vesicles and other soft particles. . . . .	180



# List of Tables

2.1	D2Q9: lattice links and weights . . . . .	19
2.2	D3Q19: lattice links and weights . . . . .	20
2.3	Table showing impact of $\tau$ in the BGK collision scheme . . . . .	22
3.1	BGK Microcurrent - 2D static Drop . . . . .	67
3.2	BGK Microcurrent - 2D static drop, for varying surface tension values	69
3.3	Stability table for an advecting fluid test, where $H = 0$ . . . . .	71
4.1	D2Q9 MRT collision matrix notation . . . . .	81
4.2	MRT Microcurrent - 2D static Drop. . . . .	89
4.3	Relative error relating to data in Figure 4.6 . . . . .	94
4.4	Relative error relating to data in Figure 4.8 . . . . .	97
5.1	D3Q19 lattice structure . . . . .	128
5.2	Co-ordinate frame notation table . . . . .	142
5.3	Sampled Phase Diagram . . . . .	151
5.4	Grid convergence study data looking at the effect of grid resolution on vesicle profile. . . . .	155
5.5	Eigenvalues of the Inertia tensor for both Prolate and Torus Vesicles .	158
5.6	Force parameterisations effect on vesicle stiffness - Surface plots . . .	162
5.7	Shear recovery of a bicuspid Vesicle - surface plots . . . . .	165
6.1	4 Vesicles sedimenting error . . . . .	178

# List of Abbreviations

<b>LBM</b>	. . . . .	Lattice Boltzmann Method.
<b>LGA</b>	. . . . .	Lattice Gas Cellular Automata.
<b>CFD</b>	. . . . .	Computational Fluid Dynamics.
<b>DPD</b>	. . . . .	Dissipative Particle Dynamics.
<b>SPH</b>	. . . . .	Smoothed Particle Hydrodynamics.
<b>MD</b>	. . . . .	Molecular Dynamics.
<b>BGK</b>	. . . . .	Bhatnagar Gross and Krook.
<b>TRT</b>	. . . . .	Two-Relaxation Time.
<b>MRT</b>	. . . . .	Multi-Relaxation Time.
<b>MCLBM</b>	. . .	Multi-Component Lattice Boltzmann Method.
<b>cMCLBM</b>	. . .	Chromodynamic Multi-Component Lattice Boltzmann Method.
<b>BBBC</b>	. . . . .	Bounce Back Boundary Conditions.
<b>OGBB</b>	. . . . .	On-Grid Bounce Back.
<b>MGBB</b>	. . . . .	Mid-Grid Bounce Back.
<b>RBC</b>	. . . . .	Red Blood Cell.
<b>FEM</b>	. . . . .	Finite Element Method.
<b>BEM</b>	. . . . .	Boundary Element Method.
<b>LSM</b>	. . . . .	Lattice Spring Method.
<b>IBM</b>	. . . . .	Immersed Boundary Method.
<b>GCT</b>	. . . . .	Grid Convergence Test.
<b>GCI</b>	. . . . .	Grid Convergence Index.
<b>Ma</b>	. . . . .	Mach number.
<b>Re</b>	. . . . .	Reynolds number.
<b>Ca</b>	. . . . .	Capillary number.
<b>We</b>	. . . . .	Weber number.
<b>Å</b>	. . . . .	Angstrom

## *List of Abbreviations*

$nm$	Nanometre
$\mu m$	Micrometre
$fs$	Femtosecond
$ns$	Nanosecond
$\mu s$	Microsecond
$\Delta x$	Lattice grid spacing.
$\Delta t$	Lattice time step.
$\underline{r}$	Lattice position.
$t$	Lattice time.
$i$	Lattice link index.
$t_i$	Lattice link weight.
$c_i$	Lattice discrete velocities.
$f_i$	Distribution function.
$f_i^{(\text{eq})}$	Equilibrium distribution function.
$\Omega$	Collision operator.
$\tau$	BGK relaxation parameter.
$A_{ij}$	Collision matrix.
$\phi_i$	Mass activation parameter.
$\underline{F}^{(a)}$	Area conserving force.
$\underline{F}^{(b)}$	Bending rigidity force.
$\underline{F}^{(l)}$	Surface tension force.
$\underline{F}^{(t)}$	Total immersed force.
$\kappa_B$	Bending rigidity constant.
$\sigma$	Surface tension constant.
$\underline{\underline{\tilde{\sigma}}}$	Stress tensor.
$\Upsilon$	Deflation parameter.
$A_0$	Target area.
$A_{\text{sphere}}$	Area of the initialised sphere.
$\rho(\underline{r})$	Total density at lattice position ( $\underline{r}$ ).
$\rho_C(\underline{r})$	Density of fluid $C$ at lattice position ( $\underline{r}$ ).
$\rho_{0C}$	Deep phase density of fluid $C$ .

## *List of Abbreviations*

$\beta$	Segregation parameter.
$\rho^N$	Phase-field.
$u_\alpha$	$\alpha$ component of velocity.
$p$	Pressure.
$c_s$	Speed of sound.
$H$	Mean curvature.
$H_0$	Spontaneous curvature.
$K$	Gaussian curvature.
$\kappa_\alpha$	$\alpha$ principle of curvature.
$\delta_{\alpha\beta}$	Kronecker delta.
$\underline{n}$	Normal.
$\hat{n}$	Unit normal.
$\Lambda$	Density ratio.
$\eta$	Kinematic viscosity.
$\nu$	Dynamic viscosity.
$\Delta_s$	Laplace-Beltrami operator.
$\nabla_s$	Surface gradient operator.
$\underline{\underline{I}}$	Inertia Tensor.

# 1

## Introduction

### Contents

---

<b>1.1</b>	<b>Background and Motivation . . . . .</b>	<b>1</b>
<b>1.2</b>	<b>Aims and Contribution of this Work . . . . .</b>	<b>3</b>
<b>1.3</b>	<b>Thesis Outline . . . . .</b>	<b>4</b>

---

### 1.1 Background and Motivation

The class of fluid mixtures described as immiscible fluids —fluids which are insoluble in each other —can be found in a variety of physical fluid flows, the classic example being that of oil and water. The understanding and modelling of such immiscible fluid flows presents itself as an important objective in many fields, where such flows are prominent, e.g., food rheology, geophysics, micro-fluidics, the study of fuel cells, etc. Flow in all these systems are most often addressed in the continuum limit of hydrodynamics. We ask in this thesis, can this same continuum limit, albeit subject to interpretation, be used to encapsulate the dynamics, in computer simulation, of more complex, hybrid objects? Specifically, by working in an adapted continuum limit, a final objective is set for the modelling of flowing red blood cells (RBCs, erythrocytes, or, more neutrally, vesicles), by treating them (erythrocytes) as one immiscible fluid (cytoplasm) submerged in a background fluid (plasma), with the membrane treated as an appropriate boundary between the two fluids (i.e., a quasi-two-dimensional surface —the interfacial region between the fluids in diffused interface models, although considered and treated as essentially two dimensional, has a small and finite thickness). Such an enquiry is permitted as a consequence of

## 1. Introduction

the natural separation of length scales in the description, the physical erythrocyte membrane having a thickness of order  $nm$ , the erythrocyte itself having a width of order  $\mu m$ . This scale separation means mesoscale fluid dynamic simulation techniques are attractive options for modelling. Of course, this approach to vesicle modelling necessarily "integrates out" some microscopic detail (e.g., the biochemical properties of the membrane) which is replaced in this work with a concept currently introduced as a "shape energy description" of the local membrane. Once this concept is established, we will ask if appropriate vesicle behaviour accrues from a computationally viable model, conceived along the lines outlined above.

If one were to successfully establish this continuum view of vesicles, then the resulting, enhanced ability to understand and model immiscible fluids acquires even greater technological importance, as further applications, in fields such as bioengineering and chemical engineering, will fall within range of simulation. A question then arises as follows. If both liquid drops and vesicles are to be retained within the same essential approach (i.e., considering vesicles as immiscible fluids with a diffused interface within the continuum approximation) then in what ways must the modelling approach differ? One would naturally assume that a vesicle model would have to include more complex mesoscale physics to describe the more elaborate behaviour of vesicles (which will, presumably, be derived from coarse-grained approximations of more detailed microscopic physics) but the additional physics must also rely upon an underlying stratum of ideas common to both vesicle and drop simulation. Put another way, a single framework methodology's vesicle limit and its drop limit (if they exist) might well both rely on common physical and dynamical principles. To address this issue, here, we are motivated to clarify the origins, within our essential method (of lattice Boltzmann simulation- see below) of the kinematic and dynamical boundary conditions (which relate the velocity and stress profiles across an interface). Put another way, with a broad spectrum of applications in view, compliance with a core set kinematic and dynamic conditions must be assured. Accordingly, the behaviour at the liquid-liquid surface is a recurrent theme throughout this thesis.

For the discussed reasons, a model which allows the simulation of such immiscible fluids, where meso-scopic physics may be incorporated, to develop an accurate continuum scale description of the fluids, is very desirable. There is only a small class of fluid solvers, appropriate for tackling the simulation of such flows. A relatively new and attractive modelling technique is the lattice Boltzmann Method (LBM), which uses a kinetic scale evolution equation to describe the hydrodynamics of fluids, consistent with the weakly compressible Navier-Stokes equations. The

## 1. Introduction

multi-component extension of LBM (MCLBM), which allows for the simulation of multiple immiscible fluids, presents itself as a natural candidate to tackle such an investigation. The chromodynamic MCLBM (cMCLBM) variant is the one implemented throughout all the work presented here.

## 1.2 Aims and Contribution of this Work

The broad aims of this work and the associated contribution to knowledge in the field centre around the extension of a MCLBM variant, namely cMCLBM —the reasons for using this variant are discussed in Chapter 2. This research focuses on the progressive development and analysis of a suite of cMCLB models, to allow for the simulation of more or less complex immiscible fluids (such as vesicles (complex —*structured membrane*) and drops (less complex —*no membrane*)), whilst providing an enhanced understanding of the simulation technique. The aims of this work, and the associated contribution to knowledge, can be stated explicitly in three, progressive tiers:

- (i) Assess the model’s kinematics and dynamics, as well as the coupling between the two, to provide a better understanding of the methodology.
  - An important component of simulating immiscible fluids at the mesoscale is the accurate simulation of the boundary between the fluids (the interface in cMCLBM). Hence, confirmation that the interface meets the kinematic and dynamic hydrodynamic boundary conditions (introduced in Chapter 2) and any subsequent understanding from this analysis, e.g., effects on the stability of the method in certain flows, will provide an important contribution to the field and enhanced methodological understanding. To achieve this, both mathematical analysis of the methodology and examination of simulation data on compliance with kinematical and dynamical boundary conditions is presented.
- (ii) Investigate the applicability of the method to immiscible fluids with a large density contrast.
  - Following (i), the applicability of the method to different flow scenarios is tested, mainly as a proxy for stability, aiming to express the model’s strengths and limitations. Again, with focus on compliance with kinematical and dynamical boundary conditions, building on the work in (i). Specifically, the aim here is to further investigate the model’s suitability for simulating fluids with large density contrasts, curved interfaces, small Reynolds numbers flows, density stratified flows and

## 1. Introduction

pseudo three-dimensional flows (i.e., axially symmetric two-dimensional flow). In doing so, this will highlight current limitations and strengths of the model, providing an enhanced understanding of the method and reveal new directions for future work.

(iii) Development of a single-framework, three-dimensional cMCLBM for simulating vesicle hydrodynamics.

- Following the enhanced understanding and conformation of our model’s kinematics and dynamic from (i) and (ii) above, the cMCLBM method is extended to the simulation of vesicle hydrodynamics in three-dimensions. The utility of such a model is discussed further in Chapter 5, however, this work presents itself as potentially the most appropriate and appealing application of the cMCLBM in its current form. Developed here is a novel, transparent, single-framework methodology for simulating vesicle hydrodynamics, tailored towards human RBCs, which has the future potential to be extended to many vesicle simulations through previously developed methodologies. The understanding of the model’s kinematics and dynamics stemming from aims (i) and (ii), helps develop the model, as well as confirm its accuracy.

## 1.3 Thesis Outline

To start this thesis, Chapter 2 gives necessary background on both hydrodynamics and lattice Boltzmann method, in order to provide context, with further chapter-specific literature found at the start of Chapters 3, 4 and 5. Chapter 3 presents work to fulfil aim (i) and is the main methodology section of this thesis. From this, Chapter 4 seeks to address aim (ii), as well as further the work in aim (i). Finally, Chapter 5 distills preceding work around aim (iii), which utilises model understanding from aims (i) and (ii). This work encapsulates the primary output from this research, which is the development of the chromodynamic model for the simulation of vesicles, tailored towards RBC dynamics. The significance of the findings in these three Chapters is then discussed and evaluated in Chapter 6, where future directions for the work are also given.



# 2

## Background in Hydrodynamics and Simulation Techniques

### Contents

---

<b>2.1</b>	<b>Introduction . . . . .</b>	<b>5</b>
<b>2.2</b>	<b>Hydrodynamics . . . . .</b>	<b>9</b>
2.2.1	Governing Equations . . . . .	9
2.2.2	Boundary Conditions . . . . .	12
2.2.3	Non-Dimensional Quantities . . . . .	16
<b>2.3</b>	<b>Lattice Boltzmann Equation Simulation . . . . .</b>	<b>18</b>
2.3.1	Development and Fundamentals . . . . .	18
2.3.2	Collision Operators . . . . .	21
2.3.3	Multi-Component Lattice Boltzmann . . . . .	26
2.3.4	Boundary Conditions . . . . .	34
<b>2.4</b>	<b>Simulation of fluids using LBM . . . . .</b>	<b>37</b>
<b>2.5</b>	<b>Concluding Remarks . . . . .</b>	<b>39</b>

---

### 2.1 Introduction

This chapter will provide much-needed background to support this thesis as follows. In the present context, an exhaustive survey is inappropriate; what is called-for is a contextualisation of the novel work presented. Accordingly, the content of this chapter is sub-divided into two sections: first the broader topic of hydrodynamics and, then, second, the more novel area of lattice Boltzmann equation simulation. The former gives an overview of key hydrodynamics relevant to the work. Therefore, the governing fluid dynamics equations, that describe the motion of the fluid at the relevant length

## *2. Background in Hydrodynamics and Simulation Techniques*

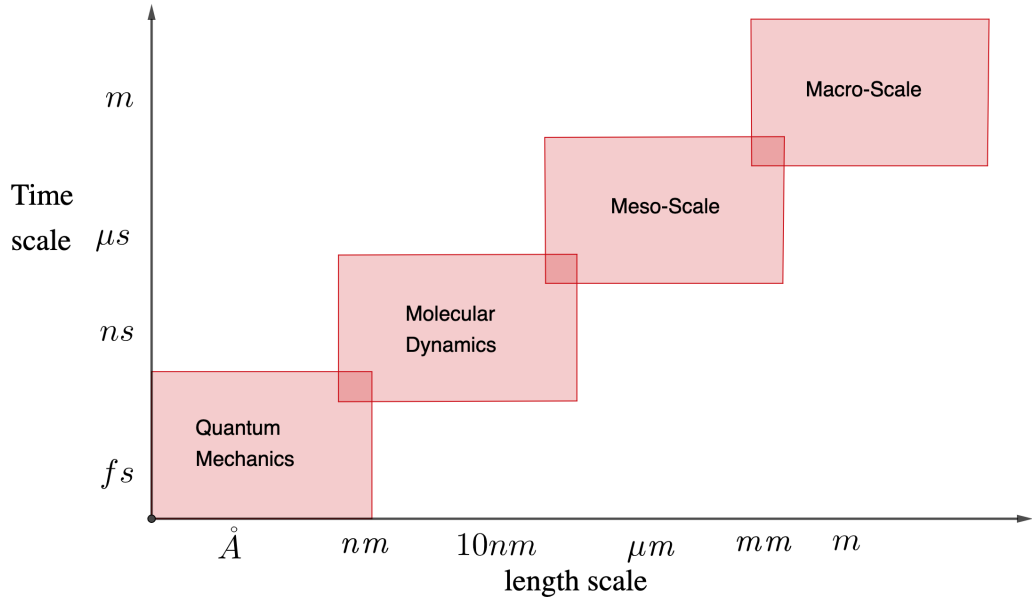
scales will be introduced, followed by a consideration of important non-dimensional quantities commonly used in fluid dynamics (which are reviewed throughout). To conclude our hydrodynamics survey, kinematic and dynamic hydrodynamic boundary conditions will be discussed, since a large proportion of the work herein alludes to these boundary conditions. The second half of this background chapter will focus on the topic of lattice Boltzmann equation simulation. Here we commence with the relevant history, development and fundamentals of the method, introducing and comparing salient collision operators and also multi-component lattice Boltzmann method (MCLBM) variants commonly implemented. To close this section, simulation boundary conditions are discussed, which will be referenced throughout the simulation results presented in the remainder of this thesis.

In order for one to discuss the relevant hydrodynamics and simulation techniques for their work, one must first be aware of the relevant length and time scales of target phenomena. Fluid flows are described at varying length and time scales and, depending upon the target scale at which one aspires to work, the governing equations of the fluid and the modelling technique that may be implemented will vary. Figure 2.1 presents the various length and time scales used within the mathematical modelling of materials and fluid flows. As the work in this thesis focuses on the investigation of immiscible drops, as well as erythrocytes (with a characteristic scale of  $\mu m$ ), it is logical, from Figure 2.1, that the modelling technique should span the mesoscale.

Researchers interested in representing the behaviour of atoms and molecules would, perhaps, deploy molecular dynamics (MD) [1, 2], which could be used to describe the evolution of a system over time, where detailed forces and interactions between molecules can be simulated. In order to produce significant results, the time scale of the simulation must be adequately long enough to model the system and associated phenomena. Due to this, and also the large number of degrees of freedom within simulations, MD simulations have high comparative computational cost and are therefore restricted in application to shorter time and length scales.

On the mesoscale, researchers interested in fluid flows that may contain some physics characteristic of smaller length scales may still wish to address moderate time and length scales. Such workers may opt for modelling techniques such as lattice Boltzmann Method (LBM) [3, 4, 5, 6], Dissipative Particle Dynamics (DPD) [7, 8, 9] and Smoothed Particle Hydrodynamics (SPH). In the case of LBM, a kinetic scale evolution equation -effectively the equation of motion of a single particle probability

## 2. Background in Hydrodynamics and Simulation Techniques



**Figure 2.1:** Schematic outlining the hierarchy of length and time scales effective within the modelling of materials and fluid flows, highlighting the scales where different descriptions operate.

distribution function - is used to describe the time evolution of the latter, over an Eulerian lattice. Importantly, the method has been shown to recover the continuum Navier-Stokes equations (through a Chapman-Enskog procedure, soon to be discussed —section 3.3.1). Dissipative Particle Dynamics (DPD) is more akin to that of MD (and hence, potentially, a more suitable approach for workers from this background) where fluid particles are essentially treated as clusters, or groups of molecules —which can be considered a coarse grained approach —where Newton laws are enforced and particle-particle interactions are simulated [7, 8]. Another Lagrangian, mesh free, fluid dynamics technique is Smoothed Particle Hydrodynamics (SPH) [10, 11], which was originally developed for astrophysical problems (where a boundary often does not exist) and later applied to fluid dynamics. Within SPH, the domain is populated by a set of particles that have material properties (such as mass and velocity), with these particles' interactions within the domain being controlled by what is known as a smoothing function. In SPH, the Navier-Stokes equations are discretised in relation to these particles, allowing the governing fluid dynamics equations to be solved. One potential advantage over DPD, is that SPH has specific physical parameters (such as viscosity), due to its direct derivation from the Navier-Stokes equations [12]. Clearly, both DPD and SPH are natural contenders for the hydrodynamic simulation of Lagrangian objects such as the vesicles and drops we consider; accordingly, some of the issues which determine our choice of LB simulation a vehicle (other than of an existing expertise, of course) is appropriate.

## 2. Background in Hydrodynamics and Simulation Techniques

When considering the relative computational cost of mesoscale simulation techniques, the coverage of published comparative studies has, until recently, been sparse. There has been a good deal of formal work comparing DPD and molecular dynamics (MD) and there is recent work comparing LBM with SPH. We return below to the comparison of DPD and LBM.

A great majority of comparative studies involving DPD relate DPD to MD and aim to show the benefits of scaling up to the meso-scale (canonically, the use in DPD of a soft conservative potential greatly increases the length of the simulation time step). Alternatively, comparing SPH and LBM, there is seemingly no great difference in the computational expense of both approaches. Within the work by Kajzer et al. [13], LBM was found to be the more efficient approach when applied to single fluids (note) large-eddy simulation (LES) results of 3D Taylor-Green vortex flow; meanwhile, in the work by Tafuni et al. [14], better performance was seen from SPH for various flows when compared to an LB approach —with both methodologies comparing well against more mature approaches (such as volume of fluid and higher order difference schemes) [14]. Work such as that reported in [15] concluded that the LBM offered a better order of convergence and higher accuracy than SPH when examining multi-phase flows, although the authors stated that SPH has a larger stability range (and in particular is more suitable to higher Mach number flows). Note, both methodologies are suitable for parallel implementation due to their locality and explicit nature. For the low Re, multi-component applications of this thesis in view, there is therefore, no significant computational advantage to either method. However, the simulation of immiscible fluid flows, supported by LBM has a large community, with already-defined, developed and documented models (to be discussed shortly), all encapsulated within amenable frameworks. This essentially logistic argument -of convenience- means that LBM is a good choice for the target application of the simulation of human RBCs, compared with SPH.

There remains the question of DPD versus LBM simulation. Certainly, DPD has been used to simulate capsules much smaller than erythrocytes, with applications to drug delivery vectors. Here, though, a quantitative comparison of the efficiency of DPD and LBM for our target application is not straightforward, for the equivalence of a DPD bead and an LB distribution function component (both, notionally mesoscale objects, note) is an open question, the address of which should precede a comparative efficiency study. Since such an investigation is an end in itself, we again fall-back on pragmatism (experience and available tools) to justify our choice of LBM as a tool. Working at this length scale allows complex boundary and interface physics to be encapsulated within models in a natural and intuitive manner, whilst still developing, *on balance*, a computationally efficient model (traditionally, with LBM,

## 2. Background in Hydrodynamics and Simulation Techniques

one cites the opportunity to avoid explicit tracking of immiscible fluid species and ready parallelisability, but is beset by criticism of the method’s profligate use of computer memory).

Where larger length and time scales need to be simulated, macro-scale modelling techniques such as traditional computational fluid dynamics (CFD) (finite volume method [16], finite element method [17], etc.) present a clear way forward. Unlike LBM, which may be described as a *bottom-up* approach to fluid dynamics, traditional CFD solves macroscopic equations of mass and motion, normally through discretisation of partial differential equations. Accordingly, these methods are often referred to as *top-down* approaches. Such methods are computationally efficient, mature, widely implemented, optimally efficient and very capable of simulating larger length and time scales of particular problems, but can often lose the ability to include important physics that originates at smaller length scales.

The differing scales and corresponding modelling techniques often interface with each other through multi-scale modelling. Multi-scale models at different length scales, help to build a more complete picture of the system being investigated. Of course, this approach aligns with physical reality, where materials and living organisms consist of a series of complex coupled systems at different length scales [18], a salient example being the meso-scale dynamical flow properties of a RBC and the micro-scale processes occurring within its membrane, that dictate properties which, in turn, influence the dynamics [19, 20].

The primary interest of this work is modelling of immiscible drops and erythrocytes, where the complex relationship at the boundary, between the fluids, is to be investigated. Hence, by using *bottom-up*, meso-scale modelling approaches, the interface between the fluids may be encapsulated with much higher accuracy, compared to at the macroscale, allowing detailed interface physics to be encapsulated, assessed and optimised. A natural candidate, then, for such an investigation, is the LBM. The benefits of using such a method for this work will, hopefully, be readily apparent; at any rate, they will be made explicitly clear in the remainder of this chapter.

## 2.2 Hydrodynamics

### 2.2.1 Governing Equations

Within the continuum description of fluid mechanics, governing fluid dynamics equations describe the macroscopic conservation of mass and momentum in a system.

## 2. Background in Hydrodynamics and Simulation Techniques

Unlike at the molecular level, where the fluid is comprised of molecules undergoing random Brownian motion, at the continuum scale, a single velocity value is assigned at every point in the fluid. (As an aside remark, the continuum concept of a fluid parcel contains many fluid molecules). Analytical solutions to these equations can only be found for very simple cases (such as flow between two parallel plates) [21], leading to the development of numerical methods to solve these equations for more complex geometries, i.e., porous media. LBM is an indirect Navier-Stokes solver, that uses a kinetic scale evolution equation to describe particle distributions, which can be shown to recover the macroscopic fluid dynamics equations to be outlined. In this section, the governing equations (Continuity, Cauchy Momentum and Navier-Stokes equations) are identified in preparation for further discussion (on how these equations link with LBM) in sections 2.3 and 3.3.1. This section will not provide detailed derivations, rather aim to present an overview —for further information the reader is referred to references [21, 22, 23, 24].

### 2.2.1.1 Continuity Equation

A fundamental equation descriptive of a fluid system is the continuity equation. Simply put, it is a continuum level description of the fact that, in a fluid system, mass is conserved. The derivation of this equation follows by considering the change of mass within a control volume, by appeal to the divergence theorem [25]. The continuity equation is given in two separate forms in Eqs. (2.1) and (2.2), with the time derivative in Eq. (2.1) giving the change in mass in the system and the divergence relating to the flow in and out of the control volume.

$$\frac{\partial \rho}{\partial t} + \nabla \cdot (\rho \underline{u}) = 0, \quad (2.1)$$

where  $\rho$ ,  $\underline{u}$  and  $\nabla$  are the fluid density, fluid velocity vector and gradient operator. An alternative form of Eq. (2.1) may be given as:

$$\frac{D\rho}{Dt} + \rho \nabla \cdot \underline{u} = 0, \quad (2.2)$$

above, the material derivative  $\frac{D\rho}{Dt}$  denotes the rate of change in density of a fluid element following the motion and is commonly used when describing fluid dynamics systems. The mathematical definition of the material derivative (of function  $f$ ) is:

$$\frac{Df}{Dt} = \frac{\partial f}{\partial t} + \underline{u} \cdot \nabla f.$$

If the fluid is incompressible, i.e.,  $\rho$  does not vary in time and space, then Eq. (2.1) can be simplified to:

$$\nabla \cdot \underline{u} = 0. \quad (2.3)$$

Hence, Eq.(2.3) is the incompressible continuity equation. Note, that an incompressible fluid flow is identified based of its Mach number (see section 2.2.3).

### 2.2.1.2 Incompressible Cauchy Momentum Equations

The general equations of motion describing the non-relativistic momentum conservation in the moving fluid can be derived from Newton's second law,  $F = ma$ . One obtains the eponymous Cauchy momentum equations, by considering flow and forces in an infinitesimal fluid element (a parcel). A full derivation can be found in [24]. The resulting incompressible Cauchy momentum equations are given in component form as:

$$\rho \frac{Du_\alpha}{Dt} = \frac{\partial \tilde{\sigma}_{\alpha\beta}}{\partial x_\beta} + \rho F_\alpha, \quad (2.4)$$

where  $\alpha, \beta = x, y, z$ ,  $F_\alpha$  is an external force, i.e., gravity and  $\tilde{\sigma}_{\alpha\beta}$  is the nine-component stress tensor. Stress is defined as a force per unit area acting on a surface element - which contains a magnitude and a direction (there being both tangential and normal stresses). Where, the eigenvalues of the stress tensor give the principle stresses which relate to the principle stress directions (stress tensor eigenvectors). Note, all terms in the above equation are on a per-unit volume basis. The first term in Eq. (2.4) represents the temporal and spatial change in momentum at a point, the second term is the total stress and the third term any force density, i.e., gravity.

In order to close Eq. (2.4), one must know the form of stress tensor  $\sigma_{\alpha\beta}$ . The effective definition of the stress tensor varies with the material one is modelling. For fluids, it will vary depending upon the fluid's classification as Newtonian or Non-Newtonian. This work deals entirely with the simulation of Newtonian fluids, i.e., water, oil etc., where the viscous stresses are related to the local strain rate. As such, the stress tensor, or constitutive equation for an incompressible Newtonian fluid may be given as [26]:

$$\tilde{\sigma}_{\alpha\beta} = -p\delta_{\alpha\beta} + \nu \left( \frac{\partial u_\alpha}{\partial x_\beta} + \frac{\partial u_\beta}{\partial x_\alpha} \right), \quad (2.5)$$

where  $p$  is hydrostatic pressure,  $\delta_{\alpha\beta}$  is the Kronecker delta function and  $\nu$  is the dynamic viscosity of the fluid. Note that, viewed as a continuum, fluid mixtures such as considered here, which contain deformable vesicles (e.g., blood, milk) are famously styled *non-Newtonian*. Non-Newtonian behaviour is emergent; of course, the components on which such mixtures are based are, intrinsically Newtonian.

### 2.2.1.3 Incompressible Navier-Stokes Equations

As stated, this work pertains to the simulation of incompressible, Newtonian fluids. Therefore, the equation that describes the momentum for such fluids is given by the incompressible form of the Navier-Stokes equations. These equations can be

## 2. Background in Hydrodynamics and Simulation Techniques

derived from the Cauchy Momentum equations, Eq. (2.4), by substituting in the constitutive equation for an incompressible Newtonian fluid, Eq. (2.5) into Eq. (2.4). After simplifying, the resultant incompressible Navier-Stokes equations are:

$$\rho \frac{D\mathbf{u}}{Dt} = -\nabla p + \eta \Delta \mathbf{u} + \mathbf{F}, \quad \nabla \cdot \mathbf{u} = 0, \quad (2.6)$$

where,  $\nu$  is the kinematic viscosity and the Laplacian operator is:

$$\Delta = \nabla \cdot \nabla = \frac{\partial^2}{\partial x_\beta \partial x_\beta}.$$

The significance of the incompressible Navier-Stokes equations, given by Eq. (2.6), can not be overstated. They allow for the description of the motion of a fluid, abstracted as infinitely divisible; therefore, these equations only remain valid while a continuum description holds —while the concept of a fluid parcel as many individual molecules (or atoms) is valid and the view of individual molecules' motions as having been in some sense averaged is not challenged.

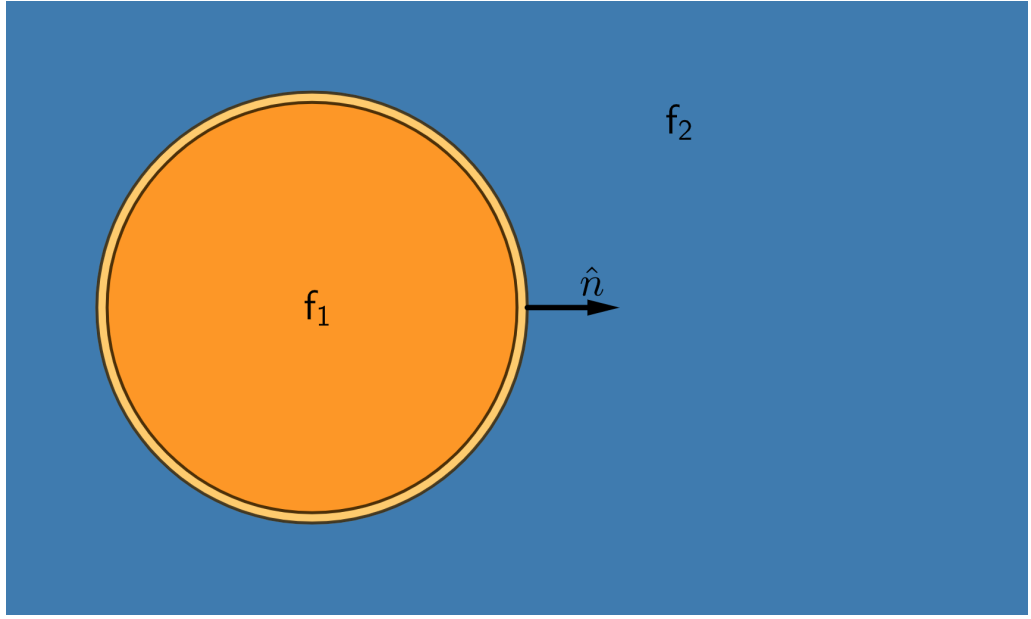
With the equations that describe the fluid behaviour now outlined, the boundary conditions at both liquid-solid and liquid-liquid interfaces need to be discussed.

### 2.2.2 Boundary Conditions

Alongside the governing partial differential equations that describe the fluid macroscopic properties over the domain, boundary conditions are needed to close fluid dynamics problems —providing vital information about how the fluid behaves at domain boundaries. As such, they need to be considered with the same attention. When looking at immiscible multi-component fluid flows —fluid flows containing multiple immiscible fluids —it is important to consider interfacial boundary conditions, imposed at a fluid-fluid interface (free surface), which should be recovered in simulation if one is to correctly capture physically consistent hydrodynamics. This section introduces two principle boundary conditions for this case, namely, the kinematic and dynamic boundary conditions. For clarity and future reference, Figure 2.2 shows two immiscible fluids,  $f_1$  and  $f_2$ ; the interface between the two fluids  $f_1$ - $f_2$  is curved, with the unit normal to the interface,  $\hat{n}$ , directed outwards, towards fluid  $f_2$ . Hypothetically, the diagram could depict an immiscible oil drop  $f_1$  submerged in water solution  $f_2$ . It should be noted that boundary conditions in the case of multi-phase flows, or where a phase transformation occurs, are not considered in this work.

For the following section of work, consider a three-dimensional case of the two-dimensional scenario depicted in Figure 2.2, such that a position on the interface





**Figure 2.2:** Schematic showing an immiscible drop, fluid  $f_1$ , submerged in a background fluid,  $f_2$ . Where, lighter orange rim shows the boundary of fluid  $f_1$ , and the unit normal of the interface,  $\hat{n}$ , is orientated pointing from  $f_1$  towards  $f_2$  as shown (although this choice is arbitrary)

between the two fluids  $f_1$  and  $f_2$  over time can be given by some function  $F(x, y, z, t) = 0$ . Assume that an excerpt of the surface is represented by a local manifold, or Monge patch and that the  $x, y$  axes are in the tangent plane of the surface excerpt. Then, by implicit function theory, a point on the interface can be given by a height function,  $h$ , meaning direction  $z$  is defined as  $z = h(x, y, t)$ . Also note that for the following work, subscript 1(2) denotes fluid 1(2), i.e.,  $\underline{u}_1$  is the velocity of fluid 1.

### 2.2.2.1 Kinematic Boundary Condition

The kinematic boundary condition encapsulates principles of mass transfer, across the interface. The two salient kinematic boundary conditions are: (i) the normal component of velocity is continuous across the interface —meaning that no holes develop in the interface, and (ii) the tangential component(s) of velocity across the interface is continuous, i.e., tangential components of velocity balance, on either side close to the interface, to avoid separation. The reader is directed to [23, 27], for further information regarding these conditions.

### Mutual Impenetrability

Starting with condition (i), a fluid parcel —a fictitious infinitesimal volume of fluid matter, whose shape can be distorted over time but the mass of the parcel remains constant (isochoric flow) —on the interface; such a parcel must remain in the interface,

## 2. Background in Hydrodynamics and Simulation Techniques

as the flow develops over time, for there is no relative motion perpendicular to the interface to act to remove it. The total mass of that fluid parcel must not change, as matter cannot be created or destroyed. This means that the interface surface must be a material invariant and as such [23]:

$$\frac{DF}{Dt} = \frac{\partial F}{\partial t} + \underline{u} \cdot \underline{\nabla} F = 0, \quad (2.7)$$

where,  $\underline{u}$  is equal to the velocity either side of the interface, i.e.,  $\underline{u}_1 = \underline{u}_2$  close to the interface. It is understood that for an implicitly defined surface, the normal to the surface may be determined by taking the gradient of the surface, where, here, it is assumed that the direction of the normal aligns with that in Figure 2.2 (points from  $f_1$  into  $f_2$ ). The unit normal to the surface is therefore given by:

$$\hat{n} = \frac{\underline{\nabla} F}{|\underline{\nabla} F|}. \quad (2.8)$$

Rearranging Eq. (2.8) and substituting into Eq. (2.7), results in the following general kinematic condition:

$$\underline{u}_1 \cdot \hat{n} = \underline{u}_2 \cdot \hat{n} = -\frac{1}{|\underline{\nabla} F|} \frac{\partial F}{\partial t}, \quad (2.9)$$

in which it follows that for the case where the interface has no time dependency, the kinematic condition simplifies to the following:

$$\underline{u}_1 \cdot \hat{n} = \underline{u}_2 \cdot \hat{n} = 0. \quad (2.10)$$

Equations (2.9, 2.10) state the normal component of velocity must be equal either side of the interface and are often referred to as the condition of mutual impenetrability. Here, Eq. (2.10) states that the normal component of velocity is zero either side of the interface; this is the case for interfaces which are not time dependent and also for boundaries between a solid, impermeable material and a fluid. Equation (2.9) represents the case where the normal component of velocity either side of the interface at a point is equal, but not necessarily zero. This results in either of two outcomes: (a) the whole interface is moving at the same velocity, thus maintaining shape and translating with the local background fluid, or (b) the normal component of velocity either side of the interface is balanced, but varies with position on the interface. This means for case (b), there would be an expected deformation of interface shape [27].

### No-Slip

Condition (ii) states that the tangential component of velocity at either side of the interface must balance, and is hence continuous across the interface, this is to avoid

## 2. Background in Hydrodynamics and Simulation Techniques

an unphysical, infinite shear at the boundary. It should be noted that this condition is often referred to as the *no-slip* condition and it only applies to viscous flows, where continuum descriptions of the fluid are valid. The tangential component of a vector can be defined as the original vector with its normal component projected out:  $\underline{v}_t = \underline{v} - \hat{n} \cdot (\underline{v} \cdot \hat{n})$ , where  $\underline{v}_t$  is the tangent component of vector  $\underline{v}$ . As such, the no-slip boundary condition may be given as:

$$\underline{u}_1 - \hat{n} \cdot (\underline{u}_1 \cdot \hat{n}) = \underline{u}_2 - \hat{n} \cdot (\underline{u}_2 \cdot \hat{n}), \quad (2.11)$$

where, Eq. (2.11) is applied only in the interfacial region and  $\underline{u}_1$  ( $\underline{u}_2$ ) denotes the fluid velocity close the interface in fluids  $f_1$  ( $f_2$ ). Equation (2.11) simplifies to the following when a fluid-solid boundary interaction is considered, where the surface has zero velocity:

$$\underline{u} - \hat{n} \cdot (\underline{u} \cdot \hat{n}) = 0, \quad (2.12)$$

which states that, at a solid boundary, with zero velocity, the fluid in contact with that boundary must have no tangential component of velocity (and no normal component of velocity if the solid surface is impermeable from Eq. (2.10)).

### 2.2.2.2 Dynamic Boundary Condition

The dynamic boundary condition for the case of a fluid-fluid interface states that there is continuous stress across the interface between the fluids (free surface). Using this statement one can formulate a stress balance between the fluids at the free surface in the normal direction [23, 27]:

$$\hat{n} \cdot \underline{\tilde{\sigma}}_1 = \hat{n} \cdot \underline{\tilde{\sigma}}_2, \quad (2.13)$$

where,  $\underline{\tilde{\sigma}}_\alpha$  is the stress tensor for fluids  $\alpha = 1, 2$ . Although Eq. (2.13) describes the stress balance between two fluids at the free-surface, it only does so adequately for flat interfaces. For curved interfaces, one must also consider the influence of surface tension as described by the Young-Laplace equation [28, 29, 30]:

$$\begin{aligned} \Delta p &= \sigma \nabla \cdot \hat{n} \\ &= \sigma \left( \frac{1}{R_1} + \frac{1}{R_2} \right) \end{aligned} \quad (2.14)$$

where,  $\Delta p$  is the pressure difference across the interface,  $\sigma$  is the surface tension (note, unrelated to the stress tensor with notation  $\tilde{\sigma}$ ) and  $R_1$ ,  $R_2$  are the principle radii of curvature. This equation describes the pressure jump at the interface between two fluids, influenced by the shape (curvature) of the interface. Surface tension  $\sigma$  drives

## 2. Background in Hydrodynamics and Simulation Techniques

the surface area of the free surface to a minimum, creating an increased internal pressure. For a spherical interface such as the one depicted in Figure 2.2, the interior fluid  $f_1$  would have a higher pressure than the exterior fluid  $f_2$  due to surface tension. As such, the normal stress balance at the free surface between fluids needs to include this description of the pressure difference and hence the effect of surface tension. Therefore, the dynamic condition of Eq. (2.13) may be adapted to the following:

$$\hat{n} \cdot \underline{\tilde{\sigma}}_1 - \hat{n} \cdot \underline{\tilde{\sigma}}_2 = -\sigma \left( \frac{1}{R_1} + \frac{1}{R_2} \right) \hat{n}. \quad (2.15)$$

This description is now termed a dynamic fluid-fluid boundary condition, since the physics of surface tension is encapsulated.

There must also be tangential stress balance across the interface. This condition can be given in the following form (where the simplification that the normal component of velocity at the interface is zero has been used —Eq. (2.9)):

$$\eta_1 \frac{\partial u_{t1}}{\partial n} = \eta_2 \frac{\partial u_{t2}}{\partial n}, \quad (2.16)$$

where,  $u_{t1}$  corresponds to the tangential component of velocity for fluid  $f_1$ ,  $\frac{\partial}{\partial n}$  corresponds to the derivative in the normal direction to the interface and  $\eta_1$  the dynamic viscosity of fluid  $f_1$ .

Equations (2.9), (2.11), (2.15) and (2.16) correspond to the key kinematic and dynamic boundary conditions discussed throughout this work. The following section will examine relevant non-dimensional quantities, which are also utilised within work.

### 2.2.3 Non-Dimensional Quantities

Non-dimensional quantities and non-dimensional numbers are used to analyse and classify flow behaviour in relation to the system being investigated within fluid mechanics. They also are utilised within LB methodology itself, when setting simulation parameters, analysing system stability and calibration of the system (law of similarity). Identified here are four key non-dimensional quantities that are discussed and used throughout different sections of this work, which are the: Reynolds (Re), Mach (Ma), Weber (We) and Capillary (Ca) numbers.

The Reynolds number (Re) is a group which quantifies the ratio of inertial to viscous forces (resistance forces between the fluid layers when subject to a shear). Its value can indicate if the flow is laminar (lower Re) - *where fluid particles flow in parallel layers* or turbulent (larger Re) - *where the fluid suffers random changes in velocity and pressure*. The Reynolds number is defined as:

$$\text{Re} = \frac{ul}{\nu} = \frac{\text{inertial forces}}{\text{viscous forces}}, \quad (2.17)$$

## 2. Background in Hydrodynamics and Simulation Techniques

where  $u$ ,  $l$  and  $\nu$  are the characteristic flow velocity, characteristic length scale and kinematic viscosity of the fluid.

The Mach number (Ma) is another important group that describes the ratio of flow velocity to the speed of sound in the medium being simulated. It is defined as:

$$\text{Ma} = \frac{u}{c_s}, \quad (2.18)$$

where  $u$ ,  $c_s$  is the local flow velocity and speed of sound. Generally, if the flow is isothermal and  $\text{Ma} \leq 0.1$ , then the flow is considered to be incompressible, i.e., compressibility effects can be ignored. This bounds the regime of viscous flow describable by the weakly compressible Navier-Stokes equations. The importance of these two dimensionless numbers within lattice Boltzmann will be further discussed shortly; these groups will also be used in subsequent work, within this thesis.

The Weber number (We) can be used to describe the ratio of inertial forces to cohesion forces (e.g., surface tension), between liquid-liquid interfaces. It can help determine if a drop will break up within a flow into small drops (i.e., larger Weber number flows —where inertial forces dominate), or maintain its shape due to dominant surface tension forces (i.e., smaller Weber number flows). It is defined as:

$$\text{We} = \frac{\rho u^2 l}{\sigma} = \frac{\text{inertial forces}}{\text{cohesion force}}, \quad (2.19)$$

where  $\rho$ ,  $u$ ,  $l$ ,  $\sigma$  are density, velocity, characteristic length scale and surface tension. Finally, the Capillary number (Ca) quantifies the relationship between viscous drag and surface tension forces; it is defined as:

$$\text{Ca} = \frac{\mu u}{\sigma} = \frac{\text{Viscous drag}}{\text{surface tension}}, \quad (2.20)$$

where  $\mu$ ,  $u$  and  $\sigma$  are dynamic viscosity, characteristic velocity and surface tension. Both the We and the Ca numbers can be used to quantify the deformation between two immiscible liquids, where inertial and viscous forces act to deform the drop, with surface tension forces working against these forces to maintain and preserve drop shape. As such, these dimensionless quantities play an important role in understanding drop behaviour in different flows and their importance will be discussed further in Chapter 4, when considering flow past a liquid drop, in which they are used to help predict drop shape.

## 2.3 Lattice Boltzmann Equation Simulation

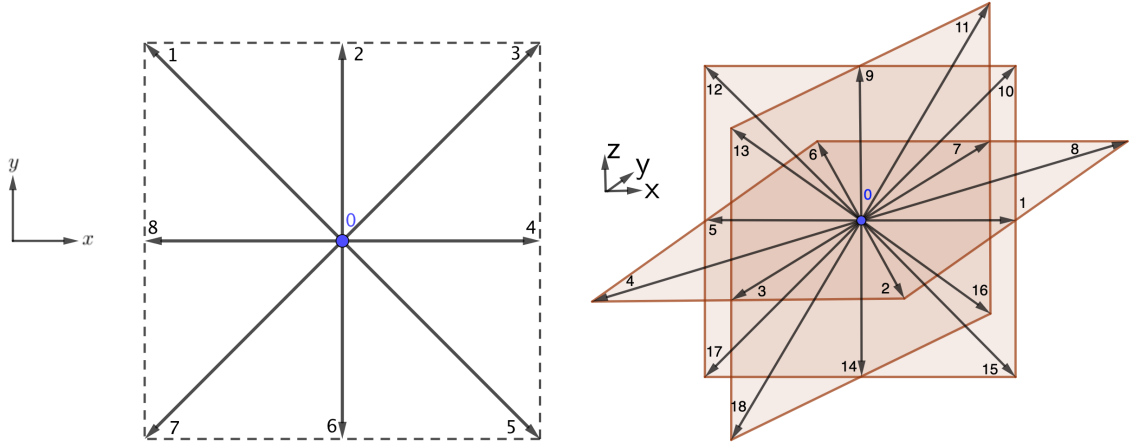
### 2.3.1 Development and Fundamentals

The lattice Boltzmann method (LBM) was developed from the method of lattice gas cellular automata (LGA), first introduced in 1973 by Hardy et al. [31]. The LGA HPP model used Boolean algebra to represent a particle either being present or not present at a given site on a square lattice where akin to the LBM, particles movement was restricted to a finite number of directions—four in this case. In order to calculate the macroscopic hydrodynamic quantities of mass and momentum, ensemble averaging was required to reduce that statistical noise which led to increased computational expense. Due to the method not recovering the Navier-Stokes equations of motion, as well as a lack of Galilean invariance, intrinsic noise and unphysical velocity dependent pressure [32], it serves only as a milestone. The idea was matured by Frisch, Hasslacher & Pomeau (1986) [33], who developed the FHP LGA, based on a hexagonal mesh that recovered the Navier-Stokes equations and allowed mass and momentum conservation. This was done by ensuring a certain lattice symmetry, affording the ability to model an isotropic fluid [34]. Following this, a further advancement of the LGA towards the LBM was the removal of the statistical noise, through the introduction of a pre-averaged distribution function as the primary quantity, replacing the Boolean operation within LGA models [3]. This work was then advanced by Higuera & Jiménez (1989) [4], who substituted the continuous, non-linear collision operator for a discrete collision rule. Since then, various collision operators have been developed, with the simplest and most popular the Bhatnagar-Gross-Krook (BGK) variant [35], discussed in the following subsection.

The LBM is an unconventional *bottom-up* approach to modelling fluid dynamics based on kinetic theory, whereas traditional *top-down* CFD starts with macroscopic equations of motion which are then discretised. Although LBM is a Navier-Stokes solver, it functions indirectly, with the lattice Boltzmann equation (LBE) regarded as a discretised approximation for solving the Boltzmann equation—which describes the dynamical behaviour of dilute gases in the thermodynamic limit. The LBM can be shown to recover the Navier-Stokes equations by appealing to Chapman-Enskog procedure, see section 3.3.1 for a full explanation. The method uses a discrete, Eulerian lattice—fixed reference grid—where particle distributions (or particle populations), representative of groups of fictitious particles, are evolved and are tracked over the lattice, as described by a time dependent distribution function  $f_i(\underline{r}, t)$ . This approach to modelling fluids is justified through the argument that microscopic behaviour of individual particles does not impact the dynamics of the

## 2. Background in Hydrodynamics and Simulation Techniques

fluid, whereas the collective behaviour of many of these individual particles (particle distributions) does describe the fluids dynamics appropriately. The fluid is assumed to be close to equilibrium locally on the lattice, with the equilibrium distribution of the fluid derived from a truncated, uniformly translating Maxwell-Boltzmann distribution (for particle velocities in an ideal gas) [6]. The distribution function  $f_i(\underline{r}, t)$ , represents the probability of finding a fluid particle travelling in lattice direction  $i$ , at lattice site  $\underline{r}$  at a particular time step  $t$  (in lattice units). The number of directions the fluid particle can move in, indexed by  $i$ , depends upon the size and dimensions of the lattice used. The common labelling convention for lattice models within LBM is DaQb, where ‘a’ is the dimension of the lattice and ‘b’ is the number of lattice links—formally the number of discrete lattice velocities. The two lattice structures used within this work are the D2Q9 lattice and the D3Q19 lattice. These lattice structures are shown in Figure 2.3.



**Figure 2.3:** Schematic showing the two lattice structures used within this work and link labelling, with (left) being the D2Q9 lattice and (right) the D3Q19 lattice.

$i$	0	1	2	3	4	5	6	7	8
$c_{ix}$	0	-1	0	1	1	1	0	-1	-1
$c_{iy}$	0	1	1	1	0	-1	-1	-1	0
$t_i$	$t_0$	$t_1$	$t_2$	$t_1$	$t_2$	$t_1$	$t_2$	$t_1$	$t_2$

**Table 2.1:** D2Q9 lattice structure, showing lattice link ( $i$ ), lattice velocity vector ( $\underline{c}_i$ ) components and lattice weights ( $t_i$ ). Here,  $t_0 = \frac{4}{9}$ ,  $t_1 = \frac{1}{36}$ ,  $t_2 = \frac{1}{9}$ .

The lattice Boltzmann equation, or evolution equation, is given as:

$$f_i(\underline{r} + \underline{c}_i \Delta t, t + \Delta t) = f_i(\underline{r}, t) + \Omega, \quad (2.21)$$

where  $\underline{r}$  corresponds to lattice site position,  $t$  is the time (in lattice units),  $\underline{c}_i$  is the lattice velocities,  $\Delta t$  corresponds to the time interval/ step and  $\Omega$  is the

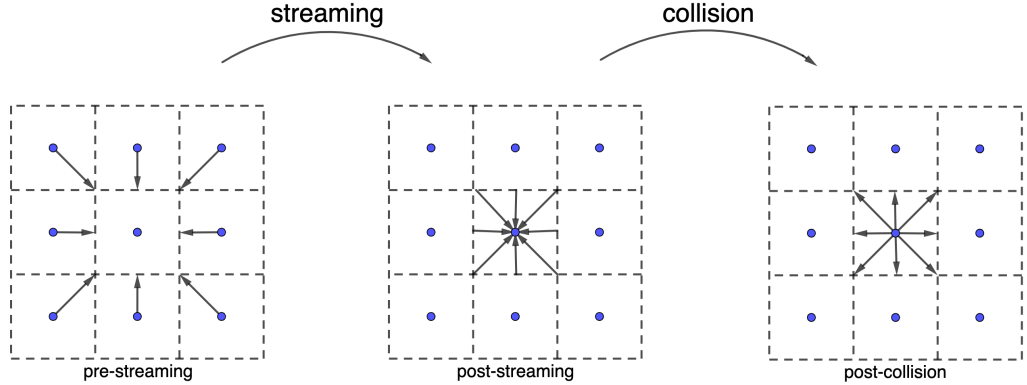
## 2. Background in Hydrodynamics and Simulation Techniques

$i$	0	1	2	3	4	5	6	7	8	9	10	11	12	13	14	15	16	17	18
$c_{ix}$	0	1	1	0	-1	-1	-1	0	1	0	1	0	-1	0	0	1	0	-1	0
$c_{iy}$	0	0	-1	-1	-1	0	1	1	1	0	0	1	0	-1	0	0	1	0	-1
$c_{iz}$	0	0	0	0	0	0	0	0	0	1	1	1	1	1	-1	-1	-1	-1	-1
$t_i$	$t_0$	$t_1$	$t_2$	$t_1$	$t_2$	$t_1$	$t_2$	$t_1$	$t_2$	$t_1$	$t_2$	$t_2$	$t_2$	$t_2$	$t_1$	$t_2$	$t_2$	$t_2$	$t_2$

**Table 2.2:** D3Q19 lattice structure, showing lattice link ( $i$ ), lattice velocity vector ( $c_i$ ) components and lattice weights ( $t_i$ ). Here,  $t_0 = \frac{1}{3}$ ,  $t_1 = \frac{1}{18}$ ,  $t_2 = \frac{1}{36}$ .

collision operator. There are different forms the collision operator can take; these are discussed further in section 2.3.2.

Equation (2.21) encapsulates two key stages within the LBM: (i) streaming; (ii) collision. In streaming, particle populations move to neighbouring cells over a time interval  $\Delta t$  and collision occurs when particles collide locally inside each grid cell and then are redistributed. Pictorially, Figure 2.4 represents the streaming and collision stages within an interior node, on the lattice, which shows the particle distribution functions propagating, colliding and redistributing over a single time step.



**Figure 2.4:** Schematic showing the streaming and collision process for one node on the domain over one time step on a D2Q9 lattice. (Left) pre-streaming stage. (Middle) post streaming where particle distributions propagate into the interior node. (Right) post collision, where particle distributions have collided and been redistributed.

During the collision process, particle distributions are relaxed towards a local equilibrium, where the equilibrium distribution function,  $f_i^{(\text{eq})}(\rho, \underline{u})$ , is given as:

$$f_i^{(\text{eq})}(\rho, \underline{u}) = t_i \rho \left( 1 + \frac{u_\alpha c_{i\alpha}}{c_s^2} + \frac{u_\alpha u_\beta c_{i\alpha} c_{i\beta}}{2c_s^4} - \frac{u^2}{2c_s^2} \right), \quad (2.22)$$

where  $\rho$  is the fluid density,  $\underline{u}$  is the fluid velocity at position  $\underline{r}$ ,  $u_\alpha$  is the  $\alpha$  component of the fluid velocity,  $c_{i\alpha}$  is the  $\alpha$  component of the lattice velocity in the  $i$ th direction,  $c_s$  is the speed of sound of the model and  $t_i$  is the lattice link weights. The lattice link weights are specific to the lattice model (i.e., DaQb) and are such to meet isotropy conditions, with these conditions being given later in section 3.3.1. For the lattice link weights used in the D2Q9 and D3Q19 models, see Tables 2.1 and 2.2.



## 2. Background in Hydrodynamics and Simulation Techniques

To calculate local macroscopic quantities, i.e., density, momentum and momentum flux, one takes the moments of the distribution function and sums them locally, at lattice sites over the lattice links. Density is found from the zeroth moment of the distribution function, momentum from the first moment and momentum flux from the second moment. These equations are expressed here:

$$\begin{aligned}\sum_i f_i &= \rho, \\ \sum_i f_i c_{i\alpha} &= \rho u_\alpha, \\ \sum_i f_i c_{i\alpha} c_{i\beta} &= \Pi_{\alpha\beta},\end{aligned}$$

where  $\Pi_{\alpha\beta}$  is the momentum flux tensor.

The above-outlined technique can be shown to have asymptotic behaviour as follows: the weakly compressible Navier-Stokes equations as the equations of motion of the macroscopic quantities  $\rho$  and  $u_\alpha$ , with an isothermal equation of state —under the low Mach number limit assumption (see section 3.3.1). Consequently, this imposes a restriction on the velocity magnitude, with  $|u| \ll c_s$ .

### 2.3.2 Collision Operators

Collision within LBM describes the relaxation of the distribution function towards an equilibrium distribution given by the uniformly translating Maxwell-Boltzmann equilibrium distribution. Physically, this reflects the collision of particles which pushes the system towards an equilibrium state. This collision process in the LBE (Eq. (2.21)) can be characterised using different collision operators  $\Omega$ , with three of the most commonly implemented algorithms in literature being: Bhatnagar Gross and Krook (BGK) [35], two-relaxation time (TRT) [36, 37] and multiple relaxation time (MRT) [38] schemes. Each operator has unique advantages and drawbacks, with differing levels of complexity (conceptually and computationally). This section aims to briefly introduce these different approaches of characterising the collision step, discussing which will be implemented in this work and why.

#### 2.3.2.1 BGK

The first and simplest collision operator commonly implemented within LB schemes is the Bhatnagar-Gross-Krook (BGK) operator [35]. The use of the BGK collision operator was extremely valuable in advancing the LBM as the approximation of the collision process reduced the mathematical difficulty involved with working with the method. The BGK approximation is still one of the most widely implemented approximations, with its popularity stemming from the fact that it retains the

## 2. Background in Hydrodynamics and Simulation Techniques

non-linearity of Boltzmann’s equation whilst providing a vast simplification [6].

The BGK collision operator, aiming to represent the inter-particle collisions that drive the system towards equilibrium, eliminates  $f_i$  distributions and replaces them with equilibrium  $f_i^{(\text{eq})}$  distributions relative to a single relaxation rate for all scales. The BGK operator is given as follows [35]:

$$\Omega = -\frac{f_i - f_i^{(\text{eq})}}{\tau}, \quad (2.23)$$

where  $f_i^{(\text{eq})}$  is the local equilibrium distribution (approximately the uniformly translating Maxwell-Boltzmann distribution) [6] and  $\tau$  is a constant value for the relaxation time—the characteristic time for the fluid to reach an equilibrium distribution locally—which is much simpler than the complex relaxation time functional introduced in the Boltzmann equation. Since the relaxation is only dependent upon  $\tau$ , it is sometimes referred to as the single-relaxation time (SRT) scheme. Through Chapman-Enskog analysis, in section 3.3.1, the relaxation time can be seen to determine the kinematic viscosity  $\nu$  (and vice-versa), with the relationship between the two imposing a resultant constraint on  $\tau$ —in order to get a physical (non-negative) kinematic viscosity—for a simple scheme being:

$$\nu = \frac{1}{3} \left( \tau - \frac{1}{2} \right), \quad \tau > \frac{1}{2}. \quad (2.24)$$

Following the constraint opposed on  $\tau$ , the value of  $\tau$  will affect how the fluid is relaxed towards equilibrium. Table 2.3 characterises the relaxation based on varying the  $\tau$  value [39]:

$\tau$ value	relaxation classification
$0.5 < \tau < 1$	over-relaxed
$\tau = 1$	fully-relaxed
$1 < \tau$	under-relaxed

**Table 2.3:** Table showing how the  $\tau$  value affects how the fluid is relaxed to equilibrium within the BGK collision operator.

The main advantage of the BGK operator is its simplicity and hence transparency, which makes it easy to implement. However, due to the simplicity, relaxation towards equilibrium takes place at a single rate for all hydrodynamic quantities, the relaxation process is not tuneable and has issues with stability for certain flows (large Reynolds number flows where one needs to avoid  $\tau \rightarrow 0.5$ ) and complex geometries (e.g., porous media, where  $\tau$  affects wall location, when bounce-back boundaries are implemented [39]).

## 2. Background in Hydrodynamics and Simulation Techniques

### 2.3.2.2 TRT

The two-relaxation time collision operator (TRT) was introduced by Ginzburg in 2005, here relaxation involves two parameters [36, 37]. The development of the TRT collision scheme arose from the more complex MRT scheme, where the number of relaxation parameters was reduced to one fixed and one tuneable (kinetic) relaxation parameter. Collision is now performed on symmetric and anti-symmetric parts of the distribution function. These distribution functions are defined as follows:

$$\begin{aligned} f_{is}^{(\text{eq})} &= f_i^{(\text{eq})} + f_{-i}^{(\text{eq})}, & f_{ia}^{(\text{eq})} &= f_i^{(\text{eq})} - f_{-i}^{(\text{eq})}, \\ f_{is} &= f_i + f_{-i}, & f_{ia} &= f_i - f_{-i}, \end{aligned} \quad (2.25)$$

where, subscript  $s$  and  $a$  correspond to symmetric and anti-symmetric, subscript  $i$  and  $-i$  correspond to link direction  $i$  and opposite link direction  $-i$ . By using two relaxation parameters, it allows for a larger toleration of fluctuations from equilibrium compared to that of the BGK collision operator.

The TRT collision operator, corresponding to the evolution equation in Eq. (2.21), is now defined as:

$$\Omega = -\frac{\Delta t}{\tau_s} \left( f_{is}(\underline{r}, t) - f_{is}^{(\text{eq})}(\rho, \underline{u}) \right) - \frac{\Delta t}{\tau_a} \left( f_{ia}(\underline{r}, t) - f_{ia}^{(\text{eq})}(\rho, \underline{u}) \right). \quad (2.26)$$

The extra degree of freedom compared to the BGK scheme affords stability gains, connected to a *magic-parameter* relating to the truncation error, that can be tuned depending upon the flow being simulated [40]. Additionally, a reduction in the need to tune individual relaxation relates to different modes within the MRT scheme helped retain the simplicity of the BGK scheme. A disadvantage of the TRT collision scheme is that the operator's mathematical derivation and presentation can make it hard to interpret and understand. Knowing this, recent efforts have been made to articulate the method and its implementation in a more transparent way [41]. This barrier, as well as the fact that the method is: (i) neither the simplest collision operator—due to needing to relax symmetric and anti-symmetric links as opposed to the single relaxation rate in the BGK operator; and (ii) not sufficiently tuneable—due to only having one free, tuneable parameter in comparison to the MRT model which has multiple, can be seen as drawbacks.

### 2.3.2.3 MRT

The final collision scheme needed to be discussed is the multi-relaxation time (MRT) scheme. Multiple-relaxation time schemes, as the name suggests, involve the use of multiple relaxation parameters, allowing the individual tuning of the relaxation of hydrodynamic quantities such as density, velocity and momentum fluxes, as well

## 2. Background in Hydrodynamics and Simulation Techniques

as some additional non-hydrodynamic “ghost” modes —modes which contain no hydrodynamic (physical) information, that can be tuned for further stability [38, 42, 43, 44, 45, 46]. An ability to relax modes at differing rates is physically consistent and thus may be seen as a more physically accurate treatment of the collision process compared to that of the BGK operator [47].

The first MRT collision scheme was introduced by D’Humières [38] as a way of removing instabilities, stemming from the BGK collision operator. Since this time, many researchers have contributed to MRT scheme literature: Lallemand et al., [42] produced an analysis which explored the tuneability of the relaxation parameters to enhance the stability of the scheme; Dellar [48] continued work considering how the non-hydrodynamic modes relate to method stability; Halliday et al. [49] developed a D2Q9 MRT collision scheme based on this prior art, with the inclusion of a Guo forcing, which was then extended to D3Q19 by Xu et al. [50].

Multi-relaxation time schemes differ from TRT and BGK schemes, where instead of performing the relaxation of distribution functions towards equilibrium in population space, relaxation occurs within moment space. First, to recover key hydrodynamic properties such as density, momentum and stress, appropriate terms are projected on the distribution function basis, creating a projection matrix of left row eigenvectors. The size of the projection matrix, and thus the number of modes, depends upon the chosen lattice structure, i.e., for the D2Q9 model there are nine modes in which only 6 are hydrodynamic modes, (having physical significance), the remaining 3 modes being the “ghost” modes [45, 46]. The collision operator for the MRT scheme, corresponding to evolution equation (2.21) is given as:

$$\Omega = \sum_j A_{ij} \left[ f_j^{(0)}(\underline{r}, t) - f_j(\underline{r}, t) \right], \quad (2.27)$$

where  $A_{ij}$  is the collision matrix  $i, j$  element. To highlight the transformation from population space to moment space, as well as the collision process, it is convenient to follow the analysis in [49] by defining the evolution equation for this MRT scheme as such, combining Eq. (2.21) and Eq. (2.27):

$$\underline{f}^\psi = \underline{f} + \underline{A} \left( \underline{f}^{(0)} - \underline{f} \right), \quad (2.28)$$

where  $\underline{f}^\psi$ ,  $\underline{f}$  and  $\underline{f}^{(0)}$  are column vectors for the post collision distribution, distribution and equilibrium distribution functions.  $\underline{A}$  is the collision matrix, which is constructed of left row eigenvectors effectively defining of hydrodynamic and non-hydrodynamic moments and their corresponding eigenvalues. The following short analysis aligns with that presented in reference [49]. A projection matrix  $\underline{M}$  —containing left row eigenvector modes which, when projected onto the distribution function set,

## 2. Background in Hydrodynamics and Simulation Techniques

recover the correct hydrodynamic properties —is projected onto Eq. (2.28) and simplified as follows [49]:

$$\begin{aligned}\underline{\underline{M}} \underline{\underline{f}}^+ &= \underline{\underline{M}} \underline{\underline{f}} + \underline{\underline{M}} \underline{\underline{A}} \left( \underline{\underline{f}}^{(0)} - \underline{\underline{f}} \right), \\ \underline{\underline{M}} \underline{\underline{f}}^+ &= \underline{\underline{M}} \underline{\underline{f}} + \underline{\underline{M}} \underline{\underline{A}} \underline{\underline{M}}^{-1} \left( \underline{\underline{M}} \underline{\underline{f}}^{(0)} - \underline{\underline{M}} \underline{\underline{f}} \right), \\ \underline{\underline{M}} \underline{\underline{f}}^+ &= \underline{\underline{M}} \underline{\underline{f}} + \underline{\underline{\Lambda}} \left( \underline{\underline{M}} \underline{\underline{f}}^{(0)} - \underline{\underline{M}} \underline{\underline{f}} \right),\end{aligned}\tag{2.29}$$

where, due to  $\underline{\underline{M}}$  containing left row eigenvectors of  $\underline{\underline{A}}$ , the eigenvalue definition that  $\underline{\underline{\Lambda}} = \underline{\underline{M}} \underline{\underline{A}} \underline{\underline{M}}^{-1}$  has been used. The outcome is a set of mode-specific lattice Boltzmann Bhatnagar–Gross–Krook (LBGK) style evolution equations, where hydrodynamic and non-hydrodynamic moments can be relaxed individually, in moment space. Following the relaxation in Eq. (2.29), the modes are converted back to population space, by inverting  $\underline{\underline{M}}$ . The MRT scheme is explained in more detail during its implementation in Chapter 4.

The benefits of using the MRT collision schemes is the enhanced stability one can gain, due to the ability to tune the relaxation of modes individually. The drawbacks of the method are its increased complexity and additional computational cost compared to the simplistic BGK collision scheme. Although, it is possible to only see a 15-20% computational overhead compared to the BGK scheme [43, 39].

### 2.3.2.4 Comparison of the Collision models

In conclusion, the collision operator one chooses to implement will highly depend upon a few factors, such as, the computational performance one is willing to accept, the complexity of the flow that is being simulated and the extent to which simulating flow close to boundaries accurately is important.

The BGK collision operator is the most transparent and simplest to implement, with just one relaxation parameter. However, it is the least stable scheme, with viscosity limitations being imposed, due to its relationship with the relaxation parameter  $\tau$ . Furthermore, when using the BGK collision operator in LB schemes, errors when simulating no-slip boundary conditions can become more severe, due to oscillations in flow fields and inaccurate boundary location, caused by the choice of  $\tau$  [51]. The TRT operator retains some of the BGK model's simplicity in comparison to the MRT scheme, as well as enhanced stability, due to an extra, tuneable, relaxation parameter. There is, of course, a computational downside to using the TRT collision operator over the BGK model, with reported CPU time being around 15 % quicker in the LBGK schemes [51].

The MRT collision scheme provides the greatest stability out of the three collision

## *2. Background in Hydrodynamics and Simulation Techniques*

operators, but is the most complex to implement, with more tuneable parameters. Because this research investigates multi-component flows, the implementation of an MRT operator would furnish welcomed, additional stability, in the face of more complex flows, and as such, we chose to implement it in a majority of the simulations. It will also produce a more physically accurate representation of flow close to no-slip boundaries. That said, in certain cases, the BGK collision scheme is utilised, in order to provide comparison across collision models, as well as transparency in mathematical analysis' —such as the Chapman-Enskog procedure.

Now the LBM collision schemes chosen for this work have been considered, we proceed to consider the other obvious degree of freedom available to us. The three most popular lattice Boltzmann methods for the simulation of immiscible multi-component fluid flows will be discussed, with emphasis placed on the selection of the most suitable method.

### **2.3.3 Multi-Component Lattice Boltzmann**

The work in this thesis focuses on the simulation of isothermal immiscible multi-component fluid flows at the mesoscale, with attention to the simulation of two-component (binary) fluid flows. The definition of a multi-component fluid flow is a flow containing two or more different fluids (i.e., a two-component fluid flow could be a mix of water and oil). A multi-phase fluid flow, in contradistinction contains multiple phases (gas, liquid and solid). Some flows can be classified as multi-component and multi-phase flows, but this work adheres strictly to the simulation of isothermal immiscible multi-component fluid flows performed within the regime of arrested coalescence. At the continuum scale, the interface between two immiscible fluids is discontinuous. At the mesoscale, within LB models, the interface between two immiscible fluids is diffused —sometimes LBM is classified as a diffused interface model, there existing a quasi two-dimensional interfacial region between the fluids. The accurate simulation of this interfacial region is extremely important, examined through the lens of recovering correct interfacial kinematics and dynamics —see section 2.2.2.

The dynamics of the fluids in a multi-component flow can be described by the governing equations (Continuity and Navier-Stokes) and also the physics of surface tension. Surface tension was briefly introduced, above, when discussing the dynamical boundary condition between two fluids, in order to help describe the pressure jump between fluids at a free surface. Surface tension, or interface tension between two fluids reflects the forces between molecules of the same and opposing fluid

## *2. Background in Hydrodynamics and Simulation Techniques*

species within the interfacial region, i.e., the surface formed by the fluids. Consider an immersed air bubble in a water solution, the interfacial tension describes the intermolecular forces between the molecules at the boundary between the air bubble and the water. Here, the pressure on either side of the interface must balance, to avoid holes forming, even though in equilibrium the pressure on the inside of the air bubble will be larger than that of the external fluid. This difference in pressure is described by the Young-Laplace equation, given in Eq. (2.14) [28, 29].

One of LBM's strengths is its ability to simulate multi-component and multi-phase flows, with little extra computational difficulty and expense. Taking the original Rothman and Keller immiscible lattice gas cellular automata model [52], Gunstensen et al., developed the first multi-component lattice Boltzmann model [53, 54]. Their model used the innate ability of LBM to simulate both fluids individually, by splitting up the distribution function, into the different species and then segregating the fluids afterwards, in a separate algorithmic step. This was the first colour-gradient model developed. Since the development by Gunstensen et al., several distinct methods of simulating multi-component flows using LBM have been outlined, which can be conveniently classified based on their physical contents [55]. The first colour-gradient or chromodynamic model [53, 54, 56, 57, 58, 59], has been enhanced since it was introduced by Gunstensen et al., and uses an immersed boundary force and an segregation rule, to simulate multi-component flows. The second, the Shan-Chen method [60, 61, 62, 63], incorporates intermolecular interactions between particle distributions and, as such, is suited to workers from a molecular dynamics background. The third, the Free-energy model [64, 65, 66], uses a thermodynamically consistent free energy functional which encapsulates the thermodynamics of the system. These are currently three of the most popular multi-component lattice Boltzmann methods implemented and, as such, they will be briefly introduced in the following sections, the choice of one of these methods for this work being justified, as well as their strengths and limitations examined. For further detail of the methods, we refer the reader to the original model papers already cited, as well as references such as [6, 67, 47, 39] and review articles: [68, 69].

### **2.3.3.1 Shan-Chen Pseudopotential Model**

The Shan-Chen pseudopotential model developed by Shan and Chen [60, 61] is capable of simulating multi-phase and multi-component flows and does so through the inclusion of intermolecular interactions between particle distributions encapsulated,

## 2. Background in Hydrodynamics and Simulation Techniques

in a forcing term. For transparency, continuing with the BGK collision operator, the forced evolution equation for the Shan-Chen pseudopotential model is given by:

$$f_i^{(\sigma)}(\underline{r} + \underline{c}_i \Delta t, t + \Delta t) = f_i^{(\sigma)}(\underline{r}, t) - \frac{\Delta t}{\tau^{(\sigma)}} \left( f_i^{(\sigma)}(\underline{r}, t) - f_i^{\text{eq}(\sigma)}(\underline{r}, t) \right) + \left( 1 - \frac{\Delta t}{2\tau^{(\sigma)}} \right) F_i^{(\sigma)}(\underline{r}, t) \Delta t, \quad (2.30)$$

where, superscript  $\sigma$  denotes the fluid component, hence  $\tau^{(\sigma)}$ ,  $F_i^{(\sigma)}$  are the corresponding relaxation time and forcing term for the fluid component  $\sigma$ . It is important to note that appropriate pairing of a force representative of the intermolecular interactions between particle distributions is crucial to the model. Shan-Chen first presented a forcing that resulted in an altered equilibrium velocity, that included the interaction force [60, 62]. It has been shown that this approach of including the forcing in the model is *unphysical*, due to a reliance of the surface tension on the relaxation a parameter,  $\tau$ , with some issues relating to stability and spurious currents' magnitude for certain relaxation values [69]. The second approach is through the use of Guo forcing [70] that removed the dependency on  $\tau$  for the surface tension, where [71] adapted the approach for the Shan-Chen pseudopotential model. Outlined here is the Guo forcing approach of [71].

The forcing term  $F_i^{(\sigma)}$  is given by [71, 39]:

$$F_i^{(\sigma)} = t_i \left( \frac{c_{i\alpha}}{c_s^2} + \frac{(c_{i\alpha}c_{i\beta} - c_s^2\delta_{\alpha\beta})u_{b\beta}}{c_s^4} \right) F_\alpha^{SC(\sigma)}, \quad (2.31)$$

where  $u_{b\beta}$  is the barycentric velocity of the fluid mixture [71]:

$$\underline{u}_b = \frac{1}{\rho} \sum_\sigma \left( \sum_i f_i^{(\sigma)} \underline{c}_i + \frac{\underline{F}^{SC(\sigma)} \Delta t}{2} \right), \quad \rho = \sum_\sigma \rho^{(\sigma)} \quad (2.32)$$

The following Shan-Chen interaction force density allows for interactions between different fluid components, i.e.,  $\sigma \neq \bar{\sigma}$  [39]:

$$\underline{F}^{SC}(\underline{r}) = -\psi^{(\sigma)}(\underline{r}) \sum_{\bar{\sigma} \neq \sigma} \mathcal{G}_{\sigma\bar{\sigma}} \sum_i t_i \psi^{(\bar{\sigma})}(\underline{r} + \underline{c}_i \Delta t) \underline{c}_i \Delta t, \quad (2.33)$$

where, when simulating two immiscible fluids, the interaction force between components  $\sigma$  and  $\bar{\sigma}$  must be negative, in order to repel the fluids and hence interactions' strength  $\mathcal{G}_{\sigma\bar{\sigma}}$  must be positive.

As with other MCLBM variants, the original Shan-Chen model suffers with spurious currents stemming from discretisation error in gradients causing an unphysical flow to form around the phase change between fluids, with the magnitude of the error increasing as the density difference between the fluids increases [69]. This



## 2. Background in Hydrodynamics and Simulation Techniques

method, in general, contains no thermodynamic consistency, with authors presenting enhanced models with thermodynamic coupling [72], although some of the developed thermodynamic models have issues with achieving larger density and viscosity ratios [69]. It is also worth noting that in order to achieve the simulation of *immiscible* fluids, the value of  $\mathcal{G}_{\sigma\bar{\sigma}}$  must be increased above a critical value to insight separation. Increasing this value does increase the sharpness of the interface, however, there are stability issues associated with this and therefore a limit on how large this value can be. Thus, as with all diffused interface models, the simulations are not truly immiscible, and the thickness of the interface may be larger in comparison to other multi-component methods depending upon the situation being simulated.

### 2.3.3.2 Free Energy Model

A thermodynamically consistent multi-component and multi-phase lattice Boltzmann variant was introduced by Swift et al., [64, 66] and is known as Free-Energy or Oxford LBM. The following outlines the key points for a Free-Energy LB model, simulating binary, immiscible fluids. Free-Energy models use a free energy functional, which is thermodynamically consistent, that forces the system towards a free energy minimised thermodynamic equilibrium. This free-energy functional is dependent upon an order parameter,  $\phi$ , that describes the concentration of fluids over the domain (see Eq. (2.35)). For a two-component system, Eq. (2.34a) represents the free energy functional consisting of the: bulk free energy  $\psi_b$ , interfacial region free energy  $\psi_g$  and fluid-solid interaction information  $\psi_s$ . There are varying models for these terms, presented in Eqs. (2.34b, 2.34c) is a simple case corresponding to Landau Free energy [73]. Note, for the following, fluid-solid interactions are excluded:

$$\Psi = \int_V [\psi_b + \psi_g] dV + \int_A \psi_s dA, \quad (2.34a)$$

$$\psi_b = c_s^2 \rho \ln \rho + \frac{A}{2} \left( \frac{\phi^4}{2} - \phi^2 \right), \quad (2.34b)$$

$$\psi_g = \frac{\sigma}{2} (\nabla \phi)^2, \quad (2.34c)$$

where,  $A$  controls fluid miscibility,  $A > 0$  ( $A < 0$ ) fluid is immiscible (miscible) and  $\sigma$  is a surface tension parameter. The order parameter  $\phi$  can be seen to heavily influence Eqs. (2.34b, 2.34c) —as expected,  $\phi$  relating to fluid concentration. The order parameter is defined as such:

$$\phi = \frac{\rho_1 - \rho_2}{\rho_1 + \rho_2} \quad (2.35)$$

where  $\rho_\alpha$  is the density of fluid component  $\alpha \in [1, 2]$  and  $\phi = 1(-1)$  corresponds to the bulk fluid phases 1(2).

## 2. Background in Hydrodynamics and Simulation Techniques

When simulating multi-component flows, an additional distribution function  $g_i$  is introduced, which can be evolved over time, using the same processes of collision and streaming, as within the standard LB evolution equation. This additional distribution function relates to the fluid concentration, given by order parameter  $\phi$  as such:

$$\sum_i g_i = \phi. \quad (2.36)$$

To couple the thermodynamics properties described in Eq. (2.34a) with the LBM, the method uses a thermodynamically consistent pressure tensor which is recovered through modification of the equilibrium distribution function, introduction of forcing [70] or a mixture of both [39].

The free energy models suffer from the same microcurrent problem common amongst multi-component lattice Boltzmann models, stemming from the use of numerical stencils to calculate derivatives. Due to the need for a second distribution function, there is some additional computational cost as well as increased complexity compared to other models. The method does however allow the interface width to be parameterised, with restrictions being introduced on the magnitude of the surface tension value. A clear advantage of this method is its built in thermodynamic consistency, which is not present within the forms of the other models outlined in this chapter.

### 2.3.3.3 Colour-Gradient/Chromodynamic Model

The colour-gradient or chromodynamic (*chromo* – *colour*) multi-component lattice Boltzmann method (cMCLBM) for simulating multiple fluids was first introduced by Gunstensen *et al.* [53] based on work in [52]. The method defines the fluids by attaching a colour label to the species, for instance for two-component fluid flows, one fluid would be defined Red  $R_i$  and the other Blue  $B_i$ , where  $C_i$  denotes the distribution function of species colour  $C \in [R, B]$ . The original method introduced surface tension via a perturbation to the collision step, with a recolouring step being used to prevent the mixing of the *immiscible* fluids, due to the notoriously highly diffusive nature of the LBM itself –streaming of particle populations. Since the original colour-gradient model introduced by [53], there have been several advances to the method: Grunau *et al.*, [56] presented a modified equilibrium distribution function, allowing some variation in density across the fluids' interface, Latva-Kokko and Rothman [74] removed the artefact of lattice pinning, by using a deterministic (formulaic) segregation step, Lishchuk *et al.*, [57] replaced the perturbation step and enforced surface tension by using a discretised body force distribution, applied in

## 2. Background in Hydrodynamics and Simulation Techniques

the interfacial region. These same authors [75] then implemented a post-collision post-recolour segregation rule, based of that of Latva-Kokko and Rothman [74] and D’Ortona et al. [76]. The extension of the methodology, to allow for the simulation of fluids with density contrasts, is discussed further in Chapters 3 and 4.

Proceeding to outline, now, the cMCLBM presented by Lishchuk et al., and Burgin et al., [75, 77], for the simulation of two immiscible fluids. The single distribution function  $f_i$  is now split up into Red and Blue species as follows:

$$f_i(\underline{r}, t) = R_i(\underline{r}, t) + B_i(\underline{r}, t), \quad (2.37)$$

where the distribution functions are evolved using a forced evolution equation [70]:

$$f_i(\underline{r} + \underline{c}_i \Delta t, t + \Delta t) = f_i(\underline{r}, t) + \Omega_i + \Delta t F_i, \quad (2.38)$$

where  $F_i$  is a forcing term written as a power series, see [70].

The macroscopic quantities are calculated as follows, with an altered velocity calculation and inclusion of a body force density [70]:

$$\rho_R(\underline{r}, t) = \sum_i R_i(\underline{r}, t), \quad \sum_i \rho_B(\underline{r}, t) = B_i(\underline{r}, t), \quad \rho = \rho_R + \rho_B, \quad (2.39)$$

$$\underline{u} = \sum_i \frac{1}{\rho} f_i(\underline{r}, t) \underline{c}_i + \frac{1}{2\rho} \underline{F}^{(l)}, \quad (2.40)$$

where  $\underline{F}^{(l)}$  (for the case of drops) is the force that applies the physics of interfacial tension, defined as follows [57],[78]:

$$\underline{F}^{(l)}(\underline{r}) = \frac{1}{2} \sigma H \nabla \rho^N. \quad (2.41)$$

The above force term is applied locally, within the interfacial region, based on the gradient of the phase-field,  $\rho^N$  (will be discussed shortly). Variation in the phase-field is only significant in the interfacial region, where a non-zero value is returned for the gradient; there is little variation in colour in the bulk of the fluids. The parameter  $\sigma$  allows the surface tension between the fluids to be tuned, and  $H$  is the local mean curvature of the interface, and can be formulated straightforwardly as follows:

$$H = \nabla \cdot \hat{n}, \quad (2.42)$$

in which, the interface unit normal  $\hat{n}$ , is found in terms of the gradient of the phase-field, which will be perpendicular to the interface:

$$\hat{n} = \frac{\nabla \rho^N}{|\nabla \rho^N|}. \quad (2.43)$$

## 2. Background in Hydrodynamics and Simulation Techniques

The phase-field  $\rho^N$  is an effective order parameter that identifies what phase one is in, i.e., where within the interface between the fluids one lies. It is defined as such for fluids without a density contrast:

$$\rho^N(\underline{r}) \equiv \frac{\rho_R - \rho_B}{\rho_R + \rho_B}, \quad (2.44)$$

where values of 1 (-1) are found in the Red (Blue) bulk sites, and any variation between -1 and 1 is the interfacial region where there is a mix of Red and Blue fluids at that lattice site. The profile of Eq. (2.44) has been shown to resemble that of a  $\tanh(\beta \underline{r})$  profile, in which a segregation parameter  $\beta$  controls interfacial width and is linked to stability (see Chapter 3).

A crucial component of the chromodynamic scheme is the inclusion of a segregation rule. The LBE is inherently dispersive, as such, poses a complication when simulating *immiscible* fluids. To prevent the mixing of species, a post-collision, post-recolour segregation rule is applied, that locally redistributes particle distributions normal to the interface, and is an adaptation of the original method [52], [76] presented by Halliday et al., in 2007 [58]:

$$C_i^{\psi\psi}(\underline{r}, t) = \frac{\rho_C(\underline{r}, t)}{\rho(\underline{r}, t)} f_i(\underline{r}, t)^\psi \pm \beta t_i \frac{\rho_R(\underline{r}, t) \rho_B(\underline{r}, t)}{\rho(\underline{r}, t)} \hat{n} \cdot \underline{c}_i \Delta t. \quad (2.45)$$

Above  $C \in [R, B]$ , superscript  $\psi$  ( $\psi\psi$ ) denotes a post-collision (post re-colour) quantity, plus (minus) corresponds to the Red (Blue) species and  $\beta$  is a chosen segregation parameter. A check that colour species and mass are conserved during segregation can be performed by summing each side on both direction and colour.

For the cMCLBM outlined, a limitation is its lack of thermodynamic consistency, which unlike the Free-Energy method, limits application to isothermal flows. Additionally, like the previously mentioned MCLBMs, unphysical spurious currents appear in the velocity fields, stemming from rounding and sampling errors [49]. It is however possible, in certain cases, to remove the micro-current and this will be discussed further in Chapter 4. The strengths of the method are its: transparency, mass conservation, ease of implementation in code and ability to apply forces encapsulating important physics without obstructive complication (will be discussed more in Chapters 4 & 5), a directly parameterisable interfacial tension, low micro-current and an amenability to analysis.

### 2.3.3.4 Review of the models

Three of the most popular lattice Boltzmann methods variants for simulating multi-component, immiscible, fluid flows have been considered. In review, they can be briefly summarised based on how they approach the task of simulating multi-component fluid flows: Shan-Chen —incorporating meso-scopic interactions between the different fluid particles, Free-Energy —use a free energy functional to describe the minimisation of the system’s free energy, where a thermodynamic pressure tensor is built-in, Chromodynamic —using a kinetic scale segregation rule that segregates the fluids post-collision, with surface tension affects applied through Guo forcing [70] in the interfacial region. One could also differentiate the Shan-Chen and Free-Energy models by considering where the phase interaction-inducing forces are introduced, with the Shan-Chen method incorporating microscopic interactions through the first moment of distribution function and the Free-Energy method incorporating meso-scopic interactions through the second moment of the distribution function —its pressure tensor [47].

For researchers with a background in molecular dynamics, the Shan-Chen pseudopotential model may be preferable, due to its foundations in microscopic interactions, which could be argued is the most physically representative of interactions between fluid elements at the mesoscale. For those interested in the thermodynamics of multi-component fluid flows, then the Free-Energy model is an obvious choice, due to its built in thermodynamic consistency. If one is interested in interfacial kinematics and dynamics, one may opt for the chromodynamic model, due to its ease of parameterisation of the interfacial region and verifiable interface kinematics and dynamics [77].

When considering which model to choose, one must consider the application of the work and which models fit that best. The work in this research considers the interfacial kinematic and dynamic boundary conditions between isothermal immiscible fluids, with the interfacial region being of critical importance. This is especially clear when aiming to simulate vesicles where the interfacial region needs to incorporate the much more complex physics associated with vesicles. In knowing this, the chromodynamic model presents itself as a clear option due to its transparent approach, control of the interfacial region, strict mass and momentum conservation and ability to include immersed forces through Guo forcing [70] with minimal complexity. With the benefits of choosing this approach becoming increasingly apparent when simulating vesicles in Chapter 5.

### 2.3.4 Boundary Conditions

In order for computational fluid dynamics techniques to be capable of simulating hydrodynamics accurately, they must contain appropriate simulation boundary conditions that reflect the physics of how the fluid behaves at domain boundaries, e.g., solid impermeable walls. Not only do the boundary conditions implemented affect the flow dynamics close to the boundary wall, but they can also have a large impact on the bulk fluid dynamics, even when simulating over larger domains. Additional to adequate boundary representation, it is common practice to use chosen boundary conditions as a way of reducing the computational run time of the simulation, e.g., by implementing periodic boundary conditions. This section will highlight the simulation boundary conditions applied within this thesis, but for further literature on different boundary conditions used in LB simulation, see references [6, 39, 79, 80].

#### 2.3.4.1 Periodic Boundary Conditions

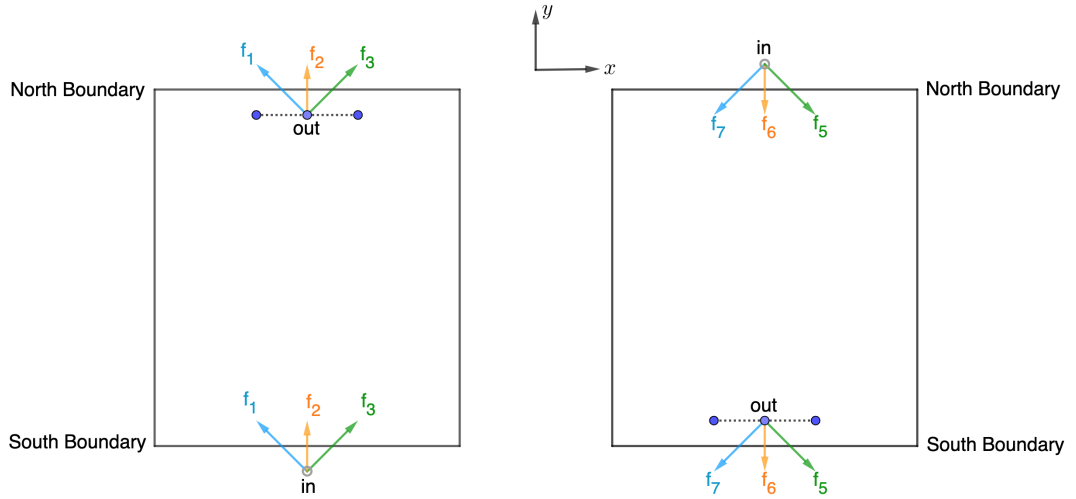
Periodic boundary conditions are one of the simplest boundary conditions to implement and can be understood simply as follows: to achieve a description of a bulk fluid, the fluid that leaves the computational domain at a given side, the fluid will immediately re-enter the domain (as though originating in a spatially tessellating, period replica of the explicitly simulated system) at the opposing side. This means that periodic boundary conditions can be used when trying to simulate a system where the flow solution is periodic within a specific direction, for example, the north and south boundaries representing flow in a long tube, in two dimensions. The physicality of periodic boundary conditions is questionable, however; its justification is based on the examination of a finite section of a flow field where the flow solution is periodic [39].

Consider a situation such as flow in a long channel, where the flow solution is periodic through the pipe. The periodic boundary conditions for this problem may be considered at the north and south boundaries of the domain, replicating a long channel. Figure 2.5 shows a schematic of these periodic boundary conditions.

#### 2.3.4.2 No-Slip: Bounce Back Boundary Conditions

A common boundary encountered in hydrodynamics is that of a solid impermeable wall. Such boundaries have flow physics described by the *no-slip* condition (discussed in section 2.2.2), which states that the solid surface is impenetrable (i.e., the normal component of velocity close to the wall ( $\underline{u} \cdot \hat{n} = 0$ )) and the tangential velocity of the fluid in contact with wall must be the same as that of the wall itself. An example

## 2. Background in Hydrodynamics and Simulation Techniques



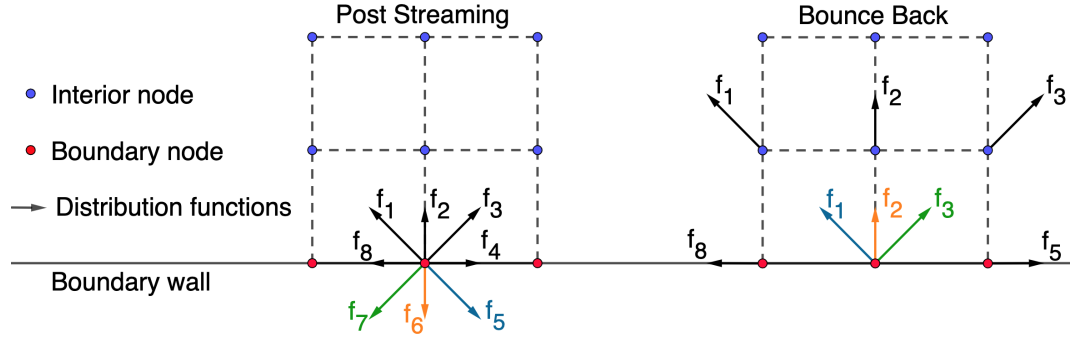
**Figure 2.5:** Schematic showing Periodic Boundary Conditions at the North and South boundaries. Note, lattice size not to scale.

where such a boundary may have relevance in this work is when simulating a channel with solid walls, i.e., a drop or vesicle in a confined passage.

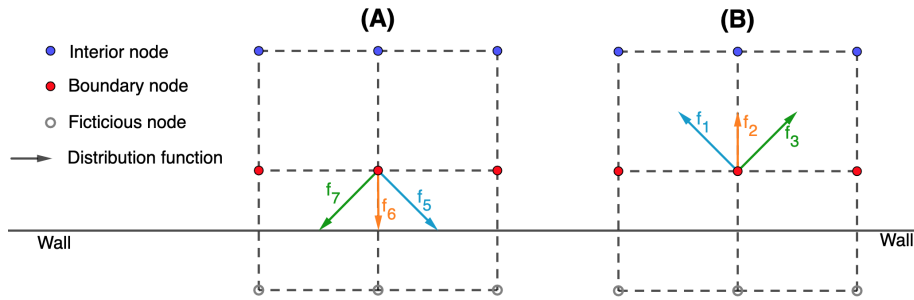
One of the strengths of LBM is that the implementation of no-slip solid wall boundaries can be quite simplistic, meaning geometries such as porous media, can be simulated without the difficulty seen in other CFD techniques. The most commonly implemented boundary in LB to mimic that of a solid wall are *bounce-back* boundary conditions (BBBCs). Within BBBC variants, particle distributions that stream toward the solid impenetrable wall, bounce back in the direction at which they approached the wall.

The first bounce-back boundary condition is shown within Figure 2.6 and is often referred to as either On-Grid or Full-Way bounce back (OGBB) [81, 82, 67]. The boundary is placed on lattice nodes where streaming distributions are reflected back in the direction which they approach the wall. Through Chapman-Enskog procedure, it can be shown that the accuracy of this BC is 1<sup>st</sup> order [34, 39]. The error stems from the influence of the relaxation parameter  $\tau$  in LBGK schemes on the boundary position, (which is not the case for TRT and MRT schemes), where Inamuro et al. [83] found that the error is close to 2<sup>nd</sup> order for appropriate  $\tau$  and lattice resolution.

A more accurate bounce back variant was proposed by Ziegler [82] called Mid-Grid or Half Way bounce back (MGBB), which can be shown to be 2<sup>nd</sup> order accurate. Like the OGBB BC, particle distributions are reflected back in the direction they stream towards the boundary wall, however now the boundary wall is located between two lattice sites (note: accuracy of the wall is still not guaranteed for LBGK schemes). This process is highlighted in Figure 2.7.



**Figure 2.6:** Schematic displaying the process of On-Grid bounce back boundary conditions.



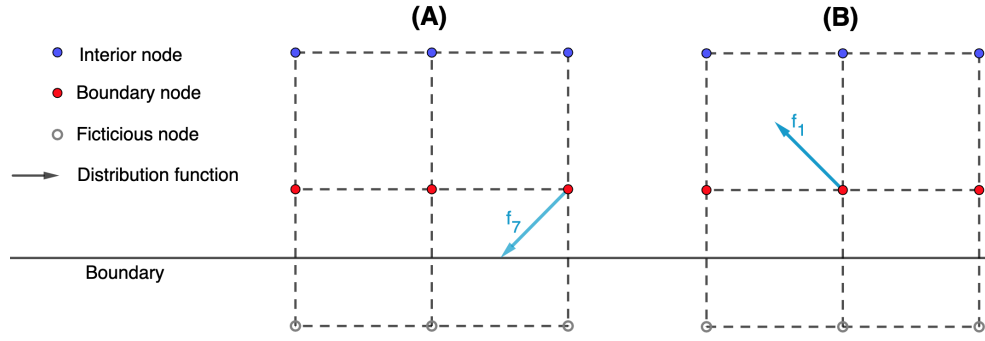
**Figure 2.7:** Schematic displaying the process of Mid-Link bounce back boundary conditions.

### 2.3.4.3 Slip Boundary Conditions

The final boundary condition introduced in this section is the Slip Boundary condition. Slip boundary conditions are often used to reflect the inclusion of a symmetry condition (axis) such as may be implemented by mid-link specular reflection. This concept is similar to that of the previously discussed mid-link bounce back boundary condition, except now distribution functions are reflected back off the boundary in a direction related to the collision angle with the wall. In this application it can be considered as a ‘perfect’ slip, where the angle in which the distribution function collides at the wall is the same as the reflection angle, such that the distribution function exerts no shear on the wall and conserves tangential momentum [84].

The implementation of this boundary condition can be used to introduce a symmetry plane and leads to the reduction of computational cost, essentially by halving the extent of the domain. This condition is applied in Chapter 4, as a means of using a two-dimensional system to capture the hydrodynamics of a three-dimensional system.





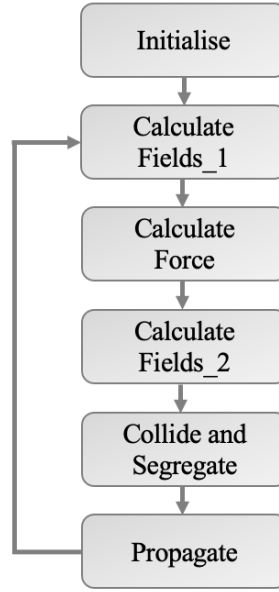
**Figure 2.8:** Schematic displaying the process of Mid-Link specular reflection boundary conditions (perfect slip).

## 2.4 Simulation of fluids using LBM

Throughout this work, focus is on the methodological developments of the class of chromodynamic multi-component lattice Boltzmann models, as such, this thesis leans towards the mathematical and developmental aspect of LB. However, the computational encapsulation of our methodologies is clearly important, not least because it facilitates validation of the models. Accordingly, this short section gives an overview of the code structure, flow simulation protocols and data post-processing used.

### Code Structure

The models developed within this thesis were encapsulated within C programming language and were written *ab initio*, with emphasis on the clarity of algorithmic encapsulation and the ease with which it (the underlying algorithm) can be manipulated. Accordingly, transparency of the sequential (non-parallel) codes was prioritised over optimisation and execution efficiency. All codes follow the same essential structure, treated as compartmentalised (modular) sections (see Figure 2.9 which shows the base structure of all codes used within this work). To start with, the lattice and fluids (represented by the primary object, the distribution function component set) are initialised for the domain. For example, in the microcurrent tests in section 4.2.3.1, a spherical drop is initialised surrounded by a background fluid in a square domain, or in section 5.3.3.3, two vesicles are initialised in line with each other within a three dimensional domain. Following this, within module ‘Calc\_Fields\_1’ the fluid’s scalar hydrodynamic observables (densities) are calculated, by summing the distribution functions on lattice links (Eq. (2.39)); first dependencies like the phase fields ( $\rho^N$  fields) and interface curvatures are then calculated, using previously-derived macroscopic densities (Eq. (2.44)). Next, the forcing that is to be applied is



**Figure 2.9:** Flow chart showing the base structure of the C codes used throughout this work, which allow the encapsulation of the developed models.

calculated, for instance, surface tension when simulating drops (Chapters 3 and 4) and surface tension, bending rigidity and area conservation forces when simulating vesicles (Chapter 5). Once these forces are assigned, the hydrodynamic velocity can be calculated, module ‘Calc\_Fields\_2’. Now, after the macroscopic density and velocity have been calculated, the equilibrium distribution function can be calculated (see Eq. (2.22)), and the distribution functions then collided (either through use of a BGK or MRT collision scheme). Following collision, the post-collision distribution functions are segregated using Eq. (2.45). These two steps are conducted within the module ‘Collide and Segregate’. Finally, the distribution functions are propagated (see Figure 2.4), the time step increased, and the process iterated back to ‘Calc\_Fields\_1’. This process corresponds to a single time-step (evolution) of the system. It is then repeated until the time step count has advanced until the set final time step. Note, all simulations reported are formally unsteady.

For all data reported, the SHU Beowulf cluster was used. Although codes are serial, the cluster allowed for a processor farm approach, in this multiple independent object codes generate data concurrently—for example, when conducting an assessment of the phase space; the search for a bicuspid parameterisation within the vesicle model (Chapter 5) may be efficiently performed within this approach.

Code run time was very variable, with some two-dimensional codes executing in minutes and with some three-dimensional multiple vesicle codes which required minimum levels of spatial resolution for computational stability taking days (e.g. the four vesicle sedimentation test shown in Chapter 6). Execution time was not deemed

## 2. Background in Hydrodynamics and Simulation Techniques

to be an impediment as a vast majority of applications reduce to parameterisation and calibration exercises which were readily amenable to a processor farm methodology. The use of serial codes means discussions surrounding computational expense and optimisation of simulations are deemed of secondary importance and are generally omitted in the following work.

### Flow Setup

Data is structured such that simulation lattice populations are base type global variables being defined at the start of the code, to allow for easy manipulation of the flow geometry being simulated. A general overview of the setting up of an arbitrary flow are as follows: (i) set the domain geometry (lattice size); (ii) set suitable initial fluid positions (i.e., where on the lattice does each fluid start, and then initialise); (iii) set the time duration of the simulation; (iv) set fluid properties (i.e., fluid densities, viscosities, surface tensions etc.); (v) set any fluid forcing (i.e., a buoyancy force); (vi) set data output files (decide what information of the flow needs outputting, i.e., velocity fields).

### Data Processing

In order to process the data, the required fields are exported to csv files and viewed with commercial software (ParaView, MATLAB, Excel). For example, when examining the steady microcurrent (see Chapter 3), the velocity field over the domain is outputted to a csv file; when examining time modalities of e.g. vesicle shape evolution, the  $\rho^N$  field was sampled at chosen times and exported to a sequence of appropriately-named csv files. The general structure of these files are given by columns of position ( $x, y, z$  columns) and then lattice properties (i.e.,  $\rho^N$  (phase field value) or  $u_x, u_y, u_z$  (lattice velocity components)). These files are then used to examine flow data by either performing post-processing in software such as MATLAB, or visualisation of the outputted data in either Excel, MATLAB or ParaView – where the use of ParaView becomes prominent when extending to three-dimensional flows.

## 2.5 Concluding Remarks

This chapter has outlined the fundamental hydrodynamics and lattice Boltzmann theory and reviewed leading work in these fields, such that the work reported in the remainder of this thesis will have context. The focus of this work is the simulation of drops and vesicles at the mesoscale, where the interface between the fluids is of interest. The hydrodynamics of the flow in such simulations at this scale —where one is considering the interior of the drop/ vesicle as one fluid and the exterior as another

## *2. Background in Hydrodynamics and Simulation Techniques*

—can be described by the incompressible Navier-Stokes and Continuity equations, outlined in section 2.2. The fundamental boundary conditions at the free-surface between the fluids —kinematical and dynamical —have been discussed, explained and referenced with their importance seen throughout this thesis. Finally, non-dimensional quantities which allow specific flows to be categorised were introduced and will be used without further discussion in the following chapters.

The lattice Boltzmann method presented itself as an obvious choice for this work due to: appropriate length and time scale, computational efficiency, Galilean invariance (the laws of motion are the same in all inertial frames), ability to simulate multi-component flows, recovery of the weakly compressible Navier-Stokes equations and diffused interface (discussed further throughout, primarily in Chapter 5). The background theory relating to LBM: history and development, the evolution equation, collision operators and simulation boundary conditions, were all reviewed. The choice of a multi-component lattice Boltzmann variant for this research being the cMCLBM has been justified and explained, with the main reasons being: control of the interfacial region, transparency, ability easily to encapsulate mesoscale physics through Guo forcing [70] and that thermodynamics are not being investigated in this work. Additionally, the collision models chosen to be implemented (BGK and MRT) within the cMCLBM model have been discussed and justified (section 2.3.2.4) with transparency and stability in mind.

From this chapter, it should be clear to the reader what the relevant hydrodynamics for this work are, as well as the simulation technique being implemented and its applicability to the simulation of drops/vesicles at the mesoscale. The remainder of this thesis now focuses on novel advancements to the cMCLBM methodology, keeping in focus the fundamental hydrodynamics outlined here. Note, Chapter specific literature is presented at the start of each chapter, where it is relevant to provide background regarding that specific area, i.e., Chapter 5 contains literature regarding the simulation of RBCs.

# 3

## Kinematics and Dynamics of Chromodynamic Multi-Component Lattice Boltzmann Equation Simulation

### Contents

---

<b>3.1</b>	<b>Introduction</b>	<b>41</b>
<b>3.2</b>	<b>Methodology</b>	<b>45</b>
3.2.1	Isothermal cMCLBM for Binary Fluid Flows with a Density Contrast	45
3.2.2	Extension to Many-Component Fluid Flows	47
<b>3.3</b>	<b>Analysis</b>	<b>49</b>
3.3.1	Dynamics	50
3.3.2	Kinematics	57
3.3.3	Dynamics and Kinematics Coupling	64
<b>3.4</b>	<b>Results</b>	<b>65</b>
3.4.1	Spurious Current	65
3.4.2	Kinematical Condition	69
<b>3.5</b>	<b>Concluding Remarks</b>	<b>75</b>

---

### 3.1 Introduction

Immiscible fluid flows can be found in both nature and industry, often with a density contrasts between the fluids —such as oil and water, where oil is less dense than water.

Flows with such moderate density contrasts are often found when studying microfluidics, which considers the behaviour of fluids at the microscale, where, unlike

### *3. Kinematics and Dynamics of Chromodynamic Multi-Component Lattice Boltzmann Equation Simulation*

at the macroscale, physical forces such as surface tension have a large impact on, e.g., the microscale fluid behaviour [85]. Understanding this behaviour and using this understanding to control the fluids has many applications in biotechnology and biomedicine. For example, droplet-based micro-fluidics can involve the study of how immiscible drops behave during collisions, whilst suspended in different fluids (which have differing densities), facilitating an increased understanding, resulting in the improved design of bioanalytical devices [86]. We note that some biomedical applications study micro-fluidic flows involving density contrasts, examples being drug delivery and cell encapsulation [87].

Industrial fluid flows like those occurring in fuel cells and batteries, which involve the conversion of chemical energy to electricity, contain multi-scale flow transport phenomena [88]. Proton exchange membrane fuel cells (PEMFCs) are regarded as a viable option for power sources in vehicles. Droplet coalesce within PEMFC flow channels is also an area of interest in understanding the channel blockages in PEMFCs [89]. Hence, using MCLBMs to simulate how droplets deform and coalesce in these channels is extremely useful. Again, such droplets often have a large density contrast, compared to the fluid they are suspended in, so the inclusion of this density ratio in simulation needs to be considered, for accurate representation of the physical processes.

The previously stated flows all have an interface between the different fluids. This interfacial region is often scaled in units of nanometres; at this scale top-down macroscale computational techniques would treat this interface as discontinuous. However, so-called mesoscale diffused interface approaches, such as MCLBM (all variants), treat this interfacial region as continuous—a diffused interface where the fluid blends from one fluid, to the other. In doing so, one avoids potential singularities, and the study of such immiscible flows becomes more appropriate and attainable by bottom-up approaches, MCLBM presenting itself as an attractive option, because:

- (i) it can be easily adapted to span the appropriate length scales;
- (ii) it has capacity to incorporate integrated micro-scale physics;
- (iii) it has the ability for code parallelisation;
- (iv) it recovers the fluid macroscopic governing equations.

An example of where this approach has great traction is when studying triple contacts, between three mutually immiscible fluids. Here, an accurate relationship between the surface tensions of the fluids, their resultant affinity towards each other and hence their segregation, can be imposed with reasonable accuracy—with correct treatment of the triple contact according with Young-Laplace Law physics [90, 91, 92, 93]. Clearly then, given the method’s existing functionality, its extension to the

### *3. Kinematics and Dynamics of Chromodynamic Multi-Component Lattice Boltzmann Equation Simulation*

simulation of immiscible fluids with larger density contrasts would extend its utility, allowing for the simulation of a larger variety of the fluid flows seen in nature and industry.

The development of MCLBMs for the simulation of immiscible fluids with density contrasts has been studied using the previously discussed variants in section 2.3.3 —(i) Shan-Chen pseudopotential (SC), (ii) Free Energy (FE), (iii) Phase-field and (iv) Colour-Gradient or Chromodynamic.

The multi-component multi-phase SC model was first introduced by Shan et al. [60, 62]; it had several limitations identified in section 2.3.3.1. The original SC model was improved by Yuan and Schaefer [94] who addressed the task of connecting the pressure in the fluids' equations of state (EOSs) with the pressure in the SC model. The outcome of this work was that both the Peng-Robinson [95] and Carnahan–Starling [96] EOSs were found to be effective in modelling large density ratios, with minimised (but still significant) spurious velocities. Zhang and Tian [97] contested that Yuan and Schaefer's approach lacked physical foundation, however, Zhang and Tian's approach is accepted to have underperformed compared to that of Yuan and Schaefer's approach, which had smaller spurious velocities and could simulate larger density contrasts. Yet even with these improvements, the spurious velocity level still limits the application of the model, to cases where these velocities do not overpower flow behaviour. For instance, the various SC models were found to be unsuitable for the simulation of Marangoni convection, for this reason [98]. Furthermore, the interface width has been reported to be larger than that in other MCLBM variants (a significant issue, for continuum scale applications, of course) and the method has stability issues [68]. Lycett-Brown and Luo [99, 100] developed a SC model with a new forcing scheme, allowing the simulation of large density contrasts  $O(1000)$ , with increased stability, implementing a cascaded-MRT collision operator. Note, their model also afforded the ability to tune surface tension, independent of density contrast —a previous problem in SC models, which was first addressed in [101].

The free energy model developed by [64, 66] has also been enhanced and extended for the simulation of immiscible flow with density ratios. Inamuro et al. [102] outlined a two-phase immiscible free-energy model, capable of simulating fluids with a large density contrast. In 2006, Zheng et al. [103] advanced a free-energy model that recovers the Cahn-Hilliard equation, side-stepping an algorithmic pressure correction, by using a particle distribution for the mean density and momentum [104]. The so-called 'phase-field' models, which are not dissimilar to the free-energy models, have also been used to simulate immiscible fluids with large density ratios (above, they are discussed with free-energy models, due to the similarity of the two). In

### *3. Kinematics and Dynamics of Chromodynamic Multi-Component Lattice Boltzmann Equation Simulation*

2013, Zu et al. [105] presented a phase-field based lattice Boltzmann method for the simulation of binary fluid systems with density contrasts. This method was then enhanced by Fakhari et al. [106], improving upon numerical stability and model efficiency and then, further again by Mitchell et al. [107], who extended the methodology to three dimensions.

Colour-Gradient (CG) and Chromodynamic models also present themselves as an attractive option for simulating immiscible fluids with a density contrast. Following several advancements to the initial CG model, in 2007, Reis et al. [108] introduced a two-dimensional CG model for simulating immiscible binary fluids with density and viscosity contrasts. In 2013, Liu et al. [109] extended this by presenting a CG model for the simulation of binary fluids with density and viscosity contrasts in three-dimensions. At a similar time, Leclaire et al. [110] introduced a CG model with an enhanced equilibrium distribution function, capable of simulating density ratios up to  $O(1000)$ . Ba et al. [111] provided a benchmark for CG models, by outlining a model capable of simulating two-phase flows at high density and Reynolds numbers. Recently, Wen et al. [112] presented an improved CG model for the simulation of fluids with density contrasts, eliminating error terms that appear in the macroscopic equation by modifying the equilibrium distribution function.

All of the MCLBM variants extended to the simulation of immiscible fluids with a density contrast should meet the kinematical conditions at the free surface (or interface) between the fluids —outlined in section 2.2.2.1. If this condition is not met, numerical instability may ensue, and worse, the physics of the flow will not be accurately represented. To enforce the kinematic condition, colour-gradient and chromodynamic models [109, 111, 112, 77] use a kinetic scale segregation rule to prevent fluid mixing and to maintain the integrity of the interfacial region between the immiscible fluids. To understand the impact of extending the cMCLBM to large density contrasts on the method’s ability to comply with the kinematical condition required at the interface, mathematical analysis of the segregation rule (model kinematics) and verifiable recovery of the macro-scale continuum fluid dynamics equations (dynamics) is clearly needed. Therefore, this chapter tackles the analysis of both the kinematics and dynamics of the cMCLBM methodology, revealing the coupling between the two and enhancing the understanding of the methodology. This is achieved by assessing the kinetic scale segregation rule. It should be noted that the segregation is controlled at the kinetic scale, but the kinematic condition refers to the continuum scale behaviour of the interface, and as such, an analysis must seek to relate the kinetic scale and the continuum scale observables in an appropriate manner.



The structure of this chapter is as follows. First, the cMCLBM will be outlined, explaining in detail the extension of the methodology for the simulation of fluids with a density contrast [77]. From this, the extension of the methodology from binary fluid flows to many fluids will also be discussed and reviewed. Having postulated a methodology, a mathematical analysis consisting of two interlinking sections (Dynamics and Kinematics) will be presented, to address the impact of the extension to large density ratios on the method's ability to correctly recover the governing fluid dynamics equations and principal interfacial kinematic condition, as well as model stability. To support the findings, simulation data will be presented, further to highlight the utility of the model. Finally, concluding remarks will be made, bridging into the work presented in Chapter 4.

## 3.2 Methodology

This methodology section will outline the cMCLBM used for the simulation of immiscible, isothermal, binary fluid flows with a large density contrast, focusing on the methodological extensions to incorporate the density difference. Aiming to provide as transparent an account as possible, of this extension and its impact on the model, the collision operator implemented here is the BGK operator [35]—which simplifies the analysis that will be presented in section 3.3.1. Additionally, although only two-component flows are examined in this chapter, the extension to the simulation of many fluids will be briefly presented, in order to provide further understanding of the methodology, as well as providing a point of reference for the upcoming work in Chapter 5.

### 3.2.1 Isothermal cMCLBM for Binary Fluid Flows with a Density Contrast

For a binary fluid flow, the distribution function in LB can now be expressed as a summation of the two distribution functions for the species designated red and blue as follows:

$$f_i(\underline{r}, t) = R_i(\underline{r}, t) + B_i(\underline{r}, t). \quad (3.1)$$

The evolution equation, incorporating forcing after Guo et al. [70] and the BGK collision operator can be expressed for the model as follows:

$$f_i(\underline{r} + \Delta t \underline{c}_i, t + \Delta t) = f_i(\underline{r}, t) - \frac{\Delta t}{\tau} (f_i(\underline{r}, t) - f_i^{(0)}(\rho, \underline{u})) + \Delta t F_i, \quad (3.2)$$

where the source term ( $F_i = F_{1i} + F_{2i}$ ) can be split up into two separate contributions:  $F_{1i}$ —a correction needed due to the introduction of a density contrast between the

### 3. Kinematics and Dynamics of Chromodynamic Multi-Component Lattice Boltzmann Equation Simulation

fluids and  $F_{2i}$  —an immersed boundary force containing surface tension physics (see section 3.3.1). The equilibrium distribution function has to be adapted to aid the simulation of density contrasts by the introduction of a parameter  $\phi_i$ , developed over time in [108, 113, 111], to be discussed shortly. The equilibrium distribution function now has the following form:

$$f_i^{(0)}(\rho, \underline{u}) = \rho\phi_i + t_i\rho \left( \frac{u_\alpha c_{i\alpha}}{c_s^2} + \frac{u_\alpha u_\beta c_{i\alpha} c_{i\beta}}{2c_s^4} - \frac{u^2}{2c_s^2} \right). \quad (3.3)$$

Identical to the unit density ratio model, the macroscopic properties are calculated using a force adjustment, outlined by Guo et al. [70]:

$$\rho_R(\underline{r}, t) = R_i(\underline{r}, t), \quad \rho_B(\underline{r}, t) = B_i(\underline{r}, t), \quad \rho = \rho_R + \rho_B, \quad (3.4)$$

$$\underline{u} = \frac{\sum_i f_i(\underline{r}, t) \underline{c}_i}{\rho} + m \frac{\underline{F}^{(l)}}{\rho}, \quad (3.5)$$

here,  $\underline{F}^{(l)}$  is the surface tension inducing Lishchuk force [57], and  $m$  is a constant to be determined. Throughout this work the following notations are used;  $\rho$ ,  $\rho_R$ ,  $\rho_B$ ,  $i$ ,  $\Delta t$ ,  $c_{i\alpha}$ ,  $t_i$ ,  $u$  and  $c_s$  denote the overall nodal density, red fluid nodal density, blue fluid nodal density, link-index, time step, the  $\alpha$  component of the  $i^{th}$  lattice basis vector, the weight for link  $i$ , fluid velocity and the colour-blind speed of sound. The inclusion of  $\phi_i$  within Eq. (3.3) affects mass activation. It does this by redistributing the mass on each of the nine links and has a relationship linked with the two ideal gas components' speed of sound [108, 113, 111, 77]:

$$\phi_i = \begin{cases} \frac{\alpha_R \rho_R}{\rho} + \frac{\alpha_B \rho_B}{\rho}, & i = 0 \\ (1 - \alpha_R) \frac{s_i \rho_R}{\rho} + (1 - \alpha_B) \frac{s_i \rho_B}{\rho}, & i \neq 0 \end{cases} \quad (3.6)$$

where  $s_i = kt_i$  is a weight factor, determined by the lattice link weights,  $t_i$ , and a constant  $k$ , determined by the lattice dimensionality ( $k = \frac{9}{5}$  for the  $D2Q9$  lattice structure). The colour-blind parameters  $\alpha_R$  and  $\alpha_B$  can be tuned to give the desired density ratio between the two species, as well as having a linking to algorithmic stability [77]. The following equation states the relationship to density ratio,  $\Lambda$  [56]:

$$\Lambda \equiv \frac{\rho_{0R}}{\rho_{0B}} = \frac{c_{sB}^2}{c_{sR}^2} = \frac{1 - \alpha_B}{1 - \alpha_R}, \quad (3.7)$$

where, the density contrast  $\Lambda$  is expressed as the density of the two species deep within their respective phases, i.e.,  $\rho_{0C}$  where  $C \in [R, B]$ .

The isothermal equation of state for a BGK model is given by  $p = \rho c_s^2$ . As such, using Eq (3.7) and the interfacial condition that pressures must be balanced at the interface, an equation of this pressure balance can be expressed as:

$$\rho_{0R}(1 - \alpha_R) = \rho_{0B}(1 - \alpha_B). \quad (3.8)$$

### 3. Kinematics and Dynamics of Chromodynamic Multi-Component Lattice Boltzmann Equation Simulation

The interface between the two fluids is now adapted for the inclusion of a density contrast between the fluids, through normalisation of the fluid densities, resulting in the following equation for the phase field—which as discussed below—resembles a  $\tanh(\beta \underline{r})$  profile:

$$\rho^N \equiv \frac{\left(\frac{\rho_R}{\rho_{0R}} - \frac{\rho_B}{\rho_{0B}}\right)}{\left(\frac{\rho_R}{\rho_{0R}} + \frac{\rho_B}{\rho_{0B}}\right)}. \quad (3.9)$$

Finally, the kinetic scale segregation rule, that aims to maintain interface integrity and prevent mixing of the fluid species has also been adapted for the inclusion of a density contrast. Below,  $\phi_i$  is included in the segregation term, to bias mass distribution on the lattice links, with the segregation rule applied here an adaptation of the original method [76] presented by Halliday et al. [58]:

$$C_i^{\psi\psi}(\underline{r}, t) = \frac{\rho_C(\underline{r}, t)}{\rho(\underline{r}, t)} f_i(\underline{r}, t)^\psi + \beta \frac{\phi_i(\underline{r}, t) \rho_R(\underline{r}, t) \rho_B(\underline{r}, t)}{\rho(\underline{r}, t)} \hat{n} \cdot \Delta t \hat{c}_i, \quad (3.10)$$

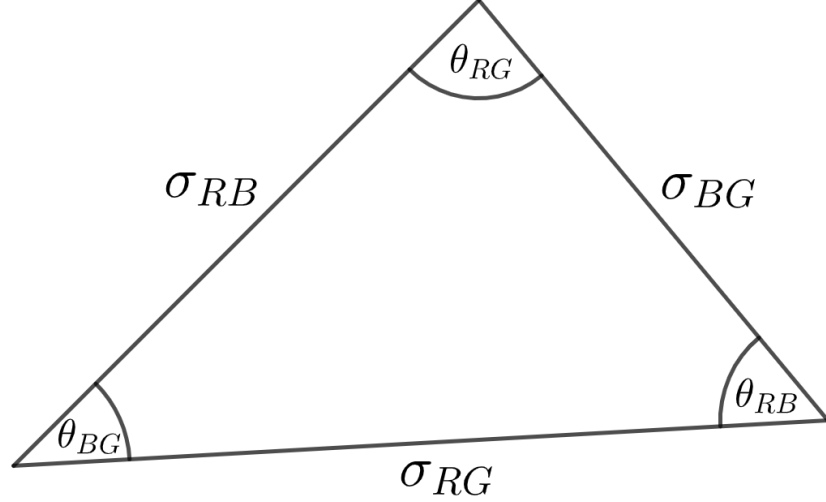
where, again  $C \in [R, B]$ , superscript  $\psi$  ( $\psi\psi$ ) denotes a post-collision (post re-colour) quantity and  $\beta$  is a chosen segregation parameter. It is essential that mass and colour is conserved during this stage, which can be checked by summing each side on both direction (index  $i$ ) and colour.

#### 3.2.2 Extension to Many-Component Fluid Flows

The methodology outlined previously is for the simulation of binary immiscible fluids with a density contrast, i.e., two-component fluid flows. However, the method is extendable to the simulation of many-components and many drops. This subsection will discuss the considerations one must make when extending to many fluids, with this issue and other considerations being further addressed in Chapter 5.

The extension to three-components or higher has been carried out using all the MCLBM variants discussed within this thesis [114, 115, 116, 117, 90, 91, 118, 92]. The colour-gradient or chromodynamic MCLBM class of models have distinct advantages when simulating ternary fluid systems, such as their strict mass conservation and ability to tune surface tension values for each fluid easily and accurately. This control over a range of surface tension values is extremely important when modelling the physics of three-phase contacts. The static mechanics of a three phase contact is given by Neumann’s triangle, which describes the force at this contact, based on the surface tensions of the fluids [119, 120]. In simple terms, the triangle relates to the surface tension forces of the fluid pairs (lengths of the triangle) at a point in space where a triple contact forms (three fluid meeting) where the angles in the

triangle correspond to the contact angles of the fluids. Again, meaning for such a triple contact, the ability to apply a variable surface tension in the cMCLBM —individual surface tension values for each fluid interface— allows control over Neumann’s triangle, as shown in Figure 3.1.



**Figure 3.1:** Neumann’s triangle for a triple contact between three fluids, denoted: Red ( $R$ ), Blue ( $B$ ) and Green ( $G$ ). The surface tensions between the fluids are given by  $\sigma_{CC'}$  and contact angles by  $\theta_{CC'}$ , where  $C \in [R, B, G]$  and  $C' \in [R, B, G]$ , with  $C \neq C'$ .

The importance of compliance with Laplace-Law triple contact physics and the Neumann’s triangle is clear when simulating fluids which have different wettability and, further, fluids which are completely immiscible. In cMCLBM however, applying only the variable surface tension values will not guarantee correct behaviour due to the inherent dispersion of the lattice Boltzmann algorithm. The segregation rule outlined previously is also needed to minimise fluid mixing in the interfacial region. The segregation rule has been adjusted and enhanced over time, to treat this triple contact [90, 91, 92]. Yuan et al. [92] outlined an enhanced segregation rule, which recovered convincing results of three-phase simulations, the following is an overview of this segregation process. The segregation parameter (or interface width) between two fluids  $C$  and  $C'$  is given by  $\beta_{CC'}$  and is now variable in relation to the surface tension values between the fluids. The value of  $\beta_{CC'}$  is calculated through first evaluating whether a Neumann’s triangle is present in Eq. (3.11a), then using this value to determine how the interface width between fluids  $C$  and  $C'$  should be perturbed to give correct wettability of the fluids —Eqs. (3.11b,3.11c). The steps for this, then, were given by Yuan et al., in 2019 [92]:

$$X_{CC'} = \frac{\sigma_{C''C}^2 + \sigma_{C''C'}^2 - \sigma_{CC'}^2}{2\sigma_{C''C}\sigma_{C''C'}}, \quad (3.11a)$$

$$\beta_{CC'} = \beta^0 + \beta^0 \min \left( \frac{35\rho_C\rho_{C'}\rho_{C''}}{\rho^3}, 1 \right) g(X_{CC'}), \quad (3.11b)$$

$$g(X_{CC'}) = \begin{cases} 1, & X_{CC'} < -1. \\ 1 - \sin(\arccos(X_{CC'})), & -1 \leq X_{CC'} < 0 \\ \sin(\arccos(X_{CC'})) - 1, & 0 \leq X_{CC'} < 1 \\ -1, & X_{CC'} > 1. \end{cases} \quad (3.11c)$$

where,  $C \neq C' \neq C''$  are three separate fluids.

The downside of the current multi-phase and multi-fluid methodologies is that, although the cMCLBM allows high tune-ability and control of the surface tensions and fluid-fluid contacts, with only small increase in methodological complexity, it comes at an increase of computational cost. Currently, interfaces between each pair of fluids are defined, and as such the number of interfaces needed dramatically increases with the number of fluids, where the number of interfaces in relation to the number of fluids  $n$ , can be given by:

$$\text{No. of interfaces} = \frac{n(n-1)}{2}. \quad (3.12)$$

From this result, it follows that the amount of storage needed increases quickly as the number of fluids increases, as well as computational run time due to the need to loop over more interface pairs when calculating the phase-fields, unit normals, segregation etc.

Clearly then, addressing this problem would increase the scalability and reduce computational expense of the cMCLBM models. Through making well-justified assumptions and neglecting redundant contact physics, it is possible to reduce computational expense and the number of interface pairs. This observation will be discussed further in Chapters 5 and 6 when simulating multiple red blood cells.

### 3.3 Analysis

This section investigates performing two interlinked sets of analyses —dynamics and kinematics. These analyses provide an enhanced understanding of cMCLBMs, which are applied to the simulation of binary fluids with a density contrast. As will be shown below, the kinematics and the dynamics of the model are coupled, and as such, one could pose an argument for showing the kinematics analysis before the dynamics analysis or vice versa. Here, the latter approach is taken in the light of recovering an expression for the force contribution needed for the density difference correction  $F_{2i}$  introduced in Eq. (3.2).

Pursuant to a consideration of the dynamics and kinematics of the model, our aim is to quantify the utility of this class of cMCLBM models when simulating large density contrasts, with strengths and limitations of the model exposed from this analyses being discussed.

### 3.3.1 Dynamics

Presented here is the means of recovering the weakly compressible Navier-Stokes equations from the lattice Boltzmann equation given in Eq. (3.46), using the Chapman-Enskog procedure for the two component cMCLBM with density contrasts between the fluids outlined previously. Note, the reasons for recovering the weakly compressible Navier-Stokes equations over the incompressible Navier-Stokes equations are discussed within this analysis; they essentially relate to a sonic velocity which is only of order unity; with careful parameterisation, however, the advent of the associated compressibility error may be satisfactorily controlled in the low Mach number limit. In essence, Chapman-Enskog procedure is a perturbation expansion of the distribution function about its equilibrium. This work will outline a process which will be referred to when modifying the methodology through inclusion of an MRT collision operator and also a pseudo three-dimensional system in Chapter 4. Due to this, a BGK collision scheme is implemented here, in order to increase transparency, with extra detail also being provided. From this analysis, correct dynamics will be verified and an important correction term will be recovered, which has implications on the system kinematics (discussed further in the proceeding section).

The methodology chosen for present purposes, is one which follows the overall structure of the analyses outlined by Guo et al. [70]. This methodology is chosen as it is clear and concise and it facilitates comparison between other collision models and schemes, which will be discussed later. Again, the presented analysis uses the D2Q9 model and labelling convention showed in Figure 2.3.

Starting by defining the form of the source term given in Eq. (3.2) after that of Guo et al. [70]:

$$F_i = t_i \left[ A + \frac{B c_{i\alpha}}{c_s^2} + C \frac{c_{i\alpha} c_{i\beta} - c_s^2 \delta_{\alpha\beta}}{2c_s^4} \right], \quad (3.13)$$

where the source term  $F_i$  must meet the following properties (solvability conditions):

$$\sum_i F_i = A, \quad \sum_i c_{i\alpha} F_i = B = n F_\alpha, \quad \sum_i c_{i\alpha} c_{i\beta} F_i = A c_s^2 \delta_{\alpha\beta} + \frac{1}{2} (C_{\alpha\beta} + C_{\beta\alpha}), \quad (3.14)$$

in which  $A$ ,  $B$ , the correction tensor  $\underline{C}$  and constant  $m$  in Eq. (3.5) are to be determined.

The key lattice properties (isotropies) used throughout are given as:

$$\sum_i t_i (1, (c_{i\alpha})^{2p+1}, c_{i\alpha} c_{i\beta}, c_{i\alpha} c_{i\beta} c_{i\gamma} c_{i\delta}) = (1, 0, c_s^2 \delta_{\alpha\beta}, c_s^4 \Delta_{\alpha\beta\gamma\delta}),$$

### 3. Kinematics and Dynamics of Chromodynamic Multi-Component Lattice Boltzmann Equation Simulation

where  $p \geq 0$ . The defined equilibrium distribution function  $f_i^{(0)}$  in Eq. (3.3) may hence be shown to have the following properties, which again, are necessary if one is to recover correct hydrodynamics:

$$\sum_i f_i^{(0)}(1, c_{i\alpha}, c_{i\alpha}c_{i\beta}) = (\rho, \rho u_\alpha, (2\phi_1 + 4\phi_2)\rho\delta_{\alpha\beta} + \rho u_\alpha u_\beta). \quad (3.15)$$

Functions  $\phi_1$  and  $\phi_2$  depend upon the chromodynamic field (see Eq. (3.6)) and hence the spatial-temporal variation of the isotropic term of the second moment can be modified to:

$$\sum_i f_i^{(0)} c_{i\alpha} c_{i\beta} = \left[ \frac{3}{5} ((1 - \alpha_R)\rho_R + (1 - \alpha_B)\rho_B) \delta_{\alpha\beta} + \rho u_\alpha u_\beta \right]. \quad (3.16)$$

Now, we introduce the Chapman-Enskog expansion that will be used for the kinetic equation and distribution function. The expansion splits the distribution function and time derivative into perturbed contributions, at different orders:

$$f_i = f_i^{(0)} + \epsilon f_i^{(1)} + \epsilon^2 f_i^{(2)} + \dots, \quad (3.17)$$

$$\frac{\partial}{\partial t} = \epsilon \frac{\partial}{\partial t_0} + \epsilon^2 \frac{\partial}{\partial t_1}, \quad \nabla = \epsilon \nabla_1. \quad (3.18)$$

The expansion parameter,  $\epsilon$ , is proportional to the ratio of the lattice spacing to the characteristic flow length. It should be noted that terms of order  $\epsilon^2$  or greater, in Eq. (3.17), are ignored in the proceeding analysis, due to only the two lowest orders being needed to recover the Navier-Stokes equations [39]. The approach taken when expanding the time derivative in Eq. (3.18) differs between authors, where, e.g., Guo and Mohammed [70, 121] treat the expansion as a linear composition of fast  $t_0$  and slow  $t_1$  time and Kruger and Succi [39, 122] rather as an infinite expansion of the time derivative [123].

Here, the same assumptions as Guo et al. [70] are applied:

$$\sum_i f_i^{(p)} = 0, \quad \sum_i f_i^{(p+1)} \underline{c}_i = 0, \quad p \geq 1, \quad (3.19)$$

and it now follows that:

$$\rho \underline{u} = \sum_i f_i \underline{c}_i + m \underline{F} \Delta t \Leftrightarrow \sum_i f_i^{(1)} \underline{c}_i = -m \underline{F} \Delta t. \quad (3.20)$$

The first step towards recovering the hydrodynamic behaviour of the model is to Taylor expand and apply Chapman-Enskog expansion (Eqs. (3.17,3.18)) to Eq. (3.2):

$$\begin{aligned} (\epsilon \partial_{t_0} + \epsilon^2 \partial_{t_1} + c_i \cdot \epsilon \partial_\alpha) (f_i^0 + \epsilon f_i^1) + \frac{\Delta t}{2} (\epsilon \partial_{t_0} + \epsilon^2 \partial_{t_1} + c_i \cdot \epsilon \partial_\alpha)^2 (f_i^0 + \epsilon f_i^1) \\ = -\frac{1}{\tau \Delta t} (f_i^0 + \epsilon f_i^1 + \epsilon^2 f_i^2 - f_i^{(eq)}) + \epsilon F_i. \end{aligned} \quad (3.21)$$

### 3. Kinematics and Dynamics of Chromodynamic Multi-Component Lattice Boltzmann Equation Simulation

First, evaluating the most rapid behaviour in the model, with equivalent equation in Guo et al.'s analysis [70] being Equation (9b), giving:

$$O(\epsilon) : (c_{i\alpha}\partial_\alpha + \partial_{t_0})f_i^{(0)} = -\frac{1}{\tau\Delta t}f_i^{(1)} + F_i. \quad (3.22)$$

Now, proceeding to Equation (9c) of [70] (which is the expansion to  $O(\epsilon^2)$ ), it is possible to obtain straightforwardly the following equation:

$$O(\epsilon^2) : \partial_{t_1}f_i^{(0)} + \left(1 - \frac{1}{2\tau}\right)(c_{i\alpha}\partial_\alpha + \partial_{t_0})f_i^{(1)} = -\frac{1}{\tau\Delta t}f_i^{(2)} + \frac{\Delta t}{2}(c_{i\alpha}\partial_\alpha + \partial_{t_0})F_i. \quad (3.23)$$

Starting with the  $O(\epsilon)$  equation, the zeroth and first moments are taken. The zeroth moment is:

$$\begin{aligned} \sum_i (c_{i\alpha}\partial_\alpha + \partial_{t_0})f_i^{(0)} &= \sum_i -\frac{1}{\tau\Delta t}f_i^{(1)} + \sum_i \Delta t F_i, \\ \partial_{t_0}\rho + \partial_\alpha \rho u_\alpha &= \Delta t A, \\ \partial_{t_0}\rho + \partial_\alpha \rho u_\alpha &= 0, \end{aligned} \quad (3.24)$$

where in order to retrieve the continuity equation, let  $A = 0$ , similar to the analysis in [70].

The first moment of Eq. (3.22) is evaluated as follows:

$$\begin{aligned} \sum_i (c_{i\alpha}\partial_\alpha + \partial_{t_0})f_i^{(0)}c_{i\beta} &= \sum_i -\frac{1}{\tau\Delta t}f_i^{(1)}c_{i\beta} + \sum_i \Delta t F_i c_{i\beta}, \\ \partial_\alpha \Pi_{\alpha\beta}^{(0)} + \partial_{t_0}\rho u_\beta &= \left(\frac{m}{\tau} + n\right)F_\beta. \end{aligned} \quad (3.25)$$

where, assuming that  $B_\beta = nF_\beta$ ,  $n$  is a constant to be determined and  $\Pi_{\alpha\beta}^{(0)} = (2\phi_1 + 4\phi_2)\rho\delta_{\alpha\beta} + \rho u_\alpha u_\beta$  is the zeroth-order momentum flux tensor. To recover the Euler equations, the following constraints must be met:

$$A = 0, \quad n + \frac{m}{\tau} = 1. \quad (3.26)$$

We proceed to evaluate the zeroth and first moments of the  $O(\epsilon^2)$  equation. The zeroth moment of Eq. (3.23) is:

$$\begin{aligned} \partial_{t_1} \sum_i f_i^{(0)} + \left(1 - \frac{1}{2\tau}\right) \sum_i (c_{i\alpha}\partial_\alpha + \partial_{t_0})f_i^{(1)} &= -\frac{1}{\tau\Delta t} \sum_i f_i^{(2)} + \frac{\Delta t}{2} \sum_i (c_{i\alpha}\partial_\alpha + \partial_{t_0})F_i \\ \partial_{t_1}\rho + \left(1 - \frac{1}{2\tau}\right) (\partial_\alpha (-mF_\alpha\Delta t)) &= -\frac{\Delta t}{2} (\partial_\alpha B_\alpha) \\ \partial_{t_1}\rho + \left(1 - \frac{1}{2\tau}\right) (\partial_\alpha (-mF_\alpha\Delta t)) &= -\frac{\Delta t}{2} \left(\partial_\alpha \left(1 - \frac{m}{\tau}\right) F_\alpha\right) \\ \partial_{t_1}\rho &= -\Delta t \left(\frac{1}{2} - m\right) \partial_\alpha F_\alpha. \end{aligned} \quad (3.27)$$



### 3. Kinematics and Dynamics of Chromodynamic Multi-Component Lattice Boltzmann Equation Simulation

Next, the first moment of the  $O(\epsilon^2)$  equation:

$$\begin{aligned} \partial_{t_1} \sum_i f_i^{(0)} c_{i\beta} + \left(1 - \frac{1}{2\tau}\right) \sum_i (c_{i\alpha} \partial_\alpha + \partial_{t_0}) f_i^{(1)} c_{i\beta} &= -\frac{1}{\tau \Delta t} \sum_i f_i^{(2)} c_{i\beta} \\ &+ \frac{\Delta t}{2} \sum_i (c_{i\alpha} \partial_\alpha + \partial_{t_0}) F_i c_{i\beta} \\ \partial_{t_1} (\rho u_\beta) + \left(1 - \frac{1}{2\tau}\right) \left(\Delta t \partial_{t_0} (-m F_\beta) + \partial_\alpha \Pi_{\alpha\beta}^{(1)}\right) &= -\frac{\Delta t}{2} \left(\partial_{t_0} B + \partial_\alpha \left(\frac{1}{2} (C_{\alpha\beta} + C_{\beta\alpha})\right)\right) \\ \partial_{t_1} (\rho u_\beta) &= \Delta t \left(m - \frac{1}{2}\right) \partial_{t_0} F_\beta + \partial_\alpha \cdot \sigma'_{\alpha\beta}, \end{aligned} \quad (3.28)$$

$$(3.29)$$

where  $\sigma'_{\alpha\beta} = -\left(1 - \frac{1}{2\tau}\right) \Pi_{\alpha\beta}^{(1)} - \frac{\Delta t}{4} (C_{\alpha\beta} + C_{\beta\alpha})$ . After Guo et al. [70], the following constraint on  $m$  has to be imposed, in order eventually to obtain physically correct target dynamics for the system:

$$m = \frac{1}{2}. \quad (3.30)$$

Subsequently, there result the two following equations for the zeroth moment and first moment of the  $O(\epsilon^2)$  equation and also an updated constraint on  $n$ :

$$\partial_{t_1} \rho = 0, \quad (3.31)$$

and the updated first moment equation is:

$$\partial_{t_1} (\rho u_\beta) = \partial_\alpha \cdot \sigma_{\alpha\beta}, \quad (3.32)$$

where it is now possible to express  $n$  as follows:

$$n = 1 - \frac{1}{2\tau}. \quad (3.33)$$

To evaluate Eq. (3.32), an expression for the first order momentum flux tensor  $\Pi_{\alpha\beta}^{(1)}$ , is needed. Rearranging Eq. (3.22) for  $f_i^{(1)}$  and then taking the second moment by multiplying through by  $c_{i\alpha} c_{i\beta}$  and summing on both sides  $\sum_i$ .

$$\begin{aligned} \Pi_{\alpha\beta}^{(1)} &= \sum_i f_i^{(1)} c_{i\alpha} c_{i\beta} \\ &= \sum_i \tau \Delta t \left( -(\partial_{t_0} + c_{i\gamma} \partial_\gamma) f_i^{(0)} + F_i \right) c_{i\alpha} c_{i\beta} \\ \frac{\Pi_{\alpha\beta}^{(1)}}{\tau \Delta t} &= -\partial_{t_0} [(2\phi_1 + 4\phi_2) \rho \delta_{\alpha\beta}] - \partial_{t_0} (\rho u_\alpha u_\beta) - c_s^2 \partial_\gamma (u_\delta \rho) \Delta_{\alpha\beta\gamma\delta} + \frac{1}{2} (C_{\alpha\beta} + C_{\beta\alpha}). \end{aligned} \quad (3.34)$$

For transparency, each term on the right hand side of Eq. (3.34) will be evaluated individually. The time derivative in the first term on the right hand side can be

### 3. Kinematics and Dynamics of Chromodynamic Multi-Component Lattice Boltzmann Equation Simulation

removed using the kinematical condition that color is a material invariant on the shortest time scales (Eq. (3.58)) as follows:

$$\begin{aligned}
-\partial_{t_0} [(2\phi_1 + 4\phi_2) \rho \delta_{\alpha\beta}] &= -\partial_{t_0} \frac{3}{5} [(1 - \alpha_R) \rho_R + (1 - \alpha_B) \rho_B] \delta_{\alpha\beta} \\
&= -\frac{3}{5} (1 - \alpha_R) \partial_{t_0} [\rho_R + \Lambda \rho_B] \delta_{\alpha\beta} \\
&= \frac{3}{5} (1 - \alpha_R) u_\gamma \partial_\gamma [\rho_R + \Lambda \rho_B] \delta_{\alpha\beta}.
\end{aligned} \tag{3.35}$$

Simplifying the second term on the right hand side now. Here, the product rule and then substitution from Eqs. (3.24), (3.25) and (3.16) will be used to remove time derivatives from the equation:

$$\begin{aligned}
-\partial_{t_0} (\rho u_\alpha u_\beta) &= -u_\alpha \partial_{t_0} (\rho u_\beta) - (\rho u_\beta) \partial_{t_0} u_\alpha \\
&= u_\alpha \partial_\gamma \Pi_{\beta\gamma}^{(0)} - u_\alpha F_\beta + u_\beta \partial_\gamma \Pi_{\alpha\gamma}^{(0)} + u_\beta F_\alpha - u_\alpha u_\beta \partial_\gamma u_\gamma \rho \\
&= -(u_\beta F_\alpha + u_\alpha F_\beta) + (u_\alpha \partial_\beta + u_\beta \partial_\alpha) [(2\phi_1 + 4\phi_2) \rho \delta_{\alpha\beta}] + \\
&\quad + u_\alpha \partial_\gamma (\rho u_\beta u_\gamma) + u_\beta \partial_\gamma (\rho u_\alpha u_\gamma) - u_\alpha u_\beta \partial_\gamma (\rho u_\gamma), \\
&= -(u_\beta F_\alpha + u_\alpha F_\beta) + (u_\alpha \partial_\beta + u_\beta \partial_\alpha) \frac{3}{5} (1 - \alpha_R) \partial_\gamma [\rho_R + \Lambda \rho_B], \tag{3.36}
\end{aligned}$$

where,  $u_\alpha \partial_\gamma (\rho u_\beta u_\gamma) + u_\beta \partial_\gamma (\rho u_\alpha u_\gamma) - u_\alpha u_\beta \partial_\gamma (\rho u_\gamma) = \partial_\gamma (\rho u_\alpha u_\beta u_\gamma)$ . This term is approximated to zero under the assumption of the low Mach number limit —the assumption that fluid velocity is much smaller than the speed of sound, meaning that this term is negligible (see Eq. (2.18)).

Next, evaluating the third term on the right hand side, using the tensor properties defined at the start of this analysis and, by utilising the product rule:

$$\begin{aligned}
-c_s^2 \partial_\gamma (u_\delta \rho) \Delta_{\alpha\beta\gamma\delta} &= -c_s^2 \partial_\gamma (u_\delta \rho) (\delta_{\alpha\beta} \delta_{\gamma\delta} + \delta_{\alpha\gamma} \delta_{\beta\delta} + \delta_{\alpha\delta} \delta_{\beta\gamma}) \\
&= -c_s^2 \partial_\gamma (u_\gamma \rho) \delta_{\alpha\beta} - c_s^2 \rho \partial_\alpha (u_\beta) - c_s^2 u_\beta \partial_\alpha (\rho) + \\
&\quad - c_s^2 u_\alpha \partial_\beta (\rho) - c_s^2 \rho \partial_\beta (u_\alpha). \tag{3.37}
\end{aligned}$$

Substituting the simplified expressions, given by Eqs. (3.35, 3.36, 3.37) back into the expression for the first-order momentum flux tensor, Eq. (3.34):

$$\begin{aligned}
\frac{\Pi_{\alpha\beta}^{(1)}}{\tau \Delta t} &= \frac{3}{5} (1 - \alpha_R) u_\gamma \partial_\gamma [\rho_R + \Lambda \rho_B] \delta_{\alpha\beta} + \frac{1}{2} (C_{\alpha\beta} + C_{\beta\alpha}) - (u_\beta F_\alpha + u_\alpha F_\beta) + \\
&\quad + (u_\alpha \partial_\beta + u_\beta \partial_\alpha) \frac{3}{5} (1 - \alpha_R) \partial_\gamma [\rho_R + \Lambda \rho_B] - c_s^2 u_\gamma \partial_\gamma (\rho) \delta_{\alpha\beta} + \\
&\quad - c_s^2 \rho \partial_\gamma (u_\gamma) \delta_{\alpha\beta} - c_s^2 \partial_\alpha (u_\beta) - c_s^2 u_\beta \partial_\alpha (\rho) - c_s^2 u_\alpha \partial_\beta (\rho) - c_s^2 \rho \partial_\beta (u_\alpha).
\end{aligned}$$

### 3. Kinematics and Dynamics of Chromodynamic Multi-Component Lattice Boltzmann Equation Simulation

Simplifying the above, by collecting terms together:

$$\begin{aligned}
\frac{\Pi_{\alpha\beta}^{(1)}}{\tau\Delta t} &= -\frac{\rho}{3}(\partial_\alpha u_\beta + \partial_\beta u_\alpha) + \frac{1}{2}(C_{\alpha\beta} + C_{\beta\alpha}) - (u_\alpha F_\beta + u_\beta F_\alpha) + \\
&\quad + u_\alpha \partial_\beta \Phi' + u_\beta \partial_\alpha \Phi' + u_\gamma \partial_\gamma \Phi' \delta_{\alpha\beta} + \\
&\quad - \frac{\rho}{3} \partial_\gamma u_\gamma \delta_{\alpha\beta} \\
&= -\frac{\rho}{3}(\partial_\alpha u_\beta + \partial_\beta u_\alpha) - u_\alpha (F_\beta - \partial_\beta \Phi') - u_\beta (F_\alpha - \partial_\alpha \Phi') + \\
&\quad + \left[ u_\gamma \partial_\gamma \Phi' - \frac{\rho}{3} \partial_\gamma u_\gamma \right] \delta_{\alpha\beta} + \frac{1}{2}(C_{\alpha\beta} + C_{\beta\alpha}),
\end{aligned} \tag{3.38}$$

where, for simplicity, the following definition is used:  $\Phi' = \frac{3}{5}(1 - \alpha_R)(\rho_R + \Lambda\rho_B) - \frac{1}{3}\rho$ .

Now, using the definition of the viscous stress tensor  $\sigma'_{\alpha\beta}$ , and substituting the expression from Eq. (3.38) for  $\Pi_{\alpha\beta}^{(1)}$ , results in:

$$\begin{aligned}
\sigma'_{\alpha\beta} &= -\left(1 - \frac{1}{2\tau}\right) \Pi_{\alpha\beta}^{(1)} - \frac{\Delta t}{4}(C_{\alpha\beta} + C_{\beta\alpha}), \\
&= \left(\tau - \frac{1}{2}\right) \left( \frac{\rho}{3}(\partial_\alpha u_\beta + \partial_\beta u_\alpha) + u_\alpha (F_\beta - \partial_\beta \Phi') + u_\beta (F_\alpha - \partial_\alpha \Phi') \right) + \\
&\quad - \left(\tau - \frac{1}{2}\right) \left[ u_\gamma \partial_\gamma \Phi' - \frac{\rho}{3} \partial_\gamma u_\gamma \right] \delta_{\alpha\beta} - \frac{\tau}{2}(C_{\alpha\beta} + C_{\beta\alpha}).
\end{aligned} \tag{3.39}$$

Only the first term on the right hand side is consistent with the Navier-Stokes equations. It is therefore possible to infer an error as follows:

$$\begin{aligned}
E_{\alpha\beta} &= \left(\tau - \frac{1}{2}\right) \left( u_\alpha (F_\beta - \partial_\beta \Phi') + u_\beta (F_\alpha - \partial_\alpha \Phi') \right) + \\
&\quad - \left(\tau - \frac{1}{2}\right) \left[ u_\gamma \partial_\gamma \Phi' - \frac{\rho}{3} \partial_\gamma u_\gamma \right] \delta_{\alpha\beta} - \frac{\tau}{2}(C_{\alpha\beta} + C_{\beta\alpha})
\end{aligned} \tag{3.40}$$

Therefore, in order to eliminate the error, the following choice of correction tensor  $C_{\alpha\beta}$  is made (eliminates the error):

$$C_{\alpha\beta} = \left(1 - \frac{1}{2\tau}\right) \left( u_\alpha (F_\beta - \partial_\beta \Phi') + u_\beta (F_\alpha - \partial_\alpha \Phi') - \left[ u_\gamma \partial_\gamma \Phi' - \frac{\rho}{3} \partial_\gamma u_\gamma \right] \delta_{\alpha\beta} \right). \tag{3.41}$$

Note that by setting  $\alpha_R = \alpha_B$ ,  $\Lambda \rightarrow 1$ ,  $\partial_\delta \Phi' \rightarrow 0$ , Eq. (3.41) will reduce to Equation (16) of [70].

Finally, consider Equations (6) and (20) of Guo et al., for the evolution equation source term. It has been found that, in the additional presence of large density gradients

### 3. Kinematics and Dynamics of Chromodynamic Multi-Component Lattice Boltzmann Equation Simulation

(which now characterise the inter-facial region), the BGK source term becomes:

$$F_i \equiv t_i \left\{ \left(1 - \frac{1}{2\tau}\right) \frac{F_\alpha c_{i\alpha}}{c_s^2} + \frac{1}{2c_s^4} \left(1 - \frac{1}{2\tau}\right) \left[ u_\alpha (F_\beta - \partial_\beta \Phi') + u_\beta (F_\alpha - \partial_\alpha \Phi') - \left[ u_\gamma \partial_\gamma \Phi' - \frac{\rho}{3} \partial_\gamma u_\gamma \right] \delta_{\alpha\beta} \right] \times (c_{i\alpha} c_{i\beta} - c_s^2 \delta_{\alpha\beta}) \right\}. \quad (3.42)$$

Separating the source term into two components  $F_{1i}$  and  $F_{2i}$ , where  $F_{1i}$  contains the density-difference corrections and  $F_{2i}$  contains the immersed boundary force (drop dynamics — surface tension), we have:

$$F_{1i} = \frac{1}{2c_s^4} \left(1 - \frac{1}{2\tau}\right) t_i \left[ -u_\alpha \partial_\beta \Phi' - u_\beta \partial_\alpha \Phi' - \left[ u_\gamma \partial_\gamma \Phi' - \frac{\rho}{3} \partial_\gamma u_\gamma \right] \delta_{\alpha\beta} \right] (c_{i\alpha} c_{i\beta} - c_s^2 \delta_{\alpha\beta}). \quad (3.43)$$

$$F_{2i} = t_i \left(1 - \frac{1}{2\tau}\right) \left[ \frac{F_\alpha c_{i\alpha}}{c_s^2} + \frac{(u_\beta F_\alpha + u_\alpha F_\beta) (c_{i\alpha} c_{i\beta} - c_s^2 \delta_{\alpha\beta})}{c_s^4} \right]. \quad (3.44)$$

Finally, the macroscopic equations of motion can now be recovered. For the continuity equation, combining Eqs. (3.24), (3.26), (3.27) and (3.30), we have:

$$\partial_t \rho + \partial_\alpha \rho u_\alpha = 0, \quad (3.45)$$

and by combining Eqs. (3.25, 3.26, 3.28, 3.30, 3.39, 3.41), the weakly compressible Navier-Stokes equations are recovered:

$$\partial_t \rho u_\alpha + \partial_\beta (\rho u_\alpha u_\beta) = -\partial_\alpha p + \partial_\beta \eta (\partial_\beta u_\alpha + \partial_\alpha u_\beta) + F_\alpha, \quad (3.46)$$

where pressure is defined as:  $p = \rho c_s^2$  and for the BGK collision scheme used in this LBE variant, the viscosity is defined as:

$$\eta = \frac{\rho}{3} \left( \tau - \frac{\Delta t}{2} \right). \quad (3.47)$$

In conclusion, the weakly compressible Navier-Stokes equations have been recovered as desired. However, the extension to the simulation of binary fluids with a density contrast led to more error terms in relation to the unity density contrast model [70]. The fallout from this is that alongside the source term that applies the immersed boundary force (Eq. (3.44)) found in the analysis in [70], there is now another source term that contains the corrections needed due to the extension of the model for the simulation of fluids with a density contrast (Eq. (3.43)). As such, it is important now to assess to what extent this new correction source term impacts the model, and importantly, its compliance with the continuum kinematical interface condition.

### 3.3.2 Kinematics

Multi-Component lattice Boltzmann method variants all contain a diffused interfacial region between the fluids when aiming to simulate immiscible fluid flows; this, of course, introduces an unphysical length scale into continuum simulations. In cMCLBM models, this interface scale is relatively easily tuneable; it is defined by a phase-field that catalogues the phase one is in over the lattice. This interfacial region has large importance, with immersed forces being applied in this region, aiming to enforce or, rather, manufacture, flow physics characteristic of the situation under consideration, i.e., surface tension at the interface between fluids, when modelling drops. This interface should be subject to a continuum kinematic condition, which we choose to state as follows: the interface should advect with the fluids locally (physically, if fluid<sub>1</sub> recedes from fluid<sub>2</sub> quicker than fluid<sub>2</sub> catches fluid<sub>1</sub>, a cavity will form). To check the interfaces' compliance with the kinematic condition, one must transform -pass- from the kinetic description of the fluid segregation to a continuum description. Here, an analysis is presented that provides a framework for investigating the model's compliance with this continuum kinematic condition, by assessing the segregation rule that helps maintain the interface —potentially the most crucial methodological step in color-gradient and chromodynamic models.

The following analysis provides a framework which is referenced in both Chapters 4 and 5, as well as having relevance to the whole class of chromodynamic models. The analysis considers a uniformly translating flat interface between two effectively immiscible fluids. Specifically, the interfaces mean curvature is given by  $H = 0$ . Through setting  $H = 0$ , this removes the dynamics from the model (soon to be discussed), therefore testing the pure kinematics of the model. Note, letting  $H \neq 0$  in the proceeding analysis would take away from the transparent outcome of this work, resulting in an over-elaborate perturbation of the solution soon to be given. Figure 3.2 shows a schematic of the interfacial region and the postulated flow in question:

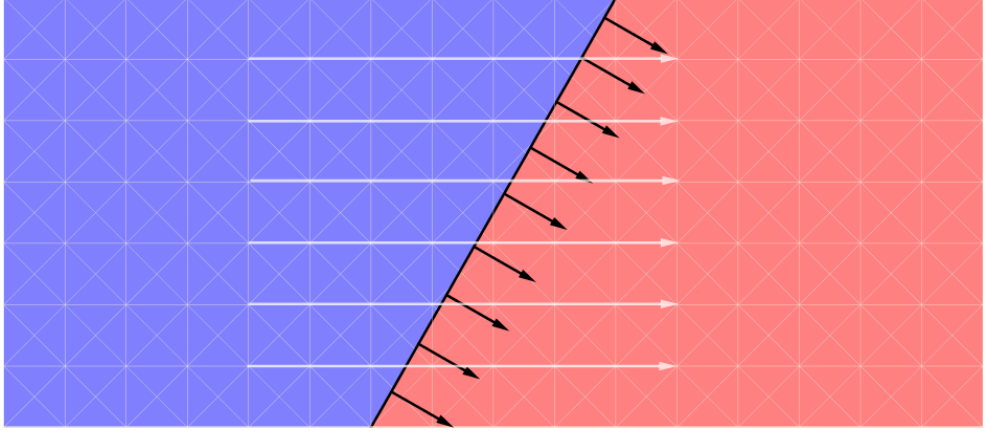
Starting with the red fluid (say), colour conservation is applied to the node lying at position  $\underline{r}$ , time  $t + \Delta t$ , to post collision, post re-colour red link populations on adjacent nodes at the previous time step  $t$ :

$$\rho_R(\underline{r}, t + \Delta t) = \sum_i R_i^{\psi\psi}(\underline{r} - \underline{c}_i \Delta t, t). \quad (3.48)$$

Substitute the post collision (post re-colour) rule for the red fluid,  $R_i^{\psi\psi}$ , into Eq. (3.48)

$$\begin{aligned} \rho_R(\underline{r}, t + \Delta t) = & \sum_{\forall i} \frac{\rho_R(\underline{r} - \Delta t \underline{c}_i)}{\rho(\underline{r} - \Delta t \underline{c}_i)} \left( f_i^{(0)}(\rho, \underline{u}) + F_i \right) \\ & + \sum_{\forall i} \beta \frac{\phi_i(\underline{r} - \Delta t \underline{c}_i) \rho_R(\underline{r} - \Delta t \underline{c}_i) \rho_B(\underline{r} - \Delta t \underline{c}_i) \hat{n} \cdot \Delta t \underline{c}_i}{\rho(\underline{r} - \Delta t \underline{c}_i)}. \end{aligned} \quad (3.49)$$

### 3. Kinematics and Dynamics of Chromodynamic Multi-Component Lattice Boltzmann Equation Simulation



**Figure 3.2:** Schematic of a uniformly translating, flat interface in the direction shown by the white arrows. Black arrows show the interface unit normal  $\hat{n}$ , where the mean curvature of the interface is set to zero ( $H = 0$ ) [77].

Note, because we are concerned with a uniformly translating fluid in the interfacial region, where  $H = 0$ , the surface tension immersed boundary force equals zero,  $F_\alpha = -\frac{1}{2}\sigma H\partial_\alpha\rho^N = 0$ . As such, from the source terms defined from the dynamics analysis (section 3.3.1) in Eqs. (3.43, 3.44), it follows that  $f_i^\psi = f_i^{(0)}(\rho, \underline{u}) + F_{1i}$  (for steady flow), where  $F_{2i} = 0$  due to presence of zero interfacial curvature. The result is that the source term is given by  $F_i = F_{1i}$ ; this therefore removes the surface tension from the analysis (dynamics), resulting in a pure kinematics test, as desired. For transparency, Eq. (3.43) is given in compressed form, for purposes of this analysis:

$$F_{1i} = F_{\alpha\beta}(\rho_R, \rho_B, \rho^N, \Lambda, \underline{u}) t_i (c_{i\alpha}c_{i\beta} - c_s^2\delta_{\alpha\beta}). \quad (3.50)$$

Substituting the expression for the equilibrium distribution function,  $f_i^{(0)}(\rho, \underline{u})$ , into Eq. (3.49) and also  $F_i = F_{1i}$ , we obtain the following:

$$\begin{aligned} \rho_R(\underline{r}, t + \Delta t) &= \sum_{\forall i} \frac{\rho_R(\underline{r} - \Delta t \underline{c}_i)}{\rho(\underline{r} - \Delta t \underline{c}_i)} \left( \rho(\underline{r} - \underline{c}_i \Delta t, t) \phi_i + t_i \rho(\underline{r} - \underline{c}_i \Delta t, t) \times \right. \\ &\quad \left. \left( \frac{u_\alpha c_{i\alpha}}{c_s^2} + \frac{u_\alpha u_\beta c_{i\alpha} c_{i\beta}}{2c_s^4} - \frac{u^2}{2c_s^2} \right) + F_{1i} \right) \\ &\quad + \sum_{\forall i} \beta \frac{\phi_i(\underline{r} - \Delta t \underline{c}_i) \rho_R(\underline{r} - \Delta t \underline{c}_i) \rho_B(\underline{r} - \Delta t \underline{c}_i) \hat{n} \cdot \Delta t \underline{c}_i}{\rho(\underline{r} - \Delta t \underline{c}_i)}, \\ \rho_R(\underline{r}, t + \Delta t) &= \sum_{\forall i} \left[ \rho_R \phi_i + \frac{\rho_R}{\rho} F_{1i} \right]_{\underline{r} - \Delta t \underline{c}_i} \\ &\quad + \sum_{\forall i} \left[ t_i \rho_R \left( \frac{u_\alpha c_{i\alpha}}{c_s^2} + \frac{u_\alpha u_\beta c_{i\alpha} c_{i\beta}}{2c_s^4} - \frac{u^2}{2c_s^2} \right) \right]_{\underline{r} - \Delta t \underline{c}_i} \\ &\quad + \Delta t \beta \sum_{\forall i} \left[ \phi_i \left( \frac{\rho_R \rho_B}{\rho} \right) n_\beta c_{i\beta} \right]_{\underline{r} - \Delta t \underline{c}_i}. \end{aligned} \quad (3.51)$$

### 3. Kinematics and Dynamics of Chromodynamic Multi-Component Lattice Boltzmann Equation Simulation

Taylor expanding about  $t$  and  $\underline{r}$  up to second order, there results the following expression:

$$\begin{aligned}
\rho_R + \Delta t \frac{\partial}{\partial t} \rho_R + \frac{1}{2} \Delta t^2 \frac{\partial^2}{\partial t^2} \rho_R &= \sum_{i=0} \left[ \left( \rho_R - \Delta t c_{i\beta} \partial_\beta \rho_R + \frac{1}{2} \Delta t^2 c_{i\beta} c_{i\gamma} \partial_\beta \partial_\gamma \rho_R \right) \phi_0 \right] \\
&+ \sum_{\forall i \neq 0} \left[ \left( \rho_R - \Delta t c_{i\beta} \partial_\beta \rho_R + \frac{1}{2} \Delta t^2 c_{i\beta} c_{i\gamma} \partial_\beta \partial_\gamma \rho_R \right) \phi_i \right] \\
&+ \sum_{\forall i} \left[ \left( \rho_R - \Delta t c_{i\beta} \partial_\beta \rho_R + \frac{1}{2} \Delta t^2 c_{i\beta} c_{i\gamma} \partial_\beta \partial_\gamma \rho_R \right) F_{1i} \right] \\
&+ \sum_{\forall i} \left[ t_i \left( \rho_R - \Delta t c_{i\gamma} \partial_\gamma \rho_R + \frac{1}{2} \Delta t^2 c_{i\gamma} c_{i\delta} \partial_\gamma \partial_\delta \rho_R \right) \frac{u_\alpha c_{i\alpha}}{c_s^2} \right] \\
&+ \sum_{\forall i} \left[ t_i \left( \rho_R - \Delta t c_{i\gamma} \partial_\gamma \rho_R + \frac{1}{2} \Delta t^2 c_{i\gamma} c_{i\theta} \partial_\gamma \partial_\theta \rho_R \right) \times \right. \\
&\quad \left. \frac{u_\alpha u_\beta c_{i\alpha} c_{i\beta}}{2c_s^4} \right] \\
&- \sum_{\forall i} \left[ t_i \left( \rho_R - \Delta t c_{i\gamma} \partial_\gamma \rho_R + \frac{1}{2} \Delta t^2 c_{i\gamma} c_{i\theta} \partial_\gamma \partial_\theta \rho_R \right) \frac{u^2}{2c_s^2} \right] \\
&+ \Delta t \beta \sum_{i=0} \left[ \left( \frac{\rho_R \rho_B}{\rho} - \Delta t c_{i\alpha} \partial_\alpha \left( \frac{\rho_R \rho_B}{\rho} \right) + \right. \right. \\
&\quad \left. \left. \frac{\Delta t^2}{2} c_{i\alpha} c_{i\beta} \partial_\alpha \partial_\beta \left( \frac{\rho_R \rho_B}{\rho} \right) \right) \phi_0 \times n_\gamma c_{i\gamma} \right] \\
&+ \Delta t \beta \sum_{\forall i \neq 0} \left[ \left( \frac{\rho_R \rho_B}{\rho} - \Delta t c_{i\alpha} \partial_\alpha \left( \frac{\rho_R \rho_B}{\rho} \right) + \right. \right. \\
&\quad \left. \left. \frac{\Delta t^2}{2} c_{i\alpha} c_{i\beta} \partial_\alpha \partial_\beta \left( \frac{\rho_R \rho_B}{\rho} \right) \right) \phi_i \times n_\gamma c_{i\gamma} \right].
\end{aligned}$$

In order to simplify the above expression, one must appeal to lattice isotropy and lattice weight  $t_i$  properties. Accordingly, the following lattice tensor conditions are used:

$$\sum_{\forall i} t_i \left[ (c_{i\alpha})^{2p+1}, c_{i\alpha} c_{i\beta}, c_{i\alpha} c_{i\beta} c_{i\gamma} c_{i\theta} \right] = (0, c_s^2 \delta_{\alpha\beta}, c_s^4 \Delta_{\alpha\beta\gamma\theta}), \quad (3.52)$$

$$\sum_{\forall i \neq 0} s_i \left[ (c_{i\alpha})^{2p+1}, c_{i\alpha} c_{i\beta}, c_{i\alpha} c_{i\beta} c_{i\gamma} c_{i\theta} \right] = (0, k c_s^2 \delta_{\alpha\beta}, k c_s^4 \Delta_{\alpha\beta\gamma\theta}), \quad (3.53)$$

where, again,  $k = \frac{9}{5}$  for the  $D2Q9$  lattice structure. Using Eqs. (3.52, 3.53), the compressed form of  $F_{1i}$  in Eq. (3.50) and the definition of  $\phi_i$  in Eq. (3.6) to simplify Eq. (3.52), and removing terms that will sum to zero, we have:

$$\rho_R + \Delta t \frac{\partial}{\partial t} \rho_R + \frac{1}{2} \Delta t^2 \frac{\partial^2}{\partial t^2} \rho_R = \rho_R \left( \frac{\alpha_R \rho_R}{\rho} + \frac{\alpha_B \rho_B}{\rho} \right)$$

3. Kinematics and Dynamics of Chromodynamic Multi-Component Lattice Boltzmann Equation Simulation

$$\begin{aligned}
& + \sum_{\forall i \neq 0} \left[ \left( \rho_R + \frac{1}{2} \Delta t^2 c_{i\beta} c_{i\gamma} \partial_\beta \partial_\gamma \rho_R \right) (1 - \alpha_R) \frac{s_i \rho_R}{\rho} \right] \\
& + \sum_{\forall i \neq 0} \left[ \left( \rho_R + \frac{1}{2} \Delta t^2 c_{i\beta} c_{i\gamma} \partial_\beta \partial_\gamma \rho_R \right) (1 - \alpha_B) \frac{s_i \rho_B}{\rho} \right] \\
& + \sum_{\forall i} \left[ \left( \rho_R + \frac{1}{2} \Delta t^2 c_{i\gamma} c_{i\delta} \partial_\gamma \partial_\delta \rho_R \right) t_i \times \right. \\
& \quad \left. F_{\alpha\beta} \left( \rho_R, \rho_B, \rho^N, \Lambda, \underline{u} \right) \left( c_{i\alpha} c_{i\beta} - c_s^2 \delta_{\alpha\beta} \right) \right] \\
& - \sum_{\forall i} \left[ t_i \left( \Delta t c_{i\gamma} \partial_\gamma \rho_R \right) \frac{u_\alpha c_{i\alpha}}{c_s^2} \right] \\
& + \sum_{\forall i} \left[ t_i \left( \rho_R + \frac{1}{2} \Delta t^2 c_{i\gamma} c_{i\theta} \partial_\gamma \partial_\theta \rho_R \right) \frac{u_\alpha u_\beta c_{i\alpha} c_{i\beta}}{2c_s^4} \right] \\
& - \sum_{\forall i} \left[ t_i \left( \rho_R + \frac{1}{2} \Delta t^2 c_{i\gamma} c_{i\theta} \partial_\gamma \partial_\theta \rho_R \right) \frac{u^2}{2c_s^2} \right] \\
& - \Delta t \beta \sum_{\forall i \neq 0} \left[ (1 - \alpha_R) \left( \Delta t c_{i\alpha} \partial_\alpha \left( \frac{\rho_R \rho_B}{\rho} \right) \right) \frac{s_i \rho_R}{\rho} n_\gamma c_{i\gamma} \right] \\
& - \Delta t \beta \sum_{\forall i \neq 0} \left[ (1 - \alpha_B) \left( \Delta t c_{i\alpha} \partial_\alpha \left( \frac{\rho_R \rho_B}{\rho} \right) \right) \frac{s_i \rho_B}{\rho} n_\gamma c_{i\gamma} \right].
\end{aligned} \tag{3.54}$$

Now, expanding the summation over lattice links  $i$ , there results the following:

$$\begin{aligned}
\rho_R + \Delta t \frac{\partial \rho_R}{\partial t} + \frac{1}{2} \Delta t^2 \frac{\partial^2 \rho_R}{\partial t^2} & = \frac{\alpha_R \rho_R^2}{\rho} + \frac{\alpha_B \rho_B \rho_R}{\rho} \\
& + (1 - \alpha_R) \left[ \frac{\rho_R^2}{\rho} + \frac{\Delta t^2}{2} \partial_\alpha \partial_\beta \left( \frac{\rho_R^2}{\rho} \right) k c_s^2 \delta_{\alpha\beta} \right] \\
& + (1 - \alpha_B) \left[ \frac{\rho_R \rho_B}{\rho} + \frac{\Delta t^2}{2} \partial_\alpha \partial_\beta \left( \frac{\rho_R \rho_B}{\rho} \right) k c_s^2 \delta_{\alpha\beta} \right] \\
& + \frac{\rho_R F_{\alpha\beta}}{\rho} \left( c_s^2 \delta_{\alpha\beta} - c_s^2 \delta_{\alpha\beta} \right) \\
& + \frac{\Delta t^2}{2} \partial_\gamma \partial_\delta \left( \frac{\rho_R F_{\alpha\beta}}{\rho} \right) \left( c_s^4 \Delta_{\alpha\beta\gamma\delta} - c_s^4 \delta_{\alpha\beta\gamma\delta} \right) \\
& - \frac{u_\gamma}{c_s^2} [\Delta t \partial_\alpha \rho_R] c_s^2 \delta_{\alpha\gamma} \\
& + \frac{u_\alpha u_\beta}{2c_s^4} \left[ \rho_R c_s^2 \delta_{\alpha\beta} + \frac{\Delta t^2}{2} \partial_\gamma \partial_\delta \rho_R c_s^4 \Delta_{\alpha\beta\gamma\delta} \right] \\
& - \frac{u^2}{2c_s^2} \left[ \rho_R + \frac{\Delta t^2}{2} \partial_\alpha \partial_\beta \rho_R c_s^2 \delta_{\alpha\beta} \right] \\
& - \Delta t \beta (1 - \alpha_R) \left[ \Delta t \partial_\alpha \left( \frac{\rho_R^2 \rho_B}{\rho^2} \right) \right] n_\gamma k c_s^2 \delta_{\alpha\gamma}
\end{aligned}$$



3. *Kinematics and Dynamics of Chromodynamic Multi-Component Lattice Boltzmann Equation Simulation*

$$- \Delta t \beta (1 - \alpha_B) \left[ \Delta t \partial_\alpha \left( \frac{\rho_R \rho_B^2}{\rho^2} \right) \right] n_\gamma k c_s^2 \delta_{\alpha\gamma}. \quad (3.55)$$

Expanding brackets and canceling terms in the above gives a final result as:

$$\begin{aligned} \Delta t \frac{\partial \rho_R}{\partial t} + \frac{1}{2} \Delta t^2 \frac{\partial^2 \rho_R}{\partial t^2} + \Delta t u_\gamma \partial_\gamma \rho_R = & \frac{\Delta t^2}{2} (1 - \alpha_R) k c_s^2 \left[ \nabla^2 \left( \frac{\rho_R^2}{\rho} \right) \right] \\ & \frac{\Delta t^2}{2} (1 - \alpha_B) k c_s^2 \left[ \nabla^2 \left( \frac{\rho_R \rho_B}{\rho} \right) \right] \\ & + \frac{u_\alpha u_\beta}{2} \Delta t^2 [\partial_\alpha \partial_\beta \rho_R] \\ & - \Delta t^2 \beta (1 - \alpha_R) k c_s^2 \left[ \partial_\alpha \left( \frac{\rho_R^2 \rho_B}{\rho^2} \right) \right] n_\alpha \\ & - \Delta t^2 \beta (1 - \alpha_B) k c_s^2 \left[ \partial_\alpha \left( \frac{\rho_R \rho_B^2}{\rho^2} \right) \right] n_\alpha \\ & + 2 c_s^4 \Delta t^2 \partial_\alpha \partial_\beta \left( \frac{\rho_R F_{\alpha\beta}}{\rho} \right), \end{aligned} \quad (3.56)$$

in which the last term on the right hand side (in Eq. (3.56)) originates in the density difference correction term,  $F_{1i}$ . Neglecting this term, i.e., considering the case of unit density ratio, results in:

$$\begin{aligned} & \Delta t \frac{\partial \rho_R}{\partial t} + \frac{1}{2} \Delta t^2 \frac{\partial^2 \rho_R}{\partial t^2} + \Delta t u_\gamma \partial_\gamma \rho_R \\ = & \frac{k}{2} c_s^2 (1 - \alpha_R) \Delta t^2 \nabla^2 \left( \frac{\rho_R^2}{\rho} \right) + \frac{k}{2} c_s^2 (1 - \alpha_B) \Delta t^2 \nabla^2 \left( \frac{\rho_R \rho_B}{\rho} \right) \\ & + \frac{1}{2} \Delta t^2 u_\alpha u_\beta \partial_\alpha \partial_\beta \rho_R \\ & - \Delta t^2 \beta (1 - \alpha_R) k c_s^2 n_\gamma \partial_\gamma \left( \frac{\rho_R^2 \rho_B}{\rho^2} \right) \\ & - \Delta t^2 \beta (1 - \alpha_B) k c_s^2 n_\gamma \partial_\gamma \left( \frac{\rho_R \rho_B^2}{\rho^2} \right). \end{aligned} \quad (3.57)$$

A similar equation to Eq. (3.57) can be produced for the blue fluid, which just exchanges  $R \leftrightarrow B$  and  $\beta \leftrightarrow (-\beta)$  in the preceding analysis.

If the most rapid colour dynamics is evaluated by considering very small  $\Delta t$  (which corresponds to spatial and temporal resolution), the resulting equations show that  $\rho_R$  and  $\rho_B$  are material invariants on the shortest time scales, satisfying the first order wave equation (advection equation), as:

$$\frac{\partial \rho_C}{\partial t_0} + \underline{u} \cdot \nabla \rho_C = 0, \quad C \in [R, B]. \quad (3.58)$$

This result is, subsequently, quoted as an assumption, in the dynamics analysis, as such, it has a direct impact on the derivation of the model dynamics. Equation (3.58)

### 3. Kinematics and Dynamics of Chromodynamic Multi-Component Lattice Boltzmann Equation Simulation

is the first order wave equation in which  $\rho_C$  satisfies with solution  $\rho_C(\underline{r}, t) = f(\underline{r} - \underline{u}t)$ . This result shows that colour is a material invariant on the shortest time scales, in which the normal to the interface has no impact on the kinematics at this time scale. Again note, this result is derived by neglecting the inclusion of a density contrast in the model, as a consequence of assigning  $F_{1i} = 0$ .

Proceeding now, we seek steady and unsteady solutions to Eq. (3.56).

#### 3.3.2.1 Steady Solution

First, seek a steady solution to Eq. (3.56). Here it will be possible to recover an exact solution. Due to considering the system at steady state, the following simplification can be made:

$$\underline{u} = 0, \quad \text{and} \quad \frac{\partial \rho_R}{\partial t} = \frac{\partial^2 \rho_R}{\partial t^2} = 0,$$

therefore,  $F_{1i} = 0$  (see Eq. (3.43) for further understanding). Applying these simplifications to Eq. (3.56) and rearranging, results in the following:

$$\begin{aligned} kC_s^2 \left[ \frac{1}{2} \nabla^2 \left( \frac{\rho_R^2}{\rho} \right) + \frac{1}{2} \frac{(1 - \alpha_B)}{(1 - \alpha_R)} \nabla^2 \left( \frac{\rho_R \rho_B}{\rho} \right) \right. \\ \left. - \beta n_\gamma \partial_\gamma \left( \frac{\rho_R^2 \rho_B}{\rho^2} \right) - \beta \frac{(1 - \alpha_B)}{(1 - \alpha_R)} n_\gamma \partial_\gamma \left( \frac{\rho_R \rho_B^2}{\rho^2} \right) \right] = 0. \end{aligned} \quad (3.59)$$

Now, search for a solution for  $\rho_R$  and  $\rho_B$ , such that the above equation is satisfied. Using the trial solution shown below, and by substituting it into Eq. (3.59), it is possible to show the solution to this equation is given by [77]:

$$\begin{aligned} \rho_R(\underline{r}) &= \frac{\rho_{0R}}{2} (1 + \tanh(\beta \hat{n} \cdot \underline{r})), \\ \rho_B(\underline{r}) &= \frac{\rho_{0B}}{2} (1 - \tanh(\beta \hat{n} \cdot \underline{r})). \end{aligned} \quad (3.60)$$

This, therefore, provides an exact solution for any density ratio between the two steady, immiscible fluids, with any orientation of their flat interface.

#### 3.3.2.2 Unsteady solution

Seeking a solution to Eq. (3.56) for the case where the fluids are uniformly translating, now. Due to the final term on the right hand side of Eq. (3.56) —which encapsulates the density difference correction —an exact solution cannot be found. Hence, the approximation of small density contrast is taken. This approximation means that the second derivative of the density correction term  $F_{\alpha\beta}$  is small and can be neglected —this assumption is further considered shortly.

### 3. Kinematics and Dynamics of Chromodynamic Multi-Component Lattice Boltzmann Equation Simulation

Straightforwardly, the solution to the approximate unsteady, problem of Eq. (3.57) is found by modifying the steady solutions given by Eqs. (3.60) as follows [77]:

$$\begin{aligned}\rho_R &= \frac{\rho_{0R}}{2} \left\{ 1 + \tanh [\beta \hat{n} \cdot (\underline{r} - \underline{u}t)] \right\}, \\ \rho_B &= \frac{\rho_{0B}}{2} \left\{ 1 - \tanh [\beta \hat{n} \cdot (\underline{r} - \underline{u}t)] \right\}, \\ \rho &= \rho_R + \rho_B,\end{aligned}\tag{3.61}$$

where, similarly to the steady solutions, the solutions can be checked via substitution into Eq. (3.57).

Accordingly, a phase field defined following equation (21) of Ba et al. [111], will now furnish physically correct behaviour under the approximation of small density ratios.

$$\rho^N \equiv \frac{\left( \frac{\rho_R}{\rho_{0R}} - \frac{\rho_B}{\rho_{0B}} \right)}{\left( \frac{\rho_R}{\rho_{0R}} + \frac{\rho_B}{\rho_{0B}} \right)} \rightarrow \tanh [\beta \hat{n} \cdot (\underline{r} - \underline{u}t)]\tag{3.62}$$

#### 3.3.2.3 Density difference error

The result given by Eq. (3.62) corresponds to the assumption that only a small density contrast is present between the fluids. Evidently, this will introduce an error into the system when trying to simulate larger density ratios. Therefore, it is now appropriate to analyse this error, by investigating it in more detail. Isolating the neglected term in Eq. (3.57):

$$E = 2c_s^4 \Delta t^2 \partial_\alpha \partial_\beta \left( \frac{\rho_R F_{\alpha\beta}}{\rho} \right).\tag{3.63}$$

Through substitution of the definition of  $F_{\alpha\beta}$  from Eq. (3.43) in section 3.3.1 and using the solutions for the density profiles given in Eq. (3.61), after lengthy algebra, it is possible to arrive at the following expression for the error term [77]:

$$\begin{aligned}E &= -2\Delta t^2 \left( 1 - \frac{1}{2\tau} \right) \left[ \partial_\alpha \partial_\beta \frac{\rho_R}{\rho} (u_\alpha \partial_\beta \rho + u_\beta \partial_\alpha \rho + u_\gamma \partial_\gamma \rho \delta_{\alpha\beta}) \right] \\ &= -4\beta \Delta t^2 \left( 1 - \frac{1}{2\tau} \right) \left( \frac{1}{\rho_{0B}} - \frac{1}{\rho_{0R}} \right) \times ((\hat{n} \cdot \nabla) (\underline{u} \cdot \nabla) + \hat{n} \cdot \underline{u} \nabla^2) \left[ \frac{\rho_R^2 \rho_B}{\rho} \right].\end{aligned}\tag{3.64}$$

Evidently, when  $\hat{n} \cdot \underline{u} = 0$  the advection error term will vanish. This means, that in cases where flow is tangent to the interface, there is no advection error, and the approximate solution is actually exact in this geometry. We are compelled to assume, at this point, that this method will be more stable for flows parallel to the interface. This hypothesis will later be examined further through simulation.

We investigate when the error is largest, by using the first equation in Eq. (3.65); it

### 3. Kinematics and Dynamics of Chromodynamic Multi-Component Lattice Boltzmann Equation Simulation

may be postulated that derivatives in  $\rho$  will take their largest value mid interface, which can be expressed as follows:

$$\partial_\beta \rho \approx \frac{\Lambda \rho_{0B} - \rho_{0B}}{\frac{1}{\beta}} = \beta (\Lambda - 1) \rho_{0B}.$$

Following algebraic simplification, and taking the maximum value of  $\frac{\rho_B}{\rho}$ , which is 1, it is possible to find an upper, maximum value for the advection error quantified as such:

$$E < \left(1 - \frac{1}{2\tau}\right) \beta u (\Lambda - 1) \rho_{0B}. \quad (3.65)$$

This term will be discussed in more detail within the results section.

#### 3.3.3 Dynamics and Kinematics Coupling

Summarising now, the findings from the previous analysis of the developed cMCLBM. From the dynamics analysis shown in section 3.3.1; it was found that in order to retrieve correct hydrodynamic behaviour (the weakly compressible Navier-Stokes equations), a new source term denoted  $F_{1i}$  had to be included. This source term contains the corrections needed to eliminate the propagated consequences of an error originating from the density contrast between the fluids. By including this new source term, the correct macroscopic governing equations were recovered.

Following the updated source term, the interface's compliance with the continuum kinematical condition –that the interface should be embedded within the local fluid and advect at the same speed locally –was analysed. This involved analysis of the post-collision kinetic segregation rule which is in common amongst the class of chromodynamic models and is designed to maintain interface integrity through reducing fluid dispersion. The segregation rule was analysed by applying colour conservation at a node lying at position  $\underline{r}$ , time  $t + \Delta t$ , to post collision, post re-colour red link populations on adjacent nodes at the previous time step  $t$ , seeking expressions for the fluid densities  $\rho_R$ ,  $\rho_B$  and fluid phase-field  $\rho^N$  for a uniformly advecting flat interface. The resulting analysis showed that an error term was present, that propagated from the new source term  $F_{1i}$  needed to recover correct dynamics. The inclusion of this error did not impact the steady solution (where this error went to zero and an exact solution for the densities was recovered). However, the unsteady solution was found by approximating the fluid density contrast as small —resulting in the source term  $F_{1i} \approx 0$ . However, this source term will produce an error when considering larger density contrasts, when it can not be approximated to zero. This error was then bounded and approximated, with the result shown in Eq. (3.65). The

error can be seen to increase with sharpness of the interface  $\beta$ , velocity  $u$  and density contrast between the fluids  $\Lambda$ .

In summary, the correction needed to recover correct hydrodynamic behaviour (i.e., retrieve the weakly compressible Navier-Stokes equations) is affecting the ability for the interface to meet the kinematical condition, due to an error term introduced from the source term correction. Thus, there is a circular relationship between the models kinematics and dynamics. With this relationship understood and its error approximated, simulation results will now proceed to consider the impact of this finding on the model's stability and applicability in flows containing large density contrasts.

## **3.4 Results**

### **3.4.1 Spurious Current**

All MCLBM variants are known to suffer from a spurious, unphysical velocity signal –a micro-current –which is most prominent close to the interfacial region between the fluids, where physically, in zero applied flow, the velocity field should be zero. This unphysical velocity can be troublesome if the magnitude of the micro-current is close to that of the characteristic velocity of the flow being investigated (such as in low Re number investigations), where in such a case it can be hard to distinguish the physical flow. The introduction of micro-current in the system stems from discretisation errors as well as the effect of discrete application, node by node, of the continuous immersed force [49] around which the algorithm is developed. The phenomenology of the effect is as expected, given its origins; the magnitude of the effect can be seen to increase with immersed force magnitude (i.e., for drops, the increase in surface tension) and also with any increase in density contrasts between the fluids [124]. Attempts have been made during the development of MCLBM models to reduce the micro-current level, through modification of equilibrium distribution function and gradient calculations [125], particularly the use of increased isotropy in the gradient operator [126]. Halliday et al. [49] investigated the micro-current within the chromodynamic class of MCLBM models. They showed that the two causes of the micro-current: (i) anisotropic gradient stencil contributions (investigated previous for the SC model in [126]) and (ii) sampling error in the continuous immersed boundary force; the outcome of the work being that the most appropriate way to reduce micro-current activity in a way which is not algorithmically and computationally restrictive is simply to use higher order isotropic stencils [49].

### 3. Kinematics and Dynamics of Chromodynamic Multi-Component Lattice Boltzmann Equation Simulation

It is therefore important to examine the micro-current level within the outlined cMCLBM for the simulation of binary fluids with a density contrast, though protracted and elaborate attempts to reduce the micro-current are beyond the scope of this work. The following content considers the micro-current level, with results showing the impact of density contrasts on its magnitude and also the effect of calculating the curvature —needed for the computation of the immersed boundary force. A single two-dimensional drop (radius  $R = 20$ ) is placed in the centre of a domain (lattice size:  $80 \times 80$ ) and left to evolve for a million time steps. Density contrasts over the range  $\Lambda = [0.001, 1000]$  were simulated, as well as two different methods of defining the mean curvature of the surface: (i) a fixed surface curvature value shown in Eq. (3.66a) and (ii) a numerically calculated surface curvature following that of Lishchuk et al. [57] in Eq. (3.66b).

$$H = \frac{1}{R}, \quad (3.66a)$$

$$H = n_x n_y (\partial_x n_y + \partial_y n_x) - n_y^2 \partial_x n_x - n_x^2 \partial_y n_y. \quad (3.66b)$$

Here, Eq. (3.66a) expresses the fact that a perfect circle (such as the drops simulated in this test, shortly) has a curvature defined by its reciprocal radius. Equation. (3.66b) corresponds to a curvature calculation that can be used for non-circular drop geometries as well, where the mean curvature is defined by taking gradients of the interface normal, then projecting-out surface normal contributions of the gradient. To numerically calculate the gradients in Eq. (3.66b), a compact 4<sup>th</sup>(O) accurate stencil was implemented as a good compromise between accuracy and implementability/computational cost [49]:

$$\partial_\alpha f = \frac{1}{c_s^2} \sum_i t_i f(\underline{r} + \underline{c}_i) c_{i\alpha} + O(c_i^4). \quad (3.67)$$

The results of this test can be seen in Table 3.1, which shows the density contrast used in the simulation  $\Lambda$ , the micro-current maximum velocity value, when using Eq. (3.66a)  $|\underline{u}|_{\max}^{\text{Hr}}$  and the maximum velocity value when using Eq. (3.66b)  $|\underline{u}|_{\max}^{\text{Hc}}$ . The table shows that maximum micro-current value increases with density contrast, with the maximum value across all density contrasts being of the order  $1 \times 10^{-4}$  lattice units. Taking  $\Lambda = 0.1$ , it can be seen that the maximum micro-current value is an order lower when the curvature is defined from initial drop radius, compared to when it is defined by the surface gradient of the normal in Eq. (3.66b), whereas at larger density ratios, the order of the micro-current amplitude becomes comparable between the two definitions of curvature. This suggests that, as the density difference increases, the numerical error involved in simulating a large density contrast is having

### 3. Kinematics and Dynamics of Chromodynamic Multi-Component Lattice Boltzmann Equation Simulation

a dominant effect on the micro-current level. It should be noted, that although micro-current levels were recorded for density difference in the range  $\Lambda = [0.001, 1000]$ , for  $\sigma = 1 \times 10^{-5}$ , the integrity of the interfacial region started to break down at density ratios  $\geq 100$ , which can be stopped through the use of a larger surface tension value.

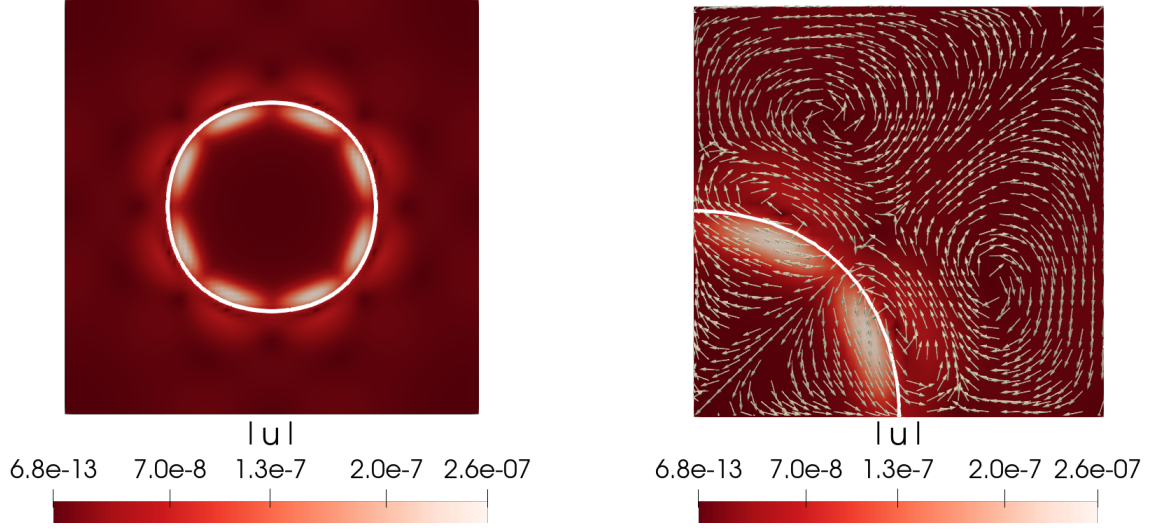
BGK collision operator: Static drop maximum microcurrent values				
$\Lambda$	$\alpha_B$	$\alpha_R$	$ \underline{u} _{\max}^{H_f}$	$ \underline{u} _{\max}^{H_c}$
0.001	0.9995	0.5	$1.04 \times 10^{-4}$	$2.54 \times 10^{-4}$
0.01	0.995	0.5	$6.93 \times 10^{-7}$	$5.92 \times 10^{-5}$
0.1	0.95	0.5	$2.60 \times 10^{-7}$	$2.68 \times 10^{-6}$
10	0.5	0.95	$6.02 \times 10^{-8}$	$8.21 \times 10^{-8}$
100	0.5	0.995	$3.48 \times 10^{-6}$	$4.51 \times 10^{-6}$
1000	0.5	0.9995	$9.61 \times 10^{-5}$	$9.61 \times 10^{-5}$

**Table 3.1:** Maximum microcurrent velocity (in lattice units) for a static drop of initial radius  $R = 20$  in a domain of  $80 \times 80$ , for  $\Lambda \in [10^{-3}, 10^3]$ ,  $\beta = 0.67$  with surface tension,  $\sigma = 1 \times 10^{-5}$ . Two different maximum microcurrent values are shown: (i)  $|\underline{u}|_{\max}^{H_f}$  and (ii)  $|\underline{u}|_{\max}^{H_c}$ , where  $H_f$  corresponds to mean curvature given by Eq. (3.66a) and  $H_c$  corresponds to mean curvature given by Eq. (3.66b).

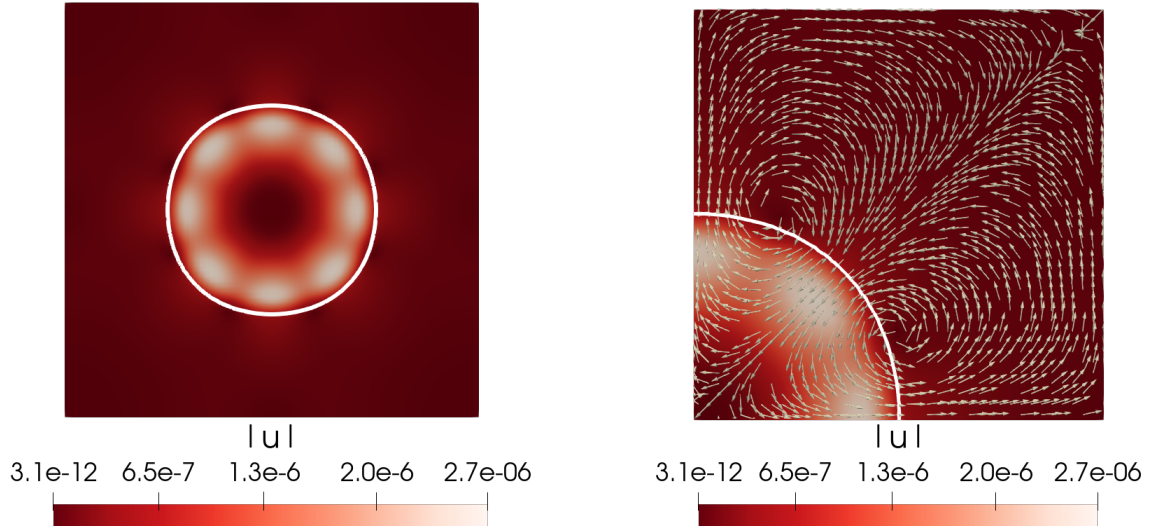
Consider now the micro-current field in more detail; Figures 3.3 and 3.4 show the micro-current plots over the lattice for a density contrast of  $\Lambda = 0.1$ , i.e., blue fluid has density 10 times that of the red fluid, in which Fig 3.3 corresponds to the simulation, where curvature is defined by Eq. (3.66a) and Fig 3.4 corresponds to the simulation where curvature is defined by Eq. (3.66b). These figures were obtained by plotting the velocity field over the domain for the test explained prior, where the drop surface was defined by using a contour taken at contour  $\rho^N = 0$ . Note, visualisation software ParaView was used to produce these plots. Considering the left images of both figures, which show the micro-current magnitude over the lattice  $|\underline{u}|$ , we see that the micro-current is an order of magnitude larger when calculating the curvature (essentially from surface gradients of the normal) and also there is a larger diffusion of the micro-current effects across the domain, unlike when using a fixed curvature value, based of the initialised drop radius —this is likely due to the numerical errors introduced by using the stencil given by Eq. (3.67). This tentative conclusion is also confirmed by the data presented in the right panels of both figures, that displays the top right quadrant of the lattice and the unscaled velocity vectors that highlight the micro-current flow. Here, Fig 3.4 highlights a larger diffusion of the micro-current field, compared to that in Fig 3.3.

As presented by Halliday et al. [49], the micro-current level also relates to a sampling

### 3. Kinematics and Dynamics of Chromodynamic Multi-Component Lattice Boltzmann Equation Simulation



**Figure 3.3:** Microcurrent profiles over the lattice for a density contrast  $\Lambda = 0.1$  and when the mean curvature is given by Eq. (3.66a). (left) shows surface plot of the microcurrent where white circular contour corresponds to  $\rho^N = 0$  plot. (right) shows the top right quadrant of the lattice, showing microcurrent surface plot, superimposed vector field of  $\underline{u}$  (not scaled) and white contour corresponding to  $\rho^N = 0$  plot.



**Figure 3.4:** Microcurrent profiles over the lattice for a density contrast  $\Lambda = 0.1$  and when the mean curvature is calculated by Eq. (3.66b). (left) shows surface plot of the microcurrent where white circular contour corresponds to  $\rho^N = 0$  plot. (right) shows the top right quadrant of the lattice, showing microcurrent surface plot, superimposed vector field of  $\underline{u}$  (not scaled) and white contour corresponding to  $\rho^N = 0$  plot.

error of the continuous immersed boundary force. Clearly then, the magnitude of the immersed boundary force will affect the magnitude of the micro-current. To evidence this, Table 3.2 shows the maximum micro-current magnitude at a density difference of  $\Lambda = 100$  for  $\sigma \in [5 \times 10^{-5}, 1 \times 10^{-2}]$ , using Eq. (3.66b) for the curvature. The results in Table 3.2 show increasing maximum micro-current level with increasing surface



BGK collision operator: Static drop maximum microcurrent values for a range of surface tension values		
$\sigma$	$\Lambda$	$ \underline{u} _{\max}^{\text{H}_c}$
$5 \times 10^{-5}$	100	$9.05 \times 10^{-6}$
$1 \times 10^{-4}$	100	$1.45 \times 10^{-5}$
$5 \times 10^{-4}$	100	$4.21 \times 10^{-5}$
$1 \times 10^{-3}$	100	$5.81 \times 10^{-5}$
$5 \times 10^{-3}$	100	$8.37 \times 10^{-5}$
$1 \times 10^{-2}$	100	$9.74 \times 10^{-5}$

**Table 3.2:** Maximum microcurrent velocity  $|\underline{u}|_{\max}^{\text{H}_c}$  (in lattice units) for a static drop of initial radius  $R = 20$  in a domain of  $80 \times 80$ , for  $\Lambda \in [10^{-3}, 10^3]$ ,  $\beta = 0.67$  with surface tension in the range  $\sigma \in [5 \times 10^{-5}, 1 \times 10^{-2}]$ .

tension. This is as expected, with a contributing factor to the micro-current being an error associated with the sampling of the immersed boundary force [49]. The integrity of the interface and ability to maintain the circular shape of the drop increases with surface tension value, although does cause increased micro-current level. However, even at  $\sigma = 0.01$ , the maximum micro-current level is  $|\underline{u}|_{\max}^{\text{H}_c} = 9.74 \times 10^{-5}$ , which is comparable to the results presented by Ba et al. [111].

### 3.4.2 Kinematical Condition

Within the analyses of section 3.3, work focused on the assessment of the compliance of the model with the continuum kinematical condition (that the interface must advect at the same speed as the locally advecting fluids, recall). From this, an error term was also highlighted, which could potentially impact the ability of the model to meet this condition and hence affect model stability. This section considers the testing of the utility of the model in dynamic flows, focusing on the maintenance of correct interface profile —defined in Eq. (3.62).

#### 3.4.2.1 Flat interface pushed perpendicular to the interface

To test our model’s stability at increasing density ratios in non-static situation, the following test was used. The two fluids were separated by a flat interface and pushed perpendicular to that interface at a velocity  $u_0$ . Stability of the model might then be argued, based on the quality of the maintained interface (smoothness, adherence to the expected *tanh* profile, etc.). To assess whether the interface had a correct profile, the kinematic condition discussed in section 2.2.2.1 is considered. The

### 3. Kinematics and Dynamics of Chromodynamic Multi-Component Lattice Boltzmann Equation Simulation

principle kinematic condition, that the interface should advect with the fluids, with no cavitation, leads to the following equations for the profiles of the red and blue fluids:

$$\begin{aligned}\frac{\rho_R(x)}{\Lambda} &= \frac{1}{2} (1 + \tanh(x - u_0 t)), \\ \rho_B(x) &= \frac{1}{2} (1 - \tanh(x - u_0 t)),\end{aligned}\tag{3.68}$$

where, in this test, the red fluid has a larger density than the blue fluid, which has a deep phase density set to  $\rho_{0B} = 1$ . The red density profile was normalised, to allow for easier visual comparison with the blue density profile, with the first quantity being divided by the density ratio,  $\Lambda$ .

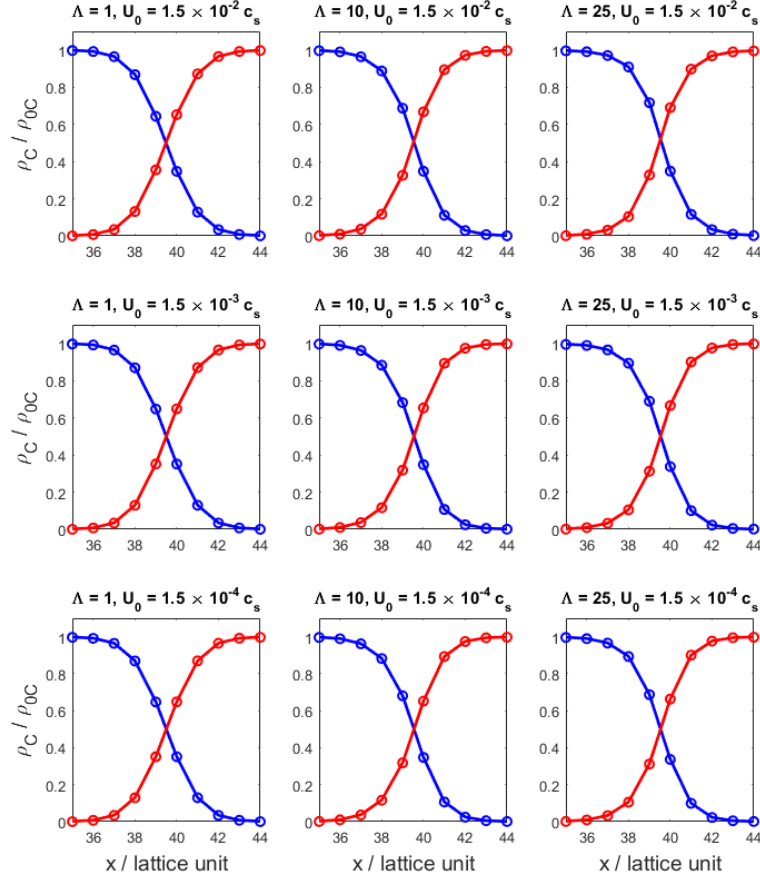
Simulations were run to equilibrium, before moving the fluid, to damp transients within the system. The then equilibrated, flat interface was centred on  $x \approx 20$  and a uniform flow applied, with velocity  $u_0$ , and the interface allowed to advect 20 lattice sites. The predicted interfaces, shown by Eqs. (3.68), were then fitted to the simulated interfaces by using least squares regression, with the quantification of the error between the actual and the predicted interface shape of the red fluid being calculated in the following way:

$$\Delta(t)^2 \equiv \sum_i \left( \rho_R(x_i, t) - \frac{\rho_{0R}}{2} (1 + \tanh(x_i - u_0 t)) \right)^2, \tag{3.69}$$

where, the summation occurs over a range larger than the interfacial region, 40 locations, to ensure any deviation from the predicted profiles was captured. To fit the predicted profile against the analytical solution for the profile,  $t$  was allowed to vary to provide the best fit, minimising the error value. From this, any result that had  $\Delta(t)^2 < 1.36 \times 10^{-3}$  was deemed stable and any above this value deemed unstable. It is also worth noting that throughout this test, it was found that the denser profile —Red—departed from that of the predicted profile before the lighter fluid —Blue. Therefore, it is assumed that the error in the denser profile will be larger at a given time compared to that of the lighter fluid.

Figure 3.5 shows the data from this test, which has all been normalised as discussed above. It can be seen that the data provide very good agreement with the profiles, for the interface given by Eqs. (3.68), and for the density ratios and flow velocities tested. Quantitative data for this test are given in Table 3.3, showing the full range of density ratios and flow velocities tested and the stability of the parameterisations based on the criteria:  $\Delta(t)^2 < 1.36 \times 10^{-3}$ . From this, it is seen that the system is stable over a wide range of density ratios and flow velocities, with large density

### 3. Kinematics and Dynamics of Chromodynamic Multi-Component Lattice Boltzmann Equation Simulation



**Figure 3.5:** Data from the advecting fluid test perpendicular to the interface, simulation data given by the points and analytical solution by the solid lines. Both densities  $\rho_C$  are equilibrated by dividing by the respective deep phase densities  $\rho_{0C}$ , with the interfaces initialised centrally around  $x = 20$  lattice units. The interface was allowed to advect 20 lattice units as a result of applying flow  $u_0 \hat{e}_x$ . The data show a range of density differences  $\Lambda$  tested with increasing values for the velocity of the flow  $u_0$  [77].

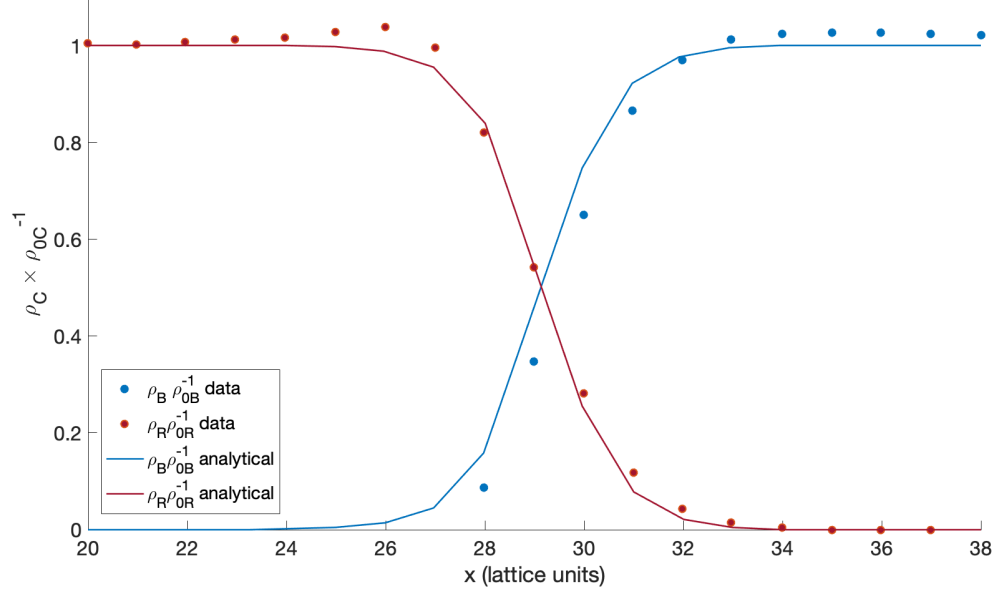
ratios achievable in slow moving flow (lower flow velocities  $u_0$ ). The system, as expected, becomes more unstable at higher density differences and also higher  $u_0$  values. Note however, within LB models there is a constraint on the maximum velocity stemming from the Mach number limit  $u_{\max} < 0.15c_s$ .

	$\Lambda$					
$\frac{u_0}{c_s}$	1	10	25	50	100	1000
0.15	stable	unstable	unstable	unstable	unstable	unstable
0.015	stable	stable	stable	stable	unstable	unstable
0.0015	stable	stable	stable	stable	stable	stable
0.00015	stable	stable	stable	stable	stable	stable

**Table 3.3:** This table displays at which density ratios and flow velocities the system is stable and unstable. The black (red) text cells correspond to the stable (unstable) simulations. Stable cells have error values defined by:  $\Delta(t)^2 < 1.36 \times 10^{-3}$  [77].

### 3. Kinematics and Dynamics of Chromodynamic Multi-Component Lattice Boltzmann Equation Simulation

Figure 3.6 shows an example where the system has become unstable and departed from the predicted profiles for the two fluids:



**Figure 3.6:** Normalised density profiles ( $\frac{\rho_C}{\rho_{0C}}$  where  $C \in [R, B]$ ) for the Red and Blue fluids. The line plots correspond to the equations for the density profiles Eqs. (3.68), and the circles to simulation data after the fluids have advected perpendicular to this interface. Here, the density ratio is  $\Lambda = 10$  and applied flow velocity  $u_0 = 0.15c_s$ . Colour Red (Blue) corresponds to the Red (Blue) fluid [77].

Here, the profiles given from simulation data (shown by the circles) correspond to a level of deviation from the predicted profiles that is deemed as unstable. Based on this result, and that of the unstable simulation in Table 3.3, it is clear there is a link between the density ratio achievable in simulation and the velocity of the fluid. The following section investigates this further through analysis of the kinematics error Eq. (3.65) stemming from the dynamics, density difference correction in Eq. (3.43).

#### 3.4.2.2 Error Analysis

As discussed, a kinematical advection error was found in section 3.3.2, which, intuitively, is set to impact the stability of the system. In an attempt to bound the error, through manipulation and simplification, an approximation of the upper bound of the error was found:

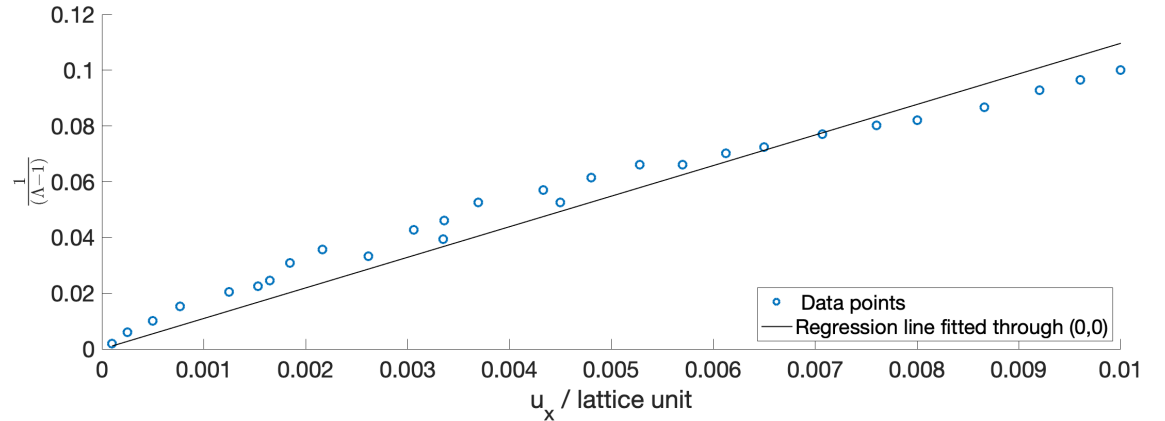
$$\Delta < \left(1 - \frac{1}{2\tau}\right) \beta u (\Lambda - 1) \rho_{0B}. \quad (3.70)$$

From Eq. (3.70), it is evident that parameters  $\beta$ ,  $u$ ,  $\Lambda$  and  $\rho_{0B}$  will all impact the size of the advection error. To increase stability of the system, one could reduce  $\beta$ . Lowering  $\beta$  increases the interfacial width and thus increases its effective resolution,

### 3. Kinematics and Dynamics of Chromodynamic Multi-Component Lattice Boltzmann Equation Simulation

i.e., the number of lattice points within the interfacial region, reducing the advection error. However, this means that, in order to obtain a physically correct system, the lattice size would need to be increased to ensure the relative thickness of the interface is low —introducing additional computational expense. As such, for current purposes, the tuning of  $\beta$  to reduce the advection error is discounted. For practical purposes, understanding the relationship between the density ratio  $\Lambda$  and the fluid velocity  $u_0$  is most important, as it will help define the utility of the model. The correlation between  $\Lambda$  and  $u_0$  for stability is supported by both Eq. (3.70) and the results in Table 3.3.

To investigate the relationship between density ratio, velocity and the stability of the system, the density ratio would be set, and then the flow velocity  $u_0$  at which the system becomes unstable identified. Instability was identified by normalising the density profile, using a least squares regression test and deeming the system unstable when the profile departed more than 5% of that of the predicted profile given by Eq. (3.68). Density ratios in the range of  $\Lambda = [10, 170]$  were simulated, with the resultant point of instability plotted on a scatter graph along with a line of best fit, displayed in Figure 3.7.



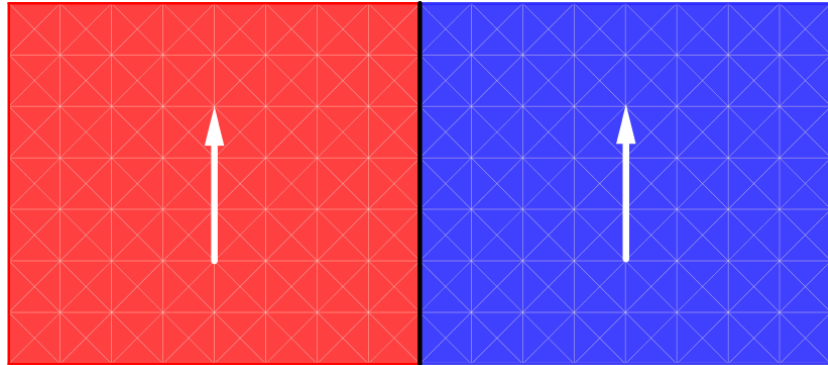
**Figure 3.7:** Scatter plot showing the correlation between the velocity the fluid is pushed at perpendicular to the interface ( $u_x$ ) against  $\frac{1}{\Lambda-1}$ . Where the circles show the point of instability when the density profile departs more than 5% of that of the predicted profile, and the black line shows a regression line fitted through the origin using least squares regression [77].

The data present results that show that, as the density ratio increases, the maximum attained velocity before the system becomes unstable decreases, put another way, at higher flow velocities the maximum density ratio achievable in simulation decreases. These data support the understanding of the interface instability, due to the advection error in Eq. (3.70), in showing there is a relationship between

the density ratio and flow velocity, which is linked to stability. The implication of these observations is that the analyses in section 3.3 have revealed a kinematical error, induced by pursuing correct dynamical behaviour, which as a result, limits the applicability of the model through decreasing its stability. This, then, needs to be considered if one is interested in simulating fluids with a large density ratio in rapid flow perpendicular to the interface, where current results show interface integrity will start to break down.

### 3.4.2.3 Flat interface pushed parallel to the interface

From the analysis in section 3.3.2, an advection error was found given in full form by Eq. (3.65). Looking, now, at flow perpendicular to the interface, i.e.,  $\hat{n} \cdot \underline{u} = 0$ , the advection error in Eq. (3.65) will equal zero in this geometry. This, then, means there is no error induced on the kinematical interfacial condition from the model dynamics. To assess the impact of this, a range of density ratios and flow velocities were tested for the flow geometry given in Figure 3.8 and flow profiles from simulation data compared against the profiles given in Eqs. (3.68), with error and hence stability being determined by Eq. (3.69). The results of this investigation were that, for a range of density contrasts up to order  $O(1000)$ , and a range of flow velocities below those that break the Ma number limit, the simulation remained stable and interfacial profiles from data matched that of the expected profiles. Therefore, for flows parallel to the interface, the model met the continuum interface kinematical condition for fluids with a large density ratio.



**Figure 3.8:** Schematic of the two fluids (red and blue) with a flat interface (solid black line) and white arrows representing the direction the velocity  $u_0$  is being applied.

### **3.5 Concluding Remarks**

The development of computational models that focus on the simulation of immiscible fluid flows which have a density contrast is of importance in both industry and nature, where such fluid flows are seen to be present. These models must meet general criteria, in order to be viable, with the desire for these models to be: stable, robust, applicable to a wide range of flow regimes, include physics appropriate of the length and time scale being simulated, and be computationally practical foremost. Mesoscale, diffused interface models, which utilise techniques such as LBM and DPD present themselves as attractive options for modelling such flows, compared to traditional continuum CFD techniques, which treat the interface between the fluids as discontinuous—which can lead to singularities and an inability to include more complex physics with origins at smaller length scales.

Based upon the data presented here, multi-component lattice Boltzmann methods are highly suitable for the simulation of immiscible fluids with density differences, due to their native, appropriate length and time scale (the interface being treated as a sharp but diffused region), ability to incorporate key physics (such as surface tension), computational efficiency (intrinsic parallelisability) and ability to simulate complex geometries (such as porous media). Both the Shan-Chen and Free-Energy/Phase-field MCLBM variants have been applied successfully to the simulation of immiscible fluids with large density ratios [102, 99, 100, 107], as well as a class of colour-gradient or chromodynamic MCLBMs [109, 111, 112, 77] that forms our principal content in this chapter. The latter variant class all use a kinetic scale segregation rule, in order to prevent fluid mixing and to maintain integrity of the interfacial region between the immiscible fluids.

The work in this chapter evidenced the development and analysis of a two-dimensional, two-component chromodynamic multi-component lattice Boltzmann model for the simulation of isothermal, binary fluids with a density ratio [77]. Specifically, we maintained a focus on understanding the kinematics and dynamics of the model, by investigating the kinetic scale segregation rule which is a common step in colour-gradient and chromodynamic MCLBMs. Here, the model's compliance with the continuum kinematical condition (that the fluids interface should advect at the same speed as the locally advecting fluids) is evaluated. Starting with the dynamics, a Chapman-Enskog procedure was used to recover the Navier-Stokes equations from the evolution equation, following the methodology of Guo et al. [70]. Due to extensions of the model (outlined at the start of the chapter), which incorporate the density ratio between the fluids, an additional correction term was identified and implemented in

### *3. Kinematics and Dynamics of Chromodynamic Multi-Component Lattice Boltzmann Equation Simulation*

the dynamics in order to recover the Navier-Stokes equations. The resultant source term was then found to impact the kinematical behaviour of the model. To assess the continuum kinematical behaviour of the model, the segregation rule was analysed in section 3.3.2. This analysis provided solutions for the profiles of the blue and red fluid densities at the continuum scale. It was found that an exact solution was only possible in steady flow, whereas an error term —stemming from the new source term needed to retrieve correct dynamics —meant that only approximate solutions were possible in un-steady flow, for fluids with small density contrasts. As such, there is a coupling between the model’s kinematics and dynamics, which in the current form, is unavoidable.

The impact of this coupling on the model’s ability to meet the kinematical interface condition was assessed through direct simulation. To do this, two different flow geometries were tested for an advecting interfaces: (i) flow perpendicular to the interfacial (ii) flow parallel to the interface. Note, these tests contained flat interfaces only, as a result, this removes the affects of surface tension, allowing focused investigation of the model’s compliance with continuum kinematical conditions (with curved interfaces later addressed in Chapter 4). To quantify the stability of the model and compliance with the interfacial kinematical condition, the simulation data profiles in tests (i) and (ii) were compared against analytical solutions for the density profiles, with a significant departure from the analytical result defining an instability. For flow parallel to the interface, the advection error found in the kinematical analysis is evidently zero, due to the fact that  $\hat{n} \cdot \underline{u} = 0$  —with the density difference source term  $F_{1i}$  having a prefactor of  $\hat{n} \cdot \underline{u}$  (see Eq. (3.65)). Data from this test showed that the simulation remained stable, with the kinematical condition met for a large range of flow velocities and density contrasts, up to order  $O(1000)$ . Considering flow perpendicular to the interface, it was found that the model became unstable when trying to simulate large density contrasts and/or large flow velocities. Analysing and approximating the advection error, it can be seen in Eq. (3.70) that the error depends upon the density contrast and flow velocity. This observation was then investigated further by examining at what flow velocity the simulation became unstable, for various density ratios over the range  $\Lambda = [10, 170]$ . Figure 3.7 showed the outcome of this investigation, where a clear correlation between the achievable flow rate and density ratio was present. Overall, this showed that when the advection error approached zero —such as for flow parallel to the interface —the model had increased stability, whereas when the advection error was present —such as for flow perpendicular to the interface —limitations on both flow velocity and density ratio achievable were imposed.



### *3. Kinematics and Dynamics of Chromodynamic Multi-Component Lattice Boltzmann Equation Simulation*

At the broadest level, the outcome of this work is a better understanding of the class of chromodynamic MCLBMs, their kinetic scale segregation rule and its ability to meet the kinematical continuum interface condition, as well as the limitations and strengths of the proposed model. It is evident that if one wishes to simulate fluids with density ratios of  $O(100)$  or greater in rapid flow, then the coupling between the model's dynamics and kinematics needs to be addressed to remove the advection error found in this work. The removal of this coupling is not straightforward, with no obvious solution that would seemingly not require significant changes to key parts of the base methodology. Two potential options may be to alter: (i) how the forcing is applied, or (ii) the distribution of lattice weights in the forcing term such that it cancels in the kinematics.

Future work should build upon the enhanced understanding of the model presented herein. Although there are seemingly limitations in rapid flow, at large density ratios, in its current form, one could consider the application of the model to low Reynolds number flows, where stability issues would be reduced, by minimising the advection error. This regime may also present one of the best opportunities for a strict review of our models compliance with principal kinematic and dynamic boundary conditions, due to the presence of analytical solutions —allowing for quantitative verification of our model. In addition, upgrading the model through the inclusion of a multi-relaxation time (MRT) scheme seems sensible, with most MCLB models presented in literature taking this approach to enhance stability. One may also consider extending the model to three-dimensional flows. The following chapter addresses these ideas, using the research from this chapter to improve the presented BGK-model, and further verify the models kinematics and dynamics.

# 4

## Extended cMCLBM for the Simulation of Drops within Stokes Flow

### Contents

---

<b>4.1</b>	<b>Introduction</b>	<b>78</b>
<b>4.2</b>	<b>MRT Two-dimensional System</b>	<b>79</b>
4.2.1	Introduction	79
4.2.2	Extension of Methodology	81
4.2.3	Results	87
<b>4.3</b>	<b>Pseudo Three-dimensional System</b>	<b>97</b>
4.3.1	Introduction	97
4.3.2	Extension of Methodology	98
4.3.3	Results	105
<b>4.4</b>	<b>Concluding Remarks</b>	<b>118</b>

---

### 4.1 Introduction

The work in this chapter is a continuation of that presented in Chapter 3, aiming to enhance the developed LBGK isothermal, multi-component chromodynamic lattice Boltzmann method for simulating fluids with a density contrast. This work encapsulates two key extensions. First, the extension to the methodology through incorporating a multi-relaxation time (MRT) collision operator (see section 4.2), where the reasons for this step, and contextualised prior work on MRT cMCLBMs, are discussed within this section. Here, the overall goal is to leverage stability gains via increased tuneability, with the work in Chapter 3 serving as a foundation. From this

#### 4. *Extended cMCLBM for the Simulation of Drops within Stokes Flow*

work, conclusions will be drawn on the utility of the developed model and will lead into the work in section 4.3, which seeks extensions to the model for the simulation of three-dimensional fluid flows. Second, in section 4.3, work investigates simulating axially-symmetric three-dimensional two-component fluid flows, by developing a pseudo three-dimensional (two-dimensional) MRT-MCLBM based on the work in section 4.2.

Throughout, emphasis is made on investigating the model's compliance with kinematical and dynamical interface boundary conditions at density contrasts between the fluids. To establish the extent to which these conditions are met by the model, comparisons are made to existing analytical theory, to facilitate benchmarking, especially of the boundary physics. From doing this, an improved understanding is gained of this class of cMCLBM, with the applicability of the model, its advantages and its drawbacks being better resolved.

## 4.2 MRT Two-dimensional System

### 4.2.1 Introduction

The model introduced in section 3 used the BGK collision operator, with the decision to do so being made on the basis of increased methodological transparency when investigating the model's kinematics and dynamics. Although the BGK collision scheme offers simplicity and transparency, it does not offer the stability that TRT and MRT collision operators provide; an observation stemming from their increased tuneability and degrees of freedom. The choice to implement the MRT collision operator in the following work is made due to it offering the largest tuneability. The inclusion of an MRT collision operator has been seen as almost a necessity when simulating flows with large density contrasts, where MCLBMs are susceptible to increased instability [127], with many authors opting for such a collision scheme [128, 129, 130, 131, 132, 111, 133, 127, 112, 134, 135]. Leclaire et al. [130] developed a cMCLBM with an MRT collision scheme, using an enhanced equilibrium distribution function in order to improve stability. Ba et al. [111] presented an two-dimensional MRT-cMCLBM, with a modified equilibrium distribution function from that of Li et al. [136], seeking to benchmark higher Reynolds number fluid flows with large density contrasts. Here, the modified equilibrium distribution function results in the off-diagonal elements of its third moment, now canceling a previously unwanted error term identified by Huang et al. [137]. The resultant outcome of the model is increased stability, due to the removal of the error term and the use of the MRT

#### 4. *Extended cMCLBM for the Simulation of Drops within Stokes Flow*

collision scheme. The model provides good results and can simulate density ratios approaching order  $O(1000)$  for static drops and layered flow, but only presents results of a largest density ratio of  $\Lambda = 3$ , for Rayleigh-Taylor instability. In 2019 Wen et al. [112] presented a three-dimensional MRT-cMCLBM, which again utilised the approach of Li et al., to obtain the desired equation for the third moment of the distribution function, with the additional unwanted terms from this being removed via a correction to the collision operator. Again, results show the ability to simulate large density ratios in static and layered flow, with low density ratios simulated for the Rayleigh-Taylor instability. Accordingly, current conclusions could be drawn to the limitations of this group of multi-component models, with applications most suited to liquid-liquid interface or liquid-gas interfaces at very low Reynolds numbers. The chromodynamic BGK model presented by Burgin et al. [77] also encounters such limitations in its current form, with the rise of an unwanted error term in the model's kinematics, which limits the density contrasts achievable in rapid flow. To assess this further, Spendlove et al. [134] considered implementing an MRT scheme into the model of Burgin et al., in order to seek stability gains and advance the model. This work is presented and discussed in this section, again with emphasis on investigating the model's kinematics and dynamics, through simulations where both flat and curved interfaces are encountered.

The MRT collision scheme of Halliday et al. [138] is implemented here; it is similar to that of Dellar [48, 139] and that of the three-dimensional MRT scheme presented by Xu et al. [50]. The evolution equation for the enhanced scheme is adapted from that of the BGK-model presented in Eq. (3.2) of Chapter 3, where the BGK collision operator is replaced with the MRT collision matrix of [138], resulting in the following kinetic equation:

$$f_i(\underline{r} + \underline{c}_i \Delta t, t + \Delta t) = f_i(\underline{r}, t) + \sum_j A_{ij} [f_j^{(0)}(\underline{r}, t) - f_j(\underline{r}, t)] + \Delta t F_i, \quad (4.1)$$

where,  $A_{ij}$  is the collision matrix and  $F_i$  is the source term which, following the work in Chapter 3, will be separated into two components  $F_i = F_{1i} + F_{2i}$  shortly.

It is worth noting before continuing, that, due to the use of the MRT collision operator, the definition of the kinematic viscosity is different to that of the BGK-model. As the value of the index  $\rho^N(\underline{r}, t)$  (phase field) identifies the fluid component at a point in the domain, it can be used to control the fluid's kinematic viscosity.

#### 4. Extended cMCLBM for the Simulation of Drops within Stokes Flow

This is achieved by introducing  $\lambda_3$  (will be discussed further shortly), which has a dependence on  $\rho^N(\underline{r}, t)$ , as follows [138]:

$$\nu(\rho^N) = \frac{1}{6} \left( \frac{2}{\lambda_3(\rho^N)} - 1 \right). \quad (4.2)$$

The kinematic viscosity is referenced when discussing simulation data, which accounts for our outlining of this equation here.  $\lambda_3$ , a parameter related to the collision process, is discussed in the following subsection which outlines the multi-relaxation time scheme.

### 4.2.2 Extension of Methodology

This section provides a detailed description of the model's enhancement (the inclusion of the MRT collision operator). It also follows the general structure of that presented by both Halliday et al., and Xu et al. [138, 50, 134]. To increase transparency and readability, Table 4.1 provides a representation of the notation used, alongside the eigenvector, eigenvalues' components, projection, eigenvalues, modes and modal equilibria for the MRT scheme [58, 50, 134], which are discussed throughout this work.

eigenvector	component	projection	eigenvalue, $\lambda_p$	mode, $m^{(p)}$	equilibrium
$\underline{h}^{(0)}$	$h_i^{(0)}$	$t_i$	0	$\rho$	$\rho$
$\underline{h}^{(1)}$	$h_i^{(1)}$	$t_i c_{ix}$	0	$\rho u_x$	$\rho u_x$
$\underline{h}^{(2)}$	$h_i^{(2)}$	$t_i c_{iy}$	0	$\rho u_y$	$\rho u_y$
$\underline{h}^{(3)}$	$h_i^{(3)}$	$t_i c_{ix}^2$	$\lambda_3$	$P_{xx}$	$\Pi_{xx}^{(0)}$
$\underline{h}^{(4)}$	$h_i^{(4)}$	$t_i c_{iy}^2$	$\lambda_3$	$P_{yy}$	$\Pi_{yy}^{(0)}$
$\underline{h}^{(5)}$	$h_i^{(5)}$	$t_i c_{ix} c_{iy}$	$\lambda_3$	$P_{xy}$	$\Pi_{xy}^{(0)}$
$\underline{h}^{(6)}$	$h_i^{(6)}$	$g_i$	$\lambda_6$	$N$	$N^{(0)}$
$\underline{h}^{(7)}$	$h_i^{(7)}$	$g_i c_{ix}$	$\lambda_7$	$J_x$	0
$\underline{h}^{(8)}$	$h_i^{(8)}$	$g_i c_{iy}$	$\lambda_7$	$J_y$	0

**Table 4.1:** Collision matrix eigenspectrum notation table. Here the left row eigenvectors, eigenvector components, projection components, eigenvalues, corresponding modal projections and equilibria are given for the collision matrix  $\underline{A}$ . Where,  $m^{(p)} \equiv \sum_i h_i^{(p)} f_i$ ,  $p \in [0, 8]$ .

Collision within the MRT scheme takes place in modal space, not population space—‘modal space’ refers to the abstract space spanned by the hydrodynamic mode vectors (which represent observables such as density, velocity and momentum flux), in contradistinction to ‘population space’, which refers to the distribution functions (or populations). Therefore, to transform to modal space, a projection matrix  $\underline{M}$  needs

#### 4. Extended cMCLBM for the Simulation of Drops within Stokes Flow

to be defined, which when projected onto the evolution equation, will recover the correct hydrodynamic modes. The scheme presented by Halliday et al. [138] extends that of Dellar [48, 139] which does not include a source term. This model utilises Guo et al. [70] forcing, as in the previous BGK-model, in order to include immersed boundary forces such as surface tension etc. The projection matrix is given by linearly-independent left row eigenvectors of the collision matrix as follows [49, 134]:

$$\underline{\underline{M}} \equiv \left( \underline{h}^{(0)}, \underline{h}^{(1)}, \dots, \underline{h}^{(8)} \right)^T, \quad (4.3)$$

where the resulting hydrodynamic and non-hydrodynamic modes are:

$$\underline{m} = \underline{\underline{M}} \underline{f} = (\rho, \rho u_x, \rho u_y, \sigma_{xx}, \sigma_{yy}, \sigma_{xy}, N, J_x, J_y)^T, \quad (4.4)$$

where modes  $N$ ,  $J_x$  and  $J_y$  are ghost modes, which contain no hydrodynamic information. Projecting with the eponymous projection matrix  $\underline{\underline{M}}$  on to Eq. (4.1), we recover the modes shown in Table. 4.1:

$$\underline{\underline{M}} \underline{f}^\psi = \underline{\underline{M}} \underline{f} + \underline{\underline{M}} \underline{A} \left( \underline{f}^{(0)} - \underline{f} \right) + \underline{\underline{M}} \underline{F}, \quad (4.5)$$

where  $\underline{F}$  denotes the column vector source term,  $\underline{f}$  is the distribution function where superscript (0) and  $\psi$  denotes the equilibrium distribution function and post collision equilibrium distribution function, respectively.

Following the assumption that the  $\underline{h}^{(n)}$  elements are left row eigenvectors of  $\underline{A}$ , meaning  $\underline{\underline{M}} \underline{A} = \underline{\underline{\Lambda}} \underline{\underline{M}}$ , we have:

$$\underline{\underline{\Lambda}} = \underline{\underline{M}} \underline{A} \underline{\underline{M}}^{-1}, \quad \underline{\underline{\Lambda}} = \text{diag}(\lambda_0, \lambda_1, \dots, \lambda_8), \quad (4.6)$$

where  $\lambda_p$  are the eigenvalues corresponding to the collision matrix. Here, the eigenvalues have the following definitions:  $\lambda_0 = \lambda_1 = \lambda_2 = 0$ , in order to get correct hydrodynamics (i.e., meet density and velocity conservation laws), and  $\lambda_3 = \lambda_4 = \lambda_5$  and  $\lambda_7 = \lambda_8$ , to be discussed. It is now possible to rewrite Eq. (4.5) in its modal components, in the following way:

$$m^{(p)+} = m^{(p)} + \lambda_p \left( m^{(0)(p)} - m^{(p)} \right) + S^{(p)}, \quad p = 0, 1, \dots, (Q-1) \quad (4.7)$$

To define Eq. (4.7), the modal source contribution  $S^{(p)}$  needs evaluating:

$$S^{(p)} = \sum_{i=0}^8 M_{pi} F_i. \quad (4.8)$$

Calculating the individual modal source components  $S^{(p)}$  (where  $F_i$  is given in Eq. (3.13)):

$$S^{(0)} = \underline{h}^{(0)} \cdot \underline{F} = \sum_i h_i^{(0)} F_i = A \equiv 0,$$

#### 4. Extended cMCLBM for the Simulation of Drops within Stokes Flow

$$\begin{aligned}
S^{(1)} = \underline{h}^{(1)} \cdot \underline{F} &= \sum_i h_i^{(1)} F_i = \sum_i c_{ix} F_i = n F_x \Delta t, \\
S^{(2)} = \underline{h}^{(2)} \cdot \underline{F} &= \sum_i h_i^{(2)} F_i = \sum_i c_{iy} F_i = n F_y \Delta t, \\
S^{(3)} = \underline{h}^{(3)} \cdot \underline{F} &= \sum_i h_i^{(3)} F_i = \sum_i c_{ix}^2 F_i = C_{xx}, \\
S^{(4)} = \underline{h}^{(4)} \cdot \underline{F} &= \sum_i h_i^{(4)} F_i = \sum_i c_{iy}^2 F_i = C_{yy}, \\
S^{(5)} = \underline{h}^{(5)} \cdot \underline{F} &= \sum_i h_i^{(5)} F_i = \sum_i c_{ix} c_{iy} F_i = \frac{1}{2} (C_{xy} + C_{yx}), \\
S^{(6)} = \underline{h}^{(6)} \cdot \underline{F} &= \sum_i h_i^{(6)} F_i = \sum_i g_i F_i = 0, \\
S^{(7)} = \underline{h}^{(7)} \cdot \underline{F} &= \sum_i h_i^{(7)} F_i = \sum_i g_i c_{ix} F_i = 0, \\
S^{(8)} = \underline{h}^{(8)} \cdot \underline{F} &= \sum_i h_i^{(8)} F_i = \sum_i g_i c_{iy} F_i = 0.
\end{aligned} \tag{4.9}$$

It can be seen that the source term  $F_i$  contains important force contributions to the hydrodynamic modes, but has no projection onto the non-hydrodynamic modes  $N$ ,  $J_x$ ,  $J_y$ .

Now, calculating the modal projection of the equilibria, we have:

$$\begin{aligned}
\underline{h}^{(0)} \cdot \underline{f}^{(0)} &= \sum_i h_i^{(0)} f_i^{(0)} = \sum_i 1_i f_i^{(0)} = \rho, \\
\underline{h}^{(1)} \cdot \underline{f}^{(0)} &= \sum_i h_i^{(1)} f_i^{(0)} = \sum_i c_{ix} f_i^{(0)} = \rho u_x, \\
\underline{h}^{(2)} \cdot \underline{f}^{(0)} &= \sum_i h_i^{(2)} f_i^{(0)} = \sum_i c_{iy} f_i^{(0)} = \rho u_y, \\
\underline{h}^{(3)} \cdot \underline{f}^{(0)} &= \sum_i h_i^{(3)} f_i^{(0)} = \sum_i c_{ix}^2 f_i^{(0)} = \Pi_{xx}^{(0)}, \\
\underline{h}^{(4)} \cdot \underline{f}^{(0)} &= \sum_i h_i^{(4)} f_i^{(0)} = \sum_i c_{iy}^2 f_i^{(0)} = \Pi_{yy}^{(0)}, \\
\underline{h}^{(5)} \cdot \underline{f}^{(0)} &= \sum_i h_i^{(5)} f_i^{(0)} = \sum_i c_{ix} c_{iy} f_i^{(0)} = \Pi_{xy}^{(0)}, \\
\underline{h}^{(6)} \cdot \underline{f}^{(0)} &= \sum_i h_i^{(6)} f_i^{(0)} = \sum_i g_i f_i^{(0)} = \frac{9}{5} \alpha_R \rho_R + \frac{9}{5} \alpha_B \rho_B - \frac{4}{5} \rho = N^{(0)}, \\
\underline{h}^{(7)} \cdot \underline{f}^{(0)} &= \sum_i h_i^{(7)} f_i^{(0)} = \sum_i g_i c_{ix} f_i^{(0)} = 0, \\
\underline{h}^{(8)} \cdot \underline{f}^{(0)} &= \sum_i h_i^{(8)} f_i^{(0)} = \sum_i g_i c_{iy} f_i^{(0)} = 0.
\end{aligned} \tag{4.10}$$

Following the results in Eqs. (4.9) and (4.10), the evolution equation for the individual modes can be formulated by evaluating Eq. (4.7):

$$i = 0 : \quad \rho^+ = \rho, \tag{4.11}$$

#### 4. Extended cMCLBM for the Simulation of Drops within Stokes Flow

$$i = 1 : \quad (\rho u_x)^+ = \rho u_x + n F_x \Delta t, \quad (4.12)$$

$$i = 2 : \quad (\rho u_y)^+ = \rho u_y + n F_y \Delta t, \quad (4.13)$$

$$i = 3, \dots, 5 : \quad (P_{\alpha\beta})^+ = P_{\alpha\beta} - \lambda_3 (P_{\alpha\beta} - \Pi_{\alpha\beta}^{(0)}) + \frac{\Delta t}{2} (C_{\alpha\beta} + C_{\beta\alpha}), \quad (4.14)$$

$$i = 6 : \quad N^+ = N - \lambda_6 (N - N^{(0)}), \quad (4.15)$$

$$i = 7, 8 : \quad J_\alpha^+ = J_\alpha - \lambda_7 J_\alpha, \quad (4.16)$$

where subscripts  $\alpha, \beta = x, y$ . The eigenvalues  $\lambda_0 = \lambda_1 = \lambda_2 = 0$ , in order to retrieve correct hydrodynamics for these modes. Additionally for the non-hydrodynamic modes  $N, J_x, J_y$ , it can be seen that if  $\lambda_6 = \lambda_7 = 1$ , the latter reduce to  $N^+ = N^{(0)}$  and  $J_x^+ = J_y^+ = 0$ .

Having determined the forced evolution equations for all the modes  $m^{(p)}$ , they must now be converted back to population space from their modal space definitions. First, defining column vectors  $\underline{k}^{(n)}$  for  $n = 0, 1, \dots, 8$ , which are formulated through Gram-Schmidt orthogonalisation [138, 134]:

$$k_i^{(0)} = 2t_i - \frac{3}{2}t_i (c_{ix}^2 + c_{iy}^2), \quad (4.17)$$

$$k_i^{(1)} = 3t_i c_{ix}, \quad (4.18)$$

$$k_i^{(2)} = 3t_i c_{iy}, \quad (4.19)$$

$$k_i^{(3)} = \frac{9}{2}t_i c_{ix}^2 - \frac{3}{2}t_i, \quad (4.20)$$

$$k_i^{(4)} = \frac{9}{2}t_i c_{iy}^2 - \frac{3}{2}t_i, \quad (4.21)$$

$$k_i^{(5)} = 9t_i c_{ix} c_{iy}, \quad (4.22)$$

$$k_i^{(6)} = \frac{1}{4}g_i t_i, \quad (4.23)$$

$$k_i^{(7)} = \frac{3}{8}g_i t_i c_{ix}, \quad (4.24)$$

$$k_i^{(8)} = \frac{3}{8}g_i t_i c_{iy}. \quad (4.25)$$

Where, by definition, the following condition is met:

$$\underline{h}^{(i)} \cdot \underline{k}^{(j)} = \delta_{ij}. \quad (4.26)$$

Hence, it is possible to define the following:

$$\underline{\underline{M}}^{-1} = (\underline{k}^{(0)}, \underline{k}^{(1)}, \dots, \underline{k}^{(8)}). \quad (4.27)$$

Having determined  $\underline{\underline{M}}^{-1}$ , to get an expression for the post-collision distribution function vector  $\underline{f}^+$ , we set:

$$\underline{f}^+ = \underline{\underline{M}}^{-1} \underline{m}^+, \quad (4.28)$$



#### 4. Extended cMCLBM for the Simulation of Drops within Stokes Flow

which, using Eqs. (4.7), (4.28), gives the following final result, after straightforward algebra[138, 134]:

$$\begin{aligned}
f_i^+ &= (M)_{ij}^{-1} m_j^+ \\
&= t_i \left\{ \left[ 2 - \frac{3}{2} (c_{ix}^2 + c_{iy}^2) \right] \rho + 3 \left( (\rho u_x)^+ c_{ix} + (\rho u_y)^+ c_{iy} \right) \right. \\
&\quad \left. + \frac{9}{2} (P_{xx}^+ c_{ix}^2 + 2P_{xy}^+ c_{ix} c_{iy} + P_{yy}^+ c_{iy}^2) - \frac{3}{2} (P_{xx}^+ + P_{yy}^+) \right. \\
&\quad \left. + \frac{1}{4} g_i N^+ + \frac{3}{8} g_i (J_x^+ c_{ix} + J_y^+ c_{iy}) \right\}.
\end{aligned}$$

Above,  $(\rho u_x)^+$ ,  $(\rho u_y)^+$ ,  $\rho^+$ ,  $P_{xx}^+$ ,  $P_{xy}^+$ ,  $P_{yy}^+$ ,  $N^+$ ,  $J_x^+$  and  $J_y^+$  are determined in Eqs. (4.11 - 4.16) above. Now the post-collision distribution function has been recovered, the post-collision segregation rule given by Eq. (3.10) can be applied, so colour is, as previously, re-allocated to reduce fluid mixing.

In conclusion, this section has highlighted the extension of the methodology from the BGK-model presented in Chapter 3, to the development of an MRT-model with enhanced tuneability —owing to the ghost modes (free parameters) that can be tuned to improve numerical stability of the system within different flow scenarios —providing a detailed mathematical description of the scheme. From this, the emergent dynamics and kinematics of the model can be assessed through both mathematical analysis and simulation data.

##### 4.2.2.1 Dynamics and Kinematics

After the method of Chapter 3, in order for our MRT cMCLBM model to have correct dynamics, the Navier-Stokes equations must be recovered. It was seen in section 3.3.1, that in order to recover the weakly compressible Navier-Stokes equations through Chapman-Enskog analysis, a correction term was needed, which is incorporated in the source term  $F_i$ . A brief dynamics, Chapman-Enskog analysis following that presented in section 3.3.1 is given in Appendix A.1.1 for the MRT-model. The principal outcome of this is the source term  $F_i$ . Comparing the resulting source term from the BGK-model, and the MRT-model, where the superscript denotes the source term's corresponding collision model:

#### 4. Extended cMCLBM for the Simulation of Drops within Stokes Flow

*BGK-model source term:*

$$F_i^{\text{BGK}} \equiv t_i \left\{ \left(1 - \frac{1}{2\tau}\right) \frac{F_\alpha c_{i\alpha}}{c_s^2} + \frac{1}{2c_s^4} \left(1 - \frac{1}{2\tau}\right) \left[ u_\alpha (F_\beta - \partial_\beta \Phi') + u_\beta (F_\alpha - \partial_\alpha \Phi') - \left[ u_\gamma \partial_\gamma \Phi' - \frac{\rho}{3} \partial_\gamma u_\gamma \right] \delta_{\alpha\beta} \right] \times (c_{i\alpha} c_{i\beta} - c_s^2 \delta_{\alpha\beta}) \right\}. \quad (4.29)$$

*MRT-model source term:*

$$F_i^{\text{MRT}} = t_i \left\{ \frac{F_\alpha c_{i\alpha}}{c_s^2} + \frac{1}{2c_s^4} \left(1 - \frac{\lambda_3}{2}\right) \left[ u_\alpha (F_\beta - \partial_\beta \Phi') + u_\beta (F_\alpha - \partial_\alpha \Phi') - \left[ u_\gamma \partial_\gamma \Phi' - \frac{\rho}{3} \partial_\gamma u_\gamma \right] \delta_{\alpha\beta} \right] \times (c_{i\alpha} c_{i\beta} - c_s^2 \delta_{\alpha\beta}) \right\}. \quad (4.30)$$

Considering both source terms, it is seen that within the MRT-model,  $\lambda_3$  replaces  $\frac{1}{\tau}$  in the analysis. However, there is another difference within the first term in Eqs. (4.29) and (4.30), where there is now no dependence on the relaxation parameter in the MRT-model. This difference is due to the constraint that arises in the BGK-model:  $(n + \frac{m}{\tau}) = 1$ , shown in [70], which does not arise in the analysis of MRT dynamics.

This difference is evident in the component of the source term responsible for applying the surface tension force, not in the terms involved in the density difference corrections. As such, the analysis of the model's kinematics in section 3.3.2 will be identical to that in this model, with the exception of  $\lambda_3$  replacing  $\frac{1}{\tau}$ . Here, the resulting approximation of the upper bound of the advection error when there is a flat interface between the fluids, due to the inclusion of large density contrasts in the model, is given as:

$$\Delta < \left(1 - \frac{\lambda_3}{2}\right) \beta u (\Lambda - 1) \rho_{0B}. \quad (4.31)$$

The outcome of this is that the inclusion of the MRT scheme produces little difference on the resultant advection error present in the BGK model outlined in Chapter 3, other than the change in relaxation parameter. Consequently, to draw further conclusions on the stability of the model and its compliance with interface kinematics and dynamics, simulation data will be compared against the theory relating to these conditions.

### 4.2.3 Results

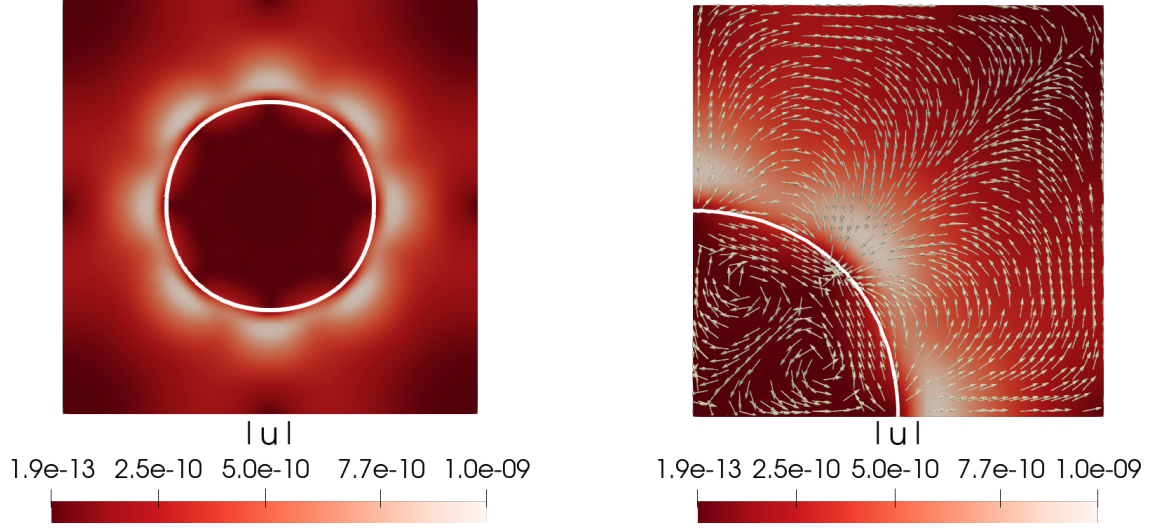
#### 4.2.3.1 Microcurrent

The first test of our two-component MRT chromodynamic model for the simulation of fluids with density contrasts, is the analysis of its microcurrent level—which, as discussed, is common across all multi-component lattice Boltzmann models. An identical test to that outlined for the BGK-model in Chapter 3 is used here, allowing for comparison between the two models. The test evaluates a static drop of radius  $R = 20$  within a lattice of size  $80 \times 80$  lu (lattice units). The microcurrent level is examined over a range of density ratios between  $\Lambda = \frac{1}{1000}$  and  $\Lambda = 1000$ , with the surface tension value for these simulations given by  $\sigma = 1 \times 10^{-5}$ . Simulations were run until steady state was reached, which was checked by inspecting when the modulus of the velocity across the lattice became steady. At the end of each simulation, the maximum velocity modulus over the domain was recorded, with results then presented within Table 4.2 (discussed shortly). Additionally, the effect of using a constant curvature value on the microcurrent level, versus calculating the curvature numerically, was again assessed. This motivated an assessment of the impact of using stencils to calculate numerical gradients needed for the curvature calculations within the model.

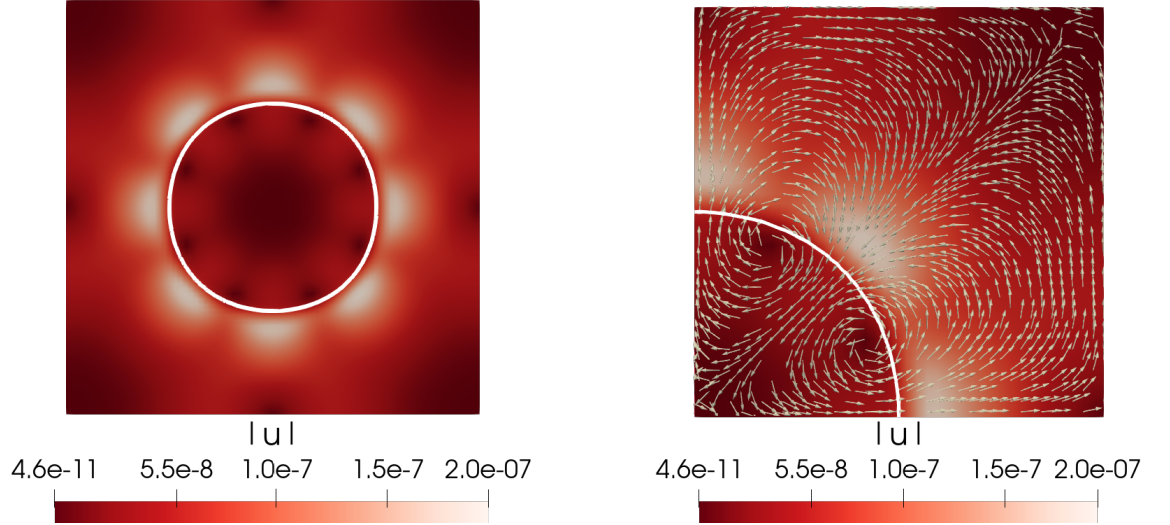
Figures 4.1 and 4.2 display the microcurrent field for the full lattice (left) and top-right quadrant of the lattice (right), where the drop (Red fluid) has density 10 and the external fluid (Blue fluid) has density 1. Figure 4.1 corresponds to a fixed value for the curvature and Figure 4.2 a numerically calculated curvature. A further quantification of this microcurrent level can be seen in Table 4.2, which shows the maximum microcurrent level over a range of density contrasts for both curvature definitions used.

Figures 4.1 and 4.2 show that, when the curvature is defined by the drop radius (results in Figure 4.1), the microcurrent level is lower and also more localised at the drop interface. In contradistinction, results in Figure 4.2 show when the curvature is calculated through the use of numerical stencils, the microcurrent level is larger and more dissipated from the interfacial region. The larger microcurrent and increased dissipation is due to numerical cut-off errors in the stencils used for the gradients, which could be further reduced through higher order numerics. Table 4.2 shows that the microcurrent levels become more comparable between the two curvature definitions at larger density ratios, with the maximum microcurrent value, over the lattice, being identical for the two curvature definitions at density ratios of order 1000. This result is due to the microcurrent level being dominated by errors introduced by

#### 4. Extended cMCLBM for the Simulation of Drops within Stokes Flow



**Figure 4.1:** Microcurrent profiles over the lattice for a density contrast  $\Lambda = 10$  and when the mean curvature is given by Eq. (3.66a). Left Figure shows surface plot of the microcurrent where white circular contour corresponds to the  $\rho^N = 0$  contour. Right Figure shows the top right quadrant of the lattice, showing microcurrent surface plot, superimposed vector field of  $\underline{u}$  (not scaled) and white contour corresponding to the  $\rho^N = 0$  contour.



**Figure 4.2:** Microcurrent profiles over the lattice for a density contrast  $\Lambda = 10$  and when the mean curvature is calculated by Eq. (3.66b). Left Figure shows surface plot of the microcurrent where white circular contour corresponds to the  $\rho^N = 0$  contour. Right Figure displays the top right quadrant of the lattice, showing microcurrent surface plot, superimposed vector field of  $\underline{u}$  (not scaled) and white contour corresponding to the  $\rho^N = 0$  contour.

the large density contrast between the fluids, hence, the impact of the less dominant numerical stencil error is unseen. Comparing the results of both the BGK-model's and MRT-model's microcurrents by examining Tables 3.1 and 4.2, it can be seen that the maximum microcurrent magnitudes are comparable across both models.

#### 4. Extended cMCLBM for the Simulation of Drops within Stokes Flow

MRT collision operator: static drop maximum microcurrent values				
$\Lambda$	$\alpha_B$	$\alpha_R$	$ \underline{u} _{\max}^{H_f}$	$ \underline{u} _{\max}^{H_c}$
0.001	0.9995	0.5	$1.13 \times 10^{-4}$	$1.13 \times 10^{-4}$
0.01	0.995	0.5	$9.89 \times 10^{-6}$	$3.28 \times 10^{-5}$
0.1	0.95	0.5	$2.92 \times 10^{-11}$	$1.22 \times 10^{-6}$
10	0.5	0.95	$1.01 \times 10^{-9}$	$1.95 \times 10^{-7}$
100	0.5	0.995	$1.96 \times 10^{-5}$	$1.98 \times 10^{-5}$
1000	0.5	0.9995	$7.91 \times 10^{-5}$	$7.91 \times 10^{-5}$

**Table 4.2:** Maximum microcurrent velocity (in lattice units) for a static drop of initial radius  $R = 20$  in a domain of  $80 \times 80$ , for  $\Lambda \in [10^{-3}, 10^3]$ ,  $\beta = 0.67$  with surface tension,  $\sigma = 1 \times 10^{-5}$ . Two different maximum microcurrent values are shown: (i)  $|\underline{u}|_{\max}^{H_f}$  and (ii)  $|\underline{u}|_{\max}^{H_c}$ , where  $H_f$  corresponds to mean curvature given by Eq. (3.66a) and  $H_c$  corresponds to mean curvature given by Eq. (3.66b).

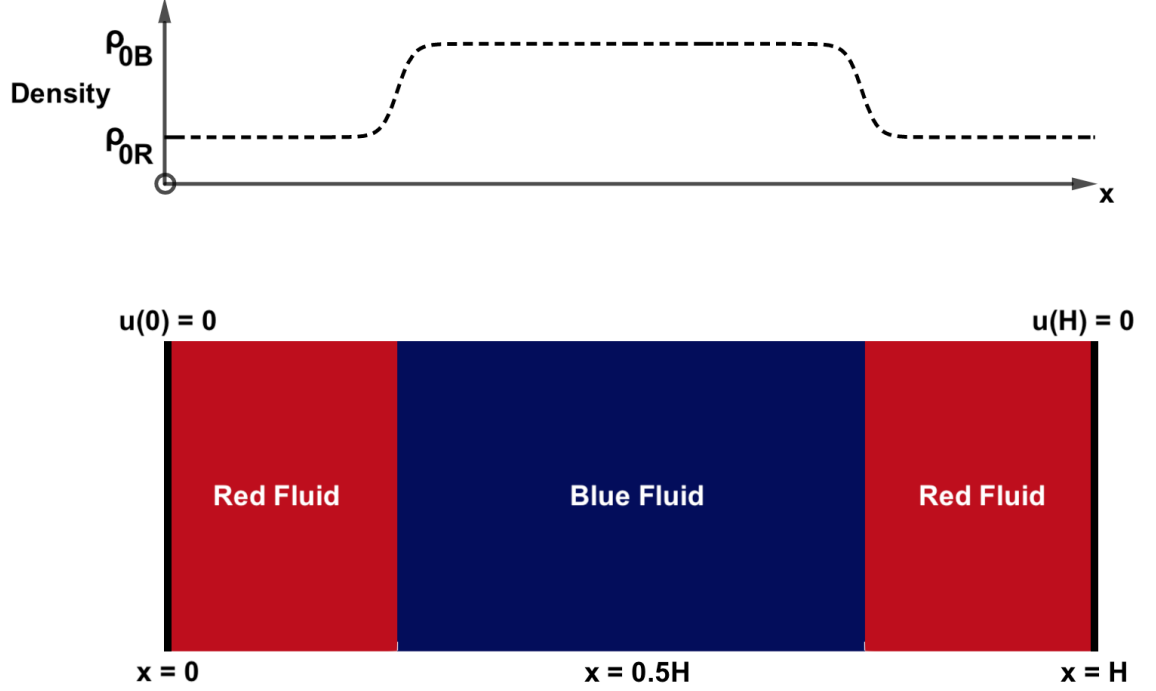
Each model has a largest microcurrent magnitude of the order  $1 \times 10^{-4}$ , which is similar to that seen in the model produced by Ba et al. [111]. However, the MRT model does have the lowest maximum microcurrent magnitude compared to the BGK model, with a lowest value in the order of  $1 \times 10^{-11}$ . The overall microcurrent level across density contrasts is acceptable and not so large that it is deemed to dominate or disrupt physical flow effects where applied flow velocities have larger magnitudes than the microcurrent. Although, particular care may need to be taken in low Reynolds number flows ( $\text{Re} \approx 0$ ) where flow velocities become of a similar order or lower than the microcurrent level. Flows in this regime are considered in detail in section 4.3. With this caveat in mind, the following tests proceed to investigate the application of the model in two-component fluid flows.

##### 4.2.3.2 Steady, pressure-driven flow with density stratification

The no-traction (or no-slip) kinematical boundary condition states that velocity tangent to the interface must be continuous across the interface, i.e., equal on either side of the free surface. To test this for our model, a steady-state test similar to that conducted by Ba et al. [111] is used. Here, two-dimensional layered pressure driven flow with transverse density stratification is examined, i.e., density of the fluids varies in the transverse (horizontal)  $x$  direction. The geometry of this flow is depicted in Figure 4.3, where a central fluid (Blue) is confined by another fluid (Red), where the areas of the total Blue and total Red fluids initialised on the lattice are equal, with no-slip boundary conditions placed at the East and West boundaries. Flow is then applied parallel to the flat interfaces between the fluids ( $y$  direction) and the simulation then ran to steady state. To benchmark this test, the  $y$ -component

#### 4. Extended cMCLBM for the Simulation of Drops within Stokes Flow

of velocity over the lattice is compared against a semi-analytical solution to this problem given in Appendix A.2.2. This differs from that of Ba et al., who compare against a solution for discontinuous variation in density, whereas the solution in Appendix A.2.2 contains continuous transverse variation in density.

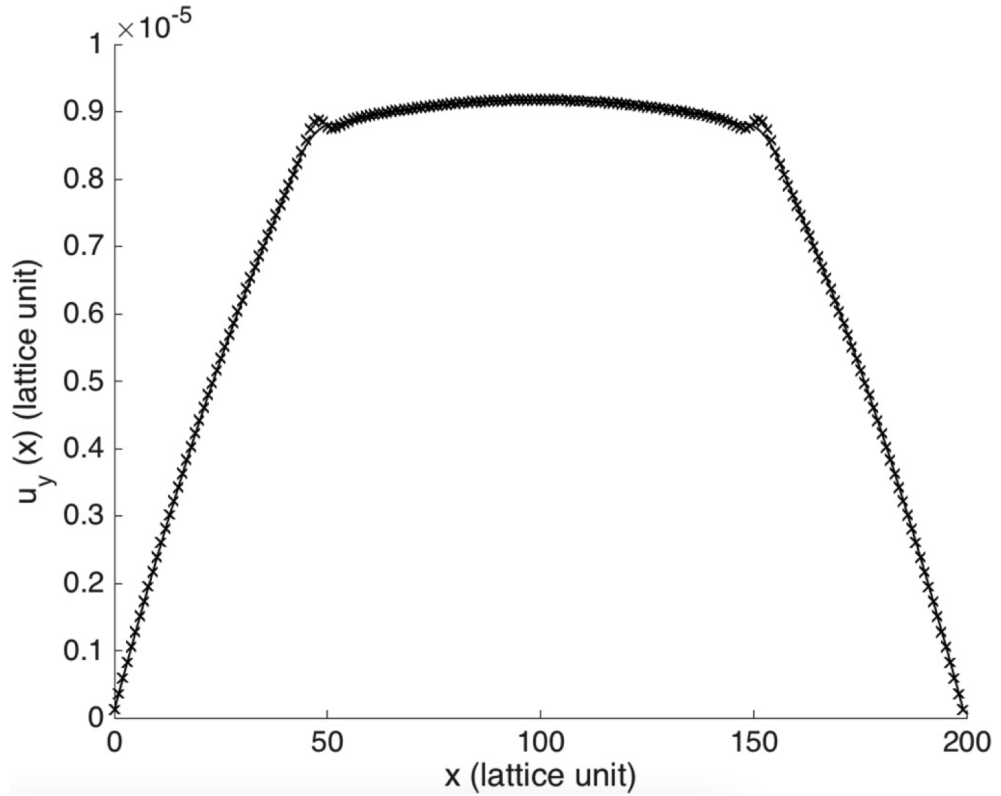


**Figure 4.3:** Schematic representation of the flow being simulated. The central fluid (Blue) is initialised between the outer fluids (Red), with both fluids occupying equal area on the lattice. The Blue fluid has density defined  $\rho_{0B}$  and Red fluid density  $\rho_{0R}$ , with the density being continuous across the interface. The fluids are confined by no-slip boundary conditions at the East and West boundaries (represented by the black walls), with periodic boundary conditions at the North and South. Simulation parameterisations are as follows:  $x$  lattice length  $L_x = 200 = H$ ,  $\alpha_B = 0.2$ ,  $\alpha_R = 0.9$ ,  $\Lambda = \frac{1}{8}$ ,  $\nu_R = \nu_B = 0.333$ ,  $\beta = 0.4$ , applied flow velocity  $U_0 \hat{e}_y = 1 \times 10^{-7}$  [134].

Simulation data for this initial test, where the Blue fluid has a density of  $\rho_{0B} = 8$  and the Red fluid density of  $\rho_{0R} = 1$ , are given in Figure 4.4.

The results in Figure 4.4 show that the developed model predicts the velocity profile of the flow well, given by the continuous black line. The achievable density ratios within this test were not as large as those presented by Ba et al., but the model performed much better than the original colour-gradient model, which struggled to predict such profiles [111]. The data show that our model is less accurate at the interfacial region between the fluids, seen at  $x = 50$  and  $x = 150$  lattice sites, however, still maintains sufficient accuracy. It was found necessary to implement higher order stencils, to calculate the numerical gradients, in order to reduce this error close to the interface, which, in turn, increased computational expense [134].

#### 4. Extended cMCLBM for the Simulation of Drops within Stokes Flow



**Figure 4.4:** Comparison of the transverse variation of the  $y$ -component of velocity between simulation data (crosses) and the semi-analytical solution (solid line), for the simulation depicted in Figure 4.3 (which also states simulation parameters) [134].

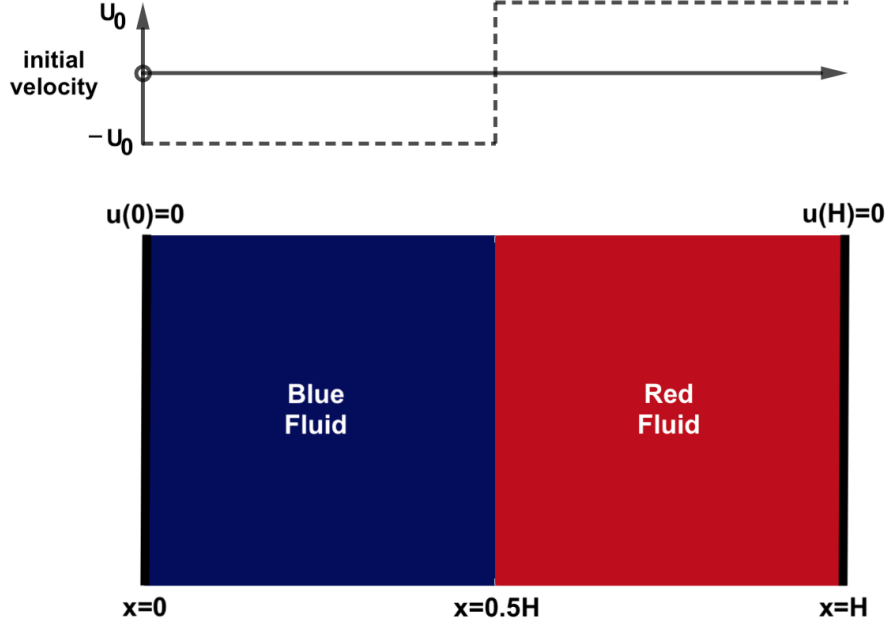
Overall, this test provides an initial benchmark that the model can predict correct velocity profiles for such a flow at limited density ratios in comparison to other models. Although the no-traction or no-slip boundary condition is recovered at the free surface, this test only evidences the steady state behaviour of the model, not dynamical behaviour. It therefore remains necessary to assess the model's ability to meet the required free surface boundary conditions within unsteady flow.

##### 4.2.3.3 Transient uni-directional flow with transverse density stratification

In order to provide a strong conformation of compliance with the kinematic and dynamic boundary conditions outlined in Chapter 2, one must check these in unsteady flow. Consider a case where two fluids of equal area are separated by a flat interface, with transverse variation in density in the  $x$  direction, and are confined by bounce-back boundary conditions at the East and West walls and periodic boundary conditions at the North and South walls. A velocity of  $U_0$  is then applied in the positive  $y$  direction—parallel to the interface—to one of the fluids (Red), and in the inverse direction to the other fluid (Blue). This geometry is explained pictorially in Figure 4.5. Once

#### 4. Extended cMCLBM for the Simulation of Drops within Stokes Flow

steady state has been reached, the flow velocities are switched off, allowing the system to recover. During this recovery, the flow velocity should be continuous across the interface —due to the no-slip condition and mutual impenetrability condition (section 2.2) —there also being instantaneous stress transmission across the interface (dynamic boundary condition).



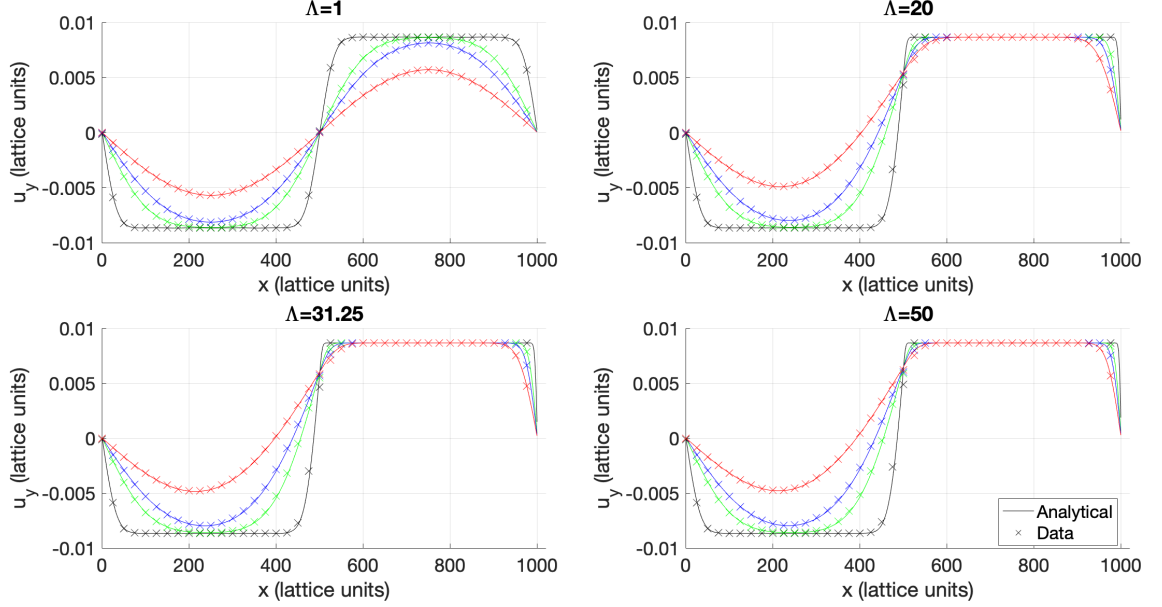
**Figure 4.5:** System geometry and initial conditions for flow being simulated. The two binary fluids (Blue and Red) are separated by a flat interface, with no-slip boundary conditions located at the East and West boundaries (highlighted by a thick black line). The segmented flow has transverse density and velocity variation, with Red (Blue) fluid density  $\rho_{0R}(\rho_{0B})$  and Red (Blue) flow velocity  $u_0\hat{e}_y$  ( $-u_0\hat{e}_y$ ). There is translational invariance in the  $y$ -direction, and both fluids inhabit equal area on the lattice [134].

In order to check this, a semi-analytical solution was found for the time-dependent velocity profile over the domain within the sharp interface limit, i.e., the interface between the two fluid is considered discontinuous. This analytical solution was found through the use of Sturm-Liouville theory, with the solution given in full in Appendix A.2.1. By obtaining an analytical solution for this scenario within the sharp interface limit, it provides a valuable way of benchmarking simulation data and validating the developed MRT MCLB model in unsteady flow through evaluating the decay of the velocity profile over time. To do this, the velocity profile was examined at increasing time steps  $t=(1000, 10000, 20000, 50000)$  (lattice units) after the flow was switched off. The density ratio between the fluids was also varied between unity and 50, with the denser fluid (Red) being on the right-hand side of the domain. The results presented in Figure 4.6 reveal that the simulation data provide strong agreement with that of the analytical solution for the velocity profile across all time



#### 4. Extended cMCLBM for the Simulation of Drops within Stokes Flow

steps and density ratios shown. It validates that there is instantaneous transmission of stress across the interface within this model by testing model dynamics, which is a more stringent test than steady-state compliance, of course.



**Figure 4.6:** Comparison of the transverse variation of the  $y$ -component of velocity between the simulation data (crosses) and semi-analytical solution (lines) over increasing time steps, where black, green, blue, red correspond to 1000, 10000, 20000, 50000 time steps. The headings of the subplots show the density ratio of the simulation  $\Lambda$ , where shear viscosity,  $\eta = \text{constant}$  and kinematic viscosity,  $\nu = \frac{\eta}{\rho}$ . The interface centres on  $x = 500$  and no-slip boundary at  $x = 0$  and  $x = 1000$  lattice units, with the fluid on the right being the denser [134].

To provide numerical validation of the strength of simulation data and its fit to the analytical solution, the domain-average relative error between the semi-analytic solution for the stream-wise velocity,  $u(x, t)$ , and the simulated solution,  $u^*(x, t)$  was calculated as follows:

$$\epsilon(t) = \frac{\sum_{x=0}^H |u(x, t) - u^*(x, t)|^2}{\max(u^*(x, t))^2}, \quad (4.32)$$

where  $x$  denotes the discrete, “on-lattice” value of the transverse co-ordinate, and  $H$  is the last lattice site of the  $x$  domain (East boundary). The relative error at each time step for density ratios greater than unity were then recovered and could be seen in Table 4.3. Table 4.3 provides quantitative data that support the results presented in Figure 4.6, showing that the simulation data provide excellent prediction of the semi-analytic solution for the stream-wise velocity. This is confirmed by the relative error never exceeding 1% over all time steps and density ratios investigated. There is a slight loss of accuracy at higher density ratios, as well as a larger relative error towards

#### 4. Extended cMCLBM for the Simulation of Drops within Stokes Flow

Relative error (%) between data and analytical solution: relating to results in Fig 4.6			
time (lu)	$\Lambda = 20$	$\Lambda = 31.25$	$\Lambda = 50$
1000	0.560	0.754	0.979
10000	0.199	0.252	0.300
20000	0.135	0.167	0.196
50000	0.075	0.092	0.115

**Table 4.3:** Table of relative (%) error shown in Eq. (4.32) relating to the density ratios and time steps in Fig 4.6. Results were normalised by dividing by the maximum velocity within the system at the corresponding time step.

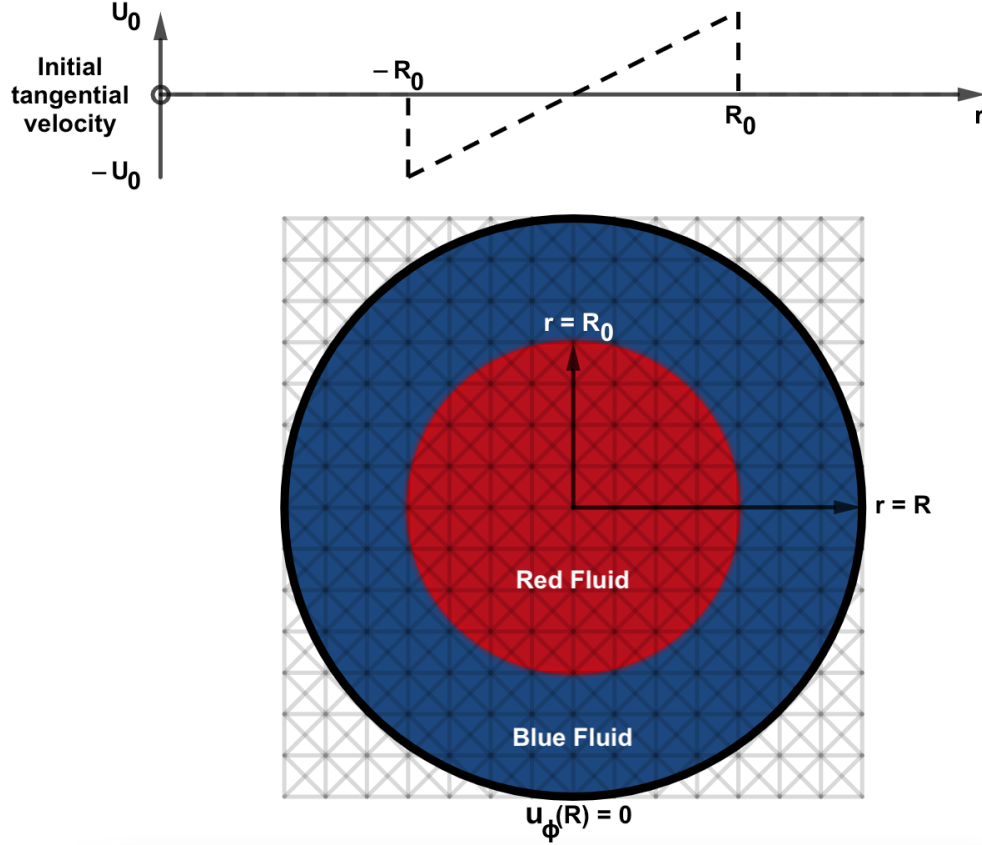
the beginning of the simulation, due to the larger flow stresses and the larger flow velocities. At larger density ratios, the lighter fluid on the left (Blue) is dragged by the denser fluid on the right (Red), causing a slower decay of the Red fluid’s velocity and an quicker increase in the Blue fluid’s velocity at larger density contrasts. These data provide strong conformation that there is instantaneous stress transmission across the interface, with flow velocity being continuous across the interface at the range of density ratios tested, causing a dynamical response between the fluids. However, this test only examines the case of a flat interface between the fluids, with the impact of non-zero interface curvature yet to be established and needed to be tested.

##### 4.2.3.4 Transient rotational multi-component flow with radial density stratification

Following on from the previous test, here, the compliance with correct interface kinematics and dynamics of continuous velocity and instantaneous stress transmission across the interface is examined for curved interfaces. To assess this, imagine a circular fluid domain defined by a polar co-ordinate system  $(r, \phi)$  in which  $r \leq R$ . An internal fluid (Red) is given by a circle of radius  $r = R_0$  (where  $R_0 < R$ ), and an external fluid (Blue) occupies the remaining domain —giving an interface of curvature  $\frac{1}{R_0}$  between the fluids. A no-slip boundary is applied at  $r = R$ , representing a solid wall. A rotational flow is then applied to the internal fluid (Red) only  $u_\phi(r)\hat{e}_\phi$  and the external fluid (Blue) velocity is set to zero, resulting in a tangentially sheared interface. A schematic highlighting the described geometry is given in Figure 4.7.

Similar to the test in section 4.2.3.3, the temporal decay of the flow is observed, but now for a curved interface. To achieve this, an analytical solution has been obtained for the tangential velocity component in the sharp interface limit —discontinuous density change across the interface —which is presented by Spendlove et al. [134]. Once steady state has been reached, the rotational flow is switched off, and the simulation is left to recover. During its recovery, the tangential velocity over the

#### 4. Extended cMCLBM for the Simulation of Drops within Stokes Flow

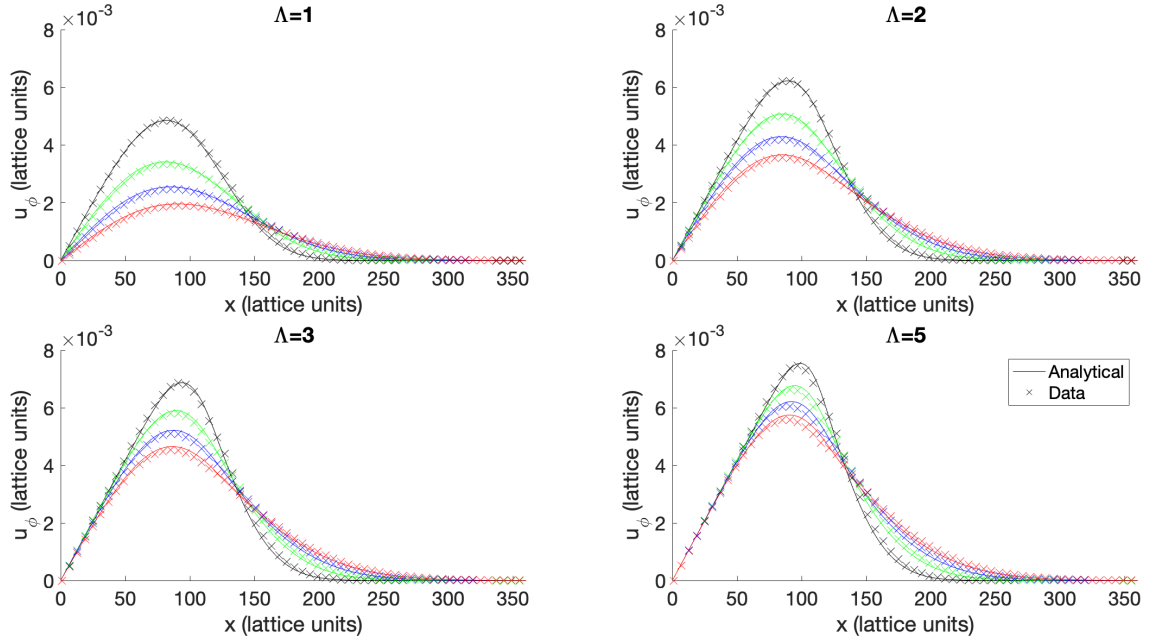


**Figure 4.7:** Schematic of system geometry and initial conditions. Here, the fluids are sheared, with the internal fluid (Red) having an initial rotational flow given by  $u_\phi(r)\hat{e}_\phi$ , and the external fluid (Blue) being at rest. The Red (Blue) fluid has density given by  $\rho_{0R}$  ( $\rho_{0B}$ ), where in the presence of a density contrast, the Red fluids density is larger [134].

domain is compared against the analytical solution for this flow (given in Appendix C of [134]) at increasing time steps  $t = (2000, 4000, 6000, 8000)$ . The range of density contrasts simulated between the fluids was  $\Lambda \in [1, 5]$ , where density ratios greater than unity correspond to the internal fluid (Red) being denser than the external fluid (Blue). Subsequently, testing the ability to meet kinematic and dynamic interface boundary conditions over a limited range of density ratios. The results of this test can be seen in Figure 4.8, which show the predicted and actual tangential components of velocity across the radius of the domain from  $r = 0$  to  $r = R$ , for increased time.

Figure 4.8 shows that the simulation data (crosses) conform with that of the analytical solution (lines) at all time steps and density ratios presented. As time increases, the tangential component of velocity starts to decay. However, as the density of the internal fluid increases, the decay of the velocity is slower over time due to the fluid's momentum being larger for larger densities. This also results in the increased dragging of the external fluid —highlighted by the sharper gradient of the red line and increased external fluid velocity at higher density ratios. This

#### 4. Extended cMCLBM for the Simulation of Drops within Stokes Flow



**Figure 4.8:** Comparison of the transverse variation of the tangential component of velocity between the simulation data (crosses) and semi-analytical solution (lines) over increasing time steps (where black, green, blue, red correspond to 2000, 4000, 6000, 8000 time steps). The headings of the subplots show the density ratio of the simulation  $\Lambda$ , where the shear viscosity,  $\eta = \text{constant}$  and kinematic viscosity,  $\nu = \frac{\eta}{\rho}$ . The interface centres on  $r = 120 = R_0$ , with a no-slip boundary present at  $r = 360 = R$  lattice units. Here, the fluid on the left (Red fluid) is the denser fluid, see Figure 4.7 for flow geometry [134].

result shows that tangential velocity is continuous across the interface —compliance with the no-slip kinematic boundary condition, but also that stress transmission across the interface is instantaneous, confirming the interface dynamics through the dragging of the external fluid. To provide quantitative evidence of the accuracy of the developed model in this test, the maximum relative error of the tangential velocity over the radial slice for the data in Figure 4.8 is calculated as follows:

$$\epsilon(t) = \frac{\max(|u(x, t) - u^*(x, t)|)}{\max(|u^*(x, t)|)}. \quad (4.33)$$

The results of this error analysis are presented in Table 4.4.

The data in Table 4.4 highlight that the maximum relative error: (i) increases with density ratio and (ii) decreases as time increases. These results are as expected, with (i) due to the associated errors in the model from simulating density contrasts and (ii) due to the flow stresses acting on the fluids decreasing over time, i.e., flow velocity decreases once rotational flow is turned off. Although the error values appear large, this is the maximum error, not the average error, which would be much smaller. It is clear that for a curved interface, the associated accuracy of the methodology decreases, resulting in the ability to only simulate lower density ratios accurately.

#### 4. *Extended cMCLBM for the Simulation of Drops within Stokes Flow*

Maximum relative error (%) between data and analytical solution: relating to results in Fig 4.8				
time (lu)	$\Lambda = 1$	$\Lambda = 2$	$\Lambda = 3$	$\Lambda = 5$
2000	6.35	8.51	10.4	12.9
4000	5.48	6.92	8.57	10.7
6000	5.39	6.67	8.04	10.0
8000	5.11	6.15	7.50	9.33

**Table 4.4:** Table of relative (%) error shown in Eq. (4.33) over differing time steps and density ratios. Results were normalised by dividing by the maximum velocity within the system at the corresponding time step.

This point is highlighted by the fact that the previous test, using a flat interface, simulated density contrasts up to  $\Lambda = 50$ .

These data hint at limitations of the developed model in simulating curved interfaces between fluids with large density contrasts. However, as discussed by evaluating the kinematical error of the model—the magnitude of the kinematical error is influenced by flow velocity and density contrast (a relationship shown in Figure 3.7). Therefore, the application of the model within low Reynolds number flow (Stokes’s Regime) may furnish the model’s most applicable area. Stokes flow, often called creeping flow, corresponds to flows where viscous forces between fluid layers dominate advective inertial forces, hence low Reynolds number (see Eq. (2.17)). Where, from the results on the model’s microcurrent, further analysis is needed if one is to extract the physical flow due to the low velocity values found in Stokes flow, more on this shortly.

## 4.3 Pseudo Three-dimensional System

### 4.3.1 Introduction

Following on from the two-dimensional MRT-model developed and analysed in section 4.2, the next extension of the methodology allows for economic simulation of three-dimensional fluid flows. As found in the preceding work, when investigating curved interfaces, the model is most applicable to low Reynolds number flow. As such, we here consider simulating axial-symmetric three-dimensional, low Reynolds number, two-component fluid flows with a density contrast. Nominally, to do this, one could extend the lattice grid to a three dimensional lattice, i.e., D3Q19, D3Q27 etc., or proceed, as here, to use a two-dimensional system to simulate axially-symmetric three-dimensional flow. By doing so, one enhances computational efficiency—reducing computational expense by two-orders of magnitude—while

#### 4. *Extended cMCLBM for the Simulation of Drops within Stokes Flow*

also allowing the behaviour of three dimensional flows to be explored. In line with the above, this section focuses on the validation of the fundamentals of the methodology —compliance with interface kinematics and dynamics, when applied to three-dimensional axial-symmetric flows with curved interfaces. To tackle this, our MRT-model as presented in section 4.2 is extended, with the resultant model then being validated against analytical benchmarks for the target flow regime.

The layout of this section is as follows. First, the extension of the two-dimensional MRT-model will be outlined, which is split into three interlinking parts: (i) The reduction from a three-dimensional system to a pseudo three-dimensional system (a two dimensional system which is used to encapsulate the flow physics of an axially-symmetric three dimensional system —rotational symmetry about an axis). (ii) The inclusion of velocity dependent force distributions in the scheme. (iii) The inclusion of an additional source term  $F_{3i}$  needed due to work in (i). Following this, simulation data will aim to address flow past a spherical and deforming drop, assessing the ability of our model to meet known kinematical and dynamical interface boundary conditions for this flow. Here, comparison against analytical solutions allow for further benchmarking of the model. Before continuing, it should be noted that in this section the following notation will be used to distinguish between discrete lattice co-ordinates and physical co-ordinates:

$$\begin{aligned}\text{discrete lattice co-ordinates :} & \quad (x^*, z^*) \\ \text{physical co-ordinates :} & \quad (x, z)\end{aligned}$$

### 4.3.2 **Extension of Methodology**

#### 4.3.2.1 **Two-dimensional representation of axially symmetric three-dimensional system**

To accurately simulate an axially symmetric three-dimensional domain using two-dimensional system, the geometry of the flow must be embedded. Panel (A) of Figure 4.9 shows the three-dimensional system in question in Cartesian co-ordinates, where variables  $x$ - $y$  span the cross-section of the passage, with long axis aligned parallel to the  $z$ -axis. There is rotational invariance about the  $z$ -axis (i.e, axially symmetric about  $z$ ). In other words, considering this system in cylindrical polar co-ordinates  $(r, z, \phi)$ , then there is invariance on the  $\phi$  coordinate. The governing hydrodynamic equations (Navier-Stokes equations and continuity

#### 4. Extended cMCLBM for the Simulation of Drops within Stokes Flow

equation for incompressible flow) are expressed as follows in cylindricals [140]:

$$\frac{\partial v_r}{\partial t} + v_r \frac{\partial v_r}{\partial r} + \frac{v_\phi}{r} \frac{\partial v_r}{\partial \phi} + v_z \frac{\partial v_r}{\partial z} - \frac{v_\phi^2}{r} \quad (4.34a)$$

$$= -\frac{1}{\rho} \frac{\partial p}{\partial r} + \frac{\eta}{\rho} \left( \frac{1}{r} \frac{\partial}{\partial r} \left( r \frac{\partial v_r}{\partial r} \right) + \frac{1}{r^2} \frac{\partial^2 v_r}{\partial \phi^2} + \frac{\partial^2 v_r}{\partial z^2} - \frac{2}{r^2} \frac{\partial v_\phi}{\partial \phi} - \frac{v_r}{r^2} \right).$$

$$\frac{\partial v_\phi}{\partial t} + v_r \frac{\partial v_\phi}{\partial r} + \frac{v_\phi}{r} \frac{\partial v_\phi}{\partial \phi} + v_z \frac{\partial v_\phi}{\partial z} + \frac{v_r v_\phi}{r} \quad (4.34b)$$

$$= -\frac{1}{\rho r} \frac{\partial p}{\partial \phi} + \frac{\eta}{\rho} \left( \frac{1}{r} \frac{\partial}{\partial r} \left( r \frac{\partial v_\phi}{\partial r} \right) + \frac{1}{r^2} \frac{\partial^2 v_\phi}{\partial \phi^2} + \frac{\partial^2 v_\phi}{\partial z^2} + \frac{2}{r^2} \frac{\partial v_r}{\partial \phi} - \frac{v_\phi}{r^2} \right).$$

$$\frac{\partial v_z}{\partial t} + v_r \frac{\partial v_z}{\partial r} + \frac{v_\phi}{r} \frac{\partial v_z}{\partial \phi} + v_z \frac{\partial v_z}{\partial z} \quad (4.34c)$$

$$= -\frac{1}{\rho} \frac{\partial p}{\partial z} + \frac{\eta}{\rho} \left( \frac{1}{r} \frac{\partial}{\partial r} \left( r \frac{\partial v_z}{\partial r} \right) + \frac{1}{r^2} \frac{\partial^2 v_z}{\partial \phi^2} + \frac{\partial^2 v_z}{\partial z^2} \right).$$

$$\frac{1}{r} \frac{\partial}{\partial r} (r v_r) + \frac{1}{r} \frac{\partial v_\phi}{\partial \phi} + \frac{\partial v_z}{\partial z} = 0. \quad (4.34d)$$

Due to the axial-symmetry of the system about the  $z$ -axis (see Figure 4.9), the azimuth  $\phi$  is ignorable, and the continuity and Navier-Stokes equations therefore simplify:

$$\frac{\partial v_r}{\partial t} + v_r \frac{\partial v_r}{\partial r} + v_z \frac{\partial v_r}{\partial z} = -\frac{1}{\rho} \frac{\partial p}{\partial r} + \frac{\eta}{\rho} \left( \frac{\partial^2 v_r}{\partial r^2} + \frac{\partial^2 v_r}{\partial z^2} + \frac{1}{r} \frac{\partial v_r}{\partial r} - \frac{v_r}{r^2} \right). \quad (4.35a)$$

$$\frac{\partial v_z}{\partial t} + v_r \frac{\partial v_z}{\partial r} + v_z \frac{\partial v_z}{\partial z} = -\frac{1}{\rho} \frac{\partial p}{\partial z} + \frac{\eta}{\rho} \left( \frac{\partial^2 v_z}{\partial r^2} + \frac{\partial^2 v_z}{\partial z^2} + \frac{1}{r} \frac{\partial v_z}{\partial r} \right). \quad (4.35b)$$

$$\frac{\partial v_r}{\partial r} + \frac{\partial v_z}{\partial z} + \frac{v_r}{r} = 0. \quad (4.35c)$$

Using transformations  $r \rightarrow x$  and  $z \rightarrow z$ , the continuity and Navier-Stokes equations are expressed in a form which brings correspondence with their rectangular forms, the difference terms being attributed to what we designate a *geometrical forcing* and a *geometrical source* term:

$$\frac{\partial v_\alpha}{\partial t} + (v \cdot \nabla) v_\alpha = -\frac{1}{\rho} \frac{\partial p}{\partial \alpha} + \frac{\eta}{\rho} \nabla^2 v_\alpha + a_\alpha, \quad \alpha = [x, z] \quad (4.36a)$$

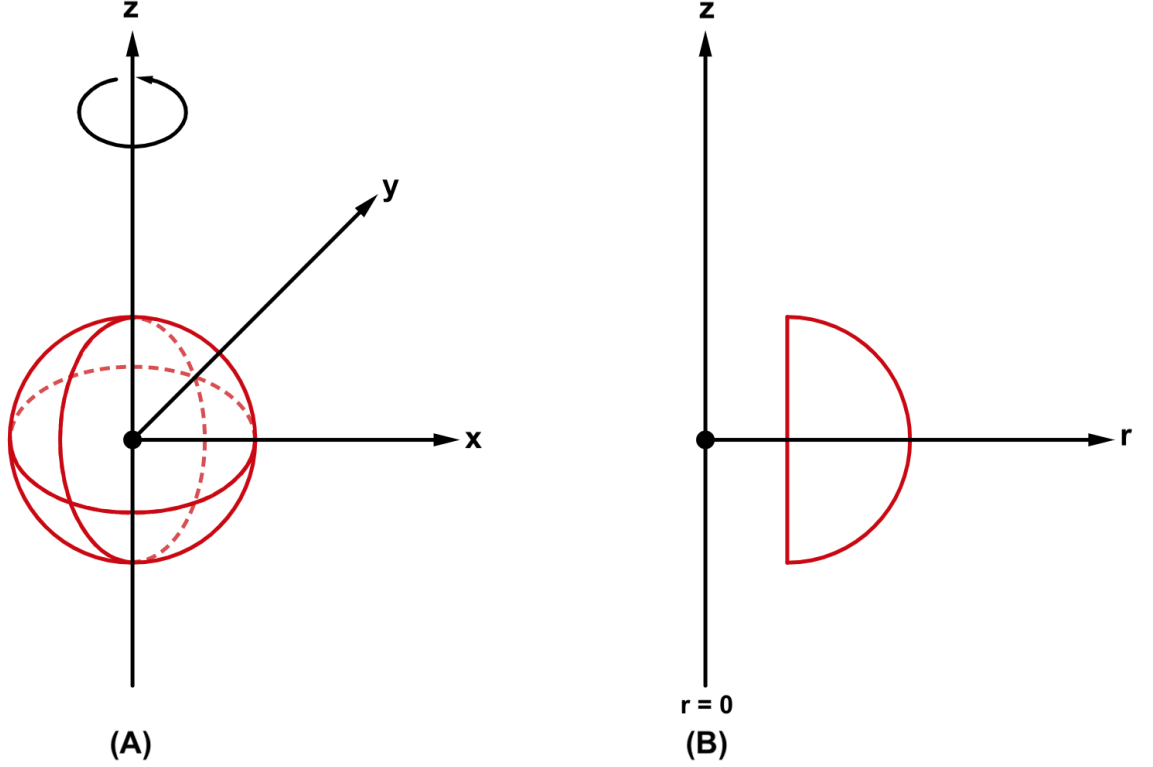
$$\frac{\partial v_x}{\partial x} + \frac{\partial v_z}{\partial z} = A, \quad (4.36b)$$

where

$$\alpha_x = \frac{\eta}{\rho} \left( \frac{1}{x} \frac{\partial v_x}{\partial x} - \frac{v_x}{x^2} \right), \quad \alpha_z = \frac{\eta}{\rho} \left( \frac{1}{x} \frac{\partial}{\partial x} v_z \right), \quad A = -\frac{v_x}{x}. \quad (4.37)$$

To transform the geometrical force terms and continuity source term in Eq (4.37), to forces with units of Newtons ( $Nm^{-3}$ ), we multiply by  $\rho$ . This allows the modified forces to be applied with the immersed body force framework, in the equations

#### 4. Extended cMCLBM for the Simulation of Drops within Stokes Flow



**Figure 4.9:** Schematic representing the reduction from the three-dimensional flow scenario to the corresponding two-dimensional system. Panel (A) shows the three-dimensional system with axial-symmetry about the  $z$  axis. Panel (B) corresponds to the pseudo three-dimensional system that aims to simulate that of panel (A). The following boundary conditions are enforced: (i) specular reflection is applied at the West wall, lattice site  $x^* = 0$  (corresponding to position  $r = 0.5$  in panel (B)), (ii) periodic boundary conditions at the North and South walls (periodic in the  $z$  direction) and (iii) mid-link bounce back applied at the East wall. Here, the red semi-circles in panel (B) corresponds to the red three-dimensional drop in panel (A) [135].

for the relative macroscopic velocities, as seen by Eq. (3.46). Consequently, this results in the following extended force terms, which may be applied in Guo's forcing framework within the lattice Boltzmann method (see section 4.3.2.2):

$$F_x = \eta \frac{\partial}{\partial x} \frac{v_x}{x}, \quad F_z = \frac{\eta}{x} \frac{\partial v_z}{\partial x}. \quad (4.38)$$

Additionally, we have the following continuity source term, which will be incorporated within the forcing term  $F_i$  (see appendix A.1.2):

$$A = -\frac{v_x}{x}. \quad (4.39)$$

Equation (4.39) amounts to a novel continuity equation source/sink, which can be understood by considering the geometry of the system. Panel (B) of Figure 4.9 represents the reduction from the three-dimensional system in panel (A) to the two-dimensional representative (which will be further discussed shortly). Take the



#### 4. Extended cMCLBM for the Simulation of Drops within Stokes Flow

spherical, three-dimensional drop given in red in panel (A) of Figure 4.9, with a small volume element given by  $rd\phi dz$ . The mass flux between the outer curved exterior and the interior of the element may be given by  $(r + dr)d\phi dz$ , where it is assumed that density  $\rho = \text{constant}$  and  $v_r = \text{constant}$ . The difference in mass flux across these surfaces gives rise to the continuity source/sink (expressed per unit volume), which is given as such for the two-dimensional, pseudo Cartesian domain:

$$\frac{\rho v_r r d\phi dz - \rho v_r (r + dr) d\phi dz}{rd\phi dz} = -\frac{\rho v_r}{r} \rightarrow \underline{A}(\underline{u}). \quad (4.40)$$

This is interesting, as the inclusion of the fact that an increase in  $r$ ,  $(r + dr)$ , in the two-dimensional system (panel (B) of Figure 4.9), corresponds to a volume increase in the three-dimensional system (panel (A) of Figure 4.9).

Within Eqs. (4.38), it is clear that the body force densities have a velocity dependence. The inclusion of velocities within these forces, and what implications this has for the model is analysed now.

##### 4.3.2.2 Velocity dependent forces in lattice Boltzmann

Equations. (4.38) show that the body force densities have a velocity dependency, which has impact on their implementation within the algorithm. Following Guo et al. [70], force densities are applied as an adjustment to the first moment of the distribution function —the lattice fluid’s macroscopic velocity. This is the crux of the problem. As defined previously, following Guo et al., the relationship between the force density and macroscopic velocity is:

$$\rho \underline{u} = \sum_i f_i \underline{c}_i + \frac{1}{2} \underline{F}. \quad (4.41)$$

If  $\underline{F}$  is dependent upon  $\underline{u}$ , such as seen in Eqs. (4.38), there is an implicit relationship. Splitting up the force density ( $\underline{F} = \underline{F}(\underline{u}) + \underline{G}$ ) into velocity dependent  $\underline{F}(\underline{u})$  and independent  $\underline{G}$  contributions:

$$\rho \underline{u} = \sum_i f_i \underline{c}_i + \frac{1}{2} (\underline{F}(\underline{u}) + \underline{G}), \quad (4.42)$$

Substituting in Eqs. (4.38) and rewriting Eq. (4.42) in component form results in a system of two de-coupled, partial differential equations for  $\underline{u}$ :

$$\begin{aligned} \rho u_x &= \sum_i f_i c_{ix} + \frac{1}{2} \eta \frac{\partial}{\partial x} \left( \frac{u_x}{x} \right) + \frac{1}{2} G_x. \\ \rho u_z &= \sum_i f_i c_{iz} + \frac{1}{2} \frac{\eta}{x} \frac{\partial}{\partial x} (u_z) + \frac{1}{2} G_z. \end{aligned}$$

#### 4. Extended cMCLBM for the Simulation of Drops within Stokes Flow

Through redefinition, the above equations are expressible as:

$$\rho u_x - \frac{1}{2}\eta \frac{\partial}{\partial x} \left( \frac{u_x}{x} \right) = S_x, \quad (4.44a)$$

$$\rho u_z - \frac{1}{2} \frac{\eta}{x} \frac{\partial}{\partial x} (u_z) = S_z, \quad (4.44b)$$

where, the following quantities have been defined:

$$S_x = \sum_i f_i c_{ix} + \frac{1}{2}G_x, \quad S_z = \sum_i f_i c_{iz} + \frac{1}{2}G_z, \quad S_0 = \sum_i f_i = \rho. \quad (4.45)$$

**Seeking**  $u_x$

Substituting Eq. (4.45) into (4.44a) to eliminate  $\rho$  and using the following relationship between dynamic and kinematic viscosity  $\eta = \nu\rho$ . Eq. (4.44a) becomes:

$$S_0 u_x = S_x + \frac{1}{2} S_0 \nu \frac{\partial}{\partial x} \left( \frac{u_x}{x} \right). \quad (4.46)$$

Note here, evaluating Eq. (4.46) as  $x \rightarrow \infty$ , results in:

$$S_0 u_x \rightarrow S_x \quad \Longleftrightarrow \quad u_x \rightarrow \frac{S_x}{S_0}.$$

Rearranging Eq. (4.46), we have:

$$\begin{aligned} u_x &= \frac{S_x}{S_0} + \frac{\nu}{2} \frac{\partial}{\partial x} \left( \frac{u_x}{x} \right), \\ \frac{\nu}{2} \frac{\partial}{\partial x} \left( \frac{u_x}{x} \right) - u_x &= -\frac{S_x}{S_0}, \\ \frac{\partial}{\partial x} \left( \frac{u_x}{x} \right) - \frac{2}{\nu} u_x &= -\frac{2}{\nu} \frac{S_x}{S_0}, \\ \frac{1}{x} \frac{\partial u_x}{\partial x} - \frac{1}{x^2} u_x - \frac{2}{\nu} u_x &= -\frac{2}{\nu} \frac{S_x}{S_0}, \\ \frac{\partial u_x}{\partial x} - \left( \frac{1}{x} + \frac{2x}{\nu} \right) u_x &= -\frac{2x}{\nu} \frac{S_x}{S_0}. \end{aligned} \quad (4.47)$$

To solve Eq. (4.47), an integrating factor is introduced:

$$\text{integrating factor} = \exp \left( -\ln(x) - \frac{x^2}{\nu} \right) = \frac{1}{x} \exp \left( -\frac{x^2}{\nu} \right). \quad (4.48)$$

Using Eq. (4.48), Eq. (4.47) can be rewritten as

$$\frac{\partial}{\partial x} \left( u_x \frac{1}{x} \exp \left( -\frac{x^2}{\nu} \right) \right) = -\frac{2x}{\nu} \frac{1}{x} \exp \left( -\frac{x^2}{\nu} \right) \frac{S_x}{S_0}.$$

Now, integrating:

$$u_x \frac{1}{x} \exp \left( -\frac{x^2}{\nu} \right) \Bigg|_{x_0}^{\infty} = \frac{S_x}{S_0} \int \frac{1}{x} \frac{\partial}{\partial x} \exp \left( -\frac{x^2}{\nu} \right) dx + \phi(z).$$

#### 4. Extended cMCLBM for the Simulation of Drops within Stokes Flow

We now use integration by parts; also simplifying:

$$\begin{aligned}
\frac{1}{x} u_x \exp\left(-\frac{x^2}{\nu}\right) \Big|_{x_0}^{\infty} &= \frac{S_x}{S_0} \left[ \frac{1}{x} \exp\left(-\frac{x^2}{\nu}\right) \Big|_{x_0}^{\infty} - \int_{x_0}^{\infty} -\frac{1}{x^2} \exp\left(-\frac{x^2}{\nu}\right) dx \right], \\
\frac{1}{x} u_x \exp\left(-\frac{x^2}{\nu}\right) \Big|_{x_0}^{\infty} &= \frac{S_x}{S_0} \left[ \left(0 - \frac{1}{x_0} \exp\left(-\frac{x_0^2}{\nu}\right) + \int_{x_0}^{\infty} \frac{1}{x^2} \exp\left(-\frac{x^2}{\nu}\right) dx \right) \right], \\
-\frac{1}{x_0} u_x(x_0) \exp\left(-\frac{x_0^2}{\nu}\right) &= \frac{S_x}{S_0} \left[ -\frac{1}{x_0} \exp\left(-\frac{x_0^2}{\nu}\right) + \int_{x_0}^{\infty} \frac{1}{x^2} \exp\left(-\frac{x^2}{\nu}\right) dx \right], \\
u_x(x_0) &= \frac{S_x}{S_0} - \frac{S_x}{S_0} x_0 \exp\left(-\frac{x_0^2}{\nu}\right) \int_{x_0}^{\infty} \frac{1}{x^2} \exp\left(-\frac{x^2}{\nu}\right) dx. \quad (4.49)
\end{aligned}$$

Substituting  $\frac{x^2}{\nu} = w^2$  into Eq. (4.49), we obtain the following expression for  $u_x$

$$u_x(x_0) = \frac{S_x}{S_0} - \frac{S_x}{S_0} \exp\left(-\frac{x_0^2}{\nu}\right) \frac{x_0}{\sqrt{\nu}} \int_{\frac{x_0}{\sqrt{\nu}}}^{\infty} \frac{1}{w^2} \exp(-w^2) dw.$$

The above may be rewritten as:

$$u_x(x_0) = \frac{S_x}{S_0} \xi(\nu, x), \quad (4.50)$$

where

$$\xi(\nu, x) = 1 - \exp\left(-\frac{x_0^2}{\nu}\right) \frac{x_0}{\sqrt{\nu}} \int_{\frac{x_0}{\sqrt{\nu}}}^{\infty} \frac{1}{w^2} \exp(-w^2) dw. \quad (4.51)$$

It is evident that, to calculate  $\xi(\nu, x)$ , numerical integration is necessary. This step will be discussed shortly.

#### Seeking $u_z$

Substituting Eq. (4.45) into (4.44b) to eliminate  $\rho$  and using  $\eta = \nu\rho$ , equation. (4.44b) becomes:

$$\begin{aligned}
S_0 u_z &= S_z + \frac{1}{2} S_0 \nu \frac{1}{x} \frac{\partial u_z}{\partial x}, \\
-u_z + \frac{\nu}{2} \frac{1}{x} \frac{\partial u_z}{\partial x} &= -\frac{S_z}{S_0}, \\
\frac{\partial u_z}{\partial x} - \frac{2x}{\nu} u_z &= -\frac{2x}{\nu} \frac{S_z}{S_0}. \quad (4.52)
\end{aligned}$$

Therefore, using the following integrating factor:

$$\text{integrating factor} = \exp\left(-\frac{x^2}{\nu}\right), \quad (4.53)$$

and using Eq. (4.53), Eq. (4.52) becomes:

$$\frac{\partial}{\partial x} \left( u_z \exp\left(-\frac{x^2}{\nu}\right) \right) = -\frac{2x}{\nu} \exp\left(-\frac{x^2}{\nu}\right) \frac{S_z}{S_0}.$$

#### 4. Extended cMCLBM for the Simulation of Drops within Stokes Flow

Now, integrating:

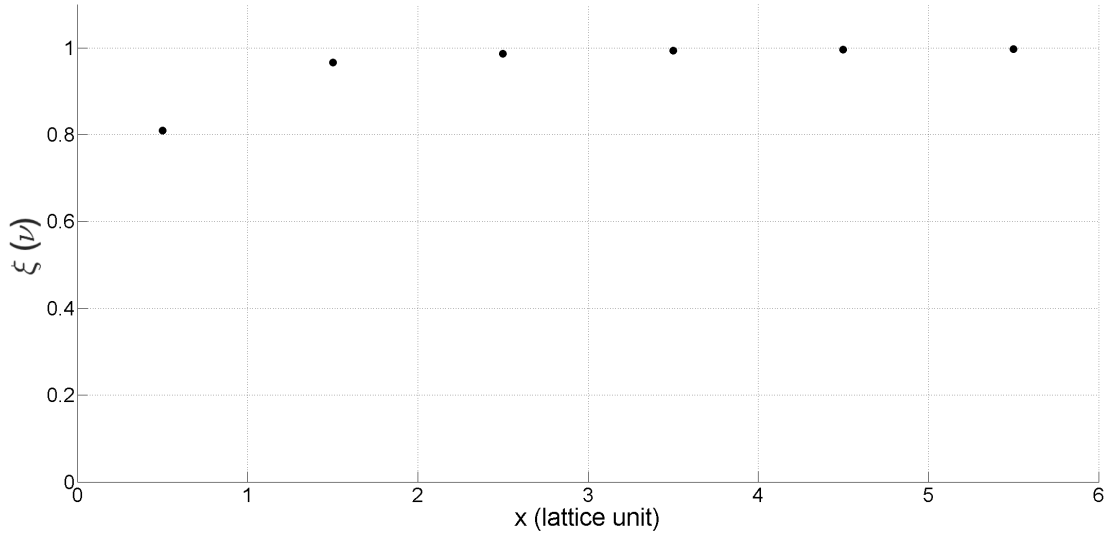
$$u_z \exp\left(-\frac{x^2}{\nu}\right) = \frac{S_z}{S_0} \int \frac{\partial}{\partial x} \exp\left(-\frac{x^2}{\nu}\right) dx,$$

$$u_z \exp\left(-\frac{x^2}{\nu}\right) = \frac{S_z}{S_0} \exp\left(-\frac{x^2}{\nu}\right).$$

The resultant of this process of integration is an explicit equation for  $u_z$ :

$$u_z = \frac{S_z}{S_0}. \quad (4.54)$$

Both components of the velocity are now defined as  $u_x$  and  $u_z$  (Eq. (4.50) and Eq. (4.54)). It was found that in order to compute  $u_x$ , numerical integration was needed—given in term  $\xi(\nu, x)$  (Eq. (4.51)). Figure 4.10 shows data for  $\nu = \frac{1}{6}$ , where Eq. (4.51) has been evaluated numerically using Simpson's rule. Apparently, the integrand in  $\xi(\nu, x)$  decays very rapidly, thus supports neglecting spatial variation in the quantity  $\frac{S_x}{S_0}$ . As such, the the pre-factor  $\xi(\nu, x^*)$  is calculated and stored pre-computation of  $u_x(x^*, z^*)$  for  $x \leq 11$  within the code—where  $\xi(\frac{1}{6}, 11^*) = 0.999$ .



**Figure 4.10:** Scatter plot showing the result of the evaluation of Eq. (4.51) through numerical integration (Simpson's rule) for  $\nu = \frac{1}{6}$  [135].

In this section, the impact of using velocity-dependent force densities and the application of them within the expression for the macroscopic velocity equation, as defined by [70], has been evaluated. It was shown that for this scenario, the coupled partial differential equations can be solved for the respective velocities, thus representing the assignment of an appropriate velocity in a quasi three-dimensional system. This work also more generally provides an example of how to treat such velocity dependent forces, which may arise in other lattice Boltzmann methods utilising Guo et al. forcing, for example in Coriolis's force in geophysical applications (where LB has considerable untapped potential) or in magnetohydrodynamics.

#### 4. Extended cMCLBM for the Simulation of Drops within Stokes Flow

##### 4.3.2.3 Dynamics

The dynamics of the two-dimensional model must now reflect that of the axial-symmetric three-dimensional system being simulated. As such, the macroscopic governing fluid dynamics equations derived in section 4.3.2.1 in Eqs. (4.36a,4.36b) must be considered. There is a clear impact to the model's dynamics, with the force densities given in Eq. (4.39) coupled into the macroscopic velocity which was discussed in section 4.3.2.2. The effect of the continuity source ( $A$ ) however propagates throughout the dynamics analysis in Appendix A.1.2, which results in an additional source term. Where the source term is now split up ( $F_i = F_{1i} + F_{2i} + F_{3i}$ ) into a density difference correction term  $F_{1i}$ , a term containing surface tension and force densities from Eq. (4.39),  $F_{2i}$ , and also a term including the new continuity source  $F_{3i}$ :

$$F_{1i} = \frac{t_i}{2c_s^4} \left(1 - \frac{\lambda_3}{2}\right) \left\{ \frac{1}{3} \rho \partial_\gamma u_\gamma \delta_{\alpha\beta} - (u_\alpha \partial_\beta \Phi' + u_\beta \partial_\alpha \Phi' + u_\gamma \partial_\gamma \Phi' \delta_{\alpha\beta}) \right\} (c_{i\alpha} c_{i\beta} - c_s^2 \delta_{\alpha\beta}), \quad (4.55)$$

$$F_{2i} = t_i \left\{ \frac{F_\alpha c_{i\alpha}}{c_s^2} + \frac{1}{2c_s^4} \left(1 - \frac{\lambda_3}{2}\right) (u_\alpha F_\beta + u_\beta F_\alpha) (c_{i\alpha} c_{i\beta} - c_s^2 \delta_{\alpha\beta}) \right\} \quad (4.56)$$

and

$$F_{3i} = t_i A - \left(1 - \frac{\lambda_3}{2}\right) A u_\alpha u_\beta - \frac{1}{3} A \delta_{\alpha\beta}. \quad (4.57)$$

The overall outcome of this transformation process is that, to simulate correct three-dimensional dynamics, an extra source term is required in addition to the density difference correction source term, alongside the more advanced velocity coupling (discussed previously in section 4.3.2.2).

##### 4.3.3 Results

To test the utility of the outlined model, simulations are run for two cases: (i) flow past a tethered spherical drop and (ii) light deformation of a sedimenting drop. These two tests allow for the benchmarking of the developed model, by again checking compliance with kinematics and dynamics principles, through comparison against known solutions.

Simulations conducted are within Stokes's regime, which evidently introduces complications, due to the nature of multi-component lattice Boltzmann models (to be discussed), but based on prior work may be the most appropriate flow regime for this model. Here, a method which allows the microcurrent to be subtracted from the flow, to expose the physical flow field (phase-field freezing) is presented. (Such a step is only available within the linear Stokes's regime of course, where solutions to the governing equation are superposable). However, it is worth noting that the range of density contrasts simulated is much lower than that of prior work in this thesis.

#### 4. Extended cMCLBM for the Simulation of Drops within Stokes Flow

The density contrast is kept below  $\Lambda = 10$ , with the importance of this work being the model's ability to meet crucial boundary conditions, not the extent to which it can simulate large density contrasts.

##### Simulation set up

Returning to Figure 4.9, panel (B) represents the simulation set-up (not to scale), of the two-dimensional (pseudo three-dimensional) system representing the axial-symmetric three-dimensional system in panel (A). Here note, the discrete lattice simulation co-ordinates of  $x^* = 0, 1, \dots, 199$ ,  $z^* = 0, 1, \dots, 299$  correspond to the Cartesian co-ordinates in Figure 4.9 of  $x = 0.5, 1.5, \dots, 199.5$ ,  $z = 0, 1, \dots, 299$ . The reason for the offset of the origin of the drop in pseudo-Cartesian co-ordinates, by  $x = 0.5$ , is to avoid a potential singularity introduced by the continuity source/sink in Eq. (4.39). Periodic boundary conditions are applied at the North and South walls, i.e., simulating an infinitely long domain in the  $z$  direction. To reflect the symmetry of the system, a mid-link bounce back *slip* boundary condition is applied to the West wall (the so called specular reflection —discussed within section 2.3.4) and a mid-link bounce back no-slip condition was applied at the East wall, to represent a solid boundary. Viscosity within the simulations is defined as stated in the simulation data captions using the relationship to the MRT eigenvalue  $\lambda_3$  (as defined by Eq. (4.2)). To simulate the liquid drop (Red fluid) in the following flows, a buoyancy force is applied in the  $z$  direction  $U_0 \rho_R \hat{e}_z$ , where the factor  $(\rho_R)$  applies this force to the liquid drop (Red fluid) only. Note, the value of the buoyancy force magnitude  $U_0$  is sufficiently small to maintain the front back symmetry —required within pure Stokes's regime —with the value increasing slightly as we move away from pure viscous flow, to invoke deformation in the latter test.

##### 4.3.3.1 Flow past a tethered spherical drop

The first test of our model is flow past a tethered spherical liquid drop in Stokes's regime, which evaluates the model's capacity to recover correct kinematics, in particular, the kinematic property of mutual impenetrability assumed through the use of the kinetic scale segregation rule analysed in section 3.3.2.

By working within Stokes's regime, where viscous forces dominate, it follows that  $\text{Re} \approx 0$  and  $\text{Ca} \approx 0$ . The Reynolds (Re) and Capillary (Ca) numbers are defined as:

$$\text{Re} = \frac{uL}{\nu}, \quad \text{Ca} = \frac{\eta V}{\sigma}, \quad (4.58)$$

where,  $u$  = velocity of the fluid with respect to the object,  $L$  = characteristic length scale,  $\nu$  = kinematic viscosity,  $\eta$  = dynamic viscosity,  $V$  = characteristic velocity and

#### 4. *Extended cMCLBM for the Simulation of Drops within Stokes Flow*

$\sigma$  = interfacial tension. To work within the desired regime, the applied buoyancy force  $U_0$  is kept low and the surface tension  $\sigma$  large enough to reduce the Capillary number and, also, prevent deformation of the drop. An artefact of working in this regime is that the microcurrent within the model will become increasingly apparent, due to: (i) the small physical flow value and (ii) the large surface tension value used, which increases the amplitude of the microcurrent. Subsequently, this presents a problem which needs to be addressed if one wishes to evaluate the physical flow field which may be infected by the parasitic signal.

The simulation geometry is that described within the simulation set up, with simulation specific parameters given in the figure captions. To attempt to provide the most transparent data, the flow external to the drop will be masked, with only the internal flow being shown. Furthermore, the assumption of uniform kinematic viscosity across the system is used, meaning the shear viscosity can be related to the density contrast as follows:

$$\frac{\eta_B}{\eta_R} = \frac{\nu \rho_{0B}}{\nu \rho_{0R}} = \frac{1}{\Lambda}. \quad (4.59)$$

The following parameters were used for this simulation: interfacial parameter  $\beta = 0.67$ , buoyancy parameter  $U_0 = 8.0 \times 10^{-9}$ , Red drop radius  $R = 20$  and kinematic viscosity  $\nu = \frac{1}{6}$ .

##### **Removal of micro-current from flow**

Before proceeding, a method (named phase-field freezing hereafter) of extracting the rest frame physical flow field of the drop through Galilean transformation and subsequent microcurrent vector subtraction is presented. Phase-field freezing is necessary in order to remove the dominant error signal (microcurrent) from the flow, subsequently allowing comparison of the flow field against analytical solutions (presented shortly). This process is highlighted within Figure 4.11, where the external flow (Blue fluid) is neglected in the figure, with intent of focusing on the drop's internal flow (Red fluid).

The first step of the phase-field freezing involves transforming the drop into rest frame. This is done by running the simulation until the flow velocity has reached steady state —determined by a constant residual velocity—where in the simulation in question, the internal fluid (Red) is pushed through the external fluid by a small buoyancy force  $U_0 \rho_R \hat{e}_z$ . Once steady state is reached, the momentum of the drop is then subtracted via a Galilean transformation to the rest frame of the drop, applied to the direction of the flow, i.e., in this case the  $z$  component of velocity. To achieve this, the average velocity of the Red fluid was subtracted, which was computed through summing contributions from annular mass volume increments:

#### 4. Extended cMCLBM for the Simulation of Drops within Stokes Flow

$$v_z \rightarrow (v_z - \langle v_z \rangle), \quad (4.60)$$

where,

$$\langle v_z \rangle = \frac{\iint_{r,z} 2\pi\rho_R(r,z)v_z(r,z)rdrdz}{\iint_{r,z} 2\pi\rho_R(r,z)rdrdz} \rightarrow \frac{\sum_{x^*,z^*} x^* \rho_R(x^*,z^*)v_z(x^*,z^*)}{\sum_{x^*,z^*} x^* \rho_R(x^*,z^*)}, \quad (4.61)$$

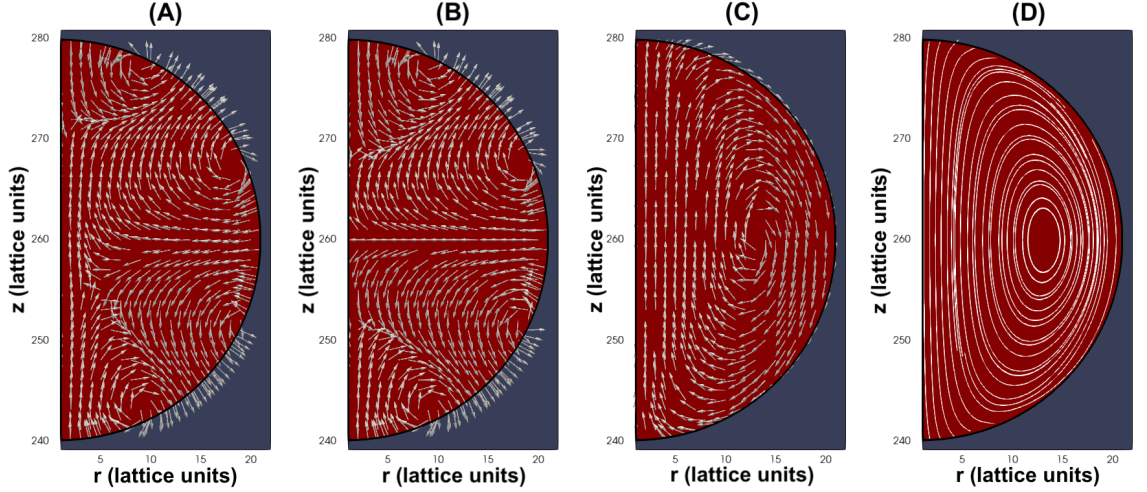
where Eq. (4.61) shows both spherical polar co-ordinates and the corresponding transformed computational co-ordinate system. This Galilean transformation shows how the simulation flow field was translated to the approximate rest frame of the drop and corresponds to the data shown within panel (A) of Figure 4.11. It is clear still that, in panel (A), the microcurrent dominates the flow signal.

To remove the microcurrent from the flow, it must first be computed for a precisely corresponding simulation. To do this, the buoyancy parameter  $U_0$ , is set to zero and the simulation evolved with no forcing, where the corresponding flow field for this simulation now represents the microcurrent signal for the flow simulated prior. Again, steady state for this simulation was verified by examining the residual velocity within the flow field. Panel (B) within Figure 4.11 displays the result of this which is the microcurrent signal corresponding to flow in panel (A). Finally, the microcurrent field, panel (B), is subtracted from the flow field, panel (A), to expose the physical flow field shown in panel (C) (vector field) and panel (D) (streamlines) of Figure 4.11.

The result of the phase-field freezing approach applied to flow past an effectively tethered drop, from initial inspection, is very encouraging. The rest frame flow field for the internal drop, post-Galilean transformation, shown in panel (A), is clearly dominated by the microcurrent signal—noting that there is flow perpendicular to the interface at the drop boundary (black line)—resulting in the physical flow not yet being distinguishable. Through vectorial subtraction of the microcurrent in panel (B) from the corresponding rest frame flow field in panel (A), it is possible to reveal the physical flow within Stokes’s regime [49], given in panels (C) and (D). The impact here is clear, with the physical flow in the rest frame now presented by a vector field and computed flow streamlines in panels (C) and (D), in which flow is now apparently parallel to the interface. This highlights compliance with the principle kinematical interface conditions of mutual impenetrability and no-slip condition perhaps more strikingly than in preceding chapters. Apparently, the phase-field freezing method provides a viable way of extracting the physical flow when working in the challenging Stokes’s regime which has increased microcurrent impact. However, this result needs to be validated against data in order to confidently validate both the developed cMCLBM and the phase-field freezing approach.



#### 4. Extended cMCLBM for the Simulation of Drops within Stokes Flow



**Figure 4.11:** Data showing the process of the phase-field freezing method for simulation of flow past an effectively tethered drop. Panel (A) shows the rest frame of the drop's internal flow field —computed using Galilean transformation given in Eq. (4.61). Panel (B) shows the internal steady state microcurrent corresponding to the flow in panel (A). Panels (C) and (D) show the physical flow vector field and streamlines found by subtracting (B) from (A). Simulation parameters are as follows:  $x^* = [0, 199]$ ,  $z^* = [0, 299]$ ,  $\nu = \frac{1}{3}$ ,  $\beta = 0.67$ ,  $R^* = 20$ ,  $G_0 = 8 \times 10^{-9}$ ,  $\text{Re} = \frac{\leq u_z > R}{\nu} < 3.0 \times 10^{-4}$ . Red fluid is the drop and Blue fluid is the external fluid [135].

#### Analytical comparison

Following from the results of the phase-field freezing approach to removing the microcurrent to reveal the internal flow field of the Red drop, the accuracy of the result must be determined through comparison with theory. Analytical calculations in [141, 142, 143] align with this work, with reference to kinematic and dynamic boundary conditions. Here, low Reynolds number flow past an axial-symmetric sphere is considered, such that the flow pattern is symmetric front to back. There is no explicit reference to interfacial tension within the theory—which does not effect this current work examining an undeformed drop—although it is assumed to be large enough to prevent deformation. In spherical co-ordinates, the velocity field is given by the following equation, where the origin is taken as the drop centre [143]:

$$v_r^s = \cos(\theta) \left( \frac{\Lambda}{1 + \Lambda} \right) \frac{U_0}{2} \left( 1 - \frac{r_s^2}{R^2} \right), \quad (4.62a)$$

$$v_\theta^s = \sin(\theta) \left( \frac{\Lambda}{1 + \Lambda} \right) \frac{U_0}{2} \left( 1 - \frac{2r_s^2}{R^2} \right), \quad (4.62b)$$

$$v_\phi^s = 0, \quad (4.62c)$$

where it follows that  $U_0 \hat{e}_z$  is the constant speed of the external flow (Blue fluid), at a large distance from the spherical drop (Red fluid),  $r_s = \sqrt{r^2 + z^2}$  is the spherical

#### 4. *Extended cMCLBM for the Simulation of Drops within Stokes Flow*

polar distance from the origin. Here, the stagnation point, which corresponds to the centre of the internal vortex of the velocity field, is always located at:

$$\text{stagnation point:} \quad r_s = \frac{R}{\sqrt{2}}, \quad \theta = \frac{\pi}{2} \quad \longrightarrow \quad x = \frac{R}{\sqrt{2}}, \quad z = 0. \quad (4.63)$$

Equation. (4.63) shows the stagnation point in both a spherical polar co-ordinate system and equivalent Cartesian system. Interestingly, the stagnation point location has no dependence on the density contrast between the two fluids, meaning it should remain fixed in space, for all simulations conducted within this test.

#### **Simulation data**

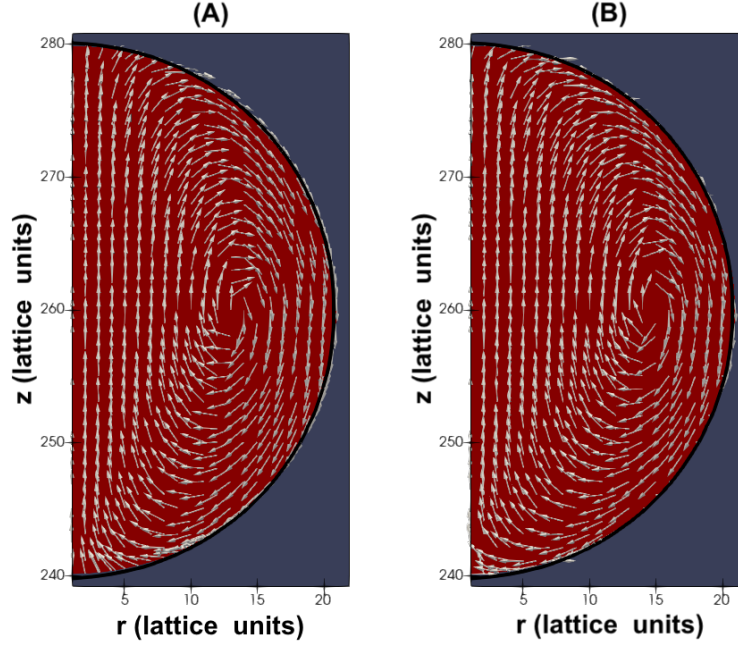
The following results are intended to benchmark and validate our model by using the test of flow past a tethered spherical drop, i.e., compare the results to theory. This process amounts to using the phase-field freezing approach to remove the microcurrent from the velocity field to expose the physical flow, and then comparing the resultant simulation data against the analytical result outlined in Eqs. (4.62a, 4.62b, 4.62c). Figure 4.12 shows the comparison of simulation data for the flow field panel (A), with analytical solution for the flow field panel (B), where a density contrast of  $\Lambda = 5$  is used (with remaining parameters listed in the figure caption):

Figure 4.12 shows that the simulation data compare well with that of the analytical solution for the drop's internal flow field, for the test of flow past a spherical liquid drop. This is evidenced by both panels having similar flow profiles, as well as the location of the stagnation point —the centre of the drop's internal vortex having the correct location. In addition, the operation of kinematic interfacial boundary conditions of mutual impenetrability and no-traction (or no-slip) condition is clearly confirmed, with flow being tangent to the interface around the perimeter of the liquid drop. These data further highlight compliance of the developed methodology with these physical boundary conditions. This qualitative result however contains no evidence with regards to the accuracy of the flow velocity magnitude, at each lattice site within the drop, with the vector plots having no relative scaling.

In order to provide quantitative data of how accurate the flow velocity is within the drop, a complimentary figure to Figure 4.12 is presented. Figure 4.13 compares the velocity field components that were given by analytical solution and theory in Eqs. (4.62a, 4.62b, 4.62c), with that of simulation data from the result of panel (A) of Figure 4.12. The panels in Figure 4.13 show comparison of simulation data and theory for:

- (A) Spherical polar tangential velocity, measured along the equator from spherical drop center.

#### 4. Extended cMCLBM for the Simulation of Drops within Stokes Flow



**Figure 4.12:** Comparison of the drop flow field between simulation data (A) and an analytical solution (B) for flow pushed past an effectively tethered spherical drop. The result within panel (B) corresponds to the analytical solution displayed in Eqs. (4.62a, 4.62b, 4.62c), which has been translated appropriately in the  $z$ -axis to allow for comparison. The result in panel (A) shows the microcurrent adjusted simulation data. The solid black line shows the phase field  $\rho^N = 0$ . The parameters for these data are as follows:  $R = 20$ ,  $x \in [0.5, 199.5]$ ,  $z \in [0, 299]$ ,  $\beta = 0.67$ ,  $G_0 = 8.0 \times 10^{-9}$  and  $\nu = \frac{1}{6}$  [135].

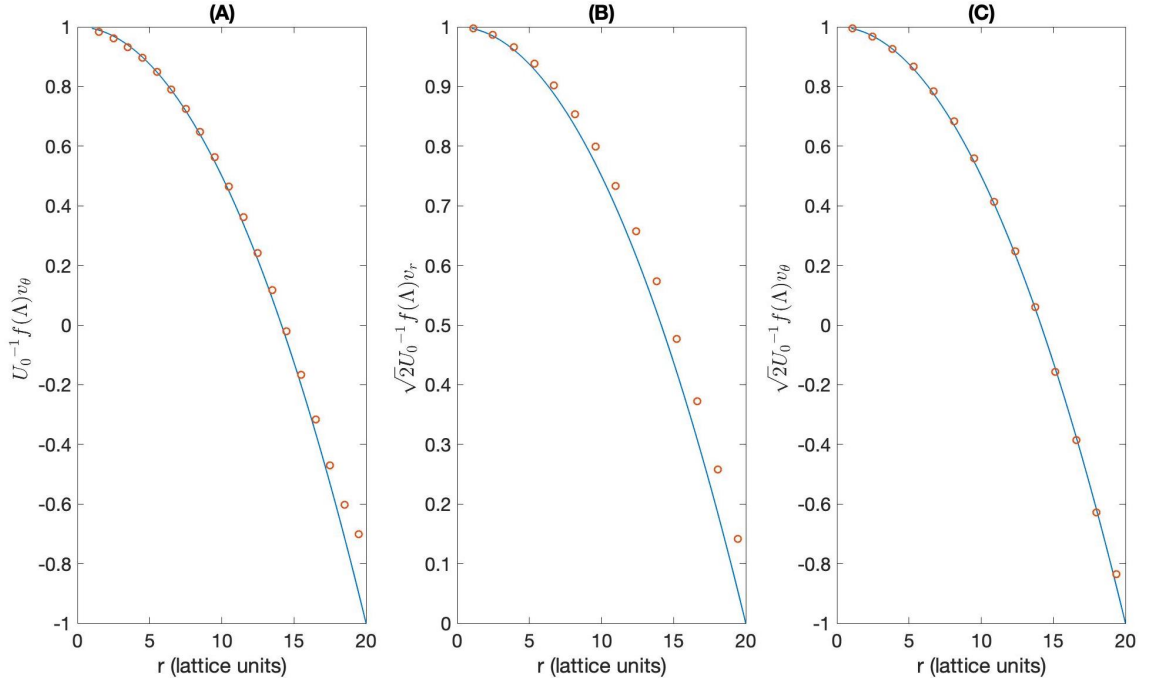
(B) Spherical polar radial velocity, measured along a line located at angle  $\frac{\pi}{4}$  from spherical drop center.

(C) Spherical polar tangential velocity, measured along a line located at angle  $\frac{\pi}{4}$  from spherical drop center.

To allow a more transparent, quantitative, comparison of theory against simulation data, the velocity components are normalised against flow velocity  $U_0$  and a factor of  $f(\Lambda) = \frac{1+\Lambda}{\Lambda}$  is used to scale the results:

Starting with the the velocity field for an equatorial section, panel (A) of Figure 4.13 shows a correct velocity profile, with tangential flow at the origin (having normalised magnitude of 1) and the flow close to the perimeter (i.e.  $r \rightarrow R$ ) tending towards  $(0, 0, -1)$ , the flow being in the opposing direction to the origin. It is also seen that the stagnation point (when  $v_\theta^s = 0$ ) is very close to that of the predicted location. Furthermore, it was found that the radial component of flow was zero at all location across the equatorial slice, i.e.  $v_r^s = 0$  —as expected. With  $v(R)_r^s = 0$  required to comply with the kinematical condition of mutual impenetrability if the drop is not translating or expanding. Panels (B) and (C) show the radial and

#### 4. Extended cMCLBM for the Simulation of Drops within Stokes Flow



**Figure 4.13:** Accompanying velocity field data to Fig. (4.12). In all panels the continuous black line corresponds to theory, and scatter points to simulation data. Panel (A) shows comparison of the spherical polar radial velocity Eq. (4.62b), measured along the equator from spherical drop center. Panel (B) shows comparison of the spherical polar radial velocity Eq. (4.62a), measured along a line located at angle  $\frac{\pi}{4}$  from spherical drop center. Panel (C) follows panel (B) but measures the tangential component of velocity [135].

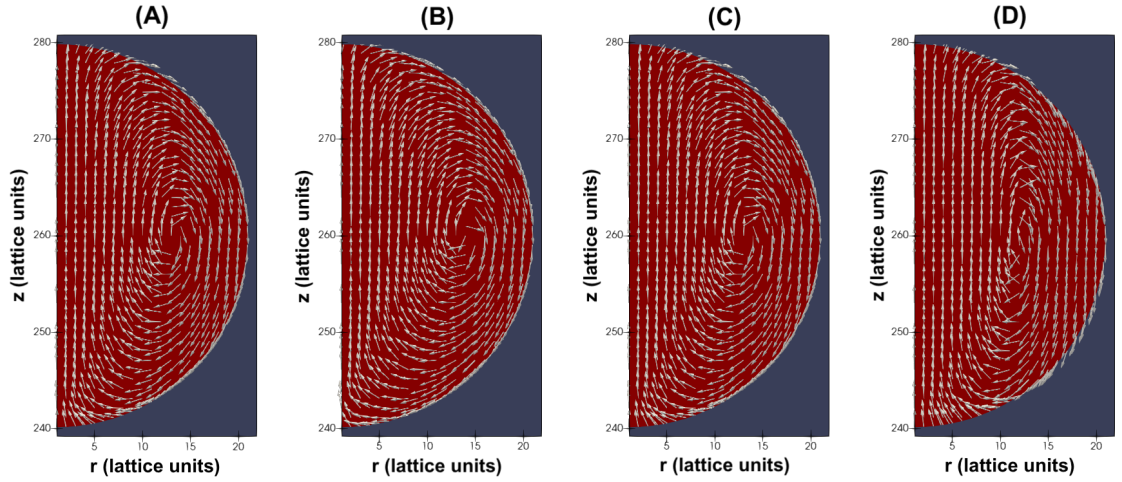
tangential components of velocity along a line taken at an angle of  $\theta = \pi/4$ , where the profiles have been multiplied by a factor of  $\sqrt{2}$  to normalise the plots. The profiles are as expected, with the radial component of velocity (panel (B)) being largest close to the origin, and zero at the interface —required for the mutual impenetrability condition. The tangential component of velocity (panel (C)) shows that the velocity is largest and positive close to the origin of the drop, and has a negative tangential velocity towards the perimeter of the drop —as expected.

Across all panels, the simulation data correspond very well with theory. It is also clear that the accuracy of the data becomes weaker as  $r \rightarrow R$ , due to the continuous interface which is somewhat diffused. However, even with the diffused nature of MCLBM interfaces, the magnitude and direction of the flow align favourably with a sensible interpretation of the relevant continuum no-traction and kinematic conditions.

Following confirmation of drop flow field profile in Figure 4.12 and, subsequently, quantitative confirmation of normalised velocity values for the tangential and radial components over the drop in Figure 4.13, a range of density ratios are now tested, to

#### 4. *Extended cMCLBM for the Simulation of Drops within Stokes Flow*

evaluate the ability of the model to meet the correct physical kinematic boundary condition at varying density contrasts. Data shown in Figure 4.14 show the internal flow of the spherical drop (Red fluid) after the corresponding microcurrent has been subtracted, using the phase-field freezing method, for density ratios  $\Lambda = 1, 3, 5, 7.5$  corresponding to panels (A,B,C,D), where for all data the flows have  $Re < 2 \times 10^{-4}$ .



**Figure 4.14:** Simulation data of the un-scaled internal flow field for varying density ratios of flow pushed past a spherical liquid drop, where the density ratio in panels (A),(B),(C),(D) are  $\Lambda = 1, 3, 5, 7.5$ . Data correspond to post application of phase-field freezing —translation to the rest frame and removal of microcurrent. All flows here are of  $Re < 2 \times 10^{-4}$  [135].

Figure 4.14 provides validation of the model, through confirmation that the stagnation point of the internal drop compares well with that of theory and does not change position as  $\Lambda$  varies, from inspection. Once again, returning to the compliance of the model with the kinematic condition of mutual impenetrability, which is apparent, now, at varying density contrasts with flow being tangent to the interface at relevant points. This point will be returned to later in the conclusion of this chapter. In addition, the clarity of the data at larger density ratios becomes more difficult to interpret, due to the stability of the method and the increased microcurrent signal as the density contrast increases.

From the results in this section, for flow past a tethered spherical drop at low Reynolds and Capillary numbers, we see very favourable results. Clearly, these data correspond to a undeformed drop. A more representative, practical test of the model would be of the drop under some level of shear-induced deformation.

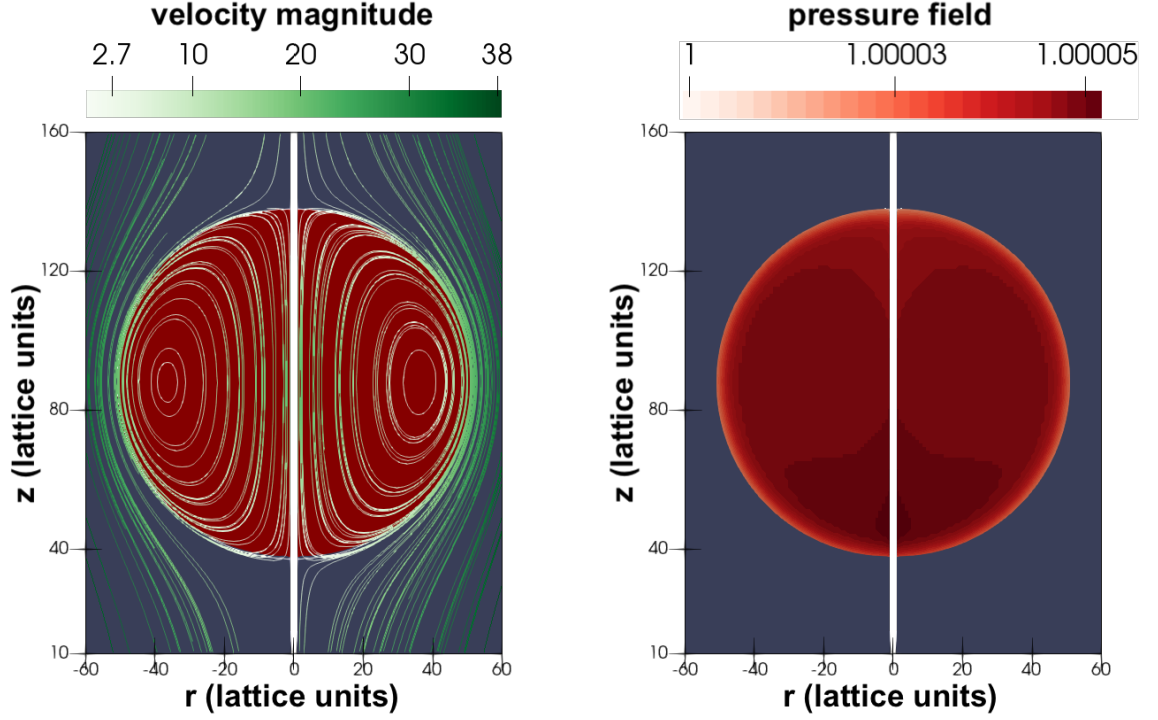
##### 4.3.3.2 Flow induced deformation of a sedimenting drop

So far, the developed method has been tested for a spherical liquid drop. Here, the model is examined when a small level of deformation is seen —still assuming, for practical purposes, a low Reynolds number approximation. Here we consider flow

#### 4. Extended cMCLBM for the Simulation of Drops within Stokes Flow

past an effectively tethered, slightly deformed liquid drop—in essence, a liquid drop sedimenting (falling) vertically, at a speed consistent with the low Reynolds number regime, which results in small levels of deformation to the liquid drop.

To further explain this test, see Figures 4.15 and 4.16, where data are presented as a meridonal plane—in which the lattice has been reflected about the  $z$ -axis to show a full slice of the still-axial-symmetric three-dimensional drop under simulation.

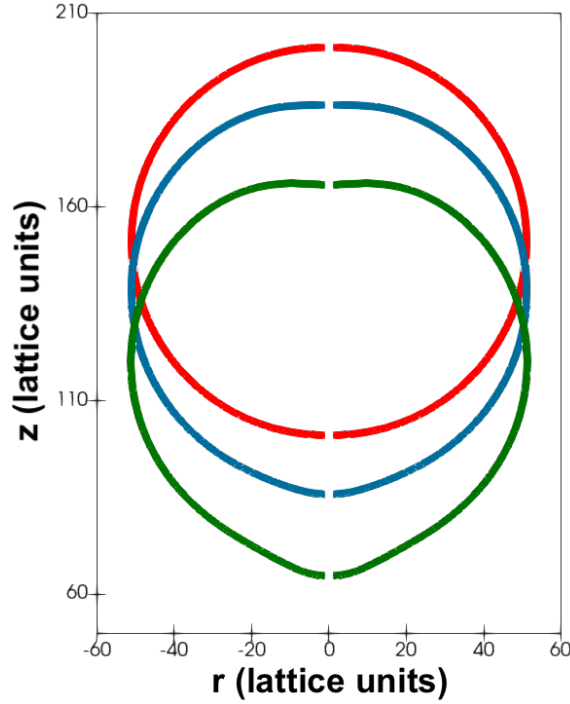


**Figure 4.15:** Both panels show a lightly deformed drop sedimenting vertically downward. Left panel shows Stokes’s stream-function over the domain, where colour corresponds to velocity magnitude (with non-dimensional units scaled). Right panel shows the pressure field, in lattice units. Note, domain reflected in the  $z$ -axis for the schematic, where the drop contour is taken at the  $\rho^N = 0$  contour. The parameter set for these data are:  $\beta = 0.3$ ,  $\Lambda = 1$ ,  $R = 50$ ,  $x^* = 0.5, 1.5, \dots, 300$ ,  $z^* = 0, 1, \dots, 400$ ,  $\nu = \frac{1}{6} = \text{constant}$  [135].

Figure 4.16 shows the time evolution of the sedimenting liquid drop at increasing time steps  $t = 0, 25000, 50000$  (Red, Blue, Green contours), when a buoyancy force  $U_0 \rho_R \hat{e}_z = -5 \times 10^{-7}$  is applied to the drop (Red fluid)—note the increase in force magnitude compared to the spherical drop case. As the drop sediments in the negative  $z$ -direction overtime, the liquid drop is deformed due to drag of the external fluid. Accompanying figure, Figure 4.15 (Left) shows the velocity magnitude field over the lattice and (Right) internal pressure field within the liquid drop, both taken in the meridonal plane at a time step where minimal deformation has occurred. Results from Figures 4.15 and 4.16 provide good initial evidence of correct kinematics and dynamics, with the velocity streamlines of the drop’s internal fluid showing correct



#### 4. Extended cMCLBM for the Simulation of Drops within Stokes Flow



**Figure 4.16:** Data showing time evolution of a sedimenting liquid drop in low Reynolds number regime, which is surrounded by an external quiescent fluid —where data are shown by a meridional section. The figure shows the drop surface ( $\rho^N = 0$  contour) at increasing lattice time steps  $t = 0, 250000, 500000$  (Red, Blue, Green lines), with the Green contour representing the steady state result. Here, simulation parameters are as follows:  $\Lambda = 5$ ,  $\beta = 0.3$ ,  $R^* = 50$ ,  $x^* = 0, 1, \dots, 600$ ,  $z^* = 0, 1, \dots, 400$ ,  $\sigma = 6.0 \times 10^{-4}$ ,  $We \leq 2.0 \times 10^{-2}$  and  $Re < 0.1$  [135].

circulation, with external streamlines moving around the perimeter of the drop. This flow can then be seen in Figure 4.16 to cause appropriate levels of deformation within the simulated regime, providing qualitative evidence of correct behaviour consistent with understanding. The next logical step would be to seek a method of quantifying the accuracy of the developed methodology for simulating this flow, although doing this for a deforming drop presents further challenges.

#### Analytical Solution

To confirm that the developed model does produce correct hydrodynamics and flow field for flow past a slightly deforming drop through quantitative analysis, the existing analytical solution for this problem, developed by Taylor and Acrivos [144], is considered. Note at this point, that this solution is harder to interpret than that previously explored for flow past a spherical drop, as discussed below.

Taylor and Acrivos found a solution to a drop under low Reynolds number motion within an unbounded, motionless external fluid at rest. Their perturbation solution predicted drop shape under light deformation, due to drag —where they considered

#### 4. Extended cMCLBM for the Simulation of Drops within Stokes Flow

an axial-symmetric system. Here, in simulation, equal kinematic viscosity is used. Applying this constraint, the deformed drop radius at spherical polar zenith angle  $\theta$  (using equation (30) derived from reference [144]) is given as:

$$\frac{R(\theta)}{R} = 1 - a_2 P_2(\cos(\theta)) - a_3 P_3(\cos(\theta)) + \dots, \quad (4.64)$$

with expansion co-efficients as follows [144]:

$$a_2 = \lambda \text{We}, \quad a_3 = \frac{3\lambda(11\Lambda + 10)}{70(\Lambda + 1)} \frac{\text{We}^2}{\text{Re}}, \quad (4.65)$$

where  $P_2(x)$  etc. is the second order Legendre polynomial [140] and  $\lambda$  is given as:

$$\lambda = \frac{1}{4(\Lambda + 1)^3} \left[ \frac{81}{80} \Lambda^3 + \frac{83}{30} \Lambda^2 + \frac{103}{40} \Lambda + \frac{5}{6} \right]. \quad (4.66)$$

Above,  $\lambda$  is independent of that used elsewhere, in chapters dealing with the MRT scheme, where it denotes collision matrix eigenvalues. No confusion should arise from this and we deem it sensible to use established notation within the present context.

The result in Eq. (4.64) provides a solution in which our model can be benchmarked against, when looking at comparing data with the predicted shape (level of deformation), for an axial-symmetric liquid drop deformed in low Reynolds number flow.

#### Simulation Data

Here, we perform limited benchmarking of the model against the analytical solution for shape profile of the axial-symmetric liquid drop deformed in low Reynolds number flow, using simulation data. Before proceeding, one must compute the location of the drop perimeter  $R(\theta)$  at angle  $\theta$  in Eq. (4.64) in terms of discrete simulation values  $R^*$  and  $(\theta^*)$ , as well as expressing the Weber (We) and Reynolds (Re) numbers required in Eq. (4.64). Within simulation, these numbers were computed as follows:

$$\text{We} = \frac{\rho_B \langle v_z \rangle^2}{\Delta p}, \quad \text{Re} = \frac{R \langle v_z \rangle}{\nu}, \quad (4.67)$$

where  $\Delta p$  is the measured pressure step across the drop interface. The pressure can be calculated from the first term in the expression of the zeroth order momentum flux tensor shown by Eq. (3.16).

To calculate the centre of mass of the liquid drop as it sediments in the negative  $z$ -direction, the following definition was used (expressed in spherical polars and computational co-ordinate system):

$$\langle z \rangle = \frac{\iint_{rz} 2\pi z \rho_R(r, z) r dr dz}{\iint_{rz} 2\pi \rho_R(r, z) r dr dz} \longrightarrow \frac{\sum_{x^*, z^*} x^* \rho_R(x^*, z^*) z^*}{\sum_{x^*, z^*} x^* \rho_R(x^*, z^*)}. \quad (4.68)$$



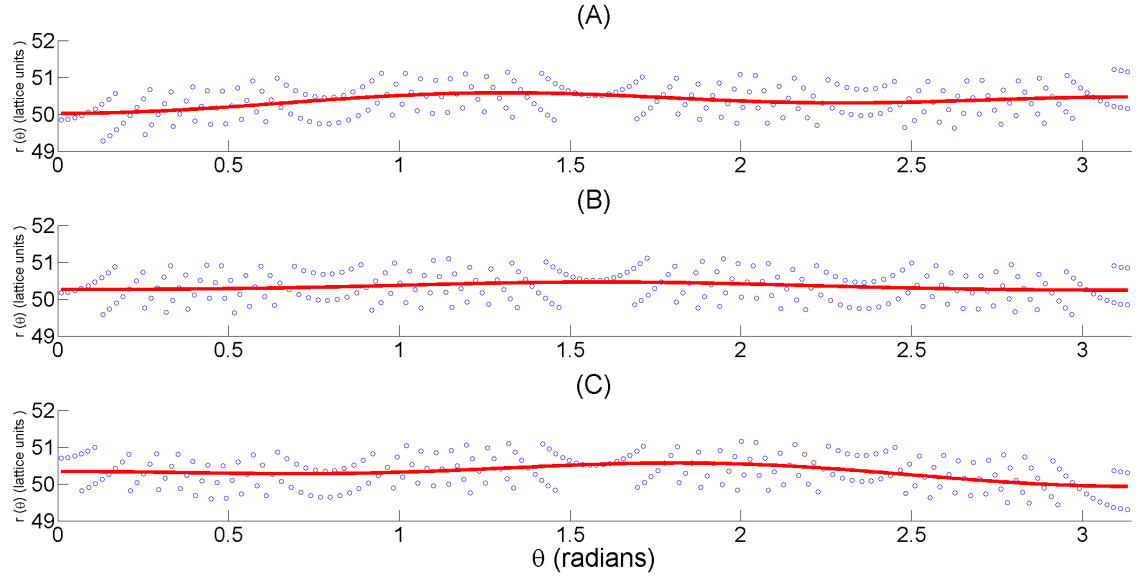
#### 4. Extended cMCLBM for the Simulation of Drops within Stokes Flow

This value could also be used to fit to Eq. (4.64). The drop surface was defined by seeking points in the interface range  $\rho^N \in [-0.2, 0.2]$ , as  $\rho^N = 0$  may not necessarily be represented by a discrete point  $(x^*, z^*)$ . From this, the radial distance and zenithal angle were computed as follows:

$$R(\theta^*) = \left( (x^* + 0.5)^2 + (z^* - \langle z \rangle)^2 \right)^{1/2}, \quad (4.69a)$$

$$\theta^* = \cos^{-1} \left( \frac{z^* - \langle z \rangle}{R^*} \right). \quad (4.69b)$$

The analytical solution for the deformed drop profile in Eq. (4.64) is now to be compared against the calculated drop profile from simulation given by Eqs. (4.69a, 4.69b). Here, the scenario of a sedimenting drop was tested for three density ratios  $\Lambda = (0.5, 1.0, 2.0)$ . The results of shape profile at steady state from these simulations are shown in Figure 4.17, where scatter points correspond to interface points in the range  $\rho^N \in [-0.2, 0.2]$ :



**Figure 4.17:** Data showing accuracy of simulating a slightly deformed drop by comparing interface data (scatter) calculated by Eqs. (4.69a, 4.69b) and perturbation calculation shown in Eq. (4.64) (red line) for predicted drop profile. Panel (A) is for density ratio  $\Lambda = 0.5$ , panel (B)  $\Lambda = 1.0$  and panel (C)  $\Lambda = 2.0$ . The parameters for these data are:  $\beta = 0.3$ ,  $R^* = 50$ ,  $x^* = 0, 1, \dots, 600$ ,  $z^* = 0, 1, \dots, 400$ ,  $\sigma = 6.0 \times 10^{-4}$ ,  $We \approx 2.0 \times 10^{-2}$  and  $Re \approx 0.01$  for all simulations [135].

Figure 4.17 shows encouraging correspondence with theory in general, with simulation data appearing to follow a similar trend to that of theory. Due to the distributed nature of the interface within multi-component lattice Boltzmann models, the data are harder to interpret, as it introduces a larger spread of data points within the interfacial region. However, this provides quantitative confirmation that the

correct drop profile can be appropriately recovered in simulation for an effectively axially-symmetric three-dimensional liquid drop deforming in low Reynolds number flow. The result strongly implies operation of correct dynamic boundary condition (of stress-transmission across the interface—which is clearly central to producing an appropriate shape—caused by the drag on the drop as it sediments). The data, however, do not show the instantaneous transmission of stress, as in previous tests conducted with the 2D MRT-model, and, also, it is clearly limited to small density contrasts, with the largest density ratio shown being of magnitude 2.

## 4.4 Concluding Remarks

Within this chapter, the BGK cMCLBM developed and presented in Chapter 3 has been extended by replacing the BGK collision operator with an MRT collision operator, as well as extending to the simulation of three-dimensional axially-symmetric fluid flows. The justification for introducing the MRT collision operator stems from the desire for increased stability in the face of more complicated forcing, which the MRT is accepted to offer in comparison the BGK scheme, due to the increased tuneability reposing in additional degrees of kinetic freedom. Clearly, then, this last step is not a unique extension; a majority of multi-component lattice Boltzmann models opt for more sophisticated collision operators such as MRT and cascade-MRT for stability gains—the former being chosen due to the increased complexity in cascade-MRT schemes. Following this, our particular MRT cMCLBM was extended to the simulation of three-dimensional axial-symmetric flows, which increases applicability of the method by being able to capture three-dimensional fluid dynamics but, crucially, brings complex but intuitively clear validation of the interfacial boundary conditions so much at issue in this work within scope of stringent validation. Put another way, the ability to simulate axial-symmetric three-dimensional flows means that a two-dimensional model can be conveniently used to simulate the flow, leveraging computational gains to observe the operation of boundary physics. Additionally, the model’s handling of geometrical forcing imparts, furthers the understanding of the ability of LB models to handle continuity flow sources and sinks, as well as the inclusion of velocity dependent forces.

The aim of this work was to analyse the fundamentals of our model—its compliance with principle kinematics and dynamics. Starting with the two-dimensional MRT-model outlined in section 4.2, it was found that there is very little difference between the resultant kinematics and dynamics in comparison to the BGK-model, apart from the change in collision parameters present in the source terms needed to recover

#### 4. *Extended cMCLBM for the Simulation of Drops within Stokes Flow*

correct dynamics. To assess the model's kinematics and dynamics, a flat interface was first tested. Here, both steady state and dynamical tests investigated compliance with interface kinematics and dynamics by shearing the fluid tangent to the interface and comparing against developed analytical solutions (tests in sections 4.2.3.2 and 4.2.3.3). The results here were that the model showed compliance with: (i) the kinematical interface conditions —with flow being continuous across the interface, and (ii) compliance with the dynamical boundary conditions —by showing instantaneous stress transmission across the interface through transient data showing fluid dragging in the test in section 4.2.3.3. Here, density ratios showed good agreement with analytical solutions for density contrasts of up to around  $\Lambda \approx 50$ . Next looking at curved interfaces, the test in section 4.2.3.4 investigated transient rotational flow by shearing the fluids tangent to their interface. The results of this test again showed compliance with both kinematical and dynamical boundary conditions, with instantaneous stress-transmission (dynamics) present. However, there was seen to be a loss in the achievable density contrast, with results showing best compliance up to density ratios around  $\Lambda = 5$ . These data support findings from Chapter 3, in that there are stability issues, which become prominent at larger density contrasts, in rapid flow and also when a curved interface is present.

From these findings, the most appropriate application of the our essential model must be the simulation of liquid-liquid interfaces at low Reynolds number, where flow velocities are low. From this, section 4.3 targeted the simulation of three-dimensional axial-symmetric fluid flows within Stokes's regime (where  $\text{Re} \rightarrow 0$ ,  $\text{We} \rightarrow 0$ ), with low density ratios between the fluids. To develop this model, the Navier-Stokes equations in cylindrical polar co-ordinates were decomposed under the assumption of axial symmetry, resulting in a spatially reduced system. The MRT-model from section 4.2 was then adjusted to recover the correct dynamics of a three-dimensional axially-symmetric system, by developing velocity dependent geometrical forces together with a continuity source/sink. The outcome was a pseudo three-dimensional model, capable of simulating axial-symmetric three-dimensional fluid flows. When working within Stokes's regime using cMCLBM, the microcurrent level dominates the physical flow field, prompting our development of a method (phase-field freezing) which removes the microcurrent, to reveal the physical flow. This approach was then used intuitively to validate the model's kinematics and dynamics in two well documented test scenarios: (i) flow past a spherical drop and (ii) flow past a deforming drop. In test (i), data were compared against an existing analytical solution for the velocity field, showing correct kinematics —with flow being tangent to the interface at all relevant points and well-aligned with the analytical

#### 4. *Extended cMCLBM for the Simulation of Drops within Stokes Flow*

solution. Again in test (ii), simulation data were compared against an analytical prediction of the deformed drop shape, with data (although harder to interpret due to the diffused interface of the method), providing good conformation of correct dynamics, i.e., the flow stresses deforming the drop appropriately. However, we found, again, the achievable density contrast was much reduced relative to flat interfaces, with the modest maximum density contrast found to be around  $\Lambda = 10$ .

The overall material -deliverable- outcome of the work in this chapter is the development of an MRT cMCLBM method capable of simulating axially-symmetric three-dimensional flows with a density contrast. However, the operation of this model has furnished possibly our most significant results which confirm -very visibly- the fundamental compliance with known, target interface kinematics and dynamics conditions, facilitated through comparison with theory across many tests. Similar to other cMCLBMs, the achievable density contrast is not as high as reported in other models (such as the Shan-Chen and Free-Energy models), which report simulations of buoyancy-driven flow of drops with density contrasts of up to order  $O(1000)$  [99, 100, 145]. Our method, however, leverages separate advantages such as ease of control over interface width and surface tension, ability to simulate large viscosity contrasts and strict mass conservation. It must be repeated that if one wishes to simulate larger density ratios using our model, the flow regime should be restricted to Stokes's flow.

Extrapolating from the outcomes of this chapter, future work should consider tackling stability issues surrounding the simulation of larger density contrasts. This requires addressing the advection error, arising in the kinematics and dynamics coupling, as well as general stability issues, introduced by using an athermal equation of state —where, at larger density contrasts, compressibility effects can start to become apparent. Very recently, Lafarge et al. (2021) [146] presented an improved colour-gradient method for the modelling of two-phase flows. These authors introduce an arbitrary equation of state, to address the stability issues stemming from the use of the athermal equation of state. In addition, a correction term was also inserted as a forcing term to improve stability. The outcome of this is enhanced stability at larger density ratios in comparison to the chromodynamic model presented in this chapter, by tackling the stability issues which are also evident in our model. Their work represents the next step in the present workflow, moving towards the simulation of liquid-gas flows using cMCLBM.

Another avenue for future investigation would be to use the enhanced understanding of the class of cMCLBMs to apply the model to fluid flows where density

#### *4. Extended cMCLBM for the Simulation of Drops within Stokes Flow*

contrasts are minimal, reliable (correct) model kinematics and dynamics is essential and analytical tractability and transparency is desired. Such an application is the content of the next chapter, where it will be seen that, indeed, the transparency and reliability of the fluid segregation step is, perhaps, the central requirement. Before proceeding, however, we remark that the fertile application of the next chapter is not the only home for the cMCLBE vehicle developed so far. For instance, it was reported by Liu et al. that viscosity contrast limitations are present within the Free-energy models (with a maximum viscosity contrast of 8) [147]; accordingly, important viscosity contrasts flows may be more suitable targets for the use of cMCLBMs. In addition, the knowledge we have so far gained in this chapter on the kinematics, treatment of velocity coupling and microcurrent elimination could also have wider implications in the development of models to be applied in biomedical science.

Setting our sights on the application of the next chapter, mammalian red blood cells can be considered (within the continuum limit approximation) as an internal immiscible incompressible fluid (cell cytoplasm), surrounded by an external immiscible fluid (blood plasma), with there only being a minimal density difference between the separated fluids. Here, the control over interface width, application of immersed forces (using methods such as Guo forcing [70]) and correct kinematics and dynamics must all be present before extensions targeting enhanced interface -membrane- physics should be considered. As such, directed and re-assured by the findings documented throughout preceding chapters, this thesis's workflow shifts towards the development and application of our essential method towards the simulation of fluid-filled vesicles, with particular focus on a biologically significant entity - the human erythrocyte or red blood cell.

# 5

## The Simulation of Fluid-Filled Vesicles using cMCLBM

### Contents

---

<b>5.1</b>	<b>Background and Motivation . . . . .</b>	<b>123</b>
5.1.1	Vesicle Physics . . . . .	123
5.1.2	Existing Methods . . . . .	125
5.1.3	Chromodynamic MCLBM approach . . . . .	127
<b>5.2</b>	<b>Extension of Methodology . . . . .</b>	<b>130</b>
5.2.1	Immersed Boundary Force . . . . .	130
5.2.2	Force Characterisation . . . . .	138
5.2.3	Computation of Membrane Forces . . . . .	141
5.2.4	Multiple Vesicles . . . . .	147
<b>5.3</b>	<b>Results . . . . .</b>	<b>148</b>
5.3.1	Steady State Equilibrium Data . . . . .	150
5.3.2	Dynamics . . . . .	159
5.3.3	Simulation of Multiple Vesicles . . . . .	165
<b>5.4</b>	<b>Concluding Remarks . . . . .</b>	<b>169</b>

---

In this chapter, understanding, methodology and critique of previous chapters' content are utilised to develop, then verify and, to a limited extent, validate a further extended cMCLBM model. The extensions presented focus on, in what previous chapters show is its most promising area of application, the low density contrast regime and, while retaining the essential kinematics, the model dynamics is substantially extended, to facilitate the simulation of vesicles. The work in Chapter 3 developed and analysed a chromodynamic MCLBM for simulating immiscible fluid flows with a density contrast, studying compliance with fundamental model kinematics and

## 5. *The Simulation of Fluid-Filled Vesicles using cMCLBM*

dynamics. Chapter 4 then extended this work, by incorporating an MRT collision scheme and applying it to simulating axially-symmetric three-dimensional flows within Stokes' regime. The salient conclusion of the work in these chapters was the assurance that the errors introduced within the model, due to the kinematics and dynamics coupling, reduced the applicability of the model (in its current form) to flows with low density contrasts, that said, it showed good compliance with kinematical and dynamical conditions at density contrasts of unity —with higher stability, due to the absence of error from simulating density contrasts.

Guided by an enhanced understanding of the model's kinematics and dynamics coupling, a cMCLBM will be developed, for simulating vesicles —with intent of parameterising the vesicles for RBC behaviour. The assumption of unit density contrast is used —which is fully consistent with RBCs —and an MRT collision scheme, similar to the one within Chapter 4, is implemented to enhance stability in the face of increased algorithmic complexity. The strengths of the cMCLBM: interface control, parameter tunability, controlled address of immiscibility, mass conservation and ease of immersed boundary force coupling, are all utilised in this Chapter; the result is an attractive model for simulating vesicles. The core methodology resembles that of Chapter 3 (with the removal of density contrasts between the fluids, i.e., effectively setting  $\rho_{0R} = \rho_{0B}$  and  $\phi_i = t_i$ ), as does the inclusion of an MRT collision scheme (Chapter 4). The principal methodological enhancement of this chapter relates to the immersed boundary force, which now does not only need to enforce surface tension effects; it also forces more complex behaviour, consistent with vesicle membranes. Therefore, this chapter has a significant focus on this immersed boundary force, providing detailed explanation of the extensions to the previously outlined methodology. All simulation data work towards providing an initial validation of the model, aiming to justify its development and its relation to current models within the field.

## 5.1 Background and Motivation

### 5.1.1 Vesicle Physics

This chapter focuses on the simulation of vesicles tailored towards human RBCs, in which the developed foundations of the model are outlined and discussed in detail. It is key to explain RBC physics and how this relates to the mechanics of a vesicle, as it is these effects which researchers are trying to capture in all models that aim to simulate vesicles such as RBCs.

## 5. The Simulation of Fluid-Filled Vesicles using *cMCLBM*

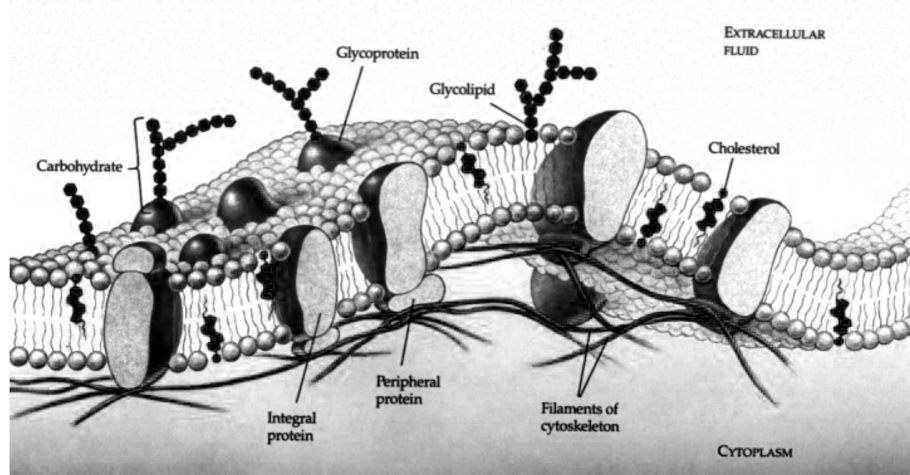
In a mechanical equilibrium, a RBC assumes a biconcave (bicuspid) shape, being approximately  $6\text{-}8\mu\text{m}$  in diameter and having a maximum thickness of  $2\mu\text{m}$  [148]. It consists of a structured, external membrane, enclosing a viscous, effectively incompressible fluid (cytoplasm) [149]. Micro-structurally, the two key components of its membrane are a phospholipid bi-layer, and protein strands, which form a “skeleton”, interlinking a set of anchoring points, within the bilayer. Figure 5.1 displays a schematic representation of a RBCs membrane structure, taken from [150], which highlights these components as well as the protein channels within the lipid bilayer. The membrane is incompressible, resisting changes in its surface area, with the bilayer also imparting bending elasticity to the membrane elasticity [151]. The thickness of the bilayer and cytoskeleton is approximately  $10\text{nm}$ , hence it has been considered to be a two-dimensional manifold, embedded within the three dimensional space [152]. RBCs are highly resistant to changes in volume, but are highly deformable (they pass through narrow capillaries, with a smaller diameter than RBCs themselves). Because the RBCs resist changes in volume, due to the incompressibility of the enclosed fluid, and also have a constant surface area—with the energy required to expand or compress the bilayer area being orders of magnitude greater than the bilayer bending energy [153], all deformation is isochoric [149]. In view of the above, it is hypothesised that the membrane may also be modelled as a quasi-two-dimensional fluid. The cytoskeleton, laying on the interior of the cell close to the phospholipid bilayer, impacts the shear resistance of the membrane, although it is considered to have little relevance to the bending rigidity of the cell [154, 153]. The shear modulus of the RBC is not explicitly modelled in this work, but it is assumed that its behaviour can be recovered from bending rigidity and surface tension effects (which can only be justified *a posteriori*; this matter will be discussed later within this chapter). As such, this work simulates vesicles—no explicit shear resistance is included and the cytoskeleton not modelled—meaning the bending energy of the model (due to the lipid bilayer) can be described via the Helfrich’s bending energy [155] (discussed further shortly).

Later within this Chapter, the simulation of multiple RBCs is targeted—in order to highlight the future extendability of the model to multiple RBC flows. The interaction between the RBCs in this model is controlled by the surface tension values between the RBCs and also the RBC-background fluid (explained further later in this Chapter), i.e., the interaction is considered from a purely hydrodynamic standpoint. However, a repulsive potential is present between cells, stemming from the negatively charged surfaces of the RBCs due to the surface glycoproteins [156] (see Figure 5.1). Forces such as this however takes place at length scales smaller than



## 5. The Simulation of Fluid-Filled Vesicles using *cMCLBM*

that simulated with this model, as such, are not included in the current work —with a detailed study of the interactions of multiple RBCs being a goal of future work. The assumption to neglect this behaviour is consistent with the assumption of the RBC description used throughout this work (modelling the membrane as an effectively two-dimensional surface) and the central investigation of model hydrodynamics.



**Figure 5.1:** A schematic of the structure of a RBC membrane, highlighting the phospholipid bilayer and the protein skeleton (cytoskeleton) [150].

### 5.1.2 Existing Methods

The modelling of RBCs and their surrounding fluid span many length scales, across the micro-, meso- and macro- scales [12]. One must first decide what the principal purpose of the desired RBC model is, i.e., the simulation of dense suspensions, or the accurate modelling of a RBC on a molecular level. This can then be used to inform one at what length scale the model should operate, and which models are appropriate. However, there are a variety of models to choose from, all with differing strengths and weaknesses. Here, what follows is a brief review of such models that operate at the mesoscopic to macroscopic scales, i.e., where the membrane is considered a continuous 2D surface. This should also help provide clarity on where this model sits alongside others in the field and its significance.

Mesoscopic modelling techniques for the simulation of RBCs are popular, due to their bottom-up approach. By starting with equations that characterise a smaller length scale, which also recover continuum momentum equations, it allows physics of smaller, sub-lattice scales to be included in a partially integrated —or low-order —form, which then projects appropriate vesicle behaviour. A common mesoscopic approach uses a mass-spring network of membrane-embedded nodal connections (this is the so-called

## 5. *The Simulation of Fluid-Filled Vesicles using cMCLBM*

lattice spring method (LSM)). The use of a mass-spring system for the simulation of a RBC membrane was first applied at the spectrin level, where such models encountered computational constraints, due to the number of vertices of their mesh [157]. This essential approach was soon expanded to the simulation of multiple erythrocytes via Dupin et al. [19] in 2007, who achieved LBM-based simulations containing 200 vesicles, at a volume fraction of 30%. Dupin et al., introduced a coarse grained Lagrangian LSM, paired with single-component LBM, which required only 400 nodes for the RBC surface. Here, the mechanics of the advecting, deformable body was characterised by the use of point masses, connected via Hookean spring elements. The vesicle surface was comprised of triangular, tessellated surface elements, with the Hookean spring elements lying tangent to these facet edges and the masses being located at the vertices of this mesh. This mesh was then embedded in a single fluid, simulated via the LBM (LBGK variant), and it (the membrane mesh) then being independently tracked during simulation. Dupin’s multi-framework approach is, in this sense, very much a pre-cursor of later, finite-element based, so called LBM-FEM methods. Various multi-framework, mass-spring approaches for the simulation of large suspensions have since been developed [158, 159, 160], with many models being incorporated into very high performance interfaces such as the Hemocell solver [159, 160]. The immediate advantage of such methods is the ability to simulate dense suspensions at reasonable computational expense. However, due to these models adopting the mass-spring system, their ability to simulate high levels of deformation accurately is a recurrent criticism, as is their robustness and —we contend —the trade-off between the physical fidelity of their representation and their computational efficiency. We hope that the work reported in this chapter provides an alternative perspective on this trade-off.

Another popular RBC membrane modelling approach, perhaps more closely related to that we report, is more clearly located at the continuum scale —with constitutive laws being used to describe the membrane, there being various material models available for the vesicle forces [161, 162, 163]. The governing equations for the membrane material are then discretised, using techniques such as finite element method (FEM), these discretised equations then being linked to the chosen fluid solver (which might well be LBM [164, 154], discrete particle dynamics (DPD) simulation or boundary element method (BEM) [165, 166, 167, 168]). Note, models using the BEM fluid solver are restricted to Stokes’ regime. Some variants link the fluid solver to the equations for the deformable body via the immersed boundary method (IBM) introduced by Peskin [169, 170]. Essentially, the Lagrangian marker nodes, advecting on the membrane surface (which are not conformed —or co-registered —to the

## 5. *The Simulation of Fluid-Filled Vesicles using cMCLBM*

fluid mesh, note) are linked to the fluid solver via distribution of the membrane forces, interpolated onto the local Eulerian nodes of the fluid solver. Such models as the aforementioned are recognised for their increased accuracy in simulating RBCs and their enhanced stability, compared to mass-spring systems, at larger levels of deformation —although care is needed when reviewing the LB lattice and FEM mesh spacing (which should be relatively similar). However, they remain multi-framework and are computationally expensive, hence, they do not suit the simulation of very dense suspensions as well the mass-spring system models discussed above. There are also resolution constraints, such as the need for an appropriate density ratio of Eulerian nodes to Lagrangian nodes, in order to accurately interpolate correct local forces. Of course, the simulation of multiple vesicles within this framework would require additional processing, to underwrite the integrity of the individual objects. Very recent efforts have improved the computational efficiency of these models, in order to allow for the simulation of many vesicles [171]. However, due to the modular, multi-framework approach —the need for multiple modelling techniques —there is a lack of transparency in their theoretical support. Here we seek to establish a method with the following advantages: (i) being single-framework; (ii) can capture the requisite physics transparently, verifiably and elegantly; (iii) the relative resolution of the membrane and the coupled fluid is equitable and directly controllable; (iv) the computational overhead acquired when dealing with multiple vesicles is very low.

At the moment, there is no universal model used for the simulation of RBCs. The model for which one opts will depend upon the application of the method, the target application and the required accuracy. The two key RBC modelling methodologies aforementioned serve as examples as follows. One would more than likely opt for the mass-spring models when simulating dense suspensions at scale, due to the computational efficiency, but, maybe, select continuum models when requiring increased accuracy, and low RBC flows. The model outlined here aims to provide a novel, third route, which has high accuracy, stability, verifiable physical fidelity and the future ability to be extended to the simulation of dense suspensions. Its final claim to novelty is that it introduces a single framework methodology —only one modelling technique is used, for both the fluid and deformable body.

### 5.1.3 Chromodynamic MCLBM approach

In the previous section, two popular approaches for modelling RBCs at the continuum and mesoscopic scale were outlined. As discussed, both groups of models had particular strengths. The remainder of the chapter now focuses exclusively on the

## 5. The Simulation of Fluid-Filled Vesicles using cMCLBM

development and validation of a novel, three-dimensional chromodynamic MCLBM, capable of simulating RBCs. This approach uses a similar chromodynamic MCLBM to that outlined in Chapter 3, to underwrite the kinematics, but now extended to three spatial dimensions, with the density ratio between the fluids conveniently set to unity ( $\Lambda = 1$ ) and with *upgraded* interface physics (specifically, a rather more complex force density, to be developed).

When extending to a three-dimensional model, the lattice structure employed is the D3Q19 lattice, where there are 19 lattice velocity vectors,  $\underline{c}_i$  (including the one at rest). Table 5.1 shows the lattice link label,  $i$ , the lattice velocity vector components, and the two lattice weights ( $t_i$ ,  $g_i$ ).

$i$	0	1	2	3	4	5	6	7	8	9	10	11	12	13	14	15	16	17	18
$c_{ix}$	0	1	1	0	-1	-1	-1	0	1	0	1	0	-1	0	0	1	0	-1	0
$c_{iy}$	0	0	-1	-1	-1	0	1	1	1	0	0	1	0	-1	0	0	1	0	-1
$c_{iz}$	0	0	0	0	0	0	0	0	0	1	1	1	1	1	-1	-1	-1	-1	-1
$t_i$	$t_0$	$t_1$	$t_2$	$t_1$	$t_2$	$t_1$	$t_2$	$t_1$	$t_2$	$t_1$	$t_2$	$t_2$	$t_2$	$t_2$	$t_1$	$t_2$	$t_2$	$t_2$	$t_2$
$g_i$	$g_0$	$g_1$	$g_2$	$g_1$	$g_2$	$g_1$	$g_2$	$g_1$	$g_2$	$g_1$	$g_2$	$g_2$	$g_2$	$g_2$	$g_1$	$g_2$	$g_2$	$g_2$	$g_2$

**Table 5.1:** D3Q19 lattice structure, showing lattice link ( $i$ ), lattice velocity vector ( $\underline{c}_i$ ) components and lattice weights ( $t_i$ ,  $g_i$ ). Here,  $t_0 = \frac{1}{3}$ ,  $t_1 = \frac{1}{18}$ ,  $t_2 = \frac{1}{36}$  and  $g_0 = 1$ ,  $g_1 = -2$ ,  $g_2 = 1$ .

Continuing with the typical colour label convention for fluid components, when simulating vesicles in this work, the internal fluid (cytoplasm) is designated red and the exterior fluid (plasma) denoted blue. The interfacial region is representative of the surface (*de facto* membrane) of the vesicle and this is where appropriate immersed boundary forces (to be determined) are applied. Figure 5.2 displays a schematic of this colour naming convention used, as well as the physical representation of the fluids.

In contradistinction to previous Chapters (3 and 4), this model uses a density ratio between the fluid of unity, i.e.,  $\rho_{0R} = \rho_{0B}$ . As such, the mass activation parameter  $\phi_i$  no longer appears, and we revert to the LBM equilibrium distribution function, cMCLBM phase-field (interface) [57] and chromodynamic segregation rule as follows:

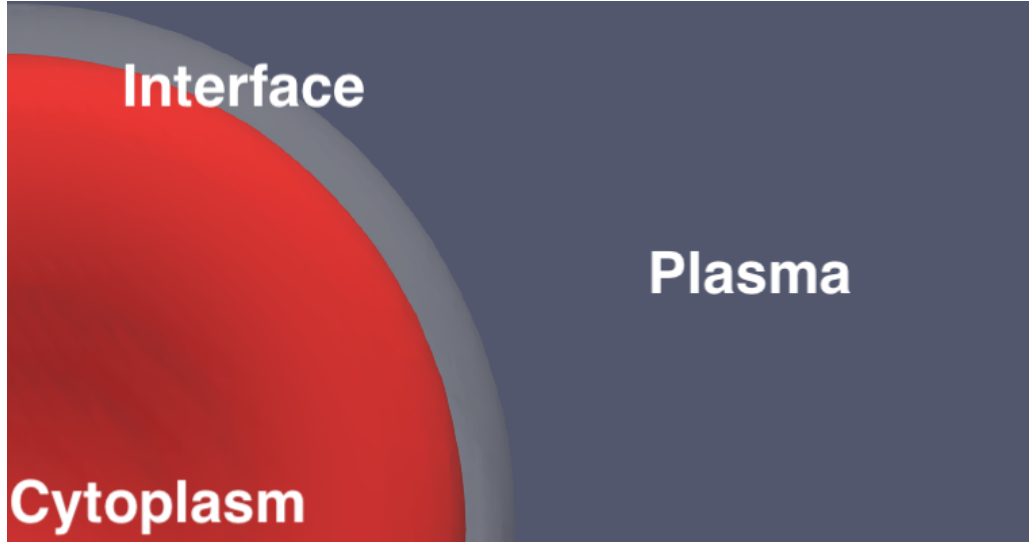
$$f_i^{(\text{eq})}(\rho, \underline{u}) = t_i \rho \left( 1 + \frac{u_\alpha c_{i\alpha}}{c_s^2} + \frac{u_\alpha u_\beta c_{i\alpha} c_{i\beta}}{2c_s^4} - \frac{u^2}{2c_s^2} \right), \quad (5.1)$$

$$\rho^N(\underline{r}, t) \equiv \frac{\rho_R(\underline{r}, t) - \rho_B(\underline{r}, t)}{\rho_R(\underline{r}, t) + \rho_B(\underline{r}, t)} \in [-1, 1], \quad (5.2)$$

$$C_i^{\psi\psi}(\underline{r}, t) = \frac{\rho_C(\underline{r}, t)}{\rho(\underline{r}, t)} f_i(\underline{r}, t)^\psi \pm \beta t_i \frac{\rho_R(\underline{r}, t) \rho_B(\underline{r}, t)}{\rho(\underline{r}, t)} \hat{n} \cdot \underline{c}_i \Delta t, \quad (5.3)$$

where all terms have the same meanings as in the previous schemes described in Chapters 3 and 4.

## 5. The Simulation of Fluid-Filled Vesicles using cMCLBM



**Figure 5.2:** Schematic outlining the assignment of the fluids in the chromodynamic MCLBM for simulating vesicles. Here, the red fluid corresponds to the cytoplasm (or the vesicle), the blue fluid the plasma (or external fluid) and the grey region to the interfacial region (or vesicle-fluid surface).

The critical change in our methodology, from simulating drops to simulating vesicles, stems from the inclusion of a more sophisticated body force —containing key surface metrics such as the principle curvatures of the surface—which aims to accurately embed vesicle behaviour. These forces are introduced as a variable body force density (or distribution) in the Navier-Stokes equations for the interfacial fluid (which is a patch within what is effectively a single fluid, note), see Eq. (5.30), and as such are incorporated in the scheme at a mesoscopic level through the macroscopic velocity relation correction [172, 70] and source terms in the kinetic scale evolution equation. The total force (decomposed by contribution) weighted by the phase-field (to allow for local application of the membrane effects in the interfacial region), are defined as follows: [57, 173, 155, 20]:

$$\underline{F}^{(t)} = \frac{1}{2} \nabla_x \rho^N \left( F^{(a)} + F^{(b)} + F^{(l)} \right), \quad (5.4)$$

where:

$$\underline{F}^{(a)} = -\alpha H (A - A_0) A \hat{n}, \quad (5.5a)$$

$$\underline{F}^{(b)} = -\kappa_B \left( \frac{3}{2} \Delta_S H + H^3 - KH \right) \hat{n}, \quad (5.5b)$$

$$\underline{F}^{(l)} = 2\sigma H \hat{n}, \quad (5.5c)$$

and contributions  $\underline{F}^{(t)}$ ,  $\underline{F}^{(a)}$ ,  $\underline{F}^{(b)}$ ,  $\underline{F}^{(l)}$  are the total force contribution, membrane area conserving force, membrane bending rigidity force and membrane surface tension force [155]. All three individual forces and their parameters will be explained in detail,

## 5. The Simulation of Fluid-Filled Vesicles using cMCLBM

in the succeeding section; for now, note that  $H$  and/or  $K$  (the mean and Gaussian membrane surface curvatures of the surface) appear in all force contributions.

This model provides a novel approach, encapsulated in a single framework structure, where no other modelling technique is needed to simulate the deformable body. The extensions to the methodology of preceding chapters, specifically the enhanced immersed boundary force (Eq. (5.4)), will now be detailed. We summarise as follows. A new approach to simulating RBCs is postulated, which: (i) is transparently encapsulated in a single framework (cMCLBM), (ii) uses an appropriate, easy to compute body force, reliant on key surface curvatures of  $H$  and  $K$ , (iii) is capable of vesicles accurately and (iv) can be extended to the simulation of multiple vesicles.

## 5.2 Extension of Methodology

In this section, the single framework methodology developed for simulating vesicles using chromodynamic MCLBM will be presented. Due to the need for minimal changes in the method relative to the chromodynamic MCLBM schemes already introduced in Chapters 3 and 4, in the present chapter, work focuses on the inclusion of the requisite membrane physics in the scheme and the efficient implementation of the immersed boundary forces that encapsulate that physics. Therefore, the membrane forces used to introduce interface fluid behaviour consistent with vesicle membranes will be explained in detail, as well as how these forces are implemented efficiently in simulation. It will become obvious to the reader that a suitable method of calculating the surface curvatures is central for the computation of these forces, leading to the work in section 5.2.3.

### 5.2.1 Immersed Boundary Force

The main difference between using chromodynamic MCLBM for simulating drops and vesicles, was the upgraded immersed boundary force. The force is applied locally in the interfacial region (*de facto* membrane) using a weight function, related to the phase-field, in which  $\rho^N = 0$  corresponds to mid-interface. Here, the immersed boundary force is discussed in more detail, including its relation to vesicle physics and the principle curvatures of the surface. Principally, the three forces characterised as area conserving, bending rigidity and surface tension forces all contribute to the final vesicle shape, however, all should be regarded as practically independent of each other for present purposes (notwithstanding that all must, presumably, derive from a single free constitutive theory of the membrane, which is, beyond the scope of the present work). As such, each force, although interrelated in the sense that they all effect vesicle behaviour, can be tuned individually.

## 5. The Simulation of Fluid-Filled Vesicles using *cMCLBM*

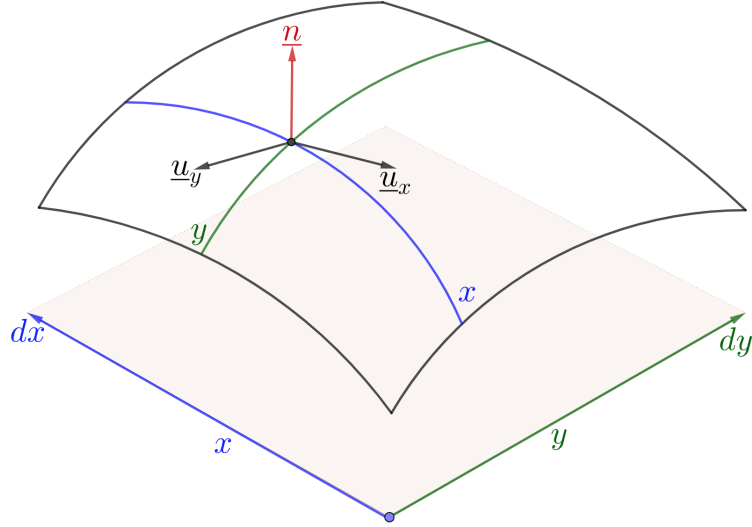
### 5.2.1.1 Area Conservation

When distinguishing between drop and erythrocyte dynamics, the conservation of surface area and volume of the internal fluid in erythrocytes is crucial. The conservation of volume stems from the membrane impermeability to cations, and the conservation of surface area is due to resistance in changes in area per molecule of the membrane bilayer [174]. The conservation of erythrocyte surface area, and volume of the incompressible fluid when subject to deformation in flow is characterised as an isochoric deformation [149]. Due to this constraint, the surface area to volume ratio is an important parameter of relative deformation, for it restricts the types of deformation available to the vesicle. Notably, a healthy human RBC has surface area much greater than that of a sphere with the same volume [175]. Here, an appropriate membrane area conservation force is outlined, that aims to conserve global surface area, but not local area, i.e., the overall area of the surface will be constant but local patch areas may, in principle, fluctuate. A volume constraint force is not required, as chromodynamic MCLBM inherits strict mass conservation, meaning volume is conserved.

For our derivation, the following assumptions about the membrane surface are made. It is isotropic, has zero preferred curvature, compressibility is controlled by a single parameter  $\alpha$  (see Eq. (5.12)), differential strain at all locations is equal and it relaxes strains rapidly in the tangential direction (this is consistent with the assumption of globally conserved area) [20]. It is therefore taken that we neglect the tangential components of  $\underline{F}^{(a)}$  (more on this shortly).

Take a small excerpt of vesicle surface, which when not constrained, is flat, and has area  $dA' = dx dy$ , such that the surface spans the limited range  $x \in [0, dx]$ ,  $y \in [0, dy]$ . In this analysis, the surface (a two-dimensional manifold in a three dimensional space) is represented as a Monge surface [176], i.e., kinematically, the movement of the manifold in space is always orthogonal to the plane. A given position on that surface is then defined by  $\underline{u}(x, y)$ . At a given point on the surface, such as where  $x, y$  intercept, the two orthogonal tangents are given by  $\underline{u}_x$  and  $\underline{u}_y$  (where  $\underline{u}_\alpha = \frac{\partial}{\partial \alpha} \underline{u}$ ). The normal at this point is then straightforwardly calculated via the cross product  $\underline{n} = \underline{u}_x \times \underline{u}_y$ . Figure 5.3 shows the surface excerpt in question, and corresponding differential geometry. The strained area with curvilinear co-ordinates

## 5. The Simulation of Fluid-Filled Vesicles using cMCLBM



**Figure 5.3:** Schematic showing an excerpt of vesicle surface, represented by a Monge patch, where position on the surface is given by  $\underline{u}(x, y)$  and the surface has unstrained area given by  $dA' = dxdy$ . The orthogonal tangent vectors at a point on the manifold are given by  $\underline{u}_\delta = \frac{\partial}{\partial \delta} \underline{u}$  where  $\delta \in [x, y]$  (black arrows), in which the normal vector is then straightforwardly calculated as such:  $\underline{n} = \underline{u}_x \times \underline{u}_y$  (red arrow) [20].

can thus be calculated by the following:

$$\begin{aligned}
 dA' &= |\underline{u}_x \times \underline{u}_y| dxdy, \\
 &= |\epsilon_{ijk}(u_j)_x(u_k)_y| dxdy, \\
 &= \sqrt{\epsilon_{ijk}\epsilon_{ilm}(u_j)_x(u_k)_y(u_l)_x(u_m)_y} dxdy, \\
 &= \sqrt{(\underline{u}_x \cdot \underline{u}_x)(\underline{u}_y \cdot \underline{u}_y) - (\underline{u}_x \cdot \underline{u}_y)^2} dxdy,
 \end{aligned} \tag{5.6}$$

in which the identity  $\epsilon_{ijk}\epsilon_{ilm} = \delta_{jl}\delta_{km} - \delta_{jm}\delta_{kl}$  has been used [140]. Following the usual practice, the previous equation can be rewritten using the coefficients of the first fundamental form of the surface, I [177]:

$$dA' = \sqrt{EG - F^2} dxdy,$$

where:

$$E = \underline{u}_x \cdot \underline{u}_x, \quad G = \underline{u}_y \cdot \underline{u}_y, \quad F = \underline{u}_x \cdot \underline{u}_y, \tag{5.7}$$

and therefore the unit normal is defined as:

$$\hat{n} = \frac{\underline{u}_x \times \underline{u}_y}{\sqrt{EG - F^2}}. \tag{5.8}$$



### 5. The Simulation of Fluid-Filled Vesicles using cMCLBM

Generalising and using this notation, the area,  $\Delta A$ , of any finite part of the membrane can be formally calculated by a surface integral:

$$\Delta A = \iint \sqrt{EG - F^2} dx dy, \quad (5.9)$$

where the integration is taken over a finite range of parameters  $x \in [0, \Delta x]$ ,  $y \in [0, \Delta y]$ .

It is also necessary to state the below approximations that will be used shortly:

$$\Delta A \approx \sqrt{EG - F^2} \Delta x \Delta y, \quad \Delta A_0 \approx \Delta x \Delta y. \quad (5.10)$$

The corresponding change in area for the constrained surface element, from the unconstrained surface element, can be examined as follows:

$$\begin{aligned} \Delta S &= \Delta A - \Delta A_0, \\ &= \sqrt{EG - F^2} \Delta x \Delta y - \Delta x \Delta y, \\ &= (\sqrt{EG - F^2} - 1) \Delta x \Delta y, \end{aligned}$$

thus, the change in local area can be characterised by the following surface integral

$$\Delta S = \iint (\sqrt{EG - F^2} - 1) dx dy, \quad (5.11)$$

where the surface integral is over the finite range  $x \in [0, \Delta x]$ ,  $y \in [0, \Delta y]$ . It follows that the free-energy density,  $A_s$ , associated with the deformation of a finite element of vesicle surface, can be written as:

$$A_s = \frac{\alpha}{2} \iint \mathbb{F}(x, y, \underline{u}, \underline{u}_x(x, y), \underline{u}_y(x, y)) dx dy, \quad (5.12)$$

where a multi-variate functional,  $\mathbb{F}$  of  $x$ ,  $y$ , is now defined as:

$$\mathbb{F}(x, y, \underline{u}, \underline{u}_x(x, y), \underline{u}_y(x, y)) = (\sqrt{EG - F^2} - 1)^2. \quad (5.13)$$

Note that  $\mathbb{F}$  does not depend, explicitly, on  $x$ ,  $y$  and  $\underline{u}$ .

In order to constrain the surface area of the vesicle, one must minimise the free-energy associated with the deformation of a general finite element of vesicle surface, given in Eq. (5.12). In order to do this, the calculus of variations are used; put another way, the multi-variate Euler-Lagrange equation for multi-dependent variables in Eq. (5.12) give the appropriate variational derivatives which are set to zero. Noting  $\mathbb{F}$  is dependent upon  $u_k(x, y)$ , (where  $k = 1, 2, 3$ ), we now minimise, i.e., seek  $\frac{\delta A_s}{\delta u_k}$ . An expression for the  $k^{th}$  component of a membrane area conserving force can thus be found by taking a variational derivative:

$$\begin{aligned} F_k^{(a)} &= \frac{\delta A_s}{\delta u_k(x, y)} = \frac{\partial \mathbb{F}}{\partial (u_k)} - \frac{\partial}{\partial x} \frac{\partial \mathbb{F}}{\partial (u_k)_x} - \frac{\partial}{\partial y} \frac{\partial \mathbb{F}}{\partial (u_k)_y}, \\ &= -\frac{\alpha}{2} \frac{\partial}{\partial x} \frac{\partial}{\partial (u_k)_x} (\sqrt{EG - F^2} - 1)^2 - \frac{\alpha}{2} \frac{\partial}{\partial y} \frac{\partial}{\partial (u_k)_y} (\sqrt{EG - F^2} - 1)^2. \end{aligned} \quad (5.14)$$

### 5. The Simulation of Fluid-Filled Vesicles using cMCLBM

For clarity, the derivatives of the first term on the right hand side of Eq. (5.14) will be evaluated separately:

$$\begin{aligned}
\frac{\alpha}{2} \frac{\partial}{\partial x} \frac{\partial}{\partial (u_k)_x} (\sqrt{EG - F^2} - 1)^2 &= \alpha \frac{\partial}{\partial x} \left[ \left( \frac{\sqrt{EG - F^2} - 1}{\sqrt{EG - F^2}} \right) \left( (u_k)_x G - (u_k)_y F \right) \right], \\
&= \alpha \frac{\partial}{\partial x} \left[ \left( \frac{\sqrt{EG - F^2} \Delta x \Delta y - \Delta x \Delta y}{\sqrt{EG - F^2} \Delta x \Delta y} \right) \times \right. \\
&\quad \left. \left( (u_k)_x G - (u_k)_y F \right) \right], \\
&\approx \alpha \left( \frac{\Delta A - \Delta A_0}{\Delta A} \right) \frac{\partial}{\partial x} \left( (u_k)_x G - (u_k)_y F \right).
\end{aligned} \tag{5.15}$$

Under the assumption that tangential stress relaxes rapidly —the relative straining of a surface area element is  $\Delta A = \Delta x \Delta y$  is constant over all surface locations  $(x, y)$  —the factorisation in the last line of Eq. (5.15) is justified. By similar analysis, the second term on the right hand side of Eq. (5.14) can be given as:

$$\frac{\alpha}{2} \frac{\partial}{\partial y} \frac{\partial}{\partial (u_k)_y} (\sqrt{EG - F^2} - 1)^2 \approx \alpha \left( \frac{\Delta A - \Delta A_0}{\Delta A} \right) \frac{\partial}{\partial y} \left( (u_k)_y E - (u_k)_x F \right). \tag{5.16}$$

Using the evaluated expressions, Eq.(5.15) and Eq.(5.16), to rewrite Eq. (5.14):

$$\begin{aligned}
F_k^{(a)} &= -\alpha \left( \frac{\Delta A - \Delta A_0}{\Delta A} \right) \times \left[ \frac{\partial}{\partial x} \left( (u_k)_x G - (u_k)_y F \right) + \frac{\partial}{\partial y} \left( (u_k)_y E - (u_k)_x F \right) \right] \\
&= -\alpha \left( \frac{\Delta A - \Delta A_0}{\Delta A} \right) \times \left[ E(u_k)_{yy} + G(u_k)_{xx} - 2F(u_k)_{xy} + (u_k)_x (G_x - F_y) + \right. \\
&\quad \left. + (u_k)_y (E_y - F_x) \right].
\end{aligned} \tag{5.17}$$

Following the assumptions previously introduced —that tangential stress relaxes rapidly and the surface is isotropic —the membrane is not differentially strained. The normal component of the force, i.e., the force perpendicular to the interface, is now projected out. The following definition for the normal component of the force is obtained:

$$\begin{aligned}
F_k^{(a)} \hat{n}_k &= -\alpha \left( \frac{\Delta A - \Delta A_0}{\Delta A} \right) \times \left[ (E \hat{n}_k (u_k)_{yy} + G \hat{n}_k (u_k)_{xx} - 2F \hat{n}_k (u_k)_{xy}) + \right. \\
&\quad \left. + \hat{n}_k (u_k)_x (G_x - F_y) + \hat{n}_k (u_k)_y (E_y - F_x) \right],
\end{aligned} \tag{5.18}$$

### 5. The Simulation of Fluid-Filled Vesicles using cMCLBM

where, from Eq. (5.8),  $\hat{n}_k(u_k)_x = \hat{n}_k(u_k)_y = 0$ . Further simplifying:

$$\begin{aligned} \underline{F}^{(a)} \cdot \underline{\hat{n}} = F_k^{(a)} \hat{n}_k &= -\alpha \left( \frac{\Delta A - \Delta A_0}{\Delta A} \right) \times \left( E \hat{n}_k(u_k)_{yy} + G \hat{n}_k(u_k)_{xx} \right. \\ &\quad \left. - 2F \hat{n}_k(u_k)_{xy} \right), \quad (5.19) \\ &= -\alpha \left( \frac{\Delta A - \Delta A_0}{\Delta A} \right) (EN + GL - 2FM), \end{aligned}$$

where  $N$ ,  $L$  and  $M$  are the coefficients of the second fundamental form of the membrane surface, usually denoted II, and used in conjunction with the first fundamental form to calculate principle curvatures of a surface [177]:

$$N = (u_k)_{yy} \cdot \hat{n}_k, \quad L = (u_k)_{xx} \cdot \hat{n}_k, \quad M = (u_k)_{xy} \cdot \hat{n}_k. \quad (5.20)$$

The mean curvature of a surface can be defined using the coefficients of I and II (the fundamental forms), shown in Eqs. (5.7) and (5.20), as follows:

$$H = \frac{1}{2} (\kappa_1 + \kappa_2) \propto \left( \frac{EN + GL - 2FM}{EG - F^2} \right). \quad (5.21)$$

Therefore, we use the definition of the mean curvature,  $H$ , in Eq. (5.21), to rewrite Eq. (5.19):

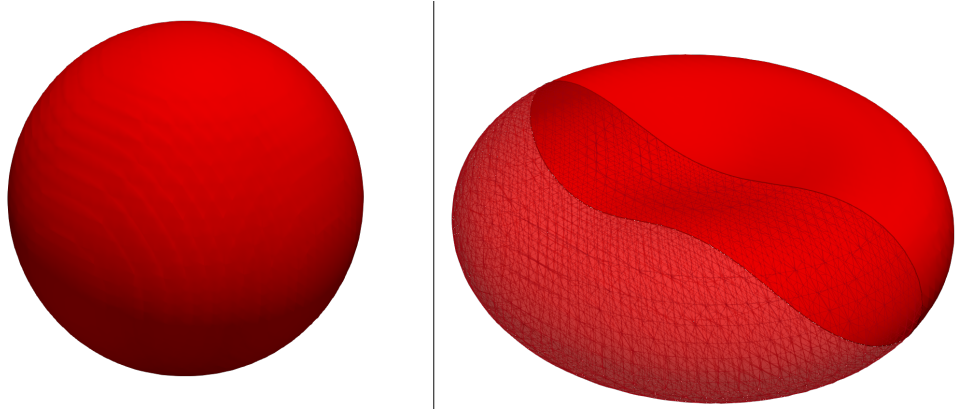
$$F_n^{(a)} \propto -\alpha H \frac{(\Delta A - \Delta A_0)}{\Delta A} (EG - F^2).$$

It is now possible to use the definition of area to replace  $(EG - F^2) \propto \Delta A^2$ , as well as absorbing constants of proportionality into  $\alpha$ . These steps result in a final expression for the normal component of the interface force component for surface area control:

$$\underline{F}^{(a)} = -\alpha H (A - A_0) A \hat{n}, \quad (5.22)$$

where, parameter  $\alpha$  clearly now only represents physical interface compressibility very broadly. Here,  $A$  is the actual area of the vesicle and  $A_0$  is the reference area (or desired cross-sectional area) of the vesicle. In simulation, the vesicle is initialised as a sphere, with defined area,  $A_{\text{sphere}}$ . The initial vesicle is then deflated by an amount proportional to the area of the sphere as such:  $A_0 = \Upsilon A_{\text{sphere}}$ , where  $\Upsilon$  is a deflation constant. The interface compressibility,  $\alpha$ , can then be used to control the rate at which the vesicle approaches its target area  $A_0$ . Figure 5.4 displays the initialised spherical vesicle (left), and the resultant bicuspid vesicle after deflation and immersed boundary forces have been applied (right). The actual area of the vesicle in simulation,  $A$ , is calculated through a weighted volume sum of the entire interfacial region, which is then divided by interfacial width to get the cross-sectional area of the interface.

## 5. The Simulation of Fluid-Filled Vesicles using cMCLBM



**Figure 5.4:** Schematic showing (left) initialised spherical vesicle with area  $A_{\text{sphere}}$  and (right) steady state bicuspid vesicle, with cross-sectional surface area  $A_0 = \Upsilon A_{\text{sphere}}$ .  $\Upsilon = 1.31$  for this case [20].

### 5.2.1.2 Bending Energy

The cell membrane, and corresponding cell physics, controls how a suspended vesicle responds under deformation within flows. The bending energy of the membrane, dictated by the cell membrane structure and properties (phospholipid bi-layer and the protein skeleton on the cytoplasm surface) has a large influence on vesicle behaviour, i.e., the membrane's bending elasticity, shear elasticity and hence surface shape. Thus, the accurate representation of the bending energy of the membrane is crucial. At a microscopic level, this may be achieved by describing the physical response in relation to the position of lipid molecules. Whereas, at the continuum scale, the membrane is treated as a continuous two-dimensional manifold, over which a shape energy can be assigned. Similar descriptions of the bending energy of the associated membrane have been proposed [178, 179, 180], a popular model (used in this work) being the Helfrich bending energy (also known as the spontaneous curvature model [181]):

$$\epsilon_{\mathbf{B}}(\underline{r}) = 2\kappa_B (H - H_0)^2 + \kappa_K K, \quad (5.23)$$

where,  $\kappa_B$ ,  $H$ ,  $H_0$ ,  $\kappa_K$  and  $K$  are the bending modulus, mean curvatures, preferred curvature, saddle spray modulus and Gaussian curvature, respectively

The bending force acting in the normal direction to the surface, related to the bending energy of the membrane (Eq. (5.23)), is variously derivable —see [179]. The resulting form of bending force implemented in this work is given by the following [173]:

$$F^{(b)} = \kappa_B C + \underline{\nabla}_s \kappa_B \cdot (\underline{\nabla}_s (H - H_0)), \quad (5.24)$$

where:

$$C = H(H^2 - H_0^2) + \frac{1}{2} \Delta_s H - (H - H_0)K. \quad (5.25)$$

## 5. The Simulation of Fluid-Filled Vesicles using cMCLBM

Equations (5.24) and (5.25) can be found in Eq.(A17) and Eq.(A18) of reference [173], and are representative of the modulus of the bending force, acting in the normal direction. Here,  $\kappa_B$ ,  $H$ ,  $H_0$ ,  $K$ ,  $\underline{\nabla}_s$  and  $\Delta_s$  are the bending rigidity, mean curvature, preferred mean curvature, Gaussian curvature, surface gradient operator and the Laplace-Beltrami operator, respectively.

Proceeding, the bending rigidity is now set constant. There is still no general consensus on a value of preferred curvature  $H_0$ , for the simulation of human RBCs, with some authors opting for  $H_0 \neq 0$  and some setting  $H_0 = 0$ . In this preliminary work,  $H_0 = 0$ , for simplicity whilst still retaining the ability to recover the desired bicuspid vesicle.

The Laplace-Beltrami operator is defined as follows:

$$\Delta_s H = \underline{\nabla}_s \cdot (\underline{\nabla}_s H). \quad (5.26)$$

Using the above definition of the Laplace Beltrami operator, as well as the preferred curvature and bending rigidity constraints, Eq. (5.24) can be simplified to the following [20]:

$$F^{(b)} = -\kappa_B \left( \frac{3}{2} \Delta_s H + H^3 - KH \right). \quad (5.27)$$

In order to accurately impart membrane bending physics, Eq. (5.27) must be implemented correctly and, of course, appropriately. This involves the computation of the mean and Gaussian curvatures, as well as the Laplace-Beltrami operator. A suitable and efficient method of computing these metrics will be investigated in section 5.2.3.

### 5.2.1.3 Surface Tension

The final force contribution incorporated in the model's immersed force distribution encapsulates the physics of surface tension. This contribution is exactly the same as that occurring in drops where the surfaces between fluids generate a tension; this has been implemented and described previously, for the simulation of immiscible liquid drops, in Chapter 3. Therefore, the reader is directed to section 2.3.3 for further detail. The surface tension force is implemented in the following form, for use with MCLBM introduced in [57] as follows:

$$F^{(t)} = 2\sigma H, \quad (5.28)$$

where,  $\sigma$  is the surface tension parameter and  $H$  is the mean curvature. Note, the importance of this force is elevated when reviewing extensions towards multiple RBC simulations, in which the force helps control the immiscibility between the fluids (vesicles). This was previously mentioned in Chapter 3, but will be further discussed and re-contextualised for the simulation of vesicles shortly.

## 5. The Simulation of Fluid-Filled Vesicles using cMCLBM

### 5.2.1.4 Total Immersed Boundary Force

The individual force components that encapsulate key vesicle physics, which act together to produce a correct vesicle profile and dynamics are the area conserving, bending and surface tension forces, which have now been outlined. These forces must be applied essentially in the interfacial region, identified from the cMCLBM (which corresponds to the vesicle surface (*de facto* membrane)) to differentially modify the fluid behaviour in that region. In order to do this, an appropriate weight function is used and the independent forces are summed vectorially:

$$\underline{F}^{(t)} = \frac{1}{2} \underline{\nabla}_X \rho^N \left( F^{(a)} + F^{(b)} + F^{(l)} \right), \quad (5.29)$$

where the chosen weight function,  $\frac{1}{2} \underline{\nabla}_X \rho^N$  [173], heavily biases the interface region, allows the immersed forces to be applied specifically in the interface region and screens the bulk fluids from its effects (thereby effecting a very useful reduction in computational overhead). In addition, it may be computed with minimal computational expense.

With the interfacial force density now defined, before continuing to simulation results and model testing, the following practicalities will be considered: (i) characterisation of the immersed boundary force through use of non-dimensional groups and (ii) accurate computation of the immersed boundary force, specifically, how conveniently to calculate membrane surface curvatures  $H$  and  $K$  for the immersed boundary force computation.

### 5.2.2 Force Characterisation

The immersed boundary force is, for present purposes, synonymous with a force density (or distribution) in the weakly compressible Navier-Stokes equations, at the continuum scale as shown below:

$$\frac{D}{Dt} \rho v_i = -c_s^2 \frac{\partial \rho}{\partial x_i} + 2\nu(\lambda_3) \frac{\partial}{\partial x_j} (\rho S_{ij}) + F_i^{(t)}, \quad (5.30)$$

the force density is then incorporated into the cMCLBM scheme in the same way as presented in Chapters 3 and 4, and analysed using the Chapman-Enskog procedure. In simulation, the continuous force distribution is, of course, effectively discretised and applied at discrete sites over the domain. The LBM scheme allows a force to be included as discrete source term samples, at the kinetic level. As such, in addition to the order of accuracy of the calculation, discretisation error associated with the discrete force is influenced by the sampling, the accuracy of the numerical gradients used in assigning its parameters, and the truncation of forcing outside the

## 5. The Simulation of Fluid-Filled Vesicles using *cMCLBM*

interfacial region. For practical purposes therefore, to guarantee linear and angular momentum conservation, on a close object, there must be adequate resolution in the interfacial region; given that, in the interfacial region, the discrete sampled force will be computed and hence applied more accurately. This will be discussed further in section 5.3.1.2.

In later work, the total immersed boundary force (Eq. (5.29)) will be characterised using non-dimensional groups, as well as the key force parameters explained further. The bending rigidity and surface tension forces have significant impact on the equilibrium vesicle shape, whereas, in equilibrium, the area conserving force does not. The area conserving force is in essence a constraint force, i.e., it aims to conserve cross-sectional surface area and is only prevalent should the vesicle drift from its target area. Once the vesicle has deflated from its original area to the target area, the area conserving force has little impact on vesicle shape. In order for the area conserving force to maintain surface area under flow stresses, it was found that  $|F^{(a)}| \propto |F^{(b)}|, |F^{(l)}|$ . If this is true,  $|F^{(a)}|$  has little effect on vesicle shape, it is therefore disregarded for the next stage of this preliminary work, when seeking to parameterise equilibrium vesicle shape. Thus the following approximation is made when seeking an equilibrium vesicle characterisation:

$$\underline{F}^{(t)} \approx \frac{1}{2} \left( \underline{\nabla}_X \rho^N \right) \left( F^{(b)} + F^{(l)} \right). \quad (5.31)$$

Before seeking to characterise this approximation, responsible for equilibrium vesicle shape, the Laplace-Beltrami operator, found in  $F^{(b)}$  (Eq. (5.27)), should be expressed in the simulation frame. The Laplace-Beltrami operator, expressed in terms of surface gradients ( $\underline{\nabla}_s$ ) is as follows:

$$\Delta_s H = \underline{\nabla}_s \cdot (\underline{\nabla}_s H).$$

Clearly, the above expression should be computed using the simulation co-ordinate frame. The surface gradient operator can be redefined in the preferred computational frame as follows. First, remove gradients in the normal direction, leaving gradients tangent to the local surface normal:

$$\frac{\partial}{\partial X_{i_s}} f = \frac{\partial}{\partial X_i} f - \hat{N}_i \hat{N}_j \frac{\partial}{\partial X_j} f, \quad i, j = 1, 2, 3 \quad (5.32)$$

i.e., the orthographic projection of the gradient onto the surface. Accordingly, the Laplace-Beltrami operator can now be defined *co-ordinate free* as:

$$\Delta_s f = \left( \frac{\partial}{\partial X_{i_s}} \right) \left( \frac{\partial}{\partial X_{i_s}} \right) f. \quad (5.33)$$

### 5. The Simulation of Fluid-Filled Vesicles using cMCLBM

Using Eqs. (5.32, 5.33), the Laplace-Beltrami of  $H$  can now be calculated by the following simplification:

$$\begin{aligned}
\Delta_s H &= \left( \frac{\partial}{\partial X_{i_s}} \right) \left( \frac{\partial}{\partial X_{i_s}} \right) H, \\
&= \frac{\partial}{\partial X_i} \left[ \frac{\partial}{\partial X_i} H - \hat{N}_i \hat{N}_j \frac{\partial}{\partial X_j} H \right], \\
&= \frac{\partial^2}{\partial X_i^2} H - \frac{\partial}{\partial X_i} \hat{N}_i \hat{N}_j \frac{\partial}{\partial X_j} H, \\
&= \frac{\partial^2}{\partial X_i^2} H - (\hat{N} \cdot \underline{\nabla}_X)^2 H - (\hat{N} \cdot \underline{\nabla}_X)(\underline{\nabla}_X \cdot \hat{N}) H, \\
&= \frac{\partial^2}{\partial X_i^2} H - (\hat{N} \cdot \underline{\nabla}_X)^2 H - 2H(\hat{N} \cdot \underline{\nabla}_X) H, \\
&= \Delta_X H - (\hat{N} \cdot \underline{\nabla}_X)^2 H + \hat{N} \cdot \underline{\nabla}_X H^2,
\end{aligned} \tag{5.34}$$

where the substitution  $(\underline{\nabla}_X \cdot \hat{N}) = 2H$  has been used. Now, from Eqs. (5.27, 5.34):

$$F^{(b)} = \kappa_B H(H^2 - K) + \frac{3}{2} \kappa_B \left( \Delta_X H - (\hat{N} \cdot \underline{\nabla}_X)^2 H + \hat{N} \cdot \underline{\nabla}_X H^2 \right), \tag{5.35}$$

and, as above, the surface tension force is:

$$F^{(l)} = 2\sigma H. \tag{5.36}$$

Let us consider non-dimensionalising the approximate force characterising equilibrium vesicle shape, in Eqs. (5.35, 5.36), using the undeformed initial vesicle radius,  $R_0$  (lattice units), as a length scale. As such:  $\kappa_{Bi} = \frac{1}{R_0} \bar{\kappa}_{Bi}$  ( $i = 1, 2$ ),  $K = \frac{1}{R_0^2} \bar{K}$ ,  $H = \frac{1}{R_0} \bar{H}$ ,  $\frac{\partial}{\partial X} = \frac{1}{R_0} \frac{\partial}{\partial \bar{X}}$  etc. Moreover, the weight function in Eq. (5.31) may be rewritten as  $\frac{1}{2} \underline{\nabla} \rho^N = \frac{1}{2} \beta (1 - \rho^{N^2}) \hat{n}$ , which, is of  $O(1)$  and hence such contributions are ignored in the following. After straightforwardly transforming variables, the following is obtained:

$$F^{(b)} = \frac{\kappa_B}{R_0^3} \bar{F}^{(b)}, \quad F^{(l)} = \frac{\sigma}{R_0} \bar{F}^{(l)}, \tag{5.37}$$

where the non-dimensional force contributions' moduli are:

$$\bar{F}^{(b)} = \bar{H}(\bar{H}^2 - \bar{K}) \tag{5.38}$$

$$\begin{aligned}
&+ \frac{3}{2} \left( \bar{\Delta}_X \bar{H} - (\hat{N} \cdot \bar{\underline{\nabla}}_X)^2 \bar{H} + \hat{N} \cdot \bar{\underline{\nabla}}_X \bar{H}^2 \right), \\
\bar{F}^{(l)} &= 2\bar{H}.
\end{aligned} \tag{5.39}$$

Therefore, from Eq. (5.37), an equilibrium vesicle profile can be characterised by these dimensionless groups:

$$\frac{\kappa_B}{R_0^3}, \quad \frac{\sigma}{R_0}. \tag{5.40}$$



## 5. The Simulation of Fluid-Filled Vesicles using cMCLBM

Alongside the dimensionless groups in Eq. (5.40), the level of deflation needs to be considered. Although it was chosen to neglect the area conserving force when considering steady state shape on justification that it only acts to conserve area but does not actually affect the shape once deflated. The deflation of the vesicle is obviously going to impact vesicle shape, as it impacts the volume to surface area ratio and hence the amount of *excess* surface area. The level of deflation,  $\Upsilon$ , controls this and is defined as the ratio of target surface area to the initial vesicle area in simulation:  $\Upsilon = \frac{A_0}{A_{\text{sphere}}}$ , where  $A_{\text{sphere}}$  is the area of the initialised vesicle and  $A_0$  the target vesicle area. Thus, a final dimensionless group relating to this vesicle deflation through choice of  $A_0$  is:

$$\frac{A_0}{R_0}. \quad (5.41)$$

Equations (5.40, 5.41) now represent a parameter space for the equilibrium vesicle shape, which is clearly  $\mathbb{R}^3$ , with three tuneable parameters  $\sigma$ ,  $\kappa_B$ ,  $A_0$  (or  $\Upsilon$ ). The parameterisation (calibration) using these dimensionless groups will be discussed further in section 5.3. However, it is worth, at this early stage, mentioning that to facilitate the parameterisation of a bicuspid vesicle, constraining of the problem to a  $\mathbb{R}^2$  parameter space seems reasonable. As discussed below, the level of deflation (or target area  $A_0$ ) may be fixed, with a value chosen based on prior literature and practical understanding. The result of this dimensional reduction corresponds to a two-dimensional slice of the three-dimensional phase-space, within which it is still possible to recover a wide range of equilibrium vesicle shapes, including the desired bicuspid vesicle.

### 5.2.3 Computation of Membrane Forces

The immersed boundary force contributions (Eqs. (5.22, 5.27, 5.28)) presented in the previous sections need to be computed in a manner which is: (i) computationally efficient, with (ii) the embedded surface metrics computed with sufficient accuracy. All three immersed boundary forces were dependent upon either the mean curvature ( $H$ ), Gaussian curvature ( $K$ ) or both. Hence, a method of computing the principle curvatures of the surface,  $\kappa_1$  and  $\kappa_2$  is needed, in order calculate the surface curvatures:

$$H = \frac{1}{2}(\kappa_1 + \kappa_2), \quad K = \kappa_1 \kappa_2. \quad (5.42)$$

Outlined here is a method of computing these surface curvatures in a way that meets both requirements (i) and (ii). In the laboratory frame, i.e, the frame corresponding to the simulation co-ordinate reference frame, denoted  $\underline{R} = (X, Y, Z)$ , the normal to the surface  $\hat{N}(\underline{R})$  is conveniently computed from the (normalised) local gradient of

## 5. The Simulation of Fluid-Filled Vesicles using cMCLBM

the interface ( $\rho^N$ ). Since the normal is also already required within the cMCLBM algorithm, its computation represents no further overhead. Due to the ease of computation of the normal by using optimum, compact stencils, we seek to compute the requisite surface curvatures from the unit normal, within the laboratory frame. For clarity, before starting the analysis, it makes sense to point out the notation used in the analysis as well as the fundamental steps. The three co-ordinate frames referenced and their notation can be found in Table 5.2 (note: in all frames, the surface normal is aligned with their related  $Z$ ,  $z$ ,  $z'$  axis).

Co-ordinate Frame Notation Table		
Frame	Co-ordinate notation	Normal notation
Laboratory (Simulation) $\Sigma_L$	$\underline{R} = (X, Y, Z)$	$\hat{N} = (\hat{N}_X, \hat{N}_Y, \hat{N}_Z)$
Surface (General) $\Sigma$	$\underline{r} = (x, y, z)$	$\hat{n} = (\hat{n}_x, \hat{n}_y, \hat{n}_z)$
Surface (Specific) $\Sigma'$	$\underline{r}' = (x', y', z')$	$\hat{n}' = (\hat{n}'_x, \hat{n}'_y, \hat{n}'_z)$

**Table 5.2:** Table outlining the three co-ordinate frames, ( $\Sigma_L$ ,  $\Sigma$ ,  $\Sigma'$ ) and corresponding notation. Where  $\Sigma_L$  is the simulation frame,  $\Sigma$  is a local surface frame where the tangent vector do not align with the principle curvatures of the surface,  $\Sigma'$  is a local surface frame where the tangent vector do align with the principle curvatures of the surface.

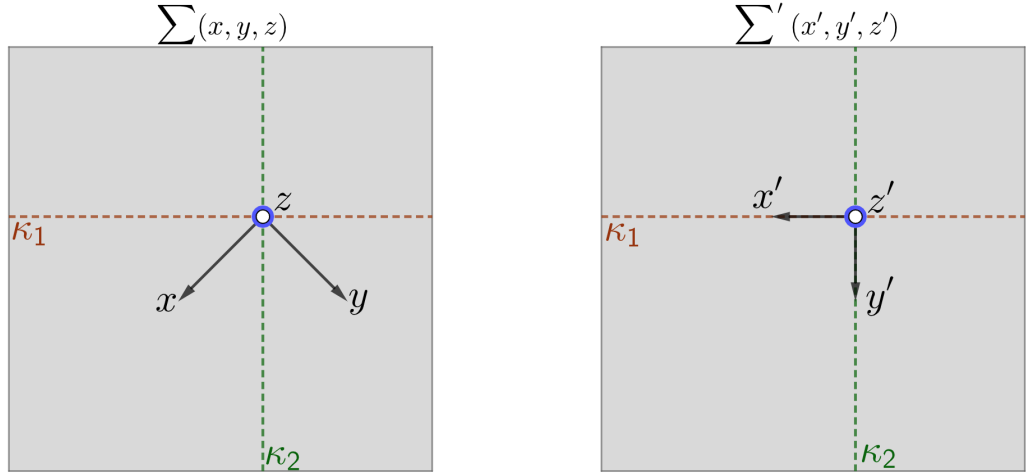
The methodology for finding the principle curvatures of the surface, from the surface normal, can be summarised in the following steps: (i) Find a local surface (membrane) tangent plane basis, in terms of globally measured  $\hat{N}$  (unit normal), i.e., *transform from laboratory frame  $\Sigma_L$  to surface general frame  $\Sigma$* . (ii) Apply an Euler rotation about the normal  $\hat{n}$  such that the tangent axes align with the principal curvatures of the surface, i.e., *transform from surface general frame  $\Sigma$  to surface specific frame  $\Sigma'$* . (iii) Identify the definitions for the principle curvatures,  $\kappa_1$ ,  $\kappa_2$ . (v) Calculate the terms needed for the computation of the subsequent equations for the surface curvatures.

In the following, we start from step (ii) and return to step (i) at the end, in order to connect the results to the laboratory frame. This choice was made to increase transparency of the mathematical working, however, still following the same essential steps outlined prior.

### 5.2.3.1 Finding the principle curvatures of the surface in non-simulation frame

Choose a point  $P$  on the local surface  $S$ , where the normal to the surface  $\hat{n}$  ( $\hat{n}'$ ) at this point is aligned with the  $z$  ( $z'$ ) axis for the two local surface co-ordinate frames  $\Sigma$  ( $\Sigma'$ ). Thus, the  $x, y$  ( $x', y'$ ) axes are tangent to the surface at point  $P$ , where, for frame  $\Sigma'$  the  $x', y'$  axes align with the principle curvatures of the surface.

## 5. The Simulation of Fluid-Filled Vesicles using cMCLBM



**Figure 5.5:** Schematic showing the two local co-ordinate frames from a view looking down the normal to the surface ( $z, z'$  axis); General frame  $\Sigma(x, y, z)$  (left) and Specific frame  $\Sigma'(x', y', z')$  (right). Within the General frame, the orthogonal tangent plane ( $x, y$ ) does not align with the principal curvatures of the surface. Whereas in the Specific frame, the orthogonal tangent plane ( $x', y'$ ) aligns with the principal curvatures of the surface ( $\kappa_1, \kappa_2$ ).

This geometry is shown in Figure 5.5, registered to a line of sight down the surface normal. Point  $P$  is taken to be located at  $x = y = z = 0$  ( $x' = y' = z' = 0$ ), and  $S$  is defined implicitly as  $F(x, y, z) = 0$ .  $z$  is an function, which is evaluated from  $x, y$  and is effectively defined by:

$$z = f(x, y). \quad (5.43)$$

The above effective manifold is a Monge surface —a surface, or patch, that is given by its height over a plane which is usually a function of the orthogonal co-ordinates of that plane —with  $x, y$  characterising the tangent plane of the surface, Eq. (5.43) represents a local membrane patch on which  $\rho^N = \text{constant}$ . (Here, of course, the constant changes as one moves through the interfacial region of the system in the  $z$  direction.) Expressing  $f(x, y)$  as the 2<sup>nd</sup> degree Taylor expansion polynomial for an expansion about point  $P = (0, 0, 0)$  gives:

$$f(x, y) = [f]_P + x[f_x]_P + y[f_y]_P + \frac{x^2}{2}[f_{xx}]_P + xy[f_{xy}]_P + \frac{y^2}{2}[f_{yy}]_P + O(x^3, y^3), \quad (5.44)$$

where, index  $x, y$  on  $f$ , denotes differentiation of  $f$  with respect to  $x, y$ . The first term can be evaluated as  $[f]_P = 0$  by definition, as the origin of  $\Sigma$  is taken to be at  $P = (0, 0, 0)$ . Further, the linear terms,  $x[f_x]_P = y[f_y]_P = 0$ , as the co-ordinates  $x, y$  are supposed to lie in the tangent plane to the surface  $S$  at point  $P$ . Accordingly, Eq. (5.44) becomes:

$$f(x, y) = Ax^2 + By^2 + Cxy + O(x^3, y^3), \quad (5.45)$$

### 5. The Simulation of Fluid-Filled Vesicles using cMCLBM

in which the constant terms are defined:

$$A = \frac{1}{2}[f_{xx}]_P, \quad B = \frac{1}{2}[f_{yy}]_P, \quad C = f_{xy} = [f_{yx}]_P, \quad (5.46)$$

where all the derivatives in Eq. (5.46) are evaluated at the point  $P$ .  $f(x, y)$  may now be written in the following matrix form:

$$f(x, y) = \underline{r} \underline{\underline{M}} \underline{r}^T, \quad \underline{\underline{M}} = \frac{1}{2} \begin{pmatrix} 2A & C & 0 \\ C & 2B & 0 \\ 0 & 0 & 0 \end{pmatrix}. \quad (5.47)$$

The matrix,  $\underline{\underline{M}}$  encapsulates all second derivatives of  $f(x, y)$  evaluated at  $P$  (it is the Hessian matrix of  $f$  at  $P$  [182]).

At this stage,  $f(x, y)$  is defined in co-ordinate frame  $\Sigma$ . In order to calculate the principle curvatures of the surface, it is necessary to transform from frame  $\Sigma$  to frame  $\Sigma'$ , where, recall, the tangent co-ordinate plane aligns with the principle curvatures of the surface. Remember that in both frames,  $\hat{n}$  ( $\hat{n}'$ ) both align with the  $z$  ( $z'$ ) axis. Thus, in order to align the  $x, y$  axes with the principle curvatures of the surface, frame  $\Sigma(x, y, z)$  must be rotated about  $\hat{e}_z$ , such that the resultant frame is  $\Sigma'(x, y, z)$ . This rotation by angle  $\theta$  will subsequently mean that  $C = 0$ , whereupon the frame has been successfully transformed to  $\Sigma'(x, y, z)$ .

Using the orthogonal Euler rotation matrices ( $\underline{\underline{R}}_z(\theta)$ ), it is possible to write equations for the position vectors of the surface as:

$$\underline{r}'^T = \underline{\underline{R}}_z(\theta) \underline{r}^T, \quad \underline{r}^T = \underline{\underline{R}}_z(\theta)^T \underline{r}'^T, \quad \underline{r} = \underline{r}' \underline{\underline{R}}_z(\theta). \quad (5.48)$$

Now seeking the value of  $\alpha$  using Eq. (5.48):

$$\begin{aligned} \underline{r} &= \underline{r}' \underline{\underline{R}}_z(\theta), \\ \underline{r} &= \begin{pmatrix} \cos(\theta) & -\sin(\theta) & 0 \\ \sin(\theta) & \cos(\theta) & 0 \\ 0 & 0 & 1 \end{pmatrix} \underline{r}' \\ \begin{pmatrix} x \\ y \\ z \end{pmatrix} &= \begin{pmatrix} \cos(\theta)x' + \sin(\theta)y' \\ -\sin(\theta)x' + \cos(\theta)y' \\ z' \end{pmatrix}. \end{aligned} \quad (5.49)$$

Substituting  $x, y, z$  from Eq. (5.49) into Eq. (5.45), after some simple algebra, the above equation reduces to:

$$\begin{aligned} f(x, y) &= [A \cos^2(\theta) + B \sin^2(\theta) - C \cos(\theta) \sin(\theta)] x'^2 + \\ &\quad [A \sin^2(\theta) + B \cos^2(\theta) + C \cos(\theta) \sin(\theta)] y'^2 + \\ &\quad [(A - B) \sin(2\theta) + C \cos(2\theta)] x' y'. \end{aligned}$$

## 5. The Simulation of Fluid-Filled Vesicles using *cMCLBM*

In order for the  $x, y$  axes to point in the direction of the principle curvatures of the surface, the cross term ( $x'y'$  term) must be zero. Hence, one can find the corresponding value of  $\theta$  for by requiring the cross  $x'y'$  term to vanish:

$$(B - A)\sin(2\theta) = C\cos(2\theta),$$

$$\theta = \frac{1}{2}\tan^{-1}\left(\frac{C}{B - A}\right). \quad (5.50)$$

Now that angle  $\theta$  has been defined, using Eq. (5.48), the surface  $f(x, y)$  can be transformed so as to be defined in terms of the variables of the frame  $\Sigma'(x, y, z)$ , as follows:

$$f(x', y') = \underline{r}' \underline{M}' \underline{r}'^T, \quad \underline{M}' = \underline{R}_z(\theta) \underline{M} \underline{R}_z(\theta)^T, \quad (5.51)$$

where:

$$\underline{M}' = \text{diag}(\kappa_1, \kappa_2, 0), \quad (5.52)$$

and from prior analysis, curvatures  $\kappa_1, \kappa_2$  are defined as

$$\begin{aligned} \kappa_1 &= f_{xx}\cos^2(\theta) + f_{yy}\sin^2(\theta) + f_{xy}\sin(2\theta), \\ \kappa_2 &= f_{xx}\sin^2(\theta) + f_{yy}\cos^2(\theta) - f_{xy}\sin(2\theta). \end{aligned} \quad (5.53)$$

Note, summing  $\kappa_1$  and  $\kappa_2$  results in  $\kappa_1 + \kappa_2 = f_{xx} + f_{yy}$ . The latter, will be discussed further shortly, can be rewritten as  $2H = -\nabla \cdot \hat{n}$  and, as such, the definition of mean curvature is as expected, namely:  $H = \frac{1}{2}(\kappa_1 + \kappa_2)$ .

We conclude this part of our analysis. By applying a rotation of  $\theta$  (defined in Eq. (5.50)) about the normal to the surface ( $\hat{e}_z$ ), the axes that span the tangent to the surface have been aligned with the principal curvatures of the surface ( $\kappa_1, \kappa_2$ ). The surface is thus defined as:

$$f(x', y') = \frac{1}{2}\kappa_1 x'^2 + \frac{1}{2}\kappa_2 y'^2, \quad (5.54)$$

with  $\kappa_1$  and  $\kappa_2$ , (see Eq. (5.53)), clearly the principal curvatures of S at P. Henceforth, the mean ( $H$ ) and Gaussian ( $K$ ) curvature of the surface are defined via the principle curvatures, as given in Eqs (5.42)

### 5.2.3.2 Relating Laboratory frame $\Sigma_L$ to Surface frame $\Sigma'$

So far, an equation for the principle curvatures of a surface have been recovered from an arbitrary frame, in which the  $x$  and  $y$  axes at point  $P$  span the tangent plane of the surface and the  $z$  axis is normal to the surface, at that point. In this section, this frame is related to the laboratory frame  $\Sigma_L$  and in doing so, the curvatures of the surface can then be calculated in the simulation frame using Eq. (5.53).

### 5. The Simulation of Fluid-Filled Vesicles using cMCLBM

The local co-ordinate frame  $\Sigma$  may be constructed from the simulation frame  $\Sigma_L$ , through the use of the easily computable normal  $\hat{N}$ . Since axis  $\hat{e}_z$  aligns with the normal, it is defined as such in the laboratory frame:

$$\hat{e}_z = \left( [\hat{N}_X]_P, [\hat{N}_Y]_P, [\hat{N}_Z]_P \right), \quad (5.55)$$

where then the tangent plane axis can be constructed through appeal to the definitions of the dot and cross products. A possible co-ordinate geometry can be defined as follows, relating solely to the normal components in the lab frame:

$$\begin{aligned} \hat{e}_x &= \frac{1}{\sqrt{1 - [N_Z]_P^2}} \left( -[\hat{N}_Y]_P, [\hat{N}_X]_P, 0 \right), \\ \hat{e}_z \times \hat{e}_x = \hat{e}_y &= \frac{1}{\sqrt{1 - [N_Z]_P^2}} \left( -[\hat{N}_X \hat{N}_Z]_P, -[\hat{N}_Y \hat{N}_Z]_P, [(1 - \hat{N}_Z^2)]_P \right). \end{aligned} \quad (5.56)$$

For this particular choice, at locations where  $N_z \rightarrow 1$ , the error in the calculation will be amplified. See appendix B for alternative choices for the co-ordinate system, which can be selected based upon relative error at a given region.

The normal in frame  $\Sigma$  can be written from Eq. (5.43) as  $\underline{n} = \underline{\nabla}_x(z - f(x, y)) = (-f_x, -f_y, 1)$ , so that, normalising, we have within the environment of P:

$$\hat{n} = -\frac{1}{\sqrt{1 + f_x^2 + f_y^2}} (f_x, f_y, -1). \quad (5.57)$$

Note that at P itself:

$$[f_x]_P = [f_y]_P = 0, \implies [\hat{n}]_P = (0, 0, 1), \quad (5.58)$$

as required. The normal can then be computed in simulation by projecting laboratory normals onto the local axis defined in Eq. (5.56):

$$\hat{n}_x = \hat{N} \cdot \hat{e}_x, \quad \hat{n}_y = \hat{N} \cdot \hat{e}_y, \quad (5.59)$$

and similarly for the local operators:

$$\frac{\partial}{\partial x} = \hat{e}_x \cdot \underline{\nabla}_X, \quad \frac{\partial}{\partial y} = \hat{e}_y \cdot \underline{\nabla}_Y. \quad (5.60)$$

Now, to calculate  $\kappa_1$  and  $\kappa_2$ ,  $[f_{xx}]_P$ ,  $[f_{xy}]_P$  and  $[f_{yy}]_P$  need to be evaluated in simulation frame. From Eq. (5.57), the following definition of  $f_x$  and  $f_y$  are found:

$$\begin{aligned} f_x &= -\hat{n}_x (1 + f_x^2 + f_y^2)^{1/2}, \\ f_y &= -\hat{n}_y (1 + f_x^2 + f_y^2)^{1/2}. \end{aligned} \quad (5.61)$$

## 5. The Simulation of Fluid-Filled Vesicles using cMCLBM

From this, calculating  $f_{xx}$  using the definition in Eq. (5.61)

$$\begin{aligned} f_{xx} &= \frac{\partial}{\partial x} \left( -\hat{n}_x (1 + f_x^2 + f_y^2)^{1/2} \right) \\ &= -\hat{n}_x \frac{f_x f_{xx} + f_y f_{yx}}{(1 + f_x^2 + f_y^2)^{1/2}} - (1 + f_x^2 + f_y^2)^{1/2} (\hat{n}_x)_x, \end{aligned} \quad (5.62)$$

which when evaluated at point  $P$ , results in the following:

$$\begin{aligned} [f_{xx}]_P &= -[(\hat{n}_x)_x]_P, \\ [f_{yy}]_P &= -[(\hat{n}_y)_y]_P, \\ [f_{xy}]_P &= -[(\hat{n}_y)_x]_P = -[(\hat{n}_x)_y]_P, \end{aligned} \quad (5.63)$$

where  $(\hat{n}_y)_x = \frac{\partial \hat{n}_y}{\partial x}$  etc.

In conclusion, the laboratory frame  $\Sigma_L$  is related to the surface frame  $\Sigma'$  through Eqs. (5.59,5.60,5.63), which can then be used to evaluate Eq. (5.53), to find the principle curvatures of the surface in laboratory frame. The final step of this workflow is presented within Appendix B.1, which documents the mathematical steps for evaluating Eqs. (5.59,5.60,5.63). The outcome is that the above-outlined methodology results in the principle curvature being calculated and defined solely from the surface normal in the laboratory frame, with the motivation being the computation of the immersed boundary forces, in a way that is as efficient, transparent, and as practically executable as possible.

### 5.2.4 Multiple Vesicles

Within Chapters 3 and 4, the work was focused on the simulation of two-component fluid flows; this would amount to the simulation of a single vesicle (RBC) within a background fluid (plasma), for the current model. Later in this Chapter and Chapter 6, the simulation of three or more components will be considered, for the case of vesicles, i.e., two or more vesicles being simulated. Within Chapter 3, the methodological extension to the simulation of many liquid drops, using chromodynamic and colour-gradient MCLBMs was discussed, with the innovations of Yuan et al. [92] prominent. The colour-gradient or cMCLBM class of models have distinct advantages when simulating ternary fluid systems, such as their strict mass conservation and ability to tune surface tension values for each fluid easily and accurately. Yuan et al. presented an enhanced segregation rule, which recovered convincing results of three-phase simulations (tertiary immiscible fluid flows), using the following segregation process. The segregation parameter (or interface width) between two fluids  $C$  and  $C'$  is controlled by  $\beta_{CC'}$  and is now made adjustable, in relation to the surface tension values between the fluids. The value of  $\beta_{CC'}$  is calculated through first evaluating

## 5. The Simulation of Fluid-Filled Vesicles using cMCLBM

whether a Neumann's triangle is present in Eq. (3.11a), then using this value to determine how the interface width between fluids  $C$  and  $C'$  should be perturbed to give correct wettability of the fluids —Eqs. (3.11b,3.11c).

For the simulation of vesicles or RBCs, the aim of this recent cMCLBE segregation is to maintain complete immiscibility between the fluids, i.e., prevent the Neumann triangle forming. From this and, also, making the assumption that the vesicles are not initially overlapping each other in simulation, if the surface tension of the vesicles ( $V$ ) relative to background fluid ( $B$ ) is given by  $\sigma_{VB} = \sigma_0$ , then on simple arguments of mechanical stability, by ensuring that the surface tension between vesicles is  $\sigma_{VV'} \geq 2\sigma_0$ , the fluids should remain completely immiscible. This then means that the equations developed in [92] can be simplified, with the  $\beta$  values for a given vesicle-background  $VB$  and vesicle-vesicle  $VV'$  pairing given as follows:

$$\beta_{VB} = \beta^0 - \beta^0 \min \left( \frac{35\rho_V \rho_B \rho_C}{\rho^3}, 1 \right) \quad (5.64a)$$

$$\beta_{VV'} = \beta^0 + \beta^0 \min \left( \frac{35\rho_V \rho_{V'} \rho_C}{\rho^3}, 1 \right) \quad (5.64b)$$

where subscripts  $B, V, V', C$  correspond respectively to the background fluid, a given vesicle, a different vesicle and the fluid component with the largest density at that site, other than the other two previously mentioned fluids in the equation. Equations (5.64a,5.64b) now represent the perturbations needed to the interface width parameter (segregation parameter) between fluid pairs, which alongside setting the surface tension value of a vesicle-vesicle interface twice to that of a vesicle-plasma interface, allowing for the simulation of many completely immiscible vesicles.

As discussed, the downside of this and other multi-fluid cMCLBMs is that although they allow high tune-ability and control of the surface tensions and fluid-fluid contacts, it comes at an increase of computational cost. With the number of interfaces in relation to the number of fluids  $n$ , being given by: No. of interfaces =  $\frac{n(n-1)}{2}$ . The reduction of the number of interfaces and, hence, the computational cost will be discussed further later in this thesis.

## 5.3 Results

A novel method of simulating vesicles in three-dimensions, using an immersed boundary force chromodynamic multi-component lattice Boltzmann variant has been outlined. Additionally, this is a computationally efficient method of calculating the



## 5. *The Simulation of Fluid-Filled Vesicles using cMCLBM*

principle curvatures of the vesicle surface in simulation, through use of an easily computable surface normal. As such, the emphasis is now on the validation of the method, by examining its equilibrium steady state and dynamical data.

First, looking at steady state equilibrium data produced by the model. In the case of zero-physical flow, only vesicle profile is at issue. The principal outcome of assessing steady state equilibrium data is to validate vesicle shape, specifically for current purposes, the ability of the method to recover a bicuspid profile representative of that of a healthy, human RBC. As a starting point, a sampled, restricted phase-space is examined to observe the range of vesicle profiles recovered by the model when parameterising with surface tension and bending rigidity, where the impact of the deflation parameter (or, equivalently, target area) is also briefly discussed. Once qualitatively correct vesicle profiles are confirmed, sufficient simulation resolution will be checked. Sufficient resolution is needed if the immersed boundary force is to be applied correctly; both resolution and accuracy of the curvature calculations being checked through a grid convergence test (GCT) and by appealing to Gauss-Bonnet theory. Once adequate resolution is confirmed, the form of the vesicle shape (or profile) is assessed for adherence to the desired bicuspid profile, through comparison against theory [183] (other vesicle profiles being reviewed through the use of a shape metric).

Subsequent to the initial validation of a steady state equilibrium conformation in the method, dynamical tests and flow data will be presented. The aim of these data is to demonstrate that the model can successfully reproduce RBC dynamics, far from its mechanical equilibrium, whilst remaining stable in simulation and retaining target physical properties (such as surface area conservation). First, the Wheeler experiment is used to validate the method in a shear flow, but also to allow immersed boundary force constants to be tuned, to replicate vesicle behaviour as accurately as possible. The physical flow behaviour during the vesicle shear will also be analysed, to highlight the ability of the method accurately to produce physically consistent flow data, at a detailed level. The pseudo-elasticity, or reversibility of the method, i.e., the ability for the vesicle to recover from shear, is presented to demonstrate stability and robustness of the model. Finally, the initial extension of the methodology to more than one vesicle is considered. Here, vesicle-vesicle interactions will be simulated, to provide initial proof that the method can be extended to multiple vesicles, using existing methodologies [184, 92]. However, many RBC deployments are clearly beyond the scope of the developmental work reported here.

### 5.3.1 Steady State Equilibrium Data

For current interests, the main demand of the model's steady state equilibrium data, is that it will, in some part of its input parameter space, recover the desired bicuspid vesicle profile. Qualitatively, this is easy to judge by inspecting steady state output vesicle profiles, and more critically, by measuring curvature values over the surface. However, the following also seeks to provide further quantitative evidence of correct bicuspid vesicle profile. Consequently, after examining the *zoo* of vesicle shapes, produced by varying the force parameters discussed in section 5.2.2, methods of assessing shape accuracy will be presented.

#### 5.3.1.1 Phase-Space

In section 5.2.2, the immersed boundary force was characterised, as well as the key parameters in the immersed boundary force discussed. Clearly, the model has a complex three dimensional phase-space, defined by three parameters which determine vesicle shape:  $\Upsilon$  - level of deflation,  $\sigma$  - interfacial tension and  $\kappa_B$  - bending rigidity. Here, the level of deflation could be replaced with target surface area  $A_0$ , used within the area conserving force. As discussed in section 5.2.2, although  $A_0$  does affect the vesicle shape produced, the area conserving force has little dynamical impact once the cross-sectional area approaches the desired area. For a correctly parameterised simulation, cross-sectional area drifts very little from the desired area.

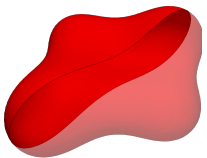
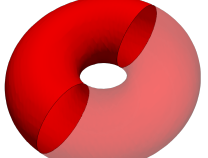
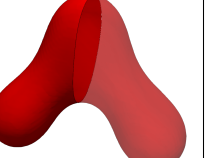
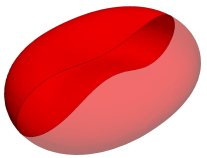
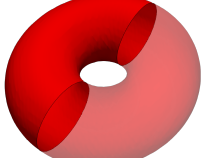
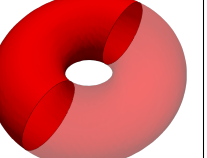
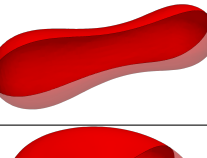
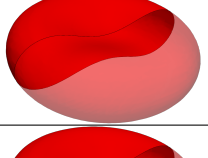
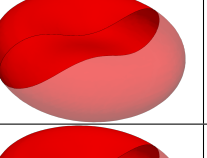

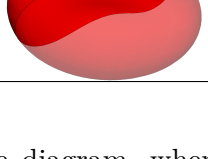
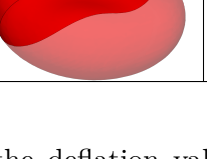
#### Restricted Phase-Space: Fixed Deflation

To ease the task of surveying the three-dimensional phase-space, the deflation value is fixed for the initial tests reported here, resulting in a convenient, two-dimensional phase-space. The choice of deflation value must presumably affect the *zoo* of shapes produced, within a space spanned by surface tension and bending rigidity values. For the following results, the deflation value was set to  $\Upsilon = 1.31$ . This value was chosen initially for deflation from prior literature, that surveyed a partial phase-space using the spontaneous curvature model, in which the authors showed that for a preferred curvature set equal to zero, oblate vesicles were recovered at a given volume to surface area ratio close to that found in our model when using  $\Upsilon = 1.31$  [185, 186]. Hence, a value of  $\Upsilon = 1.31$  is deemed as appropriate initially, when seeking to recover a bicuspid shaped vesicle. It is however worth noting that bicuspid vesicles have been recovered for much lower and larger deflation values, using our method. Anecdotally, by perturbing the  $\sigma$  and  $\kappa_B$  values used, it is possible to recover a wide range of shape profiles for many deflation values. That is, there is considerable variation of equilibrium shape with operating point location. In principle, then, this

### 5. The Simulation of Fluid-Filled Vesicles using *cMCLBM*

may facilitate the use of a smaller deflation value, to reduce computational expense (by decreasing the size of the deflated vesicle).

The vesicle shape outcomes of a sampled phase-space, where  $\Upsilon = 1.31$  and  $\sigma$  and  $\kappa_B$  values are varied, is shown in Table 5.3. This table now presents a small, but appropriate representation of a slice of the phase space when targeting a RBC profile. It is seen that by varying the surface tension and bending rigidity values, the shape outcome changes, with the effects of both varying the surface tension ( $\sigma$ ) and bending rigidity ( $\kappa_B$ ) being apparent. The simulation outputs of equilibrium vesicle shape are shown in the cells of the table, given by semi-transparent images to help highlight the vesicles' shape profiles, where visualisations were obtained through use of the ParaView software—with contours defined by the  $\rho^N = 0$  field (mid-interface). Firstly, it can be seen that the desired bicuspid has been recovered, for instance with parameterisation ( $\sigma = 0.1$ ,  $\kappa_B = 1.0$ ). It can also be seen that for a further restricted parameter space, i.e., when  $\kappa_B = 0.01$ , a range of shapes with a varying degree of symmetry have been produced. This highlights the sensitivity of the model to its parameterisation.

$\kappa_B$	$\sigma$		
	$1 \times 10^{-1}$	$1 \times 10^{-3}$	$1 \times 10^{-5}$
0.01			
0.1			
0.25			
1.0			

**Table 5.3:** A sampled, restricted phase diagram, where the deflation value is fixed ( $\Upsilon = 1.31$ ) and the bending rigidity ( $\kappa_B$ ) and surface tension ( $\sigma$ ) values are perturbed to give a range of vesicle profiles. To help highlight these profiles, semi-transparent surface plots taken at contour  $\rho^N = 0$  are shown in each grid cell [20].

## 5. The Simulation of Fluid-Filled Vesicles using cMCLBM

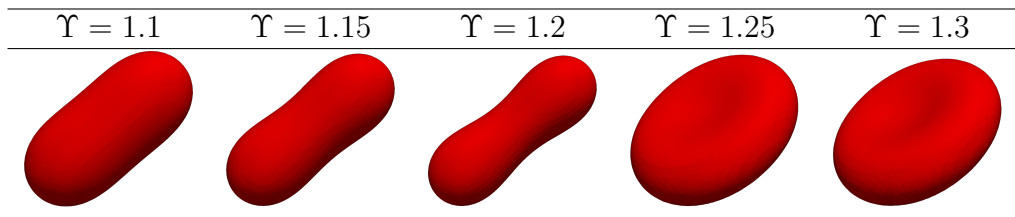
The vesicle shapes in Table 5.3 may be characterised as follows:

Oblate vesicles, occur where the shape profile is short about the axis of rotation—such as the desired bicuspid vesicle (i.e.,  $\kappa_B = 1.0$ ,  $\sigma = 0.1$ ) and the torus vesicle ( $\kappa_B = 0.1$ ,  $\sigma = 1 \times 10^{-3}$ ). Note, shapes with singular and multiple holes have been reported throughout literature [187, 188]. Prolate vesicles, which are long about the axis of rotation ( $\kappa_B = 0.25$ ,  $\sigma = 1 \times 10^{-1}$ ). Non-axially symmetric vesicles, such as the *starfish* vesicle [189, 190], ( $\kappa_B = 0.01$ ,  $\sigma = 1 \times 10^{-5}$ ) are, apparently, not new.

Between the shapes shown in Table 5.3, there are a continuum of shapes which deform between identified selections. Although these results represent only a small sample of a simplified phase-space, these data provide an qualitative conformation of the methodology, through recovering a bicuspid vesicle. The result also provides a range of parameterisation, which may later be tuned in order to recover correct RBC dynamics—to which we will return shortly.

### Variable Deflation

The sampled phase-diagram presented in Table 5.3 highlights how changing the model’s bending rigidity and surface tension parameters can affect the vesicle steady state shape outcome. However, in section 5.2.2, it was explained that the level of deflation  $\Upsilon$ , or target vesicle surface area  $A_0$ , also had an effect on vesicle steady state profile. As such, for present purposes, the bending rigidity and surface tension values are fixed, with the deflation (hence target surface area) being varied. The impact of changing the level of deflation is that it will affect how much *excess* surface area the vesicle has, as well as changing the vesicle volume to surface area ratio. Although only steady state (zero flow) data are being considered at this point, it is intuitively apparent that the level of deflation must also affect the vesicle dynamics.



**Figure 5.6:** Table showing the equilibrium steady state vesicle profiles, in zero physical flow, for a range of deflation values ( $\Upsilon$ , see table headings) and fixed  $\kappa_B = 1.25$ ,  $\sigma = 0.001$  values. The surface area of the displayed vesicles are given by  $A_0 = \Upsilon A_{\text{sphere}}$ , where  $A_{\text{sphere}} \approx 2827$ .  $\Upsilon = 1.1, 1.15, 1.2$  produce prolate vesicles, whereas larger deflation values:  $\Upsilon = 1.25, 1.3$  are seen to produce oblate vesicles.

In Table 5.6, a range of different vesicle outcomes are found for a parameterisation where  $\kappa_B = 1.25$ ,  $\sigma = 0.001$  and the deflation value varied over the range  $[1.1, 1.3]$ . The results in the table show that, for deflation values of  $\Upsilon = 1.1, 1.15, 1.2$ , prolate

## 5. The Simulation of Fluid-Filled Vesicles using *cMCLBM*

vesicles are produced at steady state, whereas at deflation values of  $\Upsilon = 1.25, 1.3$ , oblate vesicles are seen. Although the phase-space has only been subjected to a limited, coarse grained sampling thus far (due to the computational costs involved in searching the entire phase-space in fine detail) the results in Table 5.6 are qualitatively understandable. Here it should be noted that the parameterisation of complex, computationally expensive models, the fine structure of their parameter space, its global and local structure and the analysis of variation, are a subject in itself. Due to the profile of a RBC (which when compared to a sphere, has a much smaller volume to surface area ratio), one would expect that, to retrieve a bicuspid shape, an appropriate amount of deflation (hence *excess* surface area) is needed, in order for the vesicle to deform from the initialised spherical vesicle of area  $A_{\text{sphere}}$  into the bicuspid vesicle of area  $A_0$ . However, for prolate vesicles, one may assume that a smaller amount of excess surface area is needed for the initially spherical vesicle to transform into a prolate vesicle. This observation clearly does not mean that prolate vesicles can not be recovered for larger deflation values, but it may help provide an initial estimate of the deflation value when aiming to recover a specific profile. A similar idea was deployed when choosing a deflation value of  $\Upsilon = 1.31$  for the phase-diagram shown in Table 5.3, in order to increase the chance of recovering the desired bicuspid vesicle.

Seemingly, qualitatively correct bicuspid profiles are recovered in our model; nevertheless, it is important to now check that the resolution of these vesicles is appropriate. Put another way, does the simulation have appropriate resolution such that the interface is sufficiently resolved?

### 5.3.1.2 Method Accuracy

#### Adequate interfacial resolution

As stated previously, the outlined method benefits from an automatic adaptive mesh in that in the interfacial region, in which the immersed boundary force is applied, will deform with the vesicle and maintain the resolution (of the underlying lattice) throughout the simulation, without active adaptation, i.e., re-meshing for different flow-induced deformation. Hence, if one can guarantee that interfacial resolution is adequate in steady state, it should remain adequate throughout simulation, implying the immersed boundary force can be appropriately communicated locally, under flow induced deformation. If there is inadequate resolution in the interfacial region, one would expect some level of error in the communication of the immersed boundary force, leading to some level of error in the emergent vesicle profile. To verify appropriate resolution in the interfacial region, the Gaussian curvature over the surface is evaluated, using Gauss-Bonnet theory. If the interface is not adequately

## 5. The Simulation of Fluid-Filled Vesicles using cMCLBM

resolved or the curvature calculations in section 5.2.3 are inaccurate, the result will not, presumably, agree with Gauss-Bonnet theory. The Gauss-Bonnet theorem relates the surface integral of the Gaussian curvature over a two-dimensional manifold to the Euler characteristic of the manifold as follows [191]:

$$\langle K \rangle_S = \iint_M K dA = 2\pi\chi(M), \quad (5.65)$$

where, the left hand side is the surface integral over the manifold ( $M$ ),  $dA$  is the area element and  $\chi(M)$  is the Euler characteristic of the manifold.

In simulation, there is a quasi two-dimensional interface of a width controlled by segregation parameter  $\beta$ . The surface integral of the Gaussian curvature over the surface is computed by a weighted sum of the phase-field, divided by the interface width,  $\omega$ :

$$\langle K \rangle_S = \frac{1}{\omega} \sum K(\underline{r}^*) (1 - \rho^N(\underline{r}^*)^2) = 2\pi\chi(M), \quad (5.66)$$

in which the summation is taken over all discrete lattice positions  $\underline{r}^*$ , where, due to the weight of the interface, values close to mid-interface will have a larger contribution (i.e., when  $\rho^N = 0$ ). By the Gauss-Bonnet Theorem in  $\mathbb{R}^3$ , from Eq. (5.65) we should have:

$$\langle K \rangle_S = 4\pi. \quad (5.67)$$

Using the definition in Eq. (5.66), for the vesicles considered in the data of Table 5.3 (which have an un-deflated initial vesicle radius of  $R = 15$ ), the following was observed:

$$\frac{\langle K \rangle_S}{\pi} = 4.03. \quad (5.68)$$

From the above result, it is possible to conclude that the method of computing the surface curvatures outlined in section 5.2.3 is correct, and that interfacial resolution is adequate for the simulations represented in Table 5.3 (see section 5.3.1.1 for information on parameterisation). If this were otherwise, the result in Eq. (5.68) would not agree with Gauss-Bonnet theory. Obviously, there is a slight numerical error, with the result being within 1% of the target result. This is deemed to arise from sampling the discrete interface and as it can be reduced by increasing system resolution. In the context of work presented shortly, the accuracy, here, is deemed to be sufficient and system resolution to be appropriate. As such, we tentatively conclude that, throughout simulations, the vesicle interface resolution should remain appropriately resolved, due to the presence of an automatic adaptive mesh and the assurance of this verification.

Further to justify the choice of vesicle membrane resolution, a Grid Convergence Test

## 5. The Simulation of Fluid-Filled Vesicles using *cMCLBM*

(GCT) giving limited insight into the impact of resolution on vesicle shape is carried out. Starting with an un-deflated initial vesicle radius of  $R = 15$ , parameterisations and resolution were scaled respectively by factors of 1, 1.1666, 1.5 (coarse, medium, fine resolution hereafter). Slices through the axially symmetric oblate vesicle for coarse (red), medium (blue) and fine (black) resolutions are displayed in Figure 5.7, where the results have been scaled to allow them to be layered on the same figure. These data show minimal difference between vesicle shape due to the resolution. To quantify this, the results of the GCT, following Roache [192] and Celik [193], are given in Table. 5.4. Results show that, for the fine resolution —a Grid Convergence Index (GCI) is 0.39%, and for the coarse resolution —a GCI is still less than 5%, (relative to Celik’s equivalent, extrapolated (infinite resolution) maximum height parameter value 8.37 [193]). This result justifies the choice of the coarser resolution, which is an appropriate balance of computational efficiency and adequate resolution.

Resolution designation	Scale factor	Maximum height	Relative estimated % (GCI)
Coarse ( $R = 15$ )	1	8.744	−4.46
Medium ( $R = 17.5$ )	1.1666	8.511	−1.68
Fine ( $R = 22.5$ )	1.5	8.402	−0.39

**Table 5.4:** Results of a grid convergence test (GCT) examining the effects of resolution on vesicle profile. Here, the maximum height of the dumbbell ends of the vesicle profiles shown in Figure 5.7 were compared for three different resolutions; Coarse, Medium, Fine. The resolutions are defined based on the initial undeflated vesicle radius ( $R$ ), with the coarse resolution having  $R = 15$ , and the Medium and Fine resolutions having relative scale factors of 1.1666 and 1.5. The relative estimated grid convergence index (GCI) for maximum height of the dumbbell ends is 8.37 (lattice units), with the coarse resolution result being within 5% of this [20].

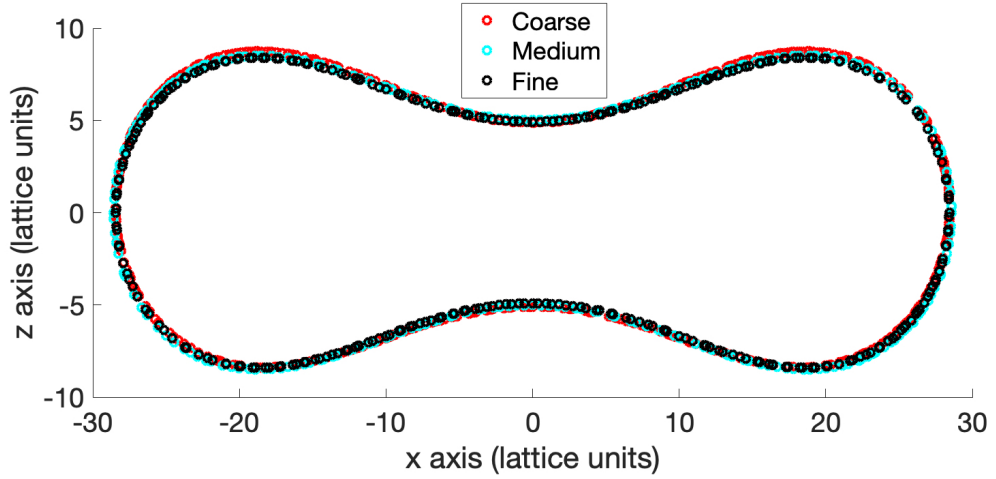
We have, in this section, confirmed appropriate resolution through compliance with (i) Gauss-Bonnet theory and (ii) results of a GCT (applied to the converged bicuspid vesicle profile). We proceed to perform further verification now.

### Quantifying Vesicle Shape

To provide quantitative conformation that the desired erythrocyte (human RBC) shape is correctly recovered, the parameterisation  $\kappa_B = 0.25, \sigma = 1 \times 10^{-5}$  seen in Table 5.3 is compared against theory. In 1972, Evans and Fung [183] developed a parametric expression, from experimental data, for erythrocyte geometry. Taking the  $x$ - $y$  co-ordinates to span the plane perpendicular to the axis of rotational symmetry ( $z$ ), the  $z$  value (depth of the our RBC) is given by [183]:

$$z = \frac{R_0}{2} \left[ 1 - \frac{r^2}{R_0^2} \right]^{\frac{1}{2}} \left[ C_0 + C_1 \frac{r^2}{R_0^2} + C_2 \frac{r^4}{R_0^4} \right], \quad (5.69)$$

## 5. The Simulation of Fluid-Filled Vesicles using cMCLBM



**Figure 5.7:** Results of a grid independence test, where the effects of lattice resolution on the equilibrium shape of a bicuspid vesicle is presented. Here, data are shown for slices taken through the vesicles  $x$ - $z$  plane for three different resolutions. These resolutions are —coarse (Red), medium (Blue) and fine (Black) —with relative lattice scale factors 1, 1.166 and 1.5 (where coarse corresponds to an initial undeformed lattice radius of  $R = 15$ ). To allow for vesicle profile comparison, results were scaled and overlaid as shown here. Note, when scaling lattice dimensions, one must also scale the surface tension and bending rigidity values as shown in Eq. (5.40). Corresponding grid convergence test (GCT) data are given in Table 5.4 [20].

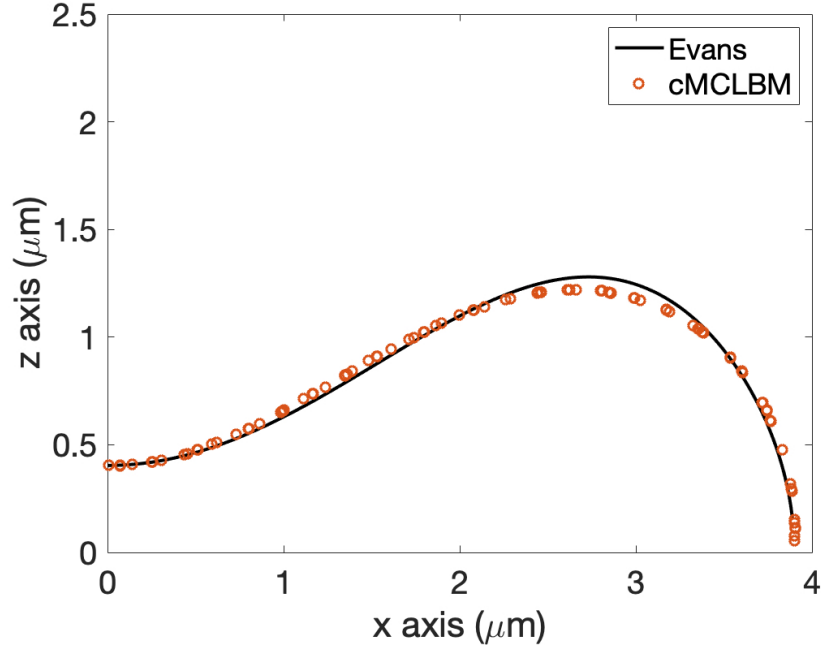
where  $R_0 = 3.91\mu\text{m}$  is a size parameter,  $C_0 = 0.81$ ,  $C_1 = 7.83$ ,  $C_2 = -4.39$  are shape constants and  $r = \sqrt{x^2 + y^2}$  [183]. Here, the values of the size and shape constants are chosen to recover erythrocyte specific geometry.

To compare simulation results against this expression, the top right quadrant of a slice taken through the centre of mass of the axially symmetric bicuspid vesicle shown in Table 5.3, (parameterisation  $\kappa_B = 0.25$ ,  $\sigma = 1 \times 10^{-5}$ ) is reviewed. Figure 5.8 compares simulation data (orange circles) and Evans and Fung’s parametric expression in Eq. (5.69) [183] (Black line), where size parameter  $R_0$  was used to fit the data. These data show that the profile developed by the cMCLBM compares well with the parametric expression for erythrocyte geometry developed from observation, by Evans and Fung, providing still further, quantitative validation of our model’s ability to recover the biologically significant RBC shape. However, this result clearly only confirms steady state shape in zero-flow- the results of the model from RBC dynamics *in silico* experiment is yet to be assessed.

Clearly in Table 5.3, a range of vesicle shapes were recovered, not just a bicuspid. Before continuing to exclusively focus on the biologically significant bicuspid profile, shape profiles of both the prolate and torus vesicles will be assessed, to provide further conformation of methodology. To evaluate these vesicle profiles, a shape



### 5. The Simulation of Fluid-Filled Vesicles using cMCLBM



**Figure 5.8:** Here, shape validation of correct steady state RBC shape is conducted through comparison of the simulation data against the result by Evans and Fung [183], who give a parametric expression of RBC shape profile (Eq. (5.69)), fitted to experimental measurement. To show this, the top right quadrant of a slice taken through the centre of mass of a bicuspid vesicle profile produced by the cMCLBM (orange) is overlayed against the expression of Evans and Fung [183] (black) [20].

metric is produced and used as a method of assessing accuracy. This metric is developed from the symmetric, nine-component inertia tensor [194]:

$$\underline{\underline{I}} = \begin{bmatrix} I_{xx} & I_{xy} & I_{xz} \\ I_{yx} & I_{yy} & I_{yz} \\ I_{zx} & I_{zy} & I_{zz} \end{bmatrix},$$

where the components are defined by the following equation, which is then adapted for computation in simulation as such:

$$I_{\alpha\beta} = \int \rho_r (||\underline{r}||^2 \delta_{\alpha\beta} - x_\alpha x_\beta) d^3r \quad \rightarrow \quad \Sigma_{\underline{r}^*} \rho_r(\underline{r}^*) (||\underline{r}^*||^2 \delta_{\alpha\beta} - x_\alpha^* x_\beta^*), \quad (5.70)$$

where,  $\alpha, \beta$  corresponds to 1, 2, 3 ( $x, y, z$ ),  $\underline{r} = (x_1, x_2, x_3)$  and the summation is taken over all discrete node positions,  $\underline{r}^*$ , within the simulation. The eigenvectors of  $\underline{\underline{I}}$  correspond to the principal axes of the inertia tensor, which for the case of symmetric vesicles can be easily pictured, with one axis aligning with the axis of rotation. The eigenvalues of  $\underline{\underline{I}}$ , denoted by  $\lambda_1, \lambda_2, \lambda_3$ , then correspond to the principal moments of inertia about the principle axes of the vesicle ( $\lambda_1$  denotes the smallest eigenvalue and  $\lambda_3$  the largest). These eigenvalues provide a quantitative metric for assessing vesicle profiles of sufficient symmetry. To further explain this, consider

## 5. The Simulation of Fluid-Filled Vesicles using cMCLBM

a prolate vesicle (*informally, pictured as a peanut shape for the case in question*). Imagining its principal axes, one aligns with the axis of rotation, the other two being orthogonal to this axis. Here, it would be expected that the principal moments of inertia would be small about the axis aligned with the axis of rotation and the other two should be degenerate and larger (a consequence of the larger spread of mass about these axes). This means that the two larger eigenvalues should be degenerate for a correctly parameterised and simulated prolate vesicle, which would have a large degree of symmetry in its profile. For a subset of vesicle shapes, which have the requisite degree of exploitable symmetry (such as oblate vesicles (bicuspid and torus)), it is possible to use expected degeneracies as a metric for vesicle profile. For instance, taking a torus vesicle, the two smaller eigenvalues will be degenerate and the eigenvalue corresponding with the axis of rotation will be larger. Hence, it could be stated, for a torus (or oblate) symmetric vesicle, that:  $\frac{\lambda_1}{\lambda_3} \approx \frac{\lambda_2}{\lambda_3}$ . Therefore, it is possible to validate equilibrium, steady state vesicle shapes, for sufficiently symmetric vesicles, by determining the degeneracy of the relevant eigenvalues.

Figure 5.9 shows the time evolution of the eigenvalues of the inertia tensor for a parameterisation that produces a prolate vesicle (top panel) and a torus vesicle (bottom panel) —with the overlaid shape profiles displayed on the plots. Here, it can be seen that the eigenvalues of the inertia tensor settle after the initial process of deflation, showing that the vesicles have reached steady state. Furthermore, the two larger (smaller) eigenvalues  $\lambda_2$  &  $\lambda_3$  ( $\lambda_1$  &  $\lambda_2$ ) become degenerate for the prolate (torus) vesicle. This shows that the vesicle profiles are as expected, and that they have the appropriate high degree of symmetry.

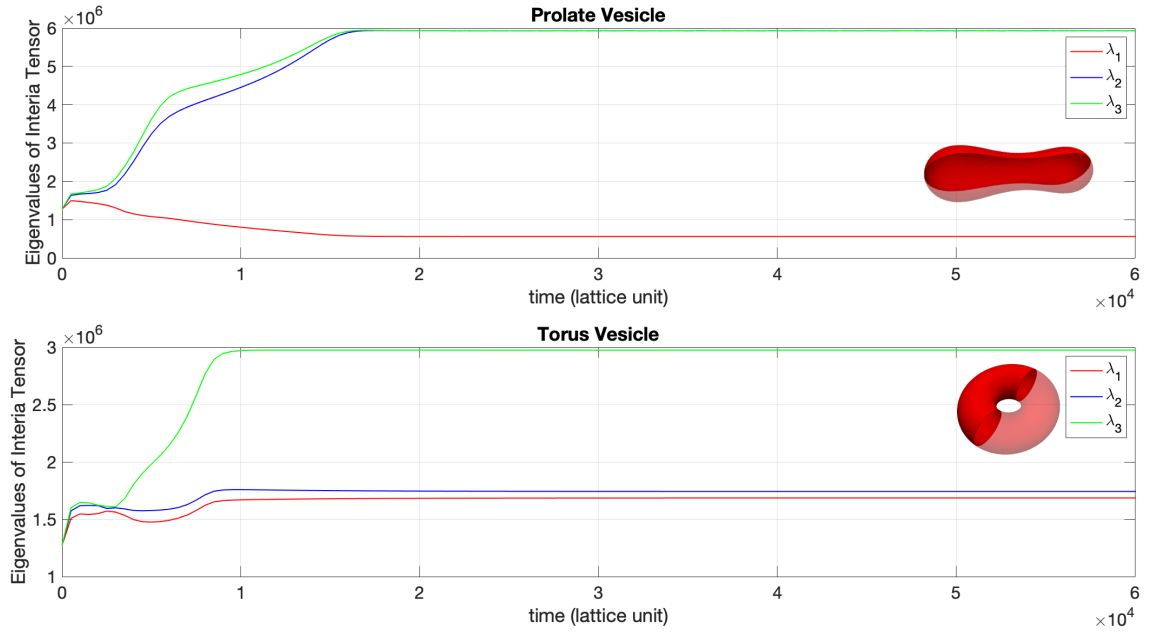
To provide quantitative analysis of this, Table 5.5 shows the eigenvalues of the prolate and torus vesicles in equilibrium (corresponding to those in Figure 5.9):

Eigenvalues of the inertia tensor for different vesicle shapes			
Vesicle shape	$\lambda_1$	$\lambda_2$	$\lambda_3$
Prolate	0.55612	6.0105	6.0121
Torus	1.6898	1.7157	2.944

**Table 5.5:** The three eigenvalues of the Inertia Tensor ( $\lambda_1, \lambda_2, \lambda_3$ ) —where  $\lambda_1$  is the smallest and  $\lambda_3$  the largest —for two equilibrium profiles: Prolate and Torus vesicles. Corresponding time evolution of these eigenvalues are shown in Figure 5.9, where for information on shape classification, see Table 5.3. All values  $\times 10^6$  [20].

The results show that the two largest eigenvalues for the prolate vesicle are degenerate within 1% and for the torus vesicle the two smallest eigenvalues are

## 5. The Simulation of Fluid-Filled Vesicles using *cMCLBM*



**Figure 5.9:** Time evolution of the eigenvalues of the inertia tensor, for a Prolate vesicle (top) and Torus vesicle (bottom), with semi-transparent vesicle profiles overlaid on the plots for clarity of shape profile. We see divergence of the largest (smallest) eigenvalues as expected for the Prolate (Torus) vesicles. The simulation parameters for the Prolate vesicle are:  $\sigma = 0.1$ ,  $\kappa_B = 0.25$ , area increase factor  $\Upsilon = 1.31$  (or system deflation) and the Torus Vesicle:  $\sigma = 1 \times 10^{-5}$ ,  $\kappa_B = 0.1$ , area increase factor  $\Upsilon = 1.31$ . With simulation parameters  $\beta = 0.6$ , drop radius= 15, lattice =  $80 \times 80 \times 80$ .

degenerate within  $\approx 3\%$  (relative to the largest of the two degenerate eigenvalues). This shows that for these vesicle parameterisations, the steady profile is accurate (due to appropriate degeneracy of the relevant eigenvalues), meaning the desired profile was underwritten by an appropriate level of symmetry.

Although accuracy of the bicuspid vesicle shape in static equilibrium (zero applied flow) has been confirmed in several tests, the data so far provide no assurance that its dynamics will replicate those of a RBC. Accordingly, the next section of work seeks to confirm this through comparison against experimental data as well as other computational models results.

### 5.3.2 Dynamics

Having now validated equilibrium, steady state vesicle shape and resolution, vesicle dynamics will be examined, focusing on the induced deformation of a bicuspid vesicle under flow shear stresses. The principal aim of the data here is too assess the ability of the developed model accurately to replicate the dynamics of a healthy, human RBC, and indirectly assess the model's robustness and stability. First, our model is validated and calibrated against experimental data by tuning immersed boundary

## 5. The Simulation of Fluid-Filled Vesicles using cMCLBM

force constants (see section 5.3.2.1). Once calibrated, further dynamical tests will assess the stability of the method under large flow stresses and aim to provide further proof of the applicability of the method to the simulation of multiple RBCs.

### 5.3.2.1 The Wheeler Test

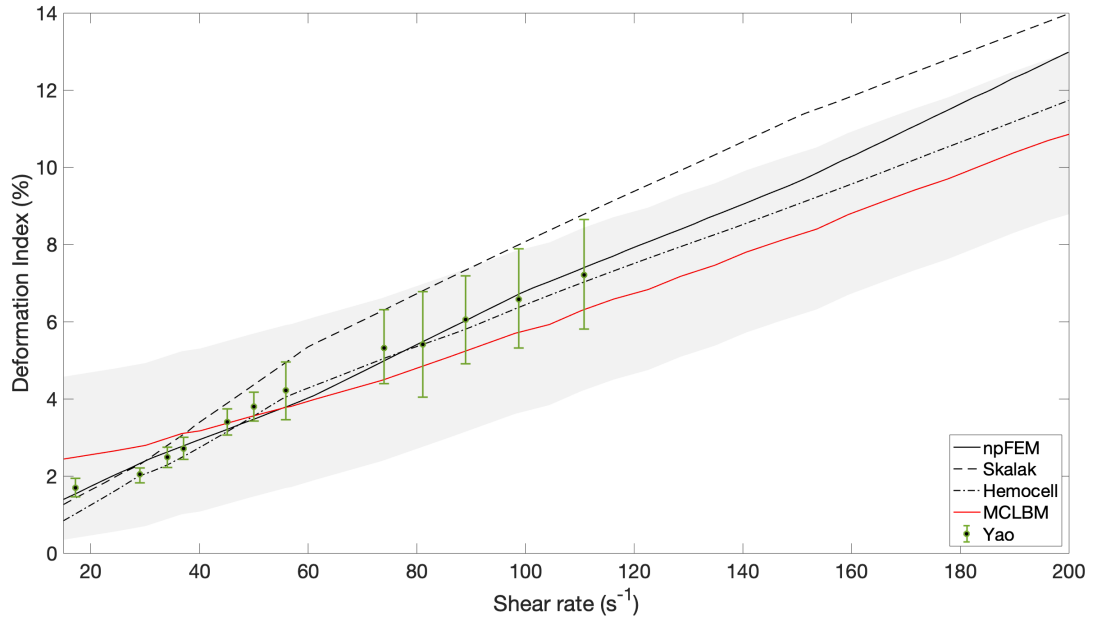
In order for our model to be used for the simulation of RBCs, it needs to successfully replicate RBC dynamics. Hence, the first dynamics test introduced below considers calibrating and validating our model against experimental data. A recognised test for benchmarking a single RBC model in dynamical flow is the Wheeler test, which has been carried out by several previously mentioned methods [161, 160, 171] and, indeed, in experiment. The Wheeler test compares *in-silico* data with that of the Wheeler test experiment, conducted by Yao et al. [195] in which a single human RBC is exposed to a fixed velocity shear flow (the shear planes of which lie perpendicular to the axis of symmetry of the RBC). To quantify the vesicle's deformation due to the shear flow, a deformation index is calculated that uses the maximal diameter of the vesicle pre and post-shear. The deformation index ( $DI$ ) has been recorded over a limited range of shear rates, with  $DI$  being defined as:

$$DI = \frac{(D_{\max}/D_0)^2 - 1}{(D_{\max}/D_0)^2 + 1} \quad (5.71)$$

where  $D_{\max}$  is the maximal diameter once the vesicle has deformed at a constant shear rate value, and  $D_0$  is the initial diameter of the equilibrium bicuspid vesicle.

Figure 5.10 displays the response by the outlined MCLBM model when subject to the Wheeler test (Red), which is compared against experimental data [195] for benchmarking (Green error bars), as well as three other RBC models' data (Black) [161, 160, 171]. The data show that the developed method follows that of the experimental data generally. Although, for the data presented by the red line, the result moves further away from the experimental data at the lower shear rates. This is due to a small shape error, there being a slight asymmetry in the equilibrium bicuspid vesicle (similar to that found for the torus vesicle in Table 5.5), which skews the results. Here, the red line shows the case where an average has been taken of the semi-minor and semi-major diameter for the  $D_0$  value, resulting in a slight overestimation of shear rates. This pathology of our data looks more prominent at smaller shear rates. Clearly, how one interprets this error, when calculating the deformation index will affect the results; were we to take the largest  $D_0$  value, then the system would have a lower deformation index for all shear rates. Therefore, to show this, a distributed region (grey shaded region) is inserted on the graph. This region accounts for two things: (i) the variation in  $D_0$  and (ii) a small range of tested  $\sigma$  and

## 5. The Simulation of Fluid-Filled Vesicles using cMCLBM

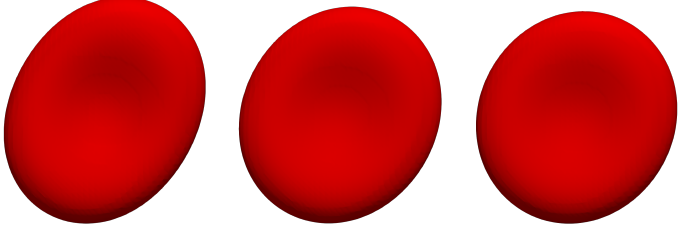


**Figure 5.10:** Results from the Wheeler test; where a single RBC is exposed to a shear perpendicular to the axis of rotation at varying shear rates. To quantify the shear induced deformation, a deformation index ( $DI$ ) is calculated (given in Eq. (5.71)). Data show comparison of simulation results with experimental data, where a given parameterisation for the cMCLBM is shown in red alongside three other models from literature (black) [160, 171, 161] and experimental data of Yao et al. [195] (Green error bars). The grey shaded region encapsulates a small shape error and also other parameterisations that fit the experimental data using the cMCLBM [20].

$\kappa_B$  values. The red line corresponds to bending rigidity, surface tension and deflation values of  $\kappa_B = 0.25$ ,  $\sigma = 1 \times 10^{-6}$ ,  $\Upsilon = 1.27$ . This parameterisation was found by matching to experimental data, but it may not necessarily be an optimum solution, due to the large number of possible parameterisations that can recover a bicuspid vesicle. Hence, the grey shaded region also encapsulates a small range of tested parameters that produced similar, but not identical results to that of the red line.

The intrinsic tuneability of the model, through its force magnitude constants, makes it very versatile, with extreme control over both steady state outcome and dynamical behaviour. Although this leverages the ability to replicate a range of behaviours, it does introduce complexity when parameterising simulations, where one may not know an appropriate initial base parameterisation. It was found that the bending rigidity value had a large affect on the dynamics of the vesicle within the Wheeler test, with reduced  $\kappa_B$  values resulting in a vesicle more susceptible to shear —less stiff. This is highlighted within Table 5.6 which shows three equilibrated sheared vesicle profiles and their corresponding deformation index. Here, bending rigidity is varied and surface tension and deflation are fixed. The vesicles were exposed to the same maximum shear as in the wheeler test, i.e., sheared perpendicular to the axis of rotation, at a shear rate of  $200s^{-1}$ .

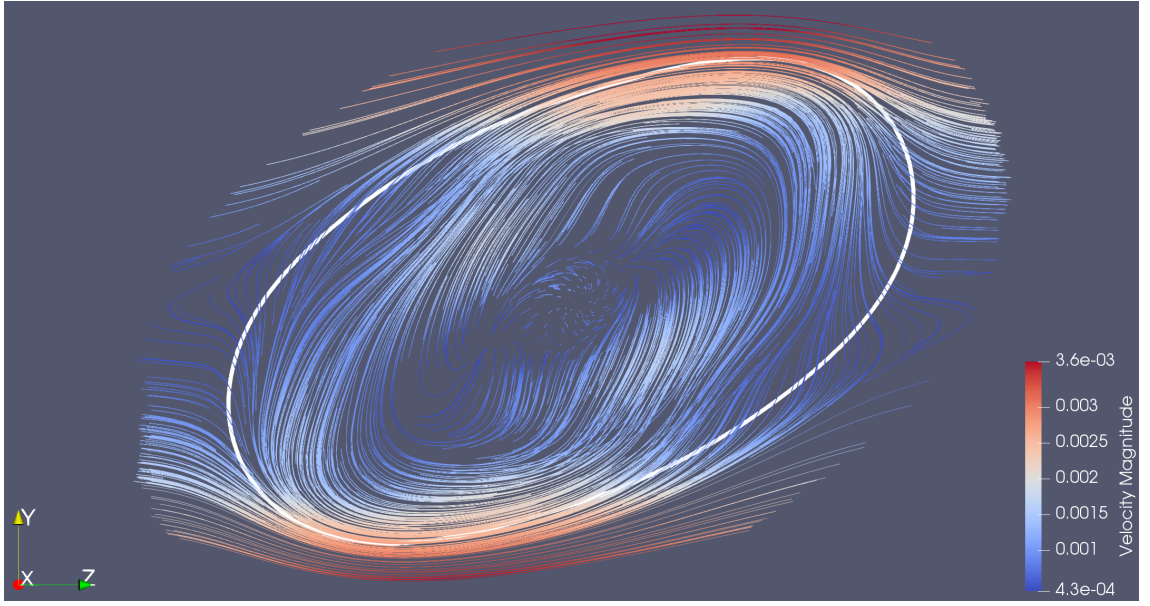
## 5. The Simulation of Fluid-Filled Vesicles using *cMCLBM*

Deformation Index and shape profile when exposed to a simple shear at varying bending rigidity			
Bending Rigidity	$\kappa_B = 0.25$	$\kappa_B = 0.40$	$\kappa_B = 0.60$
Deformation Index	10.78	4.49	4.42
			

**Table 5.6:** Table showing the equilibrium vesicle profiles when exposed to a shear (inline with the wheeler test) where the bending rigidity  $\kappa_B$  values were varied and surface tension and deflation values were set constant  $\sigma = 1 \times 10^{-5}$ ,  $\Upsilon = 1.27$ . Vesicle surface plots are taken over the  $\rho^N = 0$  contour in equilibrium, with the view looking down the axis of symmetry.

The results show that, unsurprisingly, the vesicle profile becomes less deformed for larger bending rigidity values, meaning that larger bending rigidity values result in a stiffer RBC. This tuneability could be very advantageous for workers interested in simulating diseases such as malaria, which impact the dynamics of human RBCs. Where a parameterisation for the RBCs altered, dynamical response could potentially be found, from starting with the base parameterisation for a healthy RBC, then calibrating the bending rigidity value.

So far, simulations have been calibrated against the experimental data of Yao et al. [195], revealing favourable results corresponding to RBC dynamics. Due to the limitation of experimental measurement, only a limited range of shear rates were available to compare against. In line with the previous work in this thesis, the stability and robustness of the model is assessed by evaluating the flow profile, when the vesicle is exposed to much larger flow stresses, where the resultant deformation index is  $DI = 29\%$ . The vesicle is sheared perpendicular to its axis of rotation, and run to equilibrium. To present visually interpretable data, a section is taken close to the centre of mass of the sheared vesicle, in the  $y$ - $z$  plane. Figure 5.11 shows the streak-lines of the flow within this slice of the sheared bicuspid vesicle, highlighting its flow profile through the centre of mass. The result provides conformation of a correct flow profile, where circulation within the internal fluid of the bicuspid has developed. Additionally, the velocity field can be seen to move around the vesicle (depicted by the white wireframe) in a physically appropriate manner —complying with the no-slip condition —as well as there being the appropriate gradient in velocity throughout the plane (depicted by the colour map of velocity magnitude  $|\underline{u}|$ ).



**Figure 5.11:** Result corresponding to a bicuspid vesicle, sheared perpendicular to the axis of symmetry in opposing  $z$  directions, with a deformation index of  $DI = 29\%$ . The white wire frame corresponds to the cross section of the sheared bicuspid taken through the centre of mass in the  $y$ - $z$  plane. Streamlines show the flow path in the centre of the sheared bicuspid and also the close exterior. The color map,  $|u|$ , relates to the magnitude of the velocity within the plane shown [20].

We conclude from this dynamics test that, through tuning the immersed boundary force constants, and by calibrating against experimental data of Yao et al., RBC dynamical behaviour was verified. Around the parameterisations used, the robustness and stability of the model was explored, by exposing the vesicle to much larger shear rates than those in the Wheeler test —with the resultant deformation index of the deformed vesicle exceeding twice the maximum deformation in the Wheeler test. Our results showed that simulations remained stable, with data of the internal flow field, providing appropriate circulation, and the external flow streamlines providing evidence of compliance with fundamental kinematics and dynamics explored in previous chapters. The next step of testing for this model is to assess its ability to recover from such a deformation back to its initial shape.

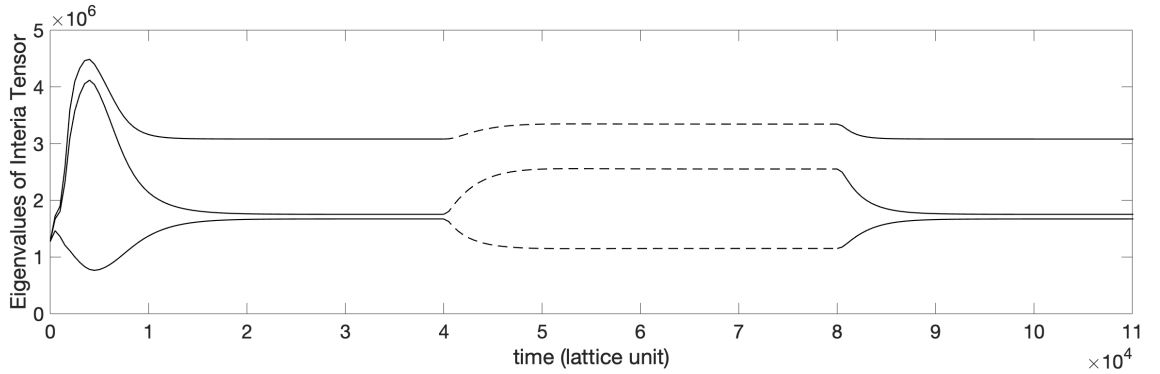
### 5.3.2.2 Shear Recovery

The previous section performed calibration and validation of the model’s dynamics, when simulating a human RBC, however, it did not provide any information about the model’s ability to recover from flow induced deformation. A human RBC is highly deformable, resulting in an ability to flow in capillaries with smaller diameters than the RBC itself. However, post deformation, when flow stresses are released, the vesicle should recover back to its bicuspid profile. To assess the ability of the

### 5. The Simulation of Fluid-Filled Vesicles using cMCLBM

model to simulate RBC reversible elasticity, a shear recovery test is conducted. In simulation, the vesicle is equilibrated as a bicuspid. Once steady state has been reached (verified by degeneracy of eigenvalues), it is exposed to a shear; once the shear has reached steady state, the shear is removed and the vesicle left to recover. Figure 5.12 shows the eigenvalues of the inertia tensor, where the dashed section corresponds to the period where the shear is applied to the vesicle. It can be seen that the eigenvalues return to prior values, verifying correct elasticity of the vesicle. Complimentary Table 5.7 shows the surface plots of the bicuspid throughout the test. There are extreme levels of deformation during the shear (far larger than that in the wheeler test), still the vesicle profile is seen to return to the same profile prior to the shear. Figures 5.12 and Table 5.7 demonstrate the reversibility of the vesicle, to recover back to its steady state, equilibrium profile (elasticity), remaining stable throughout simulation, even when exposed to larger flow stresses with resultant large levels of shape deformation.

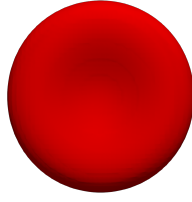
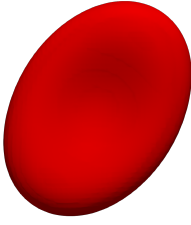
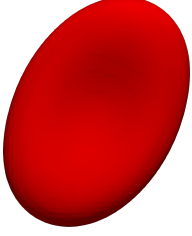
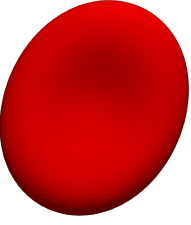
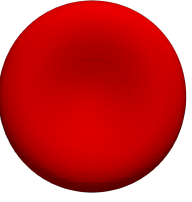
The stability and robustness of the model have now been further verified; our last set of data relate to the extension of the model to complex, multi-component flows. This investigation will focus on primarily the simulation of two vesicles, demonstrating the first step towards scaling to many vesicles.



**Figure 5.12:** Time evolution of the eigenvalues of the inertia tensor for the bicuspid vesicle, highlighting the change in vesicle shape during a shear recovery test —where the vesicle is sheared perpendicular to its axis of rotation and then left to recover. The first 40,000 time steps show the initialisation of vesicle, the dashed section shows the period where vesicle is sheared (40,000 - 80,000 time steps), and the final section where the vesicle is left to recover (time > 80,000). For these data, the simulation parameters were :  $\sigma = 0.00001$ ,  $\kappa_B = 1.0$ , area increase factor = 1.31 (or system deflation),  $\beta = 0.6$ , drop radius= 15, lattice =  $75 \times 75 \times 75$  [20].



## 5. The Simulation of Fluid-Filled Vesicles using *cMCLBM*

Shear recovery test: time evolution of vesicle profile				
4	4.5	6	8.2	11
				

**Table 5.7:** Time evolution surface plots of the bicuspid being exposed and then recovering from the shear, relating to Figure 5.12. Here, the time step corresponding to the shape is shown above the surface plots, all values  $\times 10^4$ . Surface plots taken at contour  $\rho^N = 0$ , mid interface, looking down the axis of symmetry [20].

### 5.3.3 Simulation of Multiple Vesicles

The work of this section extends the model from the simulation of a single vesicle in a background fluid (two-component fluid flow), to the simulation of multiple vesicles in a background fluid, using the assumptions and alterations to the segregation rule discussed in section 5.2.4. However, to first confirm the updated segregation rule and assumptions are valid, a spreading test is completed. After this step, a vesicle-vesicle head-on interaction is simulated, as well as the sedimentation of a vesicle column. The aim of this work is to provide initial evidence of the scalability of the methodology, as well as recovery of correct qualitative behaviour between vesicles.

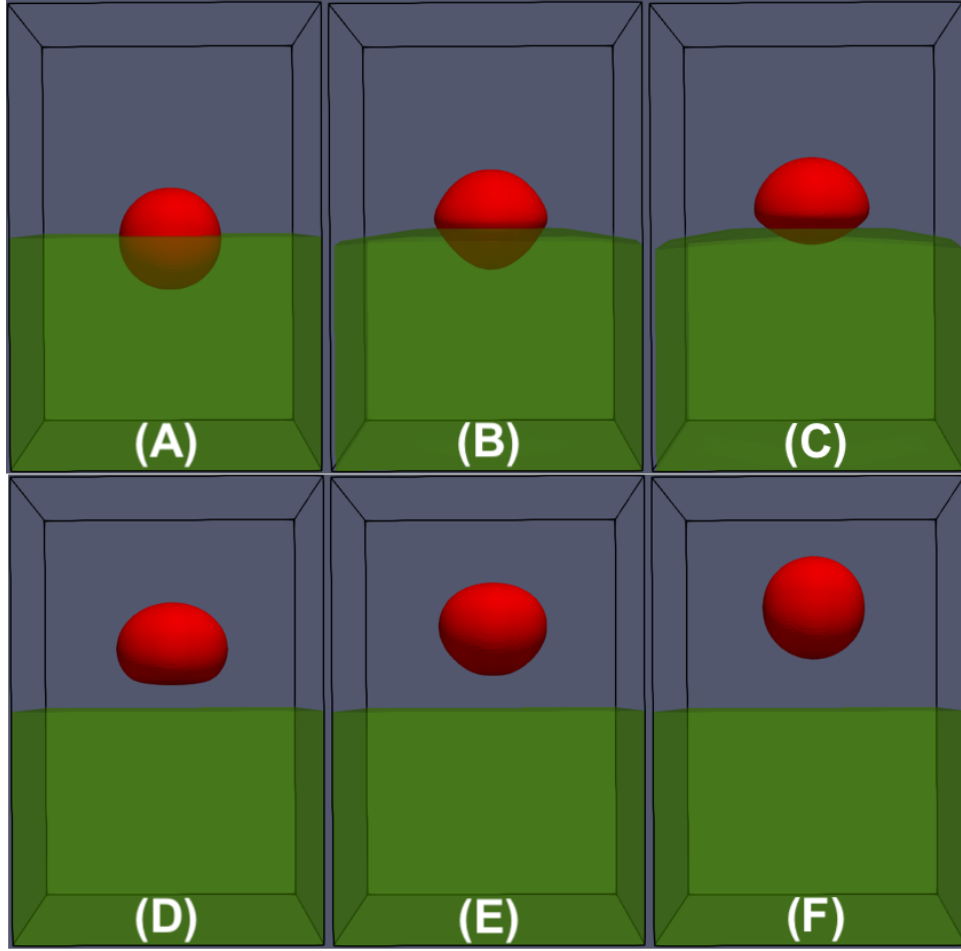
#### 5.3.3.1 Check of Fluid Segregation using Drops

As a first test of the updated fluid segregation rule, seeking to simulate completely immiscible fluids, a spreading test is used, inspired by the two-dimensional test of Yuan et al. [92]. Here, a liquid drop (Red) initialised in the centre of the domain between two stratified fluids (the bottom Green and the top Blue, in relation to the origin in the  $z$  direction). The surface tension values for this simulation were set as follows:

$$\sigma_{BR} = \sigma_{BG} = \sigma_0 \quad \text{and} \quad \sigma_{GR} = 3\sigma_0. \quad (5.72)$$

It thus follows, as the simulation is evolved over time, with no external flow, the red liquid drop should favour the blue (top) fluid, causing the green-red interface to decrease and the red drop move into the the blue (top) fluid, away from the green (bottom) fluid. If this is the case, it confirms that the segregation rule is working (and able to simulate complete spreading). Or put another way, the ability to avoid two fluids wanting to contact and mix (clearly desirable for the simulation of many

## 5. The Simulation of Fluid-Filled Vesicles using cMCLBM



**Figure 5.13:** Simulation data from the drop spreading test. Where a liquid drop (Red) is placed in the centre of domain  $80 \times 80 \times 120$ , with two stratified fluids Green (bottom) and Blue (top). Where the Green (Blue) fluid initially occupies the half the lattice  $0 \leq z \leq 60$  ( $60 \leq z \leq 120$ ) before the Red fluid is overlayed. Simulation panels show the time evolution of the simulation, with panels (A),..., (F) corresponding to  $t = (0, 1500, 2500, 4500, 20000, 100000)$  lattice time steps. The Red drop is seen to move away from the Green fluid and into the Blue. Surface tension values used for this test were:  $\sigma_{BR} = \sigma_{BG} = \sigma_0$  and  $\sigma_{GR} = 3\sigma_0$ , where  $\sigma_0 = 0.005$ .

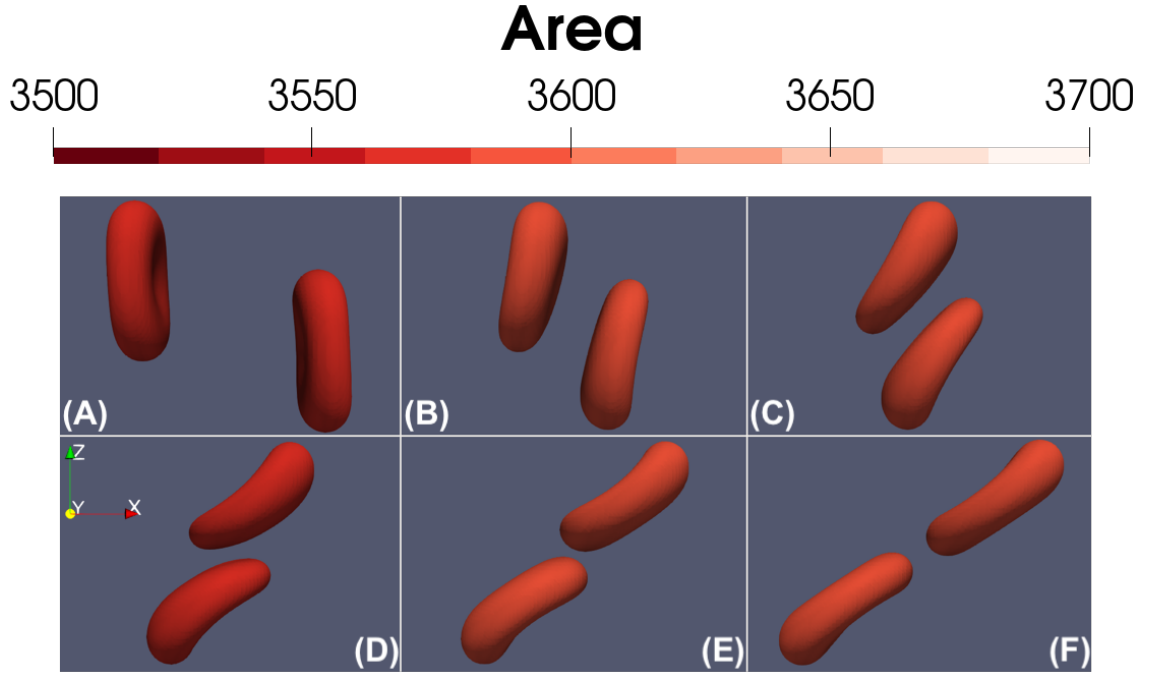
RBCs) is at issue. The simulation data from this test are shown in Figure 5.13. These data show the time evolution of the fluids within the simulation, where there is no external flow and the movement of the fluids is purely caused by surface tension effects. It can be seen that the red liquid drop does move into the blue fluid, which has a corresponding surface tension three times lower than that of the red fluid with the Green fluid. The result of the red fluid disassociating itself with the green fluid —complete fluid spreading —confirms the assumptions and reduced segregation rule, developed from that of Yuan et al. [92]. Following this validation, the rule is now implemented within our vesicle model.

### 5.3.3.2 Vesicle-Vesicle Pseudo-Ballistic Impact

Although research presented here focuses on the development of new methodologies, vesicle-vesicle interactions are considered from a long-standing perspective. Clearly, the next logical step of this work would be the extension to multiple erythrocytes, facilitating application to dense suspensions. Here, the aim is to demonstrate that our method is capable of capturing the dynamics of vesicle-vesicle interactions correctly. Accordingly, the case of two vesicle moving past each other is simulated. It is expected that the vesicles will deform and move past each other, with minimal change in volume and cross-sectional area, while maintaining stability and avoiding coalescence.

In simulation, two bicuspid vesicles are equilibrated, separated by an appropriate distance, such that there is no vesicle-vesicle interface initially, and that their axis of rotation are parallel. A buoyancy force is then applied to each vesicle in opposing directions parallel to their axis of rotation. This accelerated the vesicles and created a pseudo-ballistic impact, i.e., they move passed each other. The impact dynamics (possibly one should say lubrication regime dynamics) of the vesicles is controlled by two parameters: i) the contact angle of the vesicle (determined by the overlap of the vesicles and the direction they are moving) and ii) the velocity of the vesicles (controlled by the magnitude of the buoyancy force applied). Figure 5.14 shows six increasing time frames (A)-(F), depicting the two vesicles as they interact, with the left vesicle in frame (A) being pushed in the positive  $x$ -direction and the right vesicle in frame (A) in the negative  $x$ -direction. Panel (A) shows the initialisation of the simulation, where the vesicles start with an overlap approximately equal to the length of the radius of the vesicle, in which both vesicles have a surface area taken at the contour  $\rho^N = 0$  of  $A = 3575$ . Once the vesicles start moving towards each other, a vesicle-vesicle interface starts to form —panel (B). This then results in the vesicles orbiting around each other, to avoid coalescence. Qualitatively, this data captures the expected dynamics of the vesicle-vesicle interaction, whilst maintaining vesicle immiscibility. Quantitatively, the vesicles area was found to have a maximal relative fluctuation from the initial vesicle area in frame (A) of  $\approx 0.2\%$ , showing excellent results for the effectiveness of the area conserving force.

In simulation, to avoid coalescence of vesicles, the following modifications to the segregation are used: (i) A reduced interface width for vesicle-vesicle interface and (ii) an increased surface tension for vesicle-vesicle interfaces. The reduction in interface width for the vesicle-vesicle interface ensures no mixing of vesicle fluids, by eliminating any possibility of unphysical triple contacts forming, and favouring the background fluid-vesicles interfaces over vesicle-vesicle interfaces. To test this further, a more stringent test of two vesicles sedimenting on top of each other will be examined.

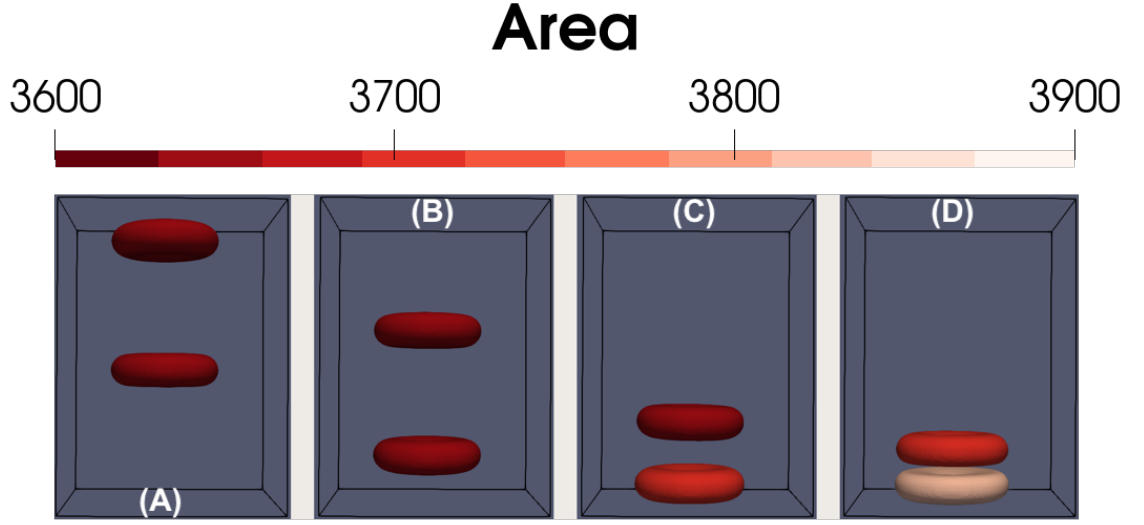


**Figure 5.14:** Data for a vesicle-vesicle pseudo-ballistic impact. Here, the left (right) vesicle in frame (A) is pushed in the positive (negative)  $x$ -direction, causing the two vesicles to interact. The frames show increasing time evolution of the simulation (A) - (F), from a profile view looking down the  $y$ -axis ( $x - z$  plane —axis orientation shown in panel (D)). The colour of the vesicles corresponds to the surface area calculated for the contour  $\rho^N = 0$  [20].

### 5.3.3.3 Sedimenting Vesicles

To further assess our model's ability to remain stable during vesicle-vesicle interactions, a sedimentation of two vesicles on top of each other is performed. Two bicuspid vesicles are initialised with their axis of rotation parallel to one another, but separated by a distance such that there is no vesicle-vesicle interface initially. No-slip boundary conditions are applied on all the walls of the lattice domain (of size  $(75 \times 75 \times 120)$ ). Once the bicuspid vesicles have reached steady state, a negative buoyancy force is applied to both of the vesicles in the  $z$  direction ( $-U_0 \hat{e}_z$ ). The vesicles then sediment towards the bottom of the simulation box, where they are forced to interact and finally settle on top of each other, i.e., to stack. The results of this test are shown in Figure 5.15, which displays the time evolution of the bicuspid vesicles ( $t=(0,20000,40000,60000)$ ) in the flow (A)-(D), where the colour map corresponds to the vesicles surface area and all simulation parameters are listed in the figure caption.

The results in Figure 5.15 show that the two bicuspid vesicles sediment vertically downwards over time, with the vesicles settling on top of each other (shown in panel (D)). The colour map corresponds to the calculated vesicle area post simulation, for the contour  $\rho^N = 0$ , using visualisation software, Paraview [196]. It is clear that



**Figure 5.15:** Simulation data of the time evolution of two bicuspid vesicles in a sedimenting flow, confined within a domain, where the colour map corresponds to the calculated vesicle surface area at the contour  $\rho^N = 0$ . The lattice domain used was  $75 \times 75 \times 120$ , with solid no-slip walls at all boundaries. The magnitude of the buoyancy force applied in the negative  $z$  direction was  $U_0 = 0.0001$ , and the initial vesicle area, given in frame (A), is approximately  $A_0 = 3631$  (where the deflation value used is  $\Upsilon = 1.31$ ).

there is a small fluctuation in the surface area when the vesicles start to interact with each other, but also when the vesicle interacts with the solid boundary at the bottom of the lattice. The desired target area of the vesicle throughout simulation is set as  $A_0 \approx 3631$ , with a maximal area in simulation recorded at  $A_{\max} \approx 3812$ . This means that the area has a maximum fluctuation about target of around 5%. Due to the bicuspid vesicles maintaining their shape profile to an appropriate degree, and taking into account that this is an extreme test of stability, with the bottom vesicle being trapped between a solid wall and a vesicle under significant compression due to the buoyancy force pushing down on it, the results are encouraging. Obviously, the area conserving force aims to maintain the cross-sectional area of the vesicle during the continuous flow stresses and compressive deformations, for current purposes, the fluctuations in area being deemed small enough not to undermine accuracy.

## 5.4 Concluding Remarks

Within this chapter, a novel methodology for simulating vesicle hydrodynamics using a single framework approach, an adapted Chromodynamic Multi-Component Lattice Boltzmann Method, has been outlined in detail, with the model tailored towards the simulation of human RBCs. This work built upon that of the previous Chapters: in Chapter 3, it was found that an advection error was present in the model's

## 5. The Simulation of Fluid-Filled Vesicles using cMCLBM

kinematics for a flat advecting interface—which was not present for density ratios of unity; in Chapter 4, the extent to the limitations of the large density contrast model was explored, showing most appropriate results for liquid-liquid interfaces within Stokes’ regime. This work confirmed the direction of exploiting model kinematics and dynamics in the regime of unity density contrasts, and motivated the novel application here, which further necessitated a multi-relaxation time scheme, and led to the development of a chromodynamic model for simulating vesicles in 3D—potentially its most suitable application. This model leverages all the key benefits of chromodynamic schemes: strict mass conservation, simulation of immiscible fluids, correct interface kinematics and dynamics, automatic adaptive meshing, and ease of interface tracking and parallelisation. Single component lattice Boltzmann methods are already utilised throughout literature in the simulation of RBCs [19, 164, 154, 171, 159, 160], however, these methodologies are modular and contain multiple modelling techniques, e.g., treating the RBC body separate to the background fluid and then coupling the two together. Our model provides a transparent approach, where only one methodology (cMCLBM) is needed to resolve the deformable body and the fluid. It is however clear that prior methodologies benefit from developmental maturity, with methodologies such as those encapsulated in HemoCell [159, 160] capable of simulating extremely dense suspensions of RBCs in their current form. Such *at scale* deployments are clearly beyond the scope of the developmental work reported here.

Simulations started by assessing the steady state, zero flow properties of the model with the intent of validating vesicle shape and appropriate simulation resolution. Starting by qualitatively cataloguing the vesicles’ shapes produced by the model, a sampled, restricted phase-space was examined with a range of vesicle shape outcomes being observed—see Figure 5.3. From both intuition and prior literature [185, 186], the deflation value was chosen with the intent of increasing the chance of recovering a bicuspid vesicle representative of a human RBC. Following qualitative validation of correct vesicle shape, checks of appropriate simulation resolution were performed. By appealing to Gauss-Bonnet theory, we checked that the curvature calculations were accurate, and that resolution was sufficient, the calculated result being within 1% of the predicted value (when using an initial un-deflated vesicle radius of  $R = 15$ ). To further support this, a grid convergence test (GCT) was performed for three grid resolutions (coarse  $R = 15$ , medium  $R = 17.5$  and fine  $R = 22.5$ ), with the coarse resolution having a grid convergence index of less than 5%, showing again, appropriate resolution—see Table 5.4. From this, an initial un-deflated vesicle radius of  $R = 15$  was chosen for the remaining simulations (mainly on the basis of computational cost). The next step was to provide quantitative evidence of correct

## 5. *The Simulation of Fluid-Filled Vesicles using cMCLBM*

vesicle shape. For the bicuspid vesicle, this was confirmed through comparison against theory developed by Evans et al. [183], for predicted erythrocyte shape —showing correct shape profile (Figure 5.8). To assess the accuracy of both the prolate and torus vesicles, correct degeneracy of the eigenvalues of the inertia tensor showed that the vesicles had the expected degree of symmetry, with data confirming this in Figure 5.9 and Table 5.5. The outcome of this steady state, zero flow investigation was that the model was shown to recover a vesicle representative of human RBC, both qualitatively and quantitatively, as well as verification of appropriate resolution within simulation —implying resolution will remain sufficient during flows due to the automatic adaptive interface.

Although a vesicle shape representative of that of a human RBC was recovered in steady state, this did not mean that it could appropriately represent the dynamics of a RBC. To verify this aspect, a standard benchmarking test is the Wheeler test, which is a comparison of simulation data against experimental data (Figure 5.10). Here, a vesicle is sheared in the plane perpendicular to its axis of rotation at differing shear rates, with the level of deformation recorded using a deformation index. By tuning of the bending rigidity and surface tension values, the susceptibility of the vesicle to shear can be altered, with the parameterisation used showing good agreement with the experimental data [195] and other models data within literature [161, 160, 171]. A slight asymmetry of the vesicle means that the data are skewed at very low shear rates, although it was concluded that this had minimal impact on simulation results at the parameterisations considered. To test the model’s robustness and ability to simulate vesicle elasticity —withstand large deformations and reverse back to initial shape profile—a shear recovery test was performed (Figure 5.12). Here, the shear rate was turned on until steady state was reached; when turned off, the vesicle was seen to retract to its bicuspid profile. This verified correct membrane elasticity, as well as platform robustness at large shear rates, i.e., stability far from mechanical equilibrium. By examining flow profile within the vesicle during a shear, we verified viable internal flow field, with the external fluid streamlines seen to be moving around the perimeter of the vesicle, as expected. Such results can only arise in the presence of appropriate kinematical and dynamical foundations as set out in previous chapters.

With the objective of assessing the model’s ability to meet both steady state and dynamical data representative of a single, human RBC and demonstrating stability far from mechanical equilibrium, work then considered the provision of initial evidence of the extension to multiple RBCs. From the work of Yuan et al. [92], a minimal but effective enhanced segregation rule, resulting in complete immiscibility of the

## 5. The Simulation of Fluid-Filled Vesicles using cMCLBM

vesicles, was used to extend the model. To verify multi-vesicle competence, a drop spreading test inspired by [92], verified that complete immiscible (or full spreading where a Neumanns triangle cannot form) was recovered (Figure 5.13). This new segregation rule was then implemented into the vesicle model, where to test the robustness of the model, a head-on collision between two vesicles being pushed by a buoyancy force was tested (Figure 5.14). This result demonstrated the stability of the model; membrane area was conserved within 1% throughout simulation, with the vesicles moving around each other and avoiding coalescence even with small impact parameter. Following this, the simulation of two vesicles sedimenting on top of each other within an enclosed box was performed (Figure 5.15). Results of this compression test showed that the vesicles settled on top of each other, where although area fluctuated by approximately 3% during simulation, vesicle shape profile looked qualitatively as expected. This further demonstrated the robustness of our model, with harsh head-on collision and large flow stresses failing to perturb stability. Although there is no comparable experimental data or theory for these tests, they serves as simple, intuitive examples of qualitatively correct vesicle-vesicle behaviour, and the ability to simulate more than two fluids (three-component flows).

Overall, we concluded from the simulation data presented, that our cMCLBM for vesicle hydrodynamics can be parameterised appropriately to simulate human RBCs, through a check of both steady state and dynamical behaviour. The ability to tune our model through assignment of the bending rigidity, surface tension and deflation parameters confers benefits and disadvantages. By increasing tuneability, a range of vesicle shapes can be simulated —not just the bicuspid vesicle —and we see that vesicle behaviour can be tuned further by controlling the immersed boundary force magnitude and the surface tension to bending rigidity ratio. This provides future possibilities for the model, such as the simulation of unhealthy human RBCs, i.e., the effects of malaria (discussed further in the next chapter), and also other soft particles. The downside of this, is that the phase-space is quite complex and simulations can be awkward to parameterise, certainly this is so without prior knowledge of the model. This observation supports the decision to exclude a membrane shear modulus *a priori*, which would presumably increase model complexity further. Parsimonious models are easier to tune —some where mechanical properties are direct input parameters [154] —and we evidence an ability to recover correct shear dynamics without inclusion of such a immersed force. Entities should not be compounded beyond necessity. Clearly, in its current form, the model has not been extended for the simulation of extremely dense suspensions, such as can be addressed by HemoCell models [159, 160], however it does furnish the requisite foundation ability to simulate vesicle-vesicle interactions.



## 5. *The Simulation of Fluid-Filled Vesicles using cMCLBM*

The computational expense surrounding the cMCLBM, when extending to many component fluid-flows, needs to be addressed if one wishes to make the method computationally amenable to the simulation of many RBCs, with this again being discussed further in the final chapter. Future directions for this work can therefore be split into three groups: (i) the extension of the methodology to many vesicles (ii) the further validation of the methodology within multiple vesicle flows and (iii) the application of the methodology to RBC flows —such as the impact of malaria on RBC dynamics. These will be discussed further in the concluding Chapter: Chapter 6.

# 6

## Conclusions and Future Work

### Contents

---

<b>6.1</b>	<b>Conclusions . . . . .</b>	<b>174</b>
<b>6.2</b>	<b>Future Work . . . . .</b>	<b>177</b>
6.2.1	Extension to the Simulation of Many Immiscible Fluids .	177
6.2.2	Modular cMCLBM . . . . .	179
6.2.3	Applications . . . . .	181

---

### 6.1 Conclusions

This thesis focuses on extensions to a specific class of multi-component lattice Boltzmann method —chromodynamic MCLBM (or cMCLBM). Chapters 3-5 progressively align with the principal aims of model development and evaluation, initially outlined in Chapter 1 and summarised below:

- Assess the model’s kinematics and dynamics, as well as the coupling between the two in order to provide an *ab initio* understanding of the cMCLBM methodology.
- Investigate and bound the applicability of the cMCLBM to immiscible fluids with a large density contrast.
- Based upon the developments itemised above, assess cMCLBM as a single-framework platform for LBM models with extended physical content, here the three dimensional simulation of vesicle membranes.

## 6. Conclusions and Future Work

Chapter 3 reviewed the chromodynamic methodology in detail, extending the base model to the simulation of fluids with a density contrast. In so doing, our intention was to increase the applicability of the model to flows which contained such density contrasts, with obvious examples being water and oil (liquid-liquid) or water and air (liquid-gas) flows. However, the stability of the colour-gradient and chromodynamic models, when extending to large density contrasts remained at issue. One source of these instabilities was our athermal equation of state (EoS) embedded in the models ( $p = \rho c_s^2 \rightarrow c_{sR}^2 \rho_R = c_{sB}^2 \rho_B$ ), where the need to maintain a low Mach number to neglect compressibility effects results in stability issues [146]. Our data revealed another error associated with the coupling of the model’s kinematics and dynamics, in the presence of a density contrast, which resulted in an interface advection error —impacting the model’s compliance with hydrodynamic boundary conditions at the free surface. The influence of this error on the stability of the model, in flows containing flat interfaces, was assessed. Our data exposed limitations of the model when applied to rapid flows and flows with large density contrasts.

Pursuant upon the outcomes of Chapter 3, Chapter 4 focused on extensions as follows: (i) Upgrading the collision operator to an MRT operator. (ii) Application of the model in axially symmetric three-dimensional low Reynolds number flows. The inclusion of an MRT collision operator is, in retrospect, a necessity in MCLBMs aiming to simulate density contrasts, due to the stability gains in certain flows, which made the model more parameterisable in general. Once implemented, further, more stringent testing of the model’s compliance with interface kinematics and dynamics (for both flat and curved interfaces) was conducted. The outcome of this investigation evidenced the same essential trends as found in the data of Chapter 3, with decreased stability at larger density contrasts, larger flow velocities, and, unfortunately, significantly curved interfaces. Due to these limitations, the application of the model within Stokes’s regime seemed the most suitable area of application- at least in its current form. In the context of the current work, this decision is not limiting, for it is within this regime of flow that one finds the analytical results which provide the validation of the kinematics and dynamics which is at issue. Accordingly, the model was extended to the simulation of axially symmetric flows, imparting the ability to simulate three-dimensional drops in low Reynolds flow as a collateral benefit. Through the use of phase-field freezing which successfully removed the dominant microcurrent signal —a pathology of Stokes’s regime MCLBM —the model generated data at lower density ratios. Our tentative conclusion following the work of Chapter 3 and Chapter 4 was that the model in its current form is, realistically, limited to liquid-liquid flows, with the simulation of liquid-gas flows currently unattainable,

## 6. Conclusions and Future Work

due to the presence of the advection error we identified and also the athermal EoS which, again in retrospect, we should not have accepted so unquestioningly. However, the albeit negative observation that the equation of state cannot be side-stepped if one aims to extend the stability of simulations is of value and, in respect of this last matter there have been recent developments, we hope motivated by the work we report, this significantly advance cMCLBM in this respect. Very recently, Lafarge et al. [146] addressed these issues, by including an arbitrary EoS and an additional forcing term leading to improved stability in their colour-gradient model, which is, otherwise, that we develop and analyse here. Their work (published in August 2021) already encapsulates the next steps we might otherwise wish to recommend, towards addressing gas-liquid simulations using the essential cMCLBM of this work. The results in this thesis showed that such errors in the current density difference cMCLBM disappeared at unit density contrasts, which regime, as a result, afforded superior stability- while of course, retaining all the benefits of cMCLBM. This observation motivated our final applications.

Following the enhanced understanding and methodological confirmations of the foundation of the chromodynamic model studied in prior chapters, Chapter 5 considered the application of our essential model - in unit density contrast form- to the simulation of fluid-filled vesicles (of course, tailored towards RBCs); this application we postulate, presents itself as the most suitable area of application for our chromodynamic model in its current form - notwithstanding its ability to tolerate the requisite extensions to the model physics. Clearly, vesicles' membranes are more physically rich objects than liquid-liquid interfaces. Chapter 5, then, encapsulated our primary methodological outcome- the development of a single-framework technique capable of simulating the dynamics of fluid-filled vesicles in three-dimensions. The fundamentals of the model, the membrane force density derivations, their parameterisation and initial characterisation was presented in detail, with simulation results being tailored towards RBC behaviour, through our tuning of force constants and model input parameter space restrictions. In contradistinction to the modular approaches present in the recent literature, which utilise multiple modelling techniques, our approach provides a transparent, single framework methodology, which benefits from all the undiluted advantages of the cMCLBM —canonically, strict mass conservation, automatic adaptive interfacial region meshing, parallelisation, ease of force coupling, direct parameterisation and robustness. Simulation data considered three areas we suggest are crucial to the applications of cMCLBM to the simulation of blood flow: (i) ensuring appropriate resolution —*Gauss-Bonnet Theory*, *GCT* and (ii) correct steady state vesicle topology

## 6. Conclusions and Future Work

—assessed through the degeneracy of the eigenvalues of the inertia tensor, comparison against Evans’ parametric expression [180] and, not least, (iii) correct dynamical behaviour — *Wheeler test, shear recovery test, dual vesicle interaction*. Although this work focused on the initial development of the model, its extension to many component flows has been discussed; it is without doubt the key objective of any future work which may or may not follow from the work reported here.

## 6.2 Future Work

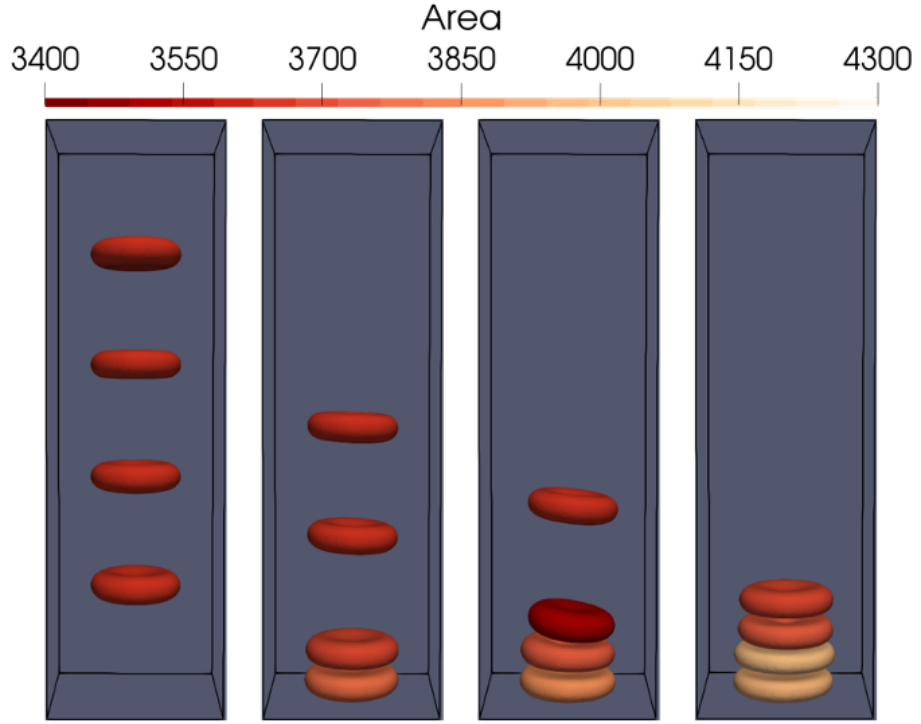
Future work recommendations following the research presented in this thesis clearly prioritises the chromodynamic model for vesicle hydrodynamics (as one might expect) and can, we believe, be split into three categories: (i) the extension of the model to many RBC (vesicle) simulations (ii) incorporation of a *modular* cMCLBM within computational interfaces and softwares and (iii) the application of the model to biological flows, i.e., malaria infected RBCs.

### 6.2.1 Extension to the Simulation of Many Immiscible Fluids

Within a drop of blood of the size of a pinhead, there are approximately  $10^6$  red blood cells, which make up around 40% of blood content by volume [197]. The extension of our chromodynamic model to the simulation of many RBCs would be the next step to improving the applicability of the model to the simulation of blood flow, where the average behaviour of large numbers of RBCs is of interest. The methodology for this step already exists in primitive form [184] but the physical processes which it facilitates are not required in the context of haemodynamics, where for example, wetting and Laplace-Young behaviour do not manifest. Put another way, one need only consider completely immiscible drops which the drops are erythrocytes. Current work has shown the model is capable of extending to a 5 fluids (4 vesicle) simulation using the existing approach. This work is summarised in Figure 6.1, which shows the sedimentation of 4 RBCs over time within a bounded domain defined by a square cross-section cylinder. Table 6.1 shows the relative error of the surface area of the vesicles in relation to the desired target area.

Current hierarchy of obstacles which our model faces with respect of efficiently extending to many RBC simulations are: (i) The need to define an interface and bear a computational overhead for each fluid, i.e.,  $n(n - 1)/2$  interfaces per  $n$  fluids. (ii) The need to segregate each fluid against, in principle, all other fluids in the segregation stage means that there are  $n$  segregation terms per fluid, for an  $n$  fluid simulation. (iii) The code requires parallelisation, so that it can run more efficiently- even in development applications.

## 6. Conclusions and Future Work



**Figure 6.1:** Evolution of the four sedimenting vesicles over time, with colour corresponding to the surface area of the vesicle taken at contour  $\rho^N = 0$ . Frames left to right show increasing time steps.

	Frame 1		Frame 2		Frame 3		Frame 4	
	Area	Error %	Area	Error %	Area	Error %	Area	Error %
Top	3632	1.917	3633	1.890	3633	1.890	3679	0.648
Top Middle	3632	1.917	3633	1.890	3505	5.347	3579	3.35
Bottom Middle	3632	1.917	3685	0.486	3754	1.377	3841	3.727
Bottom	3632	1.917	3762	1.159	3853	4.051	3921	5.887
Max error %		1.917		1.890		5.347		5.887

**Table 6.1:** Table showing the four vesicles areas at each frame shown in Figure 6.1 —with the surface taken at contour  $\rho^N = 0$ . Vesicles defined by their position during sedimentation (Top, Top Middle, Bottom Middle, Bottom), with relative surface area error shown (error in comparison to the target surface area:  $A_0 \approx 3703$ ).

To address these problems, future work should set out to re-define the phase-field between the fluids, aiming to reduce the number of interfaces needed to parity with the number of individual fluids (individual erythrocytes), i.e., define an interface between a given fluid with all the remaining fluids, viewed as a single effective species. From this, one might reconstruct the segregation rule, using a revisited phase-field, such that there is only a single segregation term per fluid. In doing so, the mathematical and computational complexity would necessarily decrease with a commensurate increase in computational efficiency, due to fewer frequently executed nested loops. Such an advance will feed into the final step which is the paralisation

## 6. Conclusions and Future Work

of the code. Lattice Boltzmann has the facility, here, due to its intrinsic locality and lattice symmetry. In doing so, it makes the code much more efficient, resulting in the ability to address larger domains over longer times. Hence, this is crucial when considering practical haemodynamics. The assumptions within these steps will reflect complete immiscibility (wetting effects are integrated out) and the vesicles are initialised in simulation such that they have no interface with each other, i.e., there is plasma (or background fluid) between the vesicles throughout simulation.

### 6.2.2 Modular cMCLBM

At the start of this thesis the following rhetorical question was set-out:

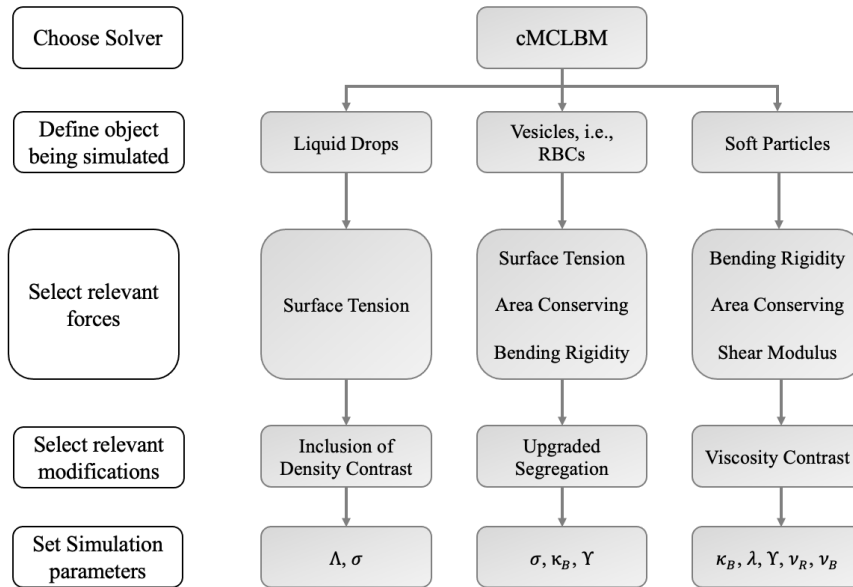
*If both liquid drops and vesicles are to be retained within the same essential approach (i.e., considering vesicles as immiscible fluids, with a diffused interface within the continuum approximation), then in what ways must the modelling approach differ?*

We have found that our cMCLBM provided a very transparent and easily adjustable framework. To address this question, the difference between the modelling of drops and vesicles, when using the cMCLBM, were found to be based around differing forms of the immersed forces, which aimed to capture the membrane physics (expressed as domain boundary conditions), some slight modification of the LB algorithm, i.e., inclusion of density contrast terms, such as the term  $\phi_i$  in the equilibrium distribution, and the segregation equations, and finally, the simulation parameterisation.

Future work could consider utilising this, by incorporating the developments presented in this thesis within computational interfaces and softwares which serve as repositories for such methods (such as DL\_MESO), allowing for increased dissemination of the models, and the continuation of a *modular* cMCLBM framework. Here, the term *modular* cMCLBM refers to the modularity of the applied immersed forces, which can, in principle, be swapped in and out to change the physics of the object the simulation is targeting, whilst still retaining the base, single framework, cMCLBM approach. An example of such a platform would be the DL\_MESO package [198], which already incorporates certain, early MCLBM models. This step could potentially allow for the model to be quickly and easily adapted for the parallel simulation of drops, vesicles and other soft particles. For instance, a hypothetical *modular* cMCLBM framework might function as follows. First, the user chooses the application fluid solver; cMCLBM in this case. Next, the user chooses the object being simulated, example choices being: liquid drops, vesicles, soft particles (i.e., capsules). Next, the relevant forces, based on the chosen object, which aim to enforce known physical

## 6. Conclusions and Future Work

behaviour of that object, are selected. Following this, any additional methodology modifications and extensions required for the simulation of that object are also selected, i.e., inclusion of a density contrast between the fluids. Finally, the user might set object specific simulation parameters, i.e., for vesicles, the surface tension, bending rigidity and deflation parameters. An example structure, or flow, of such a user interface can be seen in Figure 6.2. While the functional scope of DL\_MESO is broader, other simulations tools with much narrower scope, such as HemoCell [159, 160] might prove to be more efficient for very large scale haemodynamics studies, targeting for example, the origin constitutive relations. However, where the subtle features of the precise membrane deformation are at issue, for example when studying the intimate interaction of a few erythrocytes, the DL\_MESO encapsulation we outline above might offer an attractive approach.



**Figure 6.2:** Schematic showing an example of how a *modular* cMCLBM approach may be used for the simulation of Liquid Drops, Vesicles and other Soft Particles. Note, Soft Particles are included to show another possible area of application for the cMCLBM, where the selected relevant forces and modifications would differ depending upon the nature of the soft particle being targeted.

Generally, by incorporating such methodological advancements as those documented in this thesis (which are, note, only possible following a validation of the methodology -kinematics and dynamics- emphasised throughout), into a computational platform such as DL\_MESO, the applicability of the cMCLBM would be greatly increased. This observation applies to the inclusion of soft particles in Figure 6.2, which could be another fruitful area of application for the cMCLBM. Here, by inclusion of additional forces (for instance, a shear modulus) the method could potentially be applied to soft particle phenomena —such as that studied recently by Owen and Krüger using the FEM-LBM approach [199].



### 6.2.3 Applications

The current chromodynamic model for simulating vesicle hydrodynamic has shown an ability to replicate a correct RBC profile in steady state, as well as recover known RBC dynamics. The application of the current model to single or dual RBC flows is an obvious next step for this work. Due to the tunability of the model, a relevant first application could be the simulation of infected red blood cells (iRBCs). Diseases such as malaria can cause changes in RBC shape, dynamical response (stiffness) and also the ability to recover back to its initial profile [200]. The impact on the ability of iRBCs to pass through stenosed passageways, their shape evolution throughout this and also the impact on dual RBC flows in this passageway would be of interest and within scope of even an unevolved, current model. Data from such a model could help with the design of microfluidics devices which address the recognition and removal of iRBCs, within the human body, and applications also allowing for further testing of the stability, robustness and tunability of the parent model.

# Appendices



# Multi-Relaxation Time Chromodynamic Lattice Boltzmann Method

## Contents

---

<b>A.1 Dynamics</b>	<b>183</b>
A.1.1 Dynamics: 2D MRT cMCLBM for fluids with a large density contrast	183
A.1.2 Dynamics: Pseudo 3D MRT cMCLBM for fluids with a large density contrast	186
<b>A.2 Analytical Solutions</b>	<b>188</b>
A.2.1 Transient uni-directional multi-component flow with trans- verse density stratification	188
A.2.2 Numerical solution of steady, pressure-driven flow with density stratification	194

---

## A.1 Dynamics

### A.1.1 Dynamics: 2D MRT cMCLBM for fluids with a large density contrast

In section 3.3.1 an Chapman-Enskog analysis was presented which sought to recover the weakly compressible Navier-Stokes equations from the kinetic scale evolution equation for the BGK cMCLBM allowing for the simulation of fluids with a density contrast. This analysis was presented in full detail. Here, a much briefer analysis is presented for the MRT model outlined in section 4.2.2, which will only present

### A. Multi-Relaxation Time Chromodynamic Lattice Boltzmann Method

key equations and relate them to the BGK model analysis from section 3.3.1. Again, this analysis will follow that presented in [70], and by Spendlove et al. [134].

The MRT LBE with a force term can be expressed in the following form:

$$f_i(\underline{r} + \underline{c}_i \Delta t, t + \Delta t) = f_i(\underline{r}, t) + \sum_j A_{ij} [f_j^{(0)}(\underline{r}, t) - f_j(\underline{r}, t)] + \Delta t F_i, \quad (\text{A.1})$$

where all terms have the same definitions presented in section 4.2.2. The source term and lattice weights have the same lattice properties as that defined in section 3.3.1. Now however, the collision matrix is defined to have the following lattice properties:

$$\sum_i A_{ij} (1, c_{i\alpha}, c_{i\alpha} c_{i\beta}) = (0, 0, \lambda_3 c_{j\alpha} c_{j\beta}) \quad (\text{A.2})$$

After Taylor expanding and applying Chapman-Enskog procedure to Eq. (A.1) like in Eq. (3.21), grouping together the most rapid behaviour of the model,  $O(\epsilon)$  terms :

$$O(\epsilon) : (c_{i\alpha} \partial_\alpha + \partial_{t_0}) f_i^{(0)} = -\frac{1}{\Delta t} \sum_j A_{ij} f_j^{(1)} + F_i, \quad (\text{A.3})$$

as well as the  $O(\epsilon^2)$  terms:

$$O(\epsilon^2) : \partial_{t_1} f_i^{(0)} + (c_{i\alpha} \partial_\alpha + \partial_{t_0}) f_i^{(1)} - \frac{1}{2} (c_{i\alpha} \partial_\alpha + \partial_{t_0}) \sum_j A_{ij} f_j^{(1)} = -\frac{1}{2} (c_{i\alpha} \partial_\alpha + \partial_{t_0}) \Delta t F_i. \quad (\text{A.4})$$

Next, taking the moments of Eq. (A.3):

$$\sum_i O(\epsilon) : \partial_\alpha \rho u_\alpha + \partial_{t_0} \rho = 0, \quad (\text{A.5})$$

$$\sum_i O(\epsilon) c_{ix} : \partial_\alpha \Pi_{\alpha x}^{(0)} + \partial_{t_0} \rho u_x = n F_x, \quad (\text{A.6})$$

where unlike in the BGK variant analysis presented in section 3.3.1 and in Guo et al., there is not a constraint coupling  $n$ ,  $m$  and  $\tau$  (the collision parameter). Here, the constraint imposed on  $n$  is  $n = 1$ , with no constraint on  $m$  at  $O(\epsilon)$ .

Taking the moments of Eq. (A.4), resulting in:

$$\sum_i O(\epsilon^2) : \partial_{t_1} \rho = \left(m - \frac{n}{2}\right) \Delta t \partial_\alpha F_\alpha, \quad (\text{A.7})$$

$$\sum_i O(\epsilon^2) c_{ix} : \partial_{t_1} (\rho u_y) = \Delta t \left(m - \frac{n}{2}\right) \partial_{t_0} F_y + \partial_\alpha \sigma'_{\alpha y}, \quad (\text{A.8})$$

where the viscous stress tensor  $\sigma'_{\alpha y}$  is given by:

$$\sigma'_{\alpha y} = -\left(1 - \frac{\lambda_3}{2}\right) \Pi_{\alpha y}^{(1)} - \frac{\Delta t}{4} (C_{\alpha y} + C_{y\alpha}). \quad (\text{A.9})$$

### A. Multi-Relaxation Time Chromodynamic Lattice Boltzmann Method

and where  $\Pi_{\alpha\beta}^{(1)}$  represents the 1st order momentum flux. Due to the previous constraint on  $n$ ,  $m$  is defined as  $m = \frac{1}{2}$ , the first term in Eq. (A.8) on the right hand side is eliminated.

At this point Guo et al., has the following constraints imposed on  $n$  and  $m$ :  $m = \frac{1}{2}$ ,  $n + \frac{m}{\tau} = 1$ . Note, the constraint on  $n$  differs from the constraint in this analysis, which has consequences later.

Taking the second moment of equation (A.3) and summing on  $i$ ,  $\sum_i c_{i\alpha} c_{i\beta}$ , then rearranging for  $\Pi_{\alpha\beta}^{(1)}$  gives:

$$\begin{aligned} \frac{\Pi_{\alpha\beta}^{(1)}}{\delta t} = & -\frac{2\rho}{3\lambda_3} S_{\alpha\beta} - \frac{u_\alpha}{\lambda_3} (F_\beta - \partial_\beta \Phi') - \frac{u_\beta}{\lambda_3} (F_\alpha - \partial_\alpha \Phi') + \\ & + \frac{1}{\lambda_3} \left[ u_\gamma \partial_\gamma \Phi' - \frac{1}{3} \rho \partial_\gamma u_\gamma \right] \delta_{\alpha\beta} + \\ & + \frac{1}{2\lambda_3} (C_{\alpha\beta} + C_{\alpha\beta}). \end{aligned} \quad (\text{A.10})$$

where  $S_{\alpha\beta} = \frac{1}{2} (\partial_\alpha u_\beta + \partial_\beta u_\alpha)$ , and  $\Phi' = \frac{3}{5}(1 - \alpha_R)(\rho_R + \Lambda \rho_B) - \frac{1}{3}\rho$ , as defined in section 3.3.1.

Using the definition of the viscous stress tensor, Eq. (A.9), Eq. (A.10) and simplifying

$$\begin{aligned} \frac{\sigma'_{\alpha\beta}}{\Delta t} = & -\frac{1}{2\lambda_3} (C_{\alpha\beta} + C_{\beta\alpha}) + \frac{2}{3} \left( \frac{1}{\lambda_3} - \frac{1}{2} \right) \rho S_{\alpha\beta} + \\ & + \left( \frac{1}{\lambda_3} - \frac{1}{2} \right) [u_\alpha (F_\beta - \partial_\beta \Phi') + u_\beta (F_\alpha - \partial_\alpha \Phi')] + \\ & - \left( \frac{1}{\lambda_3} - \frac{1}{2} \right) \left[ u_\gamma \partial_\gamma \Phi' - \frac{1}{3} \rho \partial_\gamma u_\gamma \right] \delta_{\alpha\beta}. \end{aligned} \quad (\text{A.11})$$

Thus, to remove the error, the following choice of correction tensor is made:

$$\begin{aligned} C_{\alpha\beta} = & \left( 1 - \frac{\lambda_3}{2} \right) [u_\alpha (F_\beta - \partial_\beta \Phi') + u_\beta (F_\alpha - \partial_\alpha \Phi')] + \\ & - \left( 1 - \frac{\lambda_3}{2} \right) \left[ u_\gamma \partial_\gamma \Phi' - \frac{1}{3} \rho \partial_\gamma u_\gamma \right] \delta_{\alpha\beta}. \end{aligned} \quad (\text{A.12})$$

The resultant source term  $F_i$  due to this correction, previously introduced in the forced evolution equation, Eq. (A.1), has now been recovered and is given by:

$$\begin{aligned} F_i = t_i \left\{ \frac{F_\alpha c_{i\alpha}}{c_s^2} + \right. \\ \left. \frac{1}{2c_s^4} \left( 1 - \frac{\lambda_3}{2} \right) \left[ u_\alpha (F_\beta - \partial_\beta \Phi') + u_\beta (F_\alpha - \partial_\alpha \Phi') - \left[ u_\gamma \partial_\gamma \Phi' - \frac{\rho}{3} \partial_\gamma u_\gamma \right] \delta_{\alpha\beta} \right] \times \right. \\ \left. (c_{i\alpha} c_{i\beta} - c_s^2 \delta_{\alpha\beta}) \right\}, \end{aligned} \quad (\text{A.13})$$

### A. Multi-Relaxation Time Chromodynamic Lattice Boltzmann Method

where, the source term  $F_i$  is split into a part that is responsible for correcting the model dynamics in the presence of density gradients,  $F_{1i}$ , and a term responsible for applying the surface tension force  $F_{2i}$ .

$$F_{1i} = \frac{t_i}{2c_s^4} \left(1 - \frac{\lambda_3}{2}\right) \left\{ \frac{1}{3} \rho \partial_\gamma u_\gamma \delta_{\alpha\beta} - (u_\alpha \partial_\beta \Phi' + u_\beta \partial_\alpha \Phi' + u_\gamma \partial_\gamma \Phi' \delta_{\alpha\beta}) \right\} (c_{i\alpha} c_{i\beta} - c_s^2 \delta_{\alpha\beta}), \quad (\text{A.14})$$

and

$$F_{2i} = t_i \left\{ \frac{F_\alpha c_{i\alpha}}{c_s^2} + \frac{1}{2c_s^4} \left(1 - \frac{\lambda_3}{2}\right) (u_\alpha F_\beta + u_\beta F_\alpha) (c_{i\alpha} c_{i\beta} - c_s^2 \delta_{\alpha\beta}) \right\} \quad (\text{A.15})$$

#### A.1.2 Dynamics: Pseudo 3D MRT cMCLBM for fluids with a large density contrast

Here, a brief analysis is presented for the MRT model outlined in section 4.3.2, which will only present key equations and relate them to the BGK model analysis from section 3.3.1. Again, this analysis will follow that presented in [70], and by Spendlove et al. [135]. The MRT LBE with a force term can be expressed in the following form:

$$f_i(\underline{r} + \underline{c}_i \Delta t, t + \Delta t) = f_i(\underline{r}, t) + \sum_j A_{ij} [f_j^{(0)}(\underline{r}, t) - f_j(\underline{r}, t)] + \Delta t F_i, \quad (\text{A.16})$$

where all terms have the same definitions presented in section 4.2.2. The source term and lattice weights have the same lattice properties as that defined in section 3.3.1. Now however, the collision matrix is defined to have the following lattice properties:

$$\sum_i A_{ij} (1, c_{i\alpha}, c_{i\alpha} c_{i\beta}) = (0, 0, \lambda_3 c_{j\alpha} c_{j\beta}) \quad (\text{A.17})$$

After Taylor expanding and applying Chapman-Enskog procedure to Eq. (A.16) like in Eq. (3.21), grouping together the most rapid behaviour of the model,  $O(\epsilon)$  terms :

$$O(\epsilon) : (c_{i\alpha} \partial_\alpha + \partial_{t_0}) f_i^{(0)} = -\frac{1}{\Delta t} \sum_j A_{ij} f_j^{(1)} + F_i, \quad (\text{A.18})$$

as well as the  $O(\epsilon^2)$  terms:

$$O(\epsilon^2) : \partial_{t_1} f_i^{(0)} + (c_{i\alpha} \partial_\alpha + \partial_{t_0}) f_i^{(1)} - \frac{1}{2} (c_{i\alpha} \partial_\alpha + \partial_{t_0}) \sum_j A_{ij} f_j^{(1)} = -\frac{1}{2} (c_{i\alpha} \partial_\alpha + \partial_{t_0}) \Delta t F_i. \quad (\text{A.19})$$

Next, taking the moments of Eq. (A.18):

$$\sum_i O(\epsilon) : \partial_\alpha \rho u_\alpha + \partial_{t_0} \rho = A, \quad (\text{A.20})$$

$$\sum_i O(\epsilon) c_{ix} : \partial_\alpha \Pi_{\alpha x}^{(0)} + \partial_{t_0} \rho u_x = n F_x, \quad (\text{A.21})$$

### A. Multi-Relaxation Time Chromodynamic Lattice Boltzmann Method

where  $A$  is the continuity source/sink defined in Eq. (4.39), which was set equal to 0 for the previous dynamics analysis.

Taking the moments of Eq. (A.19), resulting in:

$$\sum_i O(\epsilon^2) : \quad \partial_{t_1} \rho = \left(m - \frac{n}{2}\right) \Delta t \partial_\alpha F_\alpha - \frac{1}{2} \partial_{t_0} A, \quad (\text{A.22})$$

$$\sum_i O(\epsilon^2) c_{ix} : \quad \partial_{t_1} (\rho u_y) = \Delta t \left(m - \frac{n}{2}\right) \partial_{t_0} F_y + \partial_\alpha \sigma'_{\alpha y}, \quad (\text{A.23})$$

where the viscous stress tensor  $\sigma'_{\alpha y}$  is given by

$$\sigma'_{\alpha y} = - \left(1 - \frac{\lambda_3}{2}\right) \Pi_{\alpha y}^{(1)} - \frac{\Delta t}{4} (C_{\alpha y} + C_{y\alpha}) - \frac{\Delta t}{6} A \delta_{\alpha y}. \quad (\text{A.24})$$

and where  $\Pi_{\alpha\beta}^{(1)}$  represents the 1st order momentum flux. Due to the previous constraint on  $n$ ,  $m$  is defined as  $m = \frac{1}{2}$ , the first term in Eq. (A.23) on the right hand side is eliminated.

Taking the second moment of equation (A.3) and summing on  $i$ ,  $\sum_i c_{i\alpha} c_{i\beta}$ , then rearranging for  $\Pi_{\alpha\beta}^{(1)}$  gives:

$$\begin{aligned} \frac{\Pi_{\alpha\beta}^{(1)}}{\Delta t} = & -\frac{2\rho}{3\lambda_3} S_{\alpha\beta} - \frac{u_\alpha}{\lambda_3} (F_\beta - \partial_\beta \Phi') - \frac{u_\beta}{\lambda_3} (F_\alpha - \partial_\alpha \Phi') + \\ & + \frac{1}{\lambda_3} \left[ u_\gamma \partial_\gamma \Phi' - \frac{1}{3} \rho \partial_\gamma u_\gamma \right] \delta_{\alpha\beta} + \\ & + \frac{1}{2\lambda_3} (C_{\alpha\beta} + C_{\beta\alpha}) + \frac{c_s^2}{\lambda_3} A \delta_{\alpha\beta} + \frac{1}{2\lambda_3} u_\alpha u_\beta A. \end{aligned} \quad (\text{A.25})$$

where  $S_{\alpha\beta} = \frac{1}{2} (\partial_\alpha u_\beta + \partial_\beta u_\alpha)$ , and  $\Phi' = \frac{3}{5} (1 - \alpha_R) (\rho_R + \Lambda \rho_B) - \frac{1}{3} \rho$ , as defined in section 3.3.1.

Using the definition of the viscous stress tensor, Eq. (A.24), Eq. (A.25) and simplifying:

$$\begin{aligned} \frac{\sigma'_{\alpha\beta}}{\Delta t} = & -\frac{1}{2\lambda_3} (C_{\alpha\beta} + C_{\beta\alpha}) + \frac{2}{3} \left( \frac{1}{\lambda_3} - \frac{1}{2} \right) \rho S_{\alpha\beta} + \\ & + \left( \frac{1}{\lambda_3} - \frac{1}{2} \right) [u_\alpha (F_\beta - \partial_\beta \Phi') + u_\beta (F_\alpha - \partial_\alpha \Phi')] + \\ & - \left( \frac{1}{\lambda_3} - \frac{1}{2} \right) \left[ u_\gamma \partial_\gamma \Phi' - \frac{1}{3} \rho \partial_\gamma u_\gamma \right] \delta_{\alpha\beta} \\ & - \frac{1}{3\lambda_3} A \delta_{\alpha\beta} - \left( \frac{1}{\lambda_3} - \frac{1}{2} \right) u_\alpha u_\beta A. \end{aligned} \quad (\text{A.26})$$

Thus, to remove the error, the following choice of correction tensor is made:

$$\begin{aligned} C_{\alpha\beta} = & \left(1 - \frac{\lambda_3}{2}\right) [u_\alpha (F_\beta - \partial_\beta \Phi') + u_\beta (F_\alpha - \partial_\alpha \Phi')] + \\ & - \left(1 - \frac{\lambda_3}{2}\right) \left[ u_\gamma \partial_\gamma \Phi' - \frac{1}{3} \rho \partial_\gamma u_\gamma \right] \delta_{\alpha\beta} \\ & - \frac{1}{3} A \delta_{\alpha\beta} - \left(1 - \frac{\lambda_3}{2}\right) A u_\alpha u_\beta \end{aligned} \quad (\text{A.27})$$

## A. Multi-Relaxation Time Chromodynamic Lattice Boltzmann Method

The resultant source term  $F_i$  due to this correction, previously introduced in the forced evolution equation, Eq. (A.1), has now been recovered and is given by:

$$F_i = F_{1i} + F_{2i} + F_{3i}, \quad (\text{A.28})$$

where, the source term  $F_i$  is split into: (1) a part that is responsible for correcting the model dynamics in the presence of density gradients ( $F_{1i}$ ), (2) a term responsible for applying the surface tension force ( $F_{2i}$ ) and (3) a term containing the continuity source/ sink ( $F_{3i}$ ). These terms are defined as:

$$F_{1i} = \frac{t_i}{2c_s^4} \left(1 - \frac{\lambda_3}{2}\right) \left\{ \frac{1}{3} \rho \partial_\gamma u_\gamma \delta_{\alpha\beta} - (u_\alpha \partial_\beta \Phi' + u_\beta \partial_\alpha \Phi' + u_\gamma \partial_\gamma \Phi' \delta_{\alpha\beta}) \right\} (c_{i\alpha} c_{i\beta} - c_s^2 \delta_{\alpha\beta}), \quad (\text{A.29})$$

and

$$F_{2i} = t_i \left\{ \frac{F_\alpha c_{i\alpha}}{c_s^2} + \frac{1}{2c_s^4} \left(1 - \frac{\lambda_3}{2}\right) (u_\alpha F_\beta + u_\beta F_\alpha) (c_{i\alpha} c_{i\beta} - c_s^2 \delta_{\alpha\beta}) \right\} \quad (\text{A.30})$$

and

$$F_{3i} = t_i A - \left(1 - \frac{\lambda_3}{2}\right) A u_\alpha u_\beta - \frac{1}{3} A \delta_{\alpha\beta}. \quad (\text{A.31})$$

## A.2 Analytical Solutions

### A.2.1 Transient uni-directional multi-component flow with transverse density stratification

Here, a semi-analytical solution is presented for the scenario of density stratified, uni-directional flow  $u(x)\hat{e}_y$ ,  $x$  transverse variation in density and translational invariance in the  $y$  direction. No-slip boundaries are also presented at  $x = 0$  and  $x = H$ . Noting here, that it is necessary to assume that the shear viscosity will be constant across the fluids, meaning that any variation in kinematic viscosity of the fluids stems from the variation in density. A schematic representation of the described scenario is depicted in Figure 4.5. The Navier-Stokes equation for weakly compressible fluids that represent this system are as follows:

$$\rho(x) \frac{\partial u}{\partial t} = \frac{\partial}{\partial x} \left( \eta(x) \frac{\partial}{\partial x} u(x, t) \right), \quad (\text{A.32})$$

where  $\rho$ ,  $u$ , and  $\eta$  denote the density, velocity and shear viscosity of the fluid respectively. With associated No-slip boundary conditions for the system are:

$$u(0) = u(H) = 0. \quad (\text{A.33})$$



### A. Multi-Relaxation Time Chromodynamic Lattice Boltzmann Method

From here, the analysis follows the steps taken to find a solution for  $u(x, t)$ , using the eigenbasis of the Sturm-Liouville problem, which is presented as follows [201]:

$$\frac{d}{dx} \left( \eta \frac{d\phi_n}{dx} \right) + c_n^2 \rho \phi_n = 0, \quad (\text{A.34})$$

where  $\phi_n$  represents the eigenfunction and  $c_n$  denotes the eigenvalue. The following property:

$$\int \rho \phi_n \phi_m dx = k \delta_{nm}, \quad (\text{A.35})$$

holds true for orthonormality if  $k = 1$ , where  $\delta_{nm}$  is a Kronecker delta. The Modal expansion is:

$$u(x, t) = \sum_{n=1}^{\infty} T_n(t) \phi_n(x), \quad (\text{A.36})$$

where  $T_n$  is the time-dependent modal co-efficient. Using PDE transformation (A.36) on Eq. (A.32), the following can be obtained:

$$\sum_n \left( \rho \frac{\partial T_n}{\partial t} \phi_n - T_n \frac{\partial}{\partial x} \left( \eta \frac{\partial \phi_n}{\partial x} \right) \right) = 0. \quad (\text{A.37})$$

Multiplying Eq. (A.37) through by  $\phi_m$ , and then integrating over lattice domain (e.g.  $\int_0^H dx$ ) gives:

$$\sum_n \frac{\partial T_n}{\partial t} \int_0^H \rho \phi_n \phi_m dx - \sum_n T_n \int_0^H \phi_m \frac{\partial}{\partial x} \left( \eta \frac{\partial \phi_n}{\partial x} \right) dx = 0. \quad (\text{A.38})$$

Combining Eqs. (A.34) (A.35) with Eq. (A.38), obtaining:

$$\begin{aligned} \sum_n \frac{\partial T_n}{\partial t} \delta_{nm} + \sum_n T_n c_n^2 \delta_{nm} &= 0 \\ \frac{dT_m}{dt} + c_n^2 T_m &= 0 \\ T_m &= \sigma_m e^{-c_n^2 t}, \end{aligned} \quad (\text{A.39})$$

where  $\sigma_m$  is a constant still to be determined.

Similarly, by multiplying Eq. (A.34) through by  $\phi_m$  and performing domain integration  $\int_0^H dx$ , results in the following:

$$\int_0^H \phi_m \frac{d}{dx} \left( \eta \frac{d\phi_n}{dx} \right) dx + c_n^2 \int_0^H \rho \phi_n \phi_m dx = 0. \quad (\text{A.40})$$

Performing integration by parts on the first term of Eq. (A.40) gives:

$$- \int_0^H \eta \frac{d\phi_m}{dx} \frac{d\phi_n}{dx} dx + \eta \frac{d\phi_n}{dx} \phi_m \Big|_0^H + c_n^2 \int_0^H \rho \phi_n \phi_m dx = 0. \quad (\text{A.41})$$

### A. Multi-Relaxation Time Chromodynamic Lattice Boltzmann Method

The term  $\eta \frac{d\phi_n}{dx} \phi_m \Big|_0^H$  from Eq. (A.41) equals to zero (see Eq. (A.46) later), meaning:

$$- \int_0^H \eta \frac{d\phi_m}{dx} \frac{d\phi_n}{dx} dx + c_n^2 \int_0^H \rho \phi_n \phi_m dx = 0. \quad (\text{A.42})$$

Repeating the same process for ‘ $m$ ’, and analysing the alternative S-L equation now given by:

$$\frac{d}{dx} \left( \eta \frac{d\phi_m}{dx} \right) + c_m^2 \rho \phi_m = 0,$$

leads to:

$$- \int_0^H \eta \frac{d\phi_n}{dx} \frac{d\phi_m}{dx} dx + c_m^2 \int_0^H \rho \phi_m \phi_n dx = 0. \quad (\text{A.43})$$

Now, subtracting Eq. (A.43) from Eq. (A.42), giving:

$$(c_n^2 - c_m^2) \int_0^H \rho \phi_m \phi_n dx = 0.$$

This result shows that when  $n \neq m$ , it is possible to obtain the following equation:

$$\int_0^H \rho \phi_m \phi_n dx = 0,$$

which agrees with the orthonormality property stated in Eq. (A.35).

Next, utilising the boundary conditions to support the analysis and help find a solution for the eigenfunction. First, investigating the conditions at the interface boundary. Here, Eq. (A.44) imposes the continuous eigenfuctions at the interface and Eq. (A.45) encapsulates the physics of the no traction condition:

$$\phi_n^{(1)} \left( \frac{H}{2} \right) = \phi_n^{(2)} \left( \frac{H}{2} \right), \quad (\text{A.44})$$

$$\eta_1 \phi_n^{(1)'} \left( \frac{H}{2} \right) = \eta_2 \phi_n^{(2)'} \left( \frac{H}{2} \right). \quad (\text{A.45})$$

Where the no-slip conditions in Eq. (A.33) give:

$$\left[ \phi_m \frac{d\phi_n}{dx} \right]_0^H = \phi_m(H) \frac{d\phi_n}{dx} \Big|_H - \phi_m(0) \frac{d\phi_n}{dx} \Big|_0 = 0, \quad (\text{A.46})$$

Because  $\phi_n$  is a piecewise function, the lattice can be split into 2 halves. When  $x \in [0, \frac{H}{2}]$ , the following is obtained:

$$\begin{aligned} \frac{d}{dx} \left( \eta_1 \frac{d\phi_n^{(1)}}{dx} \right) + c_n^2 \rho \phi_n^{(1)} &= 0, \\ m^2 + \frac{c_n^2}{\nu_1} &= 0, \\ m &= \pm \frac{c_n}{\sqrt{\nu_1}} i, \quad \in \mathbb{C} \end{aligned}$$

which results in:

$$\phi_n^{(1)} = A_n^{(1)} \cos\left(\frac{c_n}{\sqrt{\nu_1}}x\right) + B_n^{(1)} \sin\left(\frac{c_n}{\sqrt{\nu_1}}x\right). \quad (\text{A.47})$$

Similarly, when  $x \in \left[\frac{H}{2}, H\right]$ , the following is obtained:

$$\begin{aligned} \frac{d}{dx} \left( \eta_2 \frac{d\phi_n^{(2)}}{dx} \right) + c_n^2 \rho \phi_n^{(2)} &= 0, \\ m^2 + \frac{c_n^2}{\nu_2} &= 0, \\ m &= \pm \frac{c_n}{\sqrt{\nu_2}}i, \quad \in \mathbb{C} \end{aligned}$$

which gives:

$$\phi_n^{(2)} = A_n^{(2)} \cos\left(\frac{c_n}{\sqrt{\nu_2}}x\right) + B_n^{(2)} \sin\left(\frac{c_n}{\sqrt{\nu_2}}x\right). \quad (\text{A.48})$$

Now imposing the no-slip boundary conditions at  $x = 0, H$ , i.e. changing the boundary conditions away from periodic. This reduces Eqs. (A.47) and (A.48) to the following:

$$\phi_n^{(1)} = A_n^{(1)} \sin\left(\frac{c_n}{\sqrt{\nu_1}}x\right), \quad x \in \left[0, \frac{H}{2}\right], \quad (\text{A.49})$$

$$\phi_n^{(2)} = A_n^{(2)} \sin\left(\frac{c_n}{\sqrt{\nu_2}}(x - H)\right), \quad x \in \left[\frac{H}{2}, H\right]. \quad (\text{A.50})$$

Now using Eqs. (A.49) and (A.50) with Eq. (A.44), it is possible to show

$$\begin{aligned} \phi_n^{(1)}\left(\frac{H}{2}\right) &= \phi_n^{(2)}\left(\frac{H}{2}\right), \\ A_n^{(1)} \sin\left(\frac{c_n}{\sqrt{\nu_1}} \frac{H}{2}\right) &= A_n^{(2)} \sin\left(\frac{c_n}{\sqrt{\nu_2}} \cdot \left(-\frac{H}{2}\right)\right), \\ A_n^{(1)} \sin\left(\frac{c_n}{\sqrt{\nu_1}} \frac{H}{2}\right) + A_n^{(2)} \sin\left(\frac{c_n}{\sqrt{\nu_2}} \cdot \frac{H}{2}\right) &= 0. \end{aligned} \quad (\text{A.51})$$

Then using Eq. (A.49) and (A.50) with Eq. (A.45), gives:

$$\begin{aligned} \eta_1 \phi_n^{(1)'}\left(\frac{H}{2}\right) &= \eta_2 \phi_n^{(2)'}\left(\frac{H}{2}\right), \\ A_n^{(1)} \frac{c_n}{\sqrt{\nu_1}} \eta_1 \cos\left(\frac{c_n}{\sqrt{\nu_1}} \frac{H}{2}\right) &= A_n^{(2)} \frac{c_n}{\sqrt{\nu_2}} \eta_2 \times \\ &\quad \cos\left(\frac{c_n}{\sqrt{\nu_2}} \cdot \left(-\frac{H}{2}\right)\right), \\ A_n^{(1)} \frac{1}{\sqrt{\nu_1}} \eta_1 \cos\left(\frac{c_n}{\sqrt{\nu_1}} \frac{H}{2}\right) - A_n^{(2)} \frac{1}{\sqrt{\nu_2}} \eta_2 \cos\left(\frac{c_n}{\sqrt{\nu_2}} \cdot \left(-\frac{H}{2}\right)\right) &= 0. \end{aligned} \quad (\text{A.52})$$

### A. Multi-Relaxation Time Chromodynamic Lattice Boltzmann Method

Eqs. (A.51) and (A.52) are a pair of simultaneous equations which only have non-zero solutions for  $A_n^{(1)}$  and  $A_n^{(2)}$ , if the determinant of the matrix of coefficients equals to 0, as shown below:

$$\begin{aligned}
& -\sin\left(\frac{c_n}{\sqrt{\nu_1}} \cdot \frac{H}{2}\right) \frac{\eta_2}{\sqrt{\nu_2}} \cos\left(\frac{c_n}{\sqrt{\nu_2}} \cdot \left(-\frac{H}{2}\right)\right) - \sin\left(\frac{c_n}{\sqrt{\nu_2}} \cdot \frac{H}{2}\right) \frac{\eta_1}{\sqrt{\nu_1}} \cos\left(\frac{c_n}{\sqrt{\nu_1}} \cdot \frac{H}{2}\right) = 0, \\
& -\frac{\eta_2}{\sqrt{\nu_2}} \sin\left(\frac{c_n}{\sqrt{\nu_1}} \cdot \frac{H}{2}\right) \cos\left(\frac{c_n}{\sqrt{\nu_2}} \cdot \frac{H}{2}\right) - \frac{\eta_1}{\sqrt{\nu_1}} \sin\left(\frac{c_n}{\sqrt{\nu_2}} \cdot \frac{H}{2}\right) \cos\left(\frac{c_n}{\sqrt{\nu_1}} \cdot \frac{H}{2}\right) = 0, \\
& \frac{\eta_2}{\sqrt{\nu_2}} \sin\left(\frac{c_n}{\sqrt{\nu_1}} \cdot \frac{H}{2}\right) \cos\left(\frac{c_n}{\sqrt{\nu_2}} \cdot \frac{H}{2}\right) + \frac{\eta_1}{\sqrt{\nu_1}} \sin\left(\frac{c_n}{\sqrt{\nu_2}} \cdot \frac{H}{2}\right) \cos\left(\frac{c_n}{\sqrt{\nu_1}} \cdot \frac{H}{2}\right) = 0, \\
& \sqrt{\eta_2 \rho_2} \sin\left(\frac{c_n}{\sqrt{\nu_1}} \cdot \frac{H}{2}\right) \cos\left(\frac{c_n}{\sqrt{\nu_2}} \cdot \frac{H}{2}\right) + \sqrt{\eta_1 \rho_1} \sin\left(\frac{c_n}{\sqrt{\nu_2}} \cdot \frac{H}{2}\right) \cos\left(\frac{c_n}{\sqrt{\nu_1}} \cdot \frac{H}{2}\right) = 0.
\end{aligned} \tag{A.53}$$

Dividing Eq. (A.53) through by  $\sin\left(\frac{c_n}{\sqrt{\nu_1}} \cdot \frac{H}{2}\right) \cos\left(\frac{c_n}{\sqrt{\nu_2}} \cdot \frac{H}{2}\right) \sqrt{\eta_2 \rho_2}$ , results in:

$$1 + \frac{\sqrt{\eta_1 \rho_1} \tan\left(\frac{c_n}{\sqrt{\nu_2}} \cdot \frac{H}{2}\right)}{\sqrt{\eta_2 \rho_2} \tan\left(\frac{c_n}{\sqrt{\nu_1}} \cdot \frac{H}{2}\right)} = 0. \tag{A.54}$$

Eq. (A.54) is the secular equation to be solved for eigenvalues  $c_n$ . Let  $X = \frac{c_n H}{2}$ , and Eq. (A.54) reduces to:

$$\sqrt{\eta_2 \rho_2} \tan\left(\frac{X}{\sqrt{\nu_1}}\right) + \sqrt{\eta_1 \rho_1} \tan\left(\frac{X}{\sqrt{\nu_2}}\right) = 0. \tag{A.55}$$

Now Eq. (A.55) can be solved numerically using Newton-Raphson method as shown below. Where letting:

$$f(X) = \sqrt{\eta_2 \rho_2} \tan\left(\frac{X}{\sqrt{\nu_1}}\right) + \sqrt{\eta_1 \rho_1} \tan\left(\frac{X}{\sqrt{\nu_2}}\right),$$

and therefore:

$$\frac{df}{dx} = \sqrt{\frac{\eta_2 \rho_2}{\nu_1}} \sec^2\left(\frac{X}{\sqrt{\nu_1}}\right) + \sqrt{\frac{\eta_1 \rho_1}{\nu_2}} \sec^2\left(\frac{X}{\sqrt{\nu_2}}\right).$$

Newton-Raphson method states, for a function  $f(X) = 0$ , an approximated solution is:

$$X_1 = X_0 - \frac{f(X_0)}{f'(X_0)}.$$

where  $X_1$  is the improved estimate from initial estimate  $X_0$ . The initial estimate,  $X_0$  was obtained by observing when the profile bisected the horizontal axis. This

### A. Multi-Relaxation Time Chromodynamic Lattice Boltzmann Method

then provided a solution for the eigenvalues,  $\phi_n$ .

Next impose orthonormality when  $n = m$ :

$$\int_0^H \rho \phi_n \phi_n dx = 1. \quad (\text{A.56})$$

Substitute Eqs. (A.49) and (A.50) into Eq. (A.56) over the two intervals, obtaining:

$$\begin{aligned} \rho_1 A_n^{(1)^2} \int_0^{\frac{H}{2}} \sin^2 \left( \frac{c_n}{\sqrt{\nu_1}} x \right) dx + \rho_2 A_n^{(2)^2} \int_{\frac{H}{2}}^H \sin^2 \left( \frac{c_n}{\sqrt{\nu_2}} (x - H) \right) dx &= 1 \\ \frac{\rho_1}{2} A_n^{(1)^2} \int_0^{\frac{H}{2}} \left( 1 - \cos \left( \frac{2c_n}{\sqrt{\nu_1}} x \right) \right) dx + \frac{\rho_2}{2} A_n^{(2)^2} \int_{\frac{H}{2}}^H \left( 1 - \cos \left( \frac{2c_n}{\sqrt{\nu_2}} (x - H) \right) \right) dx &= 1 \\ \frac{\rho_1}{2} A_n^{(1)^2} \left( \frac{H}{2} - \frac{\sqrt{\nu_1}}{2c_n} \left[ \sin \left( \frac{2c_n}{\sqrt{\nu_1}} x \right) \right]_0^{\frac{H}{2}} \right) + & \\ \frac{\rho_2}{2} A_n^{(2)^2} \left( \frac{H}{2} - \frac{\sqrt{\nu_2}}{2c_n} \left[ \sin \left( \frac{2c_n}{\sqrt{\nu_2}} (x - H) \right) \right]_{\frac{H}{2}}^H \right) &= 1 \\ \frac{\rho_1}{2} A_n^{(1)^2} \left( \frac{H}{2} - \frac{\sqrt{\nu_1}}{2c_n} \sin \left( \frac{c_n}{\sqrt{\nu_1}} H \right) \right) + \frac{\rho_2}{2} A_n^{(2)^2} \left( \frac{H}{2} - \frac{\sqrt{\nu_2}}{2c_n} \sin \left( \frac{c_n}{\sqrt{\nu_2}} H \right) \right) &= 1 \end{aligned} \quad (\text{A.57})$$

Rearranging Eq. (A.51) gives the following solution for the integration constant:

$$A_n^{(2)} = - \frac{A_n^{(1)} \sin \left( \frac{c_n H}{2\sqrt{\nu_1}} \right)}{\sin \left( \frac{c_n H}{2\sqrt{\nu_2}} \right)} \quad (\text{A.58})$$

Now, finally seeking a solution to the coefficients  $\sigma_n$ . Substitute Eq. (A.39) into Eq. (A.36), obtaining

$$u(x, t) = \sum_n \sigma_n e^{-c_n^2 t} \phi_n(x),$$

which means

$$u(x, 0) = \sum_n \sigma_n \phi_n(x). \quad (\text{A.59})$$

Multiplying Eq. (A.59) through by  $\phi_m$  and  $\rho$ , and then integrating over the length of the lattice (e.g.  $\int_0^H dx$ ) gives:

$$\begin{aligned} \int_0^H u(x, 0) \phi_m \rho dx &= \int_0^H \sum_n \sigma_n \phi_n(x) \phi_m \rho dx, \\ \int_0^H u(x, 0) \phi_m \rho dx &= \sum_n \int_0^H \sigma_n \phi_n(x) \phi_m \rho dx, \\ \int_0^H u(x, 0) \phi_m \rho dx &= \sum_n \sigma_n \int_0^H \phi_n(x) \phi_m \rho dx, \\ \int_0^H u(x, 0) \phi_m \rho dx &= \sum_n \sigma_n \delta_{nm}, \\ \int_0^H u(x, 0) \phi_m \rho dx &= \sigma_m. \end{aligned} \quad (\text{A.60})$$

### A. Multi-Relaxation Time Chromodynamic Lattice Boltzmann Method

Substituting Eqs. (A.47) and (A.48) into Eq. (A.60), using its piece-wise definition gives:

$$\begin{aligned}
& \rho_1 u_1 A_m^{(1)} \int_0^{\frac{H}{2}} \sin\left(\frac{c_m}{\sqrt{\nu_1}} x\right) dx + \rho_2 u_2 A_m^{(2)} \int_{\frac{H}{2}}^H \sin\left(\frac{c_m}{\sqrt{\nu_2}} (x - H)\right) dx = \sigma_m, \\
& \rho_1 u_1 \frac{\sqrt{\nu_1}}{c_m} A_m^{(1)} \left[ -\cos\left(\frac{c_m}{\sqrt{\nu_1}} x\right) \right]_0^{\left(\frac{H}{2}\right)} + \rho_2 u_2 \frac{\sqrt{\nu_2}}{c_m} A_m^{(2)} \left[ -\cos\left(\frac{c_m}{\sqrt{\nu_2}} (x - H)\right) \right]_{\frac{H}{2}}^H = \sigma_m, \\
& \rho_1 u_1 \frac{\sqrt{\nu_1}}{c_m} A_m^{(1)} \left[ -\cos\left(\frac{c_m}{\sqrt{\nu_1}}\right) \frac{H}{2} - (-1) \right] + \\
& \quad + \rho_2 u_2 \frac{\sqrt{\nu_2}}{c_m} A_m^{(2)} \left[ -\cos\left(\frac{c_m}{\sqrt{\nu_2}} \cdot 0\right) - -\cos\left(\frac{c_m}{\sqrt{\nu_2}} \cdot \left(-\frac{H}{2}\right)\right) \right] = \sigma_m, \\
& \rho_1 u_1 \frac{\sqrt{\nu_1}}{c_m} A_m^{(1)} \left( 1 - \cos\left(\frac{c_m}{\sqrt{\nu_1}} \frac{H}{2}\right) \right) - \rho_2 u_2 \frac{\sqrt{\nu_2}}{c_m} A_m^{(2)} \left( 1 - \cos\left(\frac{c_m}{\sqrt{\nu_2}} \cdot \frac{H}{2}\right) \right) = \sigma_m.
\end{aligned} \tag{A.61}$$

Substituting into Eq. (A.61) with Eq. (A.58):

$$\begin{aligned}
& \rho_1 u_1 \frac{\sqrt{\nu_1}}{c_m} A_m^{(1)} \left( 1 - \cos\left(\frac{c_m}{\sqrt{\nu_1}} \frac{H}{2}\right) \right) + A_m^{(1)} \rho_2 u_2 \frac{\sqrt{\nu_2}}{c_m} \left( \frac{\sin\left(\frac{c_n H}{2\sqrt{\nu_1}}\right)}{\sin\left(\frac{c_n H}{2\sqrt{\nu_2}}\right)} \right) \left( 1 - \cos\left(\frac{c_m}{\sqrt{\nu_2}} \cdot \frac{H}{2}\right) \right) \\
& = \sigma_m, \\
& A_m^{(1)} \left[ \rho_1 u_1 \frac{\sqrt{\nu_1}}{c_m} \left( 1 - \cos\left(\frac{c_m}{\sqrt{\nu_1}} \frac{H}{2}\right) \right) + \rho_2 u_2 \frac{\sqrt{\nu_2}}{c_m} \left( \frac{\sin\left(\frac{c_n H}{2\sqrt{\nu_1}}\right)}{\sin\left(\frac{c_n H}{2\sqrt{\nu_2}}\right)} \right) \left( 1 - \cos\left(\frac{c_m}{\sqrt{\nu_2}} \cdot \frac{H}{2}\right) \right) \right] \\
& = \sigma_m.
\end{aligned} \tag{A.62}$$

#### A.2.2 Numerical solution of steady, pressure-driven flow with density stratification

Here, an analytical solution of steady, pressure-driven flow with transverse variational density is presented. A schematic representation of the scenario being discussed can be found in section 4.2.3.2 shown by Figure 4.3. A steady pressure gradient is applied as  $-G\hat{e}_y$ . The transverse, continuous variation of density, displayed in Figure 4.3, can be expressed using the Heaviside function,  $\Theta(x)$  as follows:

$$\begin{aligned}
\rho(x) = & \frac{1}{2} (\rho_{0R} + \rho_{0B}) + \frac{1}{2} (\rho_{0R} - \rho_{0B}) \tanh\left(\beta\left(x - \frac{H}{4}\right)\right) \Theta\left(\frac{H}{2} - x\right) \\
& + \frac{1}{2} (\rho_{0R} - \rho_{0B}) \tanh\left(\beta\left(\frac{3H}{4} - x\right)\right) \Theta\left(x - \frac{H}{2}\right),
\end{aligned} \tag{A.63}$$

Now, writing the Navier-Stokes equation for a weakly compressible lattice fluid and associated boundary and symmetry conditions that characterise this particular flow:

$$\frac{d}{dx} \left( \eta(x) \frac{d}{dx} u(x) \right) = G, \quad u(0) = u(H) = 0, \quad \left[ \frac{du}{dx} \right]_{\frac{H}{2}} = 0, \tag{A.64}$$

### A. Multi-Relaxation Time Chromodynamic Lattice Boltzmann Method

where, as used throughout,  $\rho$ ,  $u$  and  $\eta$  denote density, velocity and shear viscosity of the fluid. Noting that, using the definition of shear viscosity:

$$\nu = \frac{\eta}{\rho}, \quad (\text{A.65})$$

that is kinematic viscosity,  $\nu$ , is set constant. Then due to the continuous variation in density, the shear viscosity will also have continuous transverse variation.

Now, letting  $x \leq \frac{H}{2}$  and integrating Eq. (A.64) and applying the symmetry condition to remove the integration constant results in:

$$\frac{du}{dx} = \frac{G(2x - H)}{2\eta(x)}. \quad (\text{A.66})$$

Rearranging Eq. (A.65) and substituting for  $\eta$ , taking the constant kinematic viscosity outside the integration. Now, integrating over the range  $[0, x < \frac{H}{2}]$ , using appropriate boundary condition and a dummy variable, it is possible to obtain the following:

$$u(x) = \frac{G}{2\nu(\lambda_3)} \int_0^x \frac{(2\alpha - H)}{\rho(\alpha)} d\alpha. \quad (\text{A.67})$$

Now, the integral above can be evaluated using Simpson's rule with the expression for the density given by Eq. (A.63) to produce a semi-analytical solution for this flow.

# B

## Simulation of Vesicles

### Contents

---

B.1	Computation of vesicle surface principal curvatures . . .	196
-----	---	-----

---

### B.1 Computation of vesicle surface principal curvatures

In order to calculate the Mean and Gaussian curvatures need to compute the membrane forces, the derivatives within the principal curvature expressions, Eq. (5.53), explored further as shown in Eq. (5.63), need to be transformed into derivatives within the laboratory frame. This appendix looks at the projection of the the derivatives from the simulation frame into the surface frame, again, using the unit normal to the surface as a basis for this, where the associated error is also considered by defining three different general surface co-ordinate frames. With choice of which co-ordinate frame is most appropriate at a location being defined as when the error is minimised. Recalling that:

$$\hat{e}_z = \left( [\hat{N}_X]_P, [\hat{N}_Y]_P, [\hat{N}_Z]_P \right), \quad (\text{B.1})$$

Defining three different general surface local co-ordinate frames,  $\Sigma_1(x_1, y_1, z_1), \dots, \Sigma_3(x_3, y_3, z_3)$ . The related  $x$  axes are given as follows (found by when dotted



### B. Simulation of Vesicles

on the  $z$  axes equal 0):

$$\begin{aligned}\hat{e}_{x_1} &= \frac{1}{\sqrt{1 - [N_Z]_P^2}} \left( -[\hat{N}_Y]_P, [\hat{N}_X]_P, 0 \right), \\ \hat{e}_{x_2} &= \frac{1}{\sqrt{1 - [N_X]_P^2}} \left( 0, [\hat{N}_Z]_P, -[\hat{N}_Y]_P \right), \\ \hat{e}_{x_3} &= \frac{1}{\sqrt{1 - [N_Y]_P^2}} \left( [\hat{N}_Z]_P, 0, -[\hat{N}_X]_P \right),\end{aligned}\tag{B.2}$$

with the corresponding orthogonal (or bi-normal)  $y$  axes being given by the cross-product of the  $x$  and  $z$  axes ( $\hat{e}_{y_i} = \hat{e}_z \times \hat{e}_{x_i}$ ):

$$\begin{aligned}\hat{e}_{y_1} &= \frac{1}{\sqrt{1 - [N_Z]_P^2}} \times \left( -[\hat{N}_X \hat{N}_Z]_P, -[\hat{N}_Y \hat{N}_Z]_P, [(1 - \hat{N}_Z^2)]_P \right), \\ \hat{e}_{y_2} &= \frac{1}{\sqrt{1 - [N_X]_P^2}} \times \left( [\hat{N}_X^2 - 1]_P, [\hat{N}_X \hat{N}_Y]_P, [\hat{N}_X \hat{N}_Z]_P \right), \\ \hat{e}_{y_3} &= \frac{1}{\sqrt{1 - [N_Y]_P^2}} \times \left( -[\hat{N}_X \hat{N}_Y]_P, [(1 - \hat{N}_Y^2)]_P, -[\hat{N}_Y \hat{N}_Z]_P \right).\end{aligned}\tag{B.3}$$

Now, projecting the simulation (or laboratory) frame normal  $\hat{N}$  into each of the local surface co-ordinate frames results in:

$$\begin{aligned}\hat{n}_{x_1} &= \hat{N} \cdot \hat{e}_{x_1} = \frac{-[\hat{N}_Y]_P \hat{N}_X + [\hat{N}_X]_P \hat{N}_Y}{\sqrt{1 - [N_Z]_P^2}}, \\ \hat{n}_{x_2} &= \frac{[\hat{N}_Z]_P \hat{N}_Y - [\hat{N}_Y]_P \hat{N}_Z}{\sqrt{1 - [N_X]_P^2}}, \\ \hat{n}_{x_3} &= \frac{[\hat{N}_Z]_P \hat{N}_X - [\hat{N}_X]_P \hat{N}_Z}{\sqrt{1 - [N_Y]_P^2}}.\end{aligned}\tag{B.4}$$

$$\begin{aligned}\hat{n}_{y_1} &= \hat{N} \cdot \hat{e}_{y_1} = \frac{-[\hat{N}_X \hat{N}_Z]_P \hat{N}_X - [\hat{N}_Y \hat{N}_Z]_P \hat{N}_Y + [(1 - \hat{N}_Z^2)]_P \hat{N}_Z}{\sqrt{1 - [N_Z]_P^2}}, \\ \hat{n}_{y_2} &= \frac{[\hat{N}_X^2 - 1]_P \hat{N}_X + [\hat{N}_X \hat{N}_Y]_P \hat{N}_Y + [\hat{N}_X \hat{N}_Z]_P \hat{N}_Z}{\sqrt{1 - [N_X]_P^2}}, \\ \hat{n}_{y_3} &= \frac{-[\hat{N}_X \hat{N}_Y]_P \hat{N}_X + [(1 - \hat{N}_Y^2)]_P \hat{N}_Y - [\hat{N}_Y \hat{N}_Z]_P \hat{N}_Z}{\sqrt{1 - [N_Y]_P^2}},\end{aligned}\tag{B.5}$$

similarly, the simulation frame derivatives are projected into the local co-ordinate frame as such:

$$\frac{\partial}{\partial x_1} = \hat{e}_{x_1} \cdot \nabla_X = \frac{1}{\sqrt{1 - [N_Z]_P^2}} \left( -[\hat{N}_Y]_P \frac{\partial}{\partial X} + [\hat{N}_X]_P \frac{\partial}{\partial Y} \right),\tag{B.6}$$

### B. Simulation of Vesicles

$$\begin{aligned}
\frac{\partial}{\partial x_2} &= \frac{1}{\sqrt{1 - [N_X]_P^2}} \left( [\hat{N}_Z]_P \frac{\partial}{\partial Y} - [\hat{N}_Y]_P \frac{\partial}{\partial Z} \right), \\
\frac{\partial}{\partial x_3} &= \frac{1}{\sqrt{1 - [N_Y]_P^2}} \left( [\hat{N}_Z]_P \frac{\partial}{\partial X} - [\hat{N}_X]_P \frac{\partial}{\partial Z} \right), \\
\frac{\partial}{\partial y_1} &= \hat{e}_{y_1} \cdot \nabla_X \\
&= \frac{1}{\sqrt{1 - [N_Z]_P^2}} \left( -[\hat{N}_X \hat{N}_Z]_P \frac{\partial}{\partial X} - [\hat{N}_Y \hat{N}_Z]_P \frac{\partial}{\partial Y} + [1 - \hat{N}_Z^2]_P \frac{\partial}{\partial Z} \right), \\
\frac{\partial}{\partial y_2} &= \frac{1}{\sqrt{1 - [N_X]_P^2}} \left( [\hat{N}_X^2 - 1]_P \frac{\partial}{\partial X} + [\hat{N}_X \hat{N}_Y]_P \frac{\partial}{\partial Y} + [\hat{N}_X \hat{N}_Z]_P \frac{\partial}{\partial Z} \right), \\
\frac{\partial}{\partial y_3} &= \frac{1}{\sqrt{1 - [N_Y]_P^2}} \left( -[\hat{N}_X \hat{N}_Y]_P \frac{\partial}{\partial X} + [1 - \hat{N}_Y^2]_P \frac{\partial}{\partial Y} - [\hat{N}_Y \hat{N}_Z]_P \frac{\partial}{\partial Z} \right).
\end{aligned} \tag{B.7}$$

From this, the first order derivatives of the normal can be computed locally on the surface around point  $P$  using Eqs.(B.4, B.6). After some simplification, the expressions for the derivatives  $\left[ \frac{\partial \hat{n}_x}{\partial x} \right]_P$  in each frame are given as:

$$\begin{aligned}
\left[ \frac{\partial \hat{n}_{x_1}}{\partial x_1} \right]_P &= \frac{1}{1 - [\hat{N}_Z]_P^2} \left( [\hat{N}_Y]_P^2 (\hat{N}_X)_X + [\hat{N}_X]_P^2 (\hat{N}_Y)_Y - [\hat{N}_X \hat{N}_Y]_P \left( (\hat{N}_X)_Y + (\hat{N}_Y)_X \right) \right), \\
\left[ \frac{\partial \hat{n}_{x_2}}{\partial x_2} \right]_P &= \frac{1}{1 - [\hat{N}_X]_P^2} \left( [\hat{N}_Z]_P^2 (\hat{N}_Y)_Y + [\hat{N}_Y]_P^2 (\hat{N}_Z)_Z - [\hat{N}_Y \hat{N}_Z]_P \left( (\hat{N}_Z)_Y + (\hat{N}_Y)_Z \right) \right), \\
\left[ \frac{\partial \hat{n}_{x_3}}{\partial x_3} \right]_P &= \frac{1}{1 - [\hat{N}_Y]_P^2} \left( [\hat{N}_Z]_P^2 (\hat{N}_X)_X + [\hat{N}_X]_P^2 (\hat{N}_Z)_Z - [\hat{N}_X \hat{N}_Z]_P \left( (\hat{N}_Z)_X + (\hat{N}_X)_Z \right) \right),
\end{aligned}$$

and similarly,  $\frac{\partial \hat{n}_y}{\partial y}$  as:

$$\begin{aligned}
\left[ \frac{\partial \hat{n}_{y_1}}{\partial y_1} \right]_P &= \frac{1}{1 - [\hat{N}_Z]_P^2} \times \\
&\quad \left( [\hat{N}_X^2 \hat{N}_Z^2]_P (\hat{N}_X)_X + \hat{N}_X \hat{N}_Y \hat{N}_Z^2]_P \left( (\hat{N}_Y)_X + (\hat{N}_X)_Y \right) + \right. \\
&\quad - [\hat{N}_X \hat{N}_Z]_P [1 - \hat{N}_Z^2]_P \left( (\hat{N}_Z)_X + (\hat{N}_X)_Z \right) + [\hat{N}_Y^2 \hat{N}_Z^2]_P (\hat{N}_Y)_Y + \\
&\quad \left. + [1 - \hat{N}_Z^2]_P^2 (\hat{N}_Z)_Z - [\hat{N}_Y \hat{N}_Z]_P [1 - \hat{N}_Z^2]_P \left( (\hat{N}_Z)_Y + (\hat{N}_Y)_Z \right) \right), \\
\left[ \frac{\partial \hat{n}_{y_2}}{\partial y_2} \right]_P &= \frac{1}{1 - [\hat{N}_X]_P^2} \times \\
&\quad \left( [\hat{N}_X^2 - 1]_P^2 (\hat{N}_X)_X + [\hat{N}_X \hat{N}_Y]_P [\hat{N}_X^2 - 1]_P \left( (\hat{N}_Y)_X + (\hat{N}_X)_Y \right) + \right.
\end{aligned} \tag{B.8}$$

## B. Simulation of Vesicles

$$\begin{aligned}
& + [\hat{N}_X \hat{N}_Z]_P [\hat{N}_X^2 - 1]_P \left( (\hat{N}_Z)_X + (\hat{N}_X)_Z \right) + [\hat{N}_X^2 \hat{N}_Y^2]_P (\hat{N}_Y)_Y + \\
& + [\hat{N}_X^2 \hat{N}_Z^2]_P (\hat{N}_Z)_Z + [\hat{N}_X^2 \hat{N}_Y \hat{N}_Z]_P \left( (\hat{N}_Z)_Y + (\hat{N}_Y)_Z \right) \Bigg), \\
\left[ \frac{\partial \hat{n}_{y3}}{\partial y_3} \right]_P &= \frac{1}{1 - [\hat{N}_Y]_P^2} \times \\
& \left( [\hat{N}_X^2 \hat{N}_Y^2]_P (\hat{N}_X)_X - [\hat{N}_X \hat{N}_Y]_P [1 - \hat{N}_Y^2]_P \left( (\hat{N}_Y)_X + (\hat{N}_X)_Y \right) + \right. \\
& + [\hat{N}_X \hat{N}_Y^2 \hat{N}_Z]_P \left( (\hat{N}_Z)_X + (\hat{N}_X)_Z \right) + [1 - \hat{N}_Y^2]_P^2 (\hat{N}_Y)_Y + [\hat{N}_Y^2 \hat{N}_Z^2]_P (\hat{N}_Z)_Z + \\
& \left. - [\hat{N}_Y \hat{N}_Z]_P [1 - \hat{N}_Y^2]_P \left( (\hat{N}_Z)_Y + (\hat{N}_Y)_Z \right) \right),
\end{aligned}$$

the cross-derivatives  $\frac{\partial \hat{n}_y}{\partial x}$  are also calculated in local frame by the following:

$$\begin{aligned}
\left[ \frac{\partial \hat{n}_{y1}}{\partial x_1} \right]_P &= \frac{1}{1 - [\hat{N}_Z]_P^2} \times \tag{B.9} \\
& \left( [\hat{N}_X \hat{N}_Y \hat{N}_Z]_P \left( (\hat{N}_X)_X - (\hat{N}_Y)_Y \right) + [\hat{N}_Y^2 \hat{N}_Z]_P (\hat{N}_Y)_X + \right. \\
& \left. - [\hat{N}_X^2 \hat{N}_Z]_P (\hat{N}_X)_Y + [\hat{N}_X (1 - \hat{N}_Z^2)]_P (\hat{N}_Z)_Y - [\hat{N}_Y (1 - \hat{N}_Z^2)]_P (\hat{N}_Z)_X \right), \\
\left[ \frac{\partial \hat{n}_{y2}}{\partial x_2} \right]_P &= \frac{1}{1 - [\hat{N}_X]_P^2} \times \\
& \left( [\hat{N}_X \hat{N}_Y \hat{N}_Z]_P \left( (\hat{N}_Y)_Y - (\hat{N}_Z)_Z \right) + [\hat{N}_Z]_P [\hat{N}_X^2 - 1]_P (\hat{N}_X)_Y + \right. \\
& \left. + [\hat{N}_X \hat{N}_Z^2]_P (\hat{N}_Z)_Y - [\hat{N}_Y (\hat{N}_X^2 - 1)]_P (\hat{N}_X)_Z - [\hat{N}_X \hat{N}_Y^2]_P (\hat{N}_Y)_Z \right), \\
\left[ \frac{\partial \hat{n}_{y3}}{\partial x_3} \right]_P &= \frac{1}{1 - [\hat{N}_Y]_P^2} \times \\
& \left( [\hat{N}_X \hat{N}_Y \hat{N}_Z]_P \left( (\hat{N}_Z)_Z - (\hat{N}_X)_X \right) + \hat{N}_Z [1 - \hat{N}_Y^2]_P (\hat{N}_Y)_X + \right. \\
& \left. - [\hat{N}_Y \hat{N}_Z^2]_P (\hat{N}_Z)_X + [\hat{N}_X^2 \hat{N}_Y]_P (\hat{N}_X)_Z - [\hat{N}_X (1 - \hat{N}_Y^2)]_P (\hat{N}_Y)_Z \right).
\end{aligned}$$

The outcome of this work is that the expressions for the derivatives of the surface given in Eq. (5.63) have now been evaluated within simulation frame through reference to the unit normal  $\hat{N}$ . From this, the expressions for the principal curvatures given in Eq. (5.53) can now be calculated, and as such the membrane forces computed. Here,

### *B. Simulation of Vesicles*

three different general surface frames were defined to minimise numerical error, with the choice of which local co-ordinate frame to use at a given location being determined by the resultant error. This error depends upon which component of the unit normal is largest at that point, with when components tend towards 1, a potential singularity is avoided in the denominator by switching the choice of local co-ordinate frame.

# References

- [1] D. C. Rapaport. *The art of molecular dynamics simulation*. eng. 2nd ed. Cambridge, UK ; Cambridge University Press, 2004.
- [2] Masoud Babaei, Junju Mu, and Andrew J. Masters. “Impact of variation in multicomponent diffusion coefficients and salinity in CO<sub>2</sub>-EOR: A numerical study using molecular dynamics simulation”. In: *Journal of Petroleum Science and Engineering* 162 (2018), pp. 685–696. URL: <https://www.sciencedirect.com/science/article/pii/S0920410517308793>.
- [3] Guy R. McNamara and Gianluigi Zanetti. “Use of the Boltzmann Equation to Simulate Lattice-Gas Automata”. In: *Phys. Rev. Lett.* 61 (20 Nov. 1988), pp. 2332–2335. URL: <https://link.aps.org/doi/10.1103/PhysRevLett.61.2332>.
- [4] F. J Higuera and J Jiménez. “Boltzmann Approach to Lattice Gas Simulations”. In: *Europhysics Letters (EPL)* 9.7 (Aug. 1989), pp. 663–668.
- [5] Shiyi Chen and Gary D Doolen. “Lattice Boltzmann method for fluid flows”. eng. In: *Annual review of fluid mechanics* 30.1 (1998), pp. 329–364.
- [6] Sauro Succi. *The Lattice Boltzmann Equation for Fluid Dynamics and Beyond*. Oxford University Press, 2001.
- [7] P. J Hoogerbrugge and J. M. V. A Koelman. “Simulating Microscopic Hydrodynamic Phenomena with Dissipative Particle Dynamics”. eng. In: *Europhysics letters* 19.3 (1992), pp. 155–160.
- [8] P Español and P Warren. “Statistical Mechanics of Dissipative Particle Dynamics”. eng. In: *Europhysics letters* 30.4 (1995), pp. 191–196.
- [9] Martin Walker, Andrew J. Masters, and Mark R. Wilson. “Self-assembly and mesophase formation in a non-ionic chromonic liquid crystal system: insights from dissipative particle dynamics simulations”. In: *Phys. Chem. Chem. Phys.* 16 (42 2014), pp. 23074–23081. URL: <http://dx.doi.org/10.1039/C4CP03092C>.
- [10] RA Gingold and Joseph Monaghan. “Smoothed Particle Hydrodynamics - Theory and Application to Non-Spherical Stars”. In: *mnras* 181 (Nov. 1977), pp. 375–389.
- [11] L. Lucy. “Lucy, L.B.: Numerical approach to testing of fission hypothesis. *Astron. J.* 82(12), 1013-1024”. In: *Astron. J.* 82 (Dec. 1977), pp. 1013–1024.
- [12] Ting Ye, Nhan Phan-Thien, and Chwee Teck Lim. “Particle-based simulations of red blood cells—A review”. eng. In: *Journal of biomechanics* 49.11 (2015), pp. 2255–2266.
- [13] Adam Kajzer, J Pozorski, and K. Szewc. “Large-eddy simulations of 3D Taylor-Green vortex: comparison of Smoothed Particle Hydrodynamics, Lattice Boltzmann and Finite Volume methods”. In: *Journal of Physics: Conference Series* 530 (Aug. 2014), p. 012019.

## References

- [14] Angelo Tafuni, Maria Grazia De Giorgi, and Alessandro De Rosis. “Smoothed Particle Hydrodynamics vs Lattice Boltzmann for the solution of steady and unsteady fluid flows”. In: *Computational Particle Mechanics* (Nov. 2021).
- [15] Thomas Douillet-Grellier, Sébastien Leclaire, David Vidal, François Bertrand, and Florian De Vuyst. “Comparison of multiphase SPH and LBM approaches for the simulation of intermittent flows”. In: *Computational particle mechanics* 6.4 (2019), pp. 695–720.
- [16] Fadl Hassan Moukalled. *The Finite Volume Method in Computational Fluid Dynamics : An Advanced Introduction with OpenFOAM and Matlab*. eng. Fluid mechanics and its applications, volume 113. Lebanon: Springer, 2016.
- [17] Gouri. Dhatt. *Finite element method*. eng. Numerical methods series. London: ISTE, 2012.
- [18] Young W. Kwon. *Multiphysics and multiscale modeling : techniques and applications*. eng. Boca Raton ; CRC Press, 2016.
- [19] Michael M Dupin, Ian Halliday, Chris M Care, Lyuba Alboul, and Lance L Munn. “Modeling the flow of dense suspensions of deformable particles in three dimensions”. eng. In: *Physical review. E, Statistical, nonlinear, and soft matter physics* 75.6 Pt 2 (2007), pp. 066707–066707.
- [20] J. Spendlove, X. Xu, T. Schenkel, M. A. Seaton, I. Halliday, and J. P. Gunn. “Three-dimensional single framework multicomponent lattice Boltzmann equation method for vesicle hydrodynamics”. In: *Physics of Fluids* 33.7 (2021), p. 077110. eprint: <https://doi.org/10.1063/5.0055535>. URL: <https://doi.org/10.1063/5.0055535>.
- [21] E M. Lifshitz L D. Landau. *Fluid mechanics*. eng. 2nd ed. Course of theoretical physics ; 6. Oxford: Pergamon Press, 1987.
- [22] J. E. Marsden A. J. Chorin. eng. Texts in Applied Mathematics. Springer, 1990.
- [23] G. K. (George Keith) Batchelor. *An introduction to fluid dynamics*. eng. Cambridge mathematical library. Cambridge: Cambridge University Press, 2002 - 1967.
- [24] Pijush K. Kundu. *Fluid Mechanics*. eng. 6th ed. Academic Press, 2016.
- [25] F. W. Byron and R. W. Fuller. *The Mathematics of Classical and Quantum Physics*. Dover Publications, 1992.
- [26] Ronald L. (Ronald Lee) Panton. *Incompressible flow*. eng. 4th ed. Hoboken, N.J: Wiley, 2013.
- [27] L. Gary Leal. *Advanced Transport Phenomena: Fluid Mechanics and Convective Transport Processes*. eng. Cambridge series in chemical engineering. Cambridge: Cambridge University Press, 2007.
- [28] T Young. “III. An essay on the cohesion of fluids”. eng. In: *Philosophical Transactions of the Royal Society of London* 95.1 (1805), pp. 65–87.
- [29] Laplace. In: *Mécanique céleste* Supplement to the tenth edition (1806).
- [30] Carl Friedrich Gauss. “Principia generalia Theoriae Figurae Fluidorum in statu Aequilibræ [General principles of the theory of fluid shapes in a state of equilibrium]”. In: (1830).
- [31] J. Hardy, Y. Pomeau, and O. De Pazzis. “Time evolution of a two-dimensional classical lattice system”. In: *Physical Review Letters* 31.5 (1973), pp. 276, 279.

## References

- [32] D Arumuga Perumal and Anoop K Dass. “A Review on the development of lattice Boltzmann computation of macro fluid flows and heat transfer”. eng. In: *Alexandria Engineering Journal* 54.4 (2015), pp. 955–971.
- [33] U. Frisch, B. Hasslacher, and Y. Pomeau. “Lattice-Gas Automata for the Navier-Stokes Equation”. In: *Phys. Rev. Lett.* 56 (14 Apr. 1986), pp. 1505–1508. URL: <https://link.aps.org/doi/10.1103/PhysRevLett.56.1505>.
- [34] Dieter Wolf-Gladrow. “Lattice-Gas Cellular Automata and Lattice Boltzmann Models - An Introduction”. In: *Lattice-Gas Cellular Automata and Lattice Boltzmann Models* 1725 (Jan. 2000).
- [35] P.L. Bhatnagar, E.P. Gross, and M. Krook. “A model for collision processes in gases. I. Small amplitude processes in charged and neutral one-component systems”. In: *Physical Review* 94.3 (1954), pp. 511, 525.
- [36] Irina Ginzburg. “Generic boundary conditions for lattice Boltzmann models and their application to advection and anisotropic dispersion equations”. eng. In: *Advances in Water Resources* 28.11 (2005), pp. 1196, 1216.
- [37] Irina Ginzburg. “Equilibrium-type and link-type lattice Boltzmann models for generic advection and anisotropic-dispersion equation”. In: *Advances in Water Resources* 28.11 (2005), pp. 1171–1195. URL: <https://www.sciencedirect.com/science/article/pii/S0309170805000874>.
- [38] D’Humières.D. “Generalized Lattice-Boltzmann Equations”. In: *Rarefied Gas Dynamics: Theory and Simulations*. 1992, pp. 450–458. eprint: <https://arc.aiaa.org/doi/pdf/10.2514/5.9781600866319.0450.0458>. URL: <https://arc.aiaa.org/doi/abs/10.2514/5.9781600866319.0450.0458>.
- [39] Timm Krüger, Halim Kusumaatmaja, Alexander Kuzmin, Orest Shardt, Goncalo Silva, and Erlend Magnus Viggen. *The Lattice Boltzmann Method - Principles and Practice*. Oct. 2016.
- [40] Irina Ginzburg, Dominique Dhumieres, and Alexander Kuzmin. “Optimal Stability of Advection-Diffusion Lattice Boltzmann Models with Two Relaxation Times for Positive/Negative Equilibrium”. In: *Journal of Statistical Physics* 139 (June 2010), pp. 1090–1143.
- [41] Zhifeng Yan, Xiaofan Yang, Siliang Li, and Markus Hilpert. “Two-relaxation-time lattice Boltzmann method and its application to advective-diffusive-reactive transport”. eng. In: *Advances in Water Resources* 109 (2017), pp. 333–342.
- [42] Pierre Lallemand and Li-Shi Luo. “Theory of the lattice Boltzmann method: Dispersion, dissipation, isotropy, Galilean invariance, and stability”. In: *Phys. Rev. E* 61 (6 June 2000), pp. 6546–6562. URL: <https://link.aps.org/doi/10.1103/PhysRevE.61.6546>.
- [43] Dominique D’Humières, Irina Ginzburg, Manfred Krafczyk, Pierre Lallemand, and Li-Shi Luo. “Multiple-Relaxation-Time Lattice Boltzmann Models in Three Dimensions”. In: *Philosophical transactions. Series A, Mathematical, physical, and engineering sciences* 360 (Apr. 2002), pp. 437–51.
- [44] Alexander Kuzmin, Abdulmajeed Mohamad, and Sauro Succi. “Multi-relaxation time Lattice Boltzmann Model for multiphase flows”. In: *International Journal of Modern Physics C* 19 (June 2008).

## References

- [45] M Vergassola, R Benzi, and S Succi. “On the Hydrodynamic Behaviour of the Lattice Boltzmann Equation”. In: *Europhysics Letters (EPL)* 13.5 (Nov. 1990), pp. 411–416.
- [46] R. Benzi, S. Succi, and M. Vergassola. “The lattice Boltzmann equation: theory and applications”. In: *Physics Reports* 222.3 (1992), pp. 145–197. URL: <http://www.sciencedirect.com/science/article/pii/037015739290090M>.
- [47] Zhaoli. Guo. *Lattice Boltzmann method and its applications in engineering*. eng. Advances in computational fluid dynamics ; vol. 3. Singapore ; World Scientific, 2013.
- [48] Paul J. Dellar. “Nonhydrodynamic modes and a priori construction of shallow water lattice Boltzmann equations”. In: *Phys. Rev. E* 65 (3 Feb. 2002), p. 036309. URL: <https://link.aps.org/doi/10.1103/PhysRevE.65.036309>.
- [49] Ian Halliday, Sergey Lishchuk, Timothy Spencer, Kallum Burgin, and Torsten Schenkel. “Interfacial Micro-currents in Continuum-Scale Multi-Component Lattice Boltzmann Equation Hydrodynamics.” eng. In: (2017-06-23).
- [50] Xu Xu, Kallum Burgin, M Ellis, and Ian Halliday. “Benchmarking of three-dimensional multicomponent lattice Boltzmann equation”. eng. In: (2017-11).
- [51] Li-Shi Luo, Wei Liao, Xingwang Chen, Yan Peng, and Wei Zhang. “Numerics of the lattice Boltzmann method: Effects of collision models on the lattice Boltzmann simulations”. In: *Physical review. E, Statistical, nonlinear, and soft matter physics* 83 (May 2011), p. 056710.
- [52] D.H. Rothman and J.M. Keller. “Immiscible cellular-automaton fluids”. In: *J. Stat. Phys.; (United States)* 52 (Aug. 1988).
- [53] Gunstensen, Rothman, Zaleski, and Zanetti. “Lattice Boltzmann model of immiscible fluids”. eng. In: *Physical review. A, Atomic, molecular, and optical physics* 43.8 (1991), pp. 4320–4327.
- [54] A. K Gunstensen and D. H Rothman. “Microscopic Modeling of Immiscible Fluids in Three Dimensions by a Lattice Boltzmann Method”. eng. In: *Europhysics letters* 18.2 (1992), pp. 157–161.
- [55] D Raabe. “Overview of the lattice Boltzmann method for nano- and microscale fluid dynamics in materials science and engineering”. In: *Modelling and Simulation in Materials Science and Engineering* 12.6 (Sept. 2004), R13–R46.
- [56] Daryl Grunau, Shiyi Chen, and Kenneth Eggert. “A lattice Boltzmann model for multiphase fluid flows”. eng. In: *Physics of fluids. A, Fluid dynamics* 5.10 (1993), pp. 2557–2562.
- [57] S V Lishchuk, C M Care, and I Halliday. “Lattice Boltzmann algorithm for surface tension with greatly reduced microcurrents”. eng. In: *Physical review. E, Statistical, nonlinear, and soft matter physics* 67.3 Pt 2 (2003), pp. 036701–036701.
- [58] I Halliday, A P Hollis, and C M Care. “Lattice Boltzmann algorithm for continuum multicomponent flow”. eng. In: *Physical review. E, Statistical, nonlinear, and soft matter physics* 76.2 Pt 2 (2007), pp. 026708–026708.



## References

- [59] B Ahrenholz, J Tölke, P Lehmann, A Peters, A Kaestner, M Krafczyk, and W Durner. “Prediction of capillary hysteresis in a porous material using lattice-Boltzmann methods and comparison to experimental data and a morphological pore network model”. eng. In: *Advances in water resources* 31.9 (2008), pp. 1151–1173.
- [60] Xiaowen Shan and Hudong Chen. “Lattice Boltzmann model for simulating flows with multiple phases and components”. English. In: *Physical Review E* 47.3 (1993), pp. 1815, 1819.
- [61] Shan and Chen. “Simulation of nonideal gases and liquid-gas phase transitions by the lattice Boltzmann equation”. eng. In: *Physical review. E, Statistical physics, plasmas, fluids, and related interdisciplinary topics* 49.4 (1994), pp. 2941–2948.
- [62] Xiaowen Shan and Gary Doolen. “Multicomponent Lattice Boltzmann model with interparticle interaction”. In: *Journal of Statistical Physics* 81 (Oct. 1995), pp. 379–393.
- [63] Xiaowen Shan and Gary Doolen. “Diffusion in a multicomponent lattice Boltzmann equation model”. In: *Phys. Rev. E* 54 (4 Oct. 1996), pp. 3614–3620. URL: <https://link.aps.org/doi/10.1103/PhysRevE.54.3614>.
- [64] Michael R. Swift, W. R. Osborn, and J. M. Yeomans. “Lattice Boltzmann Simulation of Non-Ideal Fluids”. In: (1995).
- [65] E Orlandini, M. R Swift, and J. M Yeomans. “A Lattice Boltzmann Model of Binary-Fluid Mixtures”. eng. In: *Europhysics letters* 32.6 (1995), pp. 463–468.
- [66] Swift, Orlandini, Osborn, and Yeomans. “Lattice Boltzmann simulations of liquid-gas and binary fluid systems”. eng. In: *Physical review. E, Statistical physics, plasmas, fluids, and related interdisciplinary topics* 54.5 (1996), pp. 5041–5052.
- [67] Michael C Sukop. *Lattice Boltzmann modeling : an introduction for geoscientists and engineers*. Springer, 2006.
- [68] Jianhui Yang and Edo S. Boek. “A comparison study of multi-component Lattice Boltzmann models for flow in porous media applications”. In: *Computers & Mathematics with Applications* 65.6 (2013). Mesoscopic Methods in Engineering and Science, pp. 882–890. URL: <https://www.sciencedirect.com/science/article/pii/S0898122112006839>.
- [69] Li Chen, Qinjun Kang, Yutong Mu, Ya-Ling He, and Wen-Quan Tao. “A critical review of the pseudopotential multiphase lattice Boltzmann model: Methods and applications”. eng. In: *International Journal of Heat and Mass Transfer* 76.C (2014), pp. 210, 236.
- [70] Zhaoli Guo, Chuguang Zheng, and Baochang Shi. “Discrete lattice effects on the forcing term in the lattice Boltzmann method”. In: *Phys. Rev. E* 65 (4 Apr. 2002), p. 046308. URL: <https://link.aps.org/doi/10.1103/PhysRevE.65.046308>.
- [71] Marcello Sega, Mauro Sbragaglia, Sofia S. Kantorovich, and Alexey O. Ivanov. “Mesoscale structures at complex fluidfluid interfaces: a novel lattice Boltzmann/molecular dynamics coupling”. In: *Soft Matter* 9.42 (2013), pp. 10092, 10107.
- [72] M Sbragaglia and X Shan. “Consistent pseudopotential interactions in lattice Boltzmann models”. eng. In: *Physical review. E, Statistical, nonlinear, and soft matter physics* 84.3 Pt 2 (2011), pp. 036703–036703.

## References

- [73] A J Briant and J M Yeomans. “Lattice Boltzmann simulations of contact line motion. II. Binary fluids”. eng. In: *Physical review. E, Statistical, nonlinear, and soft matter physics* 69.3 (2004-03), p. 031603.
- [74] M Latva-Kokko and Daniel H Rothman. “Diffusion properties of gradient-based lattice Boltzmann models of immiscible fluids”. eng. In: *Physical review. E, Statistical, nonlinear, and soft matter physics* 71.5 Pt 2 (2005), pp. 056702–056702.
- [75] S V Lishchuk, I Halliday, and C M Care. “Multicomponent lattice Boltzmann method for fluids with a density contrast”. eng. In: *Physical review. E, Statistical, nonlinear, and soft matter physics* 77.3 Pt 2 (2008), pp. 036702–036702.
- [76] D’Ortona, Salin, Cieplak, Rybka, and Banavar. “Two-color nonlinear Boltzmann cellular automata: Surface tension and wetting”. eng. In: *Physical review. E, Statistical physics, plasmas, fluids, and related interdisciplinary topics* 51.4 (1995-04), pp. 3718–3728.
- [77] K Burgin, J Spendlove, X Xu, and I Halliday. “Kinematics of chromodynamic multicomponent lattice Boltzmann simulation with a large density contrast”. eng. In: *Physical review. E* 100.4 (2019), pp. 043310–043310.
- [78] J. Brackbill, Douglas Kothe, and Zemach CA. “A Continuum Method for Modeling Surface Tension”. In: *Journal of Computational Physics* 100 (July 1992).
- [79] Qisu Zou and Xiaoyi He. “On pressure and velocity boundary conditions for the Lattice Boltzmann BGK model”. In: *Physics of Fluids* 9 (Nov. 1996).
- [80] Bouzidi, M’hamed, Mouaouia Firdaouss, Mouaouia, Lallemand, and Pierre. “Momentum Transfer of a Boltzmann-Lattice Fluid with Boundaries”. In: *Physics of Fluids* 13 (Nov. 2001), pp. 3452–.
- [81] I. Ginzbourg and P. M. Adler. “Boundary flow condition analysis for the three-dimensional lattice Boltzmann model”. In: *J. Phys. II France* 4.2 (1994), pp. 191–214. URL: <https://doi.org/10.1051/jp2:1994123>.
- [82] Donald Ziegler. “Boundary conditions for Lattice Boltzmann simulations”. In: *Journal of Statistical Physics* 71 (June 1993), pp. 1171–1177.
- [83] Takaji Inamuro, Masato Yoshino, and Fumimaru Ogino. “A non-slip boundary condition for lattice Boltzmann simulations”. eng. In: *Physics of fluids (1994)* 7.12 (1995), pp. 2928–2930.
- [84] Mohamed Gad-el-Hak. *The MEMS handbook*. eng. Mechanical engineering handbook series. Boca Raton, FL: CRC Press, 2002.
- [85] Stéphane Colin. *Microfluidics*. eng. ISTE. London, U.K: ISTE, 2010.
- [86] A Montessori, I Halliday, M Lauricella, S.V Lishchuk, G Pontrelli, T.J Spencer, and S Succì. “Chapter 20 - Multicomponent Lattice Boltzmann Models for Biological Applications”. eng. In: *Numerical Methods and Advanced Simulation in Biomechanics and Biological Processes*. Elsevier Ltd, 2018, pp. 357–370.
- [87] Daotong Chong, XinShi Liu, HuaJie Ma, Guoyou Huang, Yu Han, XingYe Cui, Junjie Yan, and Feng Xu. “Advances in fabricating double-emulsion droplets and their biomedical applications”. In: *Microfluidics and Nanofluidics* 2015 (Sept. 2015), pp. 1071–1090.
- [88] Ao Xu, Wei Shyy, and Tianshou Zhao. “Lattice Boltzmann modeling of transport phenomena in fuel cells and flow batteries”. eng. In: *Acta mechanica Sinica* 33.3 (2017), pp. 555–574.

## References

- [89] Yuze Hou, Hao Deng, Qing Du, and Kui Jiao. “Multi-component multi-phase lattice Boltzmann modeling of droplet coalescence in flow channel of fuel cell”. eng. In: *Journal of power sources* 393 (2018), pp. 83–91.
- [90] T J Spencer, I Halliday, and C M Care. “Lattice Boltzmann equation method for multiple immiscible continuum fluids”. eng. In: *Physical review. E, Statistical, nonlinear, and soft matter physics* 82.6 Pt 2 (2010), pp. 066701–066701.
- [91] Sébastien Leclaire, Marcelo Reggio, and Jean-Yves Trépanier. “Progress and investigation on lattice Boltzmann modeling of multiple immiscible fluids or components with variable density and viscosity ratios”. In: *Journal of Computational Physics* 246 (Aug. 2013), pp. 318–342.
- [92] Yuan Yu, Haihu Liu, Dong Liang, and Yonghao Zhang. “A versatile lattice Boltzmann model for immiscible ternary fluid flows”. In: *Physics of Fluids* 31.1 (2019), p. 012108.
- [93] Yuan Yu, Dong Liang, and Haihu Liu. “Lattice Boltzmann simulation of immiscible three-phase flows with contact-line dynamics”. In: *Physical Review E* 99 (Jan. 2019).
- [94] Peng Yuan and Laura Schaefer. “Equations of state in a lattice Boltzmann model”. In: *Physics of Fluids* 18.4 (2006), p. 042101.
- [95] Ding-yu Peng and Donald Robinson. “New Two-Constant Equation of State”. In: *Industrial & Engineering Chemistry Fundamentals* 15 (Feb. 1976).
- [96] Norman F. Carnahan and Kenneth E. Starling. “Equation of State for Nonattracting Rigid Spheres”. In: *The Journal of Chemical Physics* 51.2 (1969), pp. 635–636.
- [97] Junfeng Zhang and Fuzhi Tian. “A bottom-up approach to non-ideal fluids in the lattice Boltzmann method”. In: *EPL (Europhysics Letters)* 81 (Feb. 2008), p. 66005.
- [98] Seyedamin Nabavizadeh, Mohsen Eshraghi, and Sergio Felicelli. “A Comparative Study of Multiphase Lattice Boltzmann Methods for Bubble-Dendrite Interaction during Solidification of Alloys”. In: *Applied Sciences* 9 (Dec. 2018), p. 57.
- [99] Daniel Lycett-Brown and K. Luo. “Improved forcing scheme in pseudopotential lattice Boltzmann methods for multiphase flow at arbitrarily high density ratios”. In: *Physical review. E, Statistical, nonlinear, and soft matter physics* 91 (Feb. 2015), p. 023305.
- [100] Daniel Lycett-Brown and K. Luo. “Cascaded lattice Boltzmann method with improved forcing scheme for large-density-ratio multiphase flow at high Reynolds and Weber numbers”. In: *Physical Review E* 94 (Nov. 2016).
- [101] Qing Li and K. Luo. “Achieving tunable surface tension in the pseudopotential lattice Boltzmann modeling of multiphase flows”. In: *Physical Review E* 88 (June 2013).
- [102] Takaji Inamuro, T. Ogata, S. Tajima, and N. Konishi. “A Lattice Boltzmann method for incompressible two-phase flows with large density differences”. In: *Journal of Computational Physics* 198 (Aug. 2004), pp. 628–644.

## References

- [103] H.W. Zheng, C. Shu, and Y.T. Chew. “A lattice Boltzmann model for multiphase flows with large density ratio”. In: *Journal of Computational Physics* 218.1 (2006), pp. 353–371. URL: <https://www.sciencedirect.com/science/article/pii/S002199910600088X>.
- [104] Travis Mitchell, Christopher Leonardi, and Abbas Fakhari. “Development of a three-dimensional phase-field lattice Boltzmann method for the study of immiscible fluids at high density ratios”. In: *International Journal of Multiphase Flow* 107 (May 2018), pp. 1–15.
- [105] Y. Q. Zu and S. He. “Phase-field-based lattice Boltzmann model for incompressible binary fluid systems with density and viscosity contrasts”. In: *Phys. Rev. E* 87 (4 Apr. 2013), p. 043301. URL: <https://link.aps.org/doi/10.1103/PhysRevE.87.043301>.
- [106] Abbas Fakhari, Travis Mitchell, Christopher Leonardi, and Diogo Bolster. “Improved locality of the phase-field lattice-Boltzmann model for immiscible fluids at high density ratios”. In: *Phys. Rev. E* 96 (5 Nov. 2017), p. 053301. URL: <https://link.aps.org/doi/10.1103/PhysRevE.96.053301>.
- [107] Travis Mitchell, Christopher Leonardi, and Abbas Fakhari. “Development of a three-dimensional phase-field lattice Boltzmann method for the study of immiscible fluids at high density ratios”. In: *International Journal of Multiphase Flow* 107 (May 2018), pp. 1–15.
- [108] T Reis and T N Phillips. “Lattice Boltzmann model for simulating immiscible two-phase flows”. In: *Journal of Physics A: Mathematical and Theoretical* 40.14 (Mar. 2007), pp. 4033–4053. URL: <https://doi.org/10.1088/1751-8113/40/14/018>.
- [109] Haihu Liu, Albert J Valocchi, and Qjinjun Kang. “Three-dimensional lattice Boltzmann model for immiscible two-phase flow simulations”. eng. In: *Physical review. E, Statistical, nonlinear, and soft matter physics* 85.4 Pt 2 (2012), pp. 046309–046309.
- [110] Sébastien Leclaire, Nicolas Pellerin, Marcelo Reggio, and Jean-Yves Trépanier. “Enhanced equilibrium distribution functions for simulating immiscible multiphase flows with variable density ratios in a class of lattice Boltzmann models”. In: *International Journal of Multiphase Flow* 57 (2013), pp. 159–168. URL: <https://www.sciencedirect.com/science/article/pii/S0301932213001043>.
- [111] Yan Ba, Haihu Liu, Qing Li, Qjinjun Kang, and Jinju Sun. “Multiple-relaxation-time color-gradient lattice Boltzmann model for simulating two-phase flows with high density ratio”. eng. In: *Physical review. E* 94.2-1 (2016), pp. 023310–023310.
- [112] Z. X. Wen, Q. Li, Y. Yu, and Kai H. Luo. “Improved three-dimensional color-gradient lattice Boltzmann model for immiscible two-phase flows”. In: *Phys. Rev. E* 100 (2 Aug. 2019), p. 023301. URL: <https://link.aps.org/doi/10.1103/PhysRevE.100.023301>.
- [113] Sébastien Leclaire, Marcelo Reggio, and Jean-Yves Trépanier. “Numerical evaluation of two recoloring operators for an immiscible two-phase flow lattice Boltzmann model”. In: *Applied Mathematical Modelling* 36.5 (2012), pp. 2237–2252.
- [114] Orest Shardt, J. J. Derksen, and Sushanta K. Mitra. “Simulations of Janus droplets at equilibrium and in shear”. In: *Physics of Fluids* 26.1 (2014), p. 012104.

## References

- [115] Ciro Semperebon, Timm Krüger, and Halim Kusumaatmaja. “Ternary free-energy lattice Boltzmann model with tunable surface tensions and contact angles”. In: *Phys. Rev. E* 93 (3 Mar. 2016), p. 033305. URL: <https://link.aps.org/doi/10.1103/PhysRevE.93.033305>.
- [116] M. Wöhrwag, C. Semperebon, A. Mazloomi Moqaddam, I. Karlin, and H. Kusumaatmaja. “Ternary Free-Energy Entropic Lattice Boltzmann Model with a High Density Ratio”. In: *Phys. Rev. Lett.* 120 (23 June 2018), p. 234501. URL: <https://link.aps.org/doi/10.1103/PhysRevLett.120.234501>.
- [117] Reza Haghani Hassan Abadi, Mohammad Hassan Rahimian, and Abbas Fakhari. “Conservative phase-field lattice-Boltzmann model for ternary fluids”. In: *Journal of Computational Physics* 374 (2018), pp. 668–691. URL: <https://www.sciencedirect.com/science/article/pii/S0021999118305060>.
- [118] Yuhang Fu, Shufang Zhao, Lin Bai, Yong Jin, and Yi Cheng. “Numerical study of double emulsion formation in microchannels by a ternary Lattice Boltzmann method”. In: *Chemical Engineering Science* 146 (2016), pp. 126–134. URL: <https://www.sciencedirect.com/science/article/pii/S0009250916300902>.
- [119] G.R Lester. “Contact angles of liquids at deformable solid surfaces”. eng. In: *Journal of colloid science* 16.4 (1961), pp. 315–326.
- [120] J. S. Rowlinson and B Widom. Oxford: Clarendon Press, 1982.
- [121] A. A. Mohamad. *Lattice Boltzmann Method : Fundamentals and Engineering Applications with Computer Codes*. eng. 2nd ed. 2019. London: Springer London, 2019.
- [122] S. Succi. *The lattice boltzmann equation: For complex states of flowing matter*. Jan. 2018, pp. 1–762.
- [123] Gabriel Farag, S. Zhao, Guillaume Chiavassa, and Pierre Boivin. “Consistency study of Lattice-Boltzmann schemes macroscopic limit”. In: *Physics of Fluids* 33 (Jan. 2021).
- [124] Kevin Connington and Taehun Lee. “A Review of Spurious Currents in the Lattice Boltzmann Method for Multiphase Flows”. In: *Journal of Mechanical Science and Technology* 26 (Dec. 2012).
- [125] C. M. Pooley and K. Furtado. “Eliminating spurious velocities in the free-energy lattice Boltzmann method”. In: *Phys. Rev. E* 77 (4 Apr. 2008), p. 046702. URL: <https://link.aps.org/doi/10.1103/PhysRevE.77.046702>.
- [126] Xiaowen Shan. “Analysis and reduction of the spurious current in a class of multiphase lattice Boltzmann models”. In: *Phys. Rev. E* 73 (4 Apr. 2006), p. 047701. URL: <https://link.aps.org/doi/10.1103/PhysRevE.73.047701>.
- [127] S M Sheikholeslam Noori, M Taeibi Rahni, and S A Shams Taleghani. “Multiple-relaxation time color-gradient lattice Boltzmann model for simulating contact angle in two-phase flows with high density ratio”. In: *European physical journal plus* 134 (2019).
- [128] Zhao Yu and Liang-Shih Fan. “Multirelaxation-time interaction-potential-based lattice Boltzmann model for two-phase flow”. In: *Physical review. E, Statistical, nonlinear, and soft matter physics* 82 (Oct. 2010), p. 046708.

## References

- [129] Mark Porter, Ethan Coon, Qinqun Kang, J. Moulton, and Bill Carey. “Multicomponent interparticle-potential lattice Boltzmann model for fluids with large viscosity ratios”. In: *Physical review. E, Statistical, nonlinear, and soft matter physics* 86 (Sept. 2012), p. 036701.
- [130] S Leclaire, N Pellerin, M Reggio, and J-Y Trépanier. “Unsteady immiscible multiphase flow validation of a multiple-relaxation-time lattice Boltzmann method”. In: *Journal of Physics A: Mathematical and Theoretical* 47.10 (Feb. 2014), p. 105501. URL: <https://doi.org/10.1088/1751-8113/47/10/105501>.
- [131] Haihu Liu, Albert J. Valocchi, Charles Werth, Qinqun Kang, and Mart Oostrom. “Pore-scale simulation of liquid CO<sub>2</sub> displacement of water using a two-phase lattice Boltzmann model”. In: *Advances in Water Resources* 73 (2014), pp. 144–158. URL: <https://www.sciencedirect.com/science/article/pii/S030917081400150X>.
- [132] Haibo Huang, Jun-Jie Huang, and Xi-Yun Lu. “Study of immiscible displacements in porous media using a color-gradient-based multiphase lattice Boltzmann method”. In: *Computers & Fluids* 93 (2014), pp. 164–172. URL: <https://www.sciencedirect.com/science/article/pii/S0045793014000322>.
- [133] Sébastien Leclaire, Andrea Parmigiani, Orestis Malaspinas, Bastien Chopard, and Jonas Latt. “Generalized three-dimensional lattice Boltzmann color-gradient method for immiscible two-phase pore-scale imbibition and drainage in porous media”. In: *Physical Review E* 95 (Mar. 2017), p. 033306.
- [134] J. Spendlove, X. Xu, O. J. Halliday, T. Schenkel, and I. Halliday. “Chromodynamic multirelaxation-time lattice Boltzmann scheme for fluids with density difference”. In: *Phys. Rev. E* 102 (1 July 2020), p. 013309. URL: <https://link.aps.org/doi/10.1103/PhysRevE.102.013309>.
- [135] J Spendlove, X Xu, T Schenkel, M Seaton, and I Halliday. “Chromo-dynamic multi-component lattice Boltzmann equation scheme for axial symmetry”. eng. In: *Journal of physics. A, Mathematical and theoretical* 53.14 (2020), pp. 145001–.
- [136] Q. Li, K. H. Luo, Y. L. He, Y. J. Gao, and W. Q. Tao. “Coupling lattice Boltzmann model for simulation of thermal flows on standard lattices”. In: *Phys. Rev. E* 85 (1 Jan. 2012), p. 016710. URL: <https://link.aps.org/doi/10.1103/PhysRevE.85.016710>.
- [137] Haibo Huang, Junjie Huang, XI-YUN LU, and Michael Sukop. “On simulations of high-density ratio flows using color-gradient multiphase Lattice Boltzmann models”. In: *International Journal of Modern Physics C* 24 (Apr. 2013), p. 1350021.
- [138] I. Halliday, X. Xu, and K. Burgin. “Shear viscosity of a two-dimensional emulsion of drops using a multiple-relaxation-time-step lattice Boltzmann method”. In: *Phys. Rev. E* 95 (2 Feb. 2017), p. 023301. URL: <https://link.aps.org/doi/10.1103/PhysRevE.95.023301>.
- [139] Paul J. Dellar. “Incompressible limits of lattice Boltzmann equations using multiple relaxation times”. In: *Journal of Computational Physics* 190.2 (2003), pp. 351–370. URL: <https://www.sciencedirect.com/science/article/pii/S0021999103002791>.
- [140] George B. (George Brown) Arfken. *Mathematical methods for physicists : a comprehensive guide*. eng. 7th ed. Amsterdam: Academic Press.
- [141] W. Rybczynski. “On the translatory motion of a fluid sphere in a viscous medium”. In: *Bull. Acad. Sci. Cracovie (ser. A)* 40–46 (1911).

## References

- [142] J. S. Hadamard. In: *C. R. Acad. Sci. (Paris)* 152, 1735 (1911).
- [143] John. Happel. *Low Reynolds number hydrodynamics : with special applications to particulate media*. eng. Noordhoff, 1973.
- [144] T. D. Taylor and Andreas Acrivos. “On the deformation and drag of a falling viscous drop at low Reynolds number”. In: *Journal of Fluid Mechanics* 18.3 (1964), pp. 466–476.
- [145] Takaji Inamuro, Takuya Echizen, and Fuminori Horai. “Validation of an improved lattice Boltzmann method for incompressible two-phase flows”. In: *Computers & Fluids* 175 (2018), pp. 83–90. URL: <https://www.sciencedirect.com/science/article/pii/S0045793018305255>.
- [146] Thomas Lafarge, Pierre Boivin, Nicolas Odier, and B Cuenot. “Improved color-gradient method for Lattice-Boltzmann modeling of two-phase flows”. In: *Physics of Fluids* 33 (Aug. 2021).
- [147] Haihu Liu, Qinqun Kang, Christopher Leonardi, Sebastian Schmieschek, Ariel Narváez, Bruce Jones, John Williams, Albert Valocchi, and Jens Harting. “Multiphase lattice Boltzmann simulations for porous media applications”. In: *Computational Geosciences* 20 (Aug. 2016), pp. 777–805.
- [148] Monica Diez-Silva, Ming Dao, Jongyoon Han, Chwee-Teck Lim, and Subra Suresh. “Shape and Biomechanical Characteristics of Human Red Blood Cells in Health and Disease”. eng. In: *MRS bulletin* 35.5 (2010), pp. 382–388.
- [149] Y. C. (Yuan-cheng) Fung. *Biomechanics : mechanical properties of living tissues*. eng. Second edition. New York: Springer, 1993.
- [150] Chaouqi Misbah. “Vesicles, capsules and red blood cells under flow”. In: *Journal of Physics Conference Series* 392 (Dec. 2012), pp. 2005–.
- [151] Thomas M Fischer. “Shape Memory of Human Red Blood Cells”. eng. In: *Biophysical journal* 86.5 (2004), pp. 3304–3313.
- [152] Xuejin Li, He Li, Hung-Yu Chang, George Lykotrafitis, and George Em Karniadakis. “Computational Biomechanics of Human Red Blood Cells in Hematological Disorders”. eng. In: *Journal of biomechanical engineering* 139.2 (2017), pp. 0210081–02100813.
- [153] Saša Svetina, Drago Kuzman, Richard E Waugh, Primož Ziherl, and Boštjan Žekš. “The cooperative role of membrane skeleton and bilayer in the mechanical behaviour of red blood cells”. eng. In: *Bioelectrochemistry (Amsterdam, Netherlands)* 62.2 (2004), pp. 107–113.
- [154] T. Krüger, F. Varnik, and D. Raabe. “Efficient and accurate simulations of deformable particles immersed in a fluid using a combined immersed boundary lattice Boltzmann finite element method”. eng. In: *Computers & mathematics with applications (1987)* 61.12 (2011), pp. 3485–3505.
- [155] Achim Guckenberger and Stephan Gekle. “Theory and algorithms to compute Helfrich bending forces: a review”. eng. In: *Journal of physics. Condensed matter* 29.20 (2017), pp. 203001–203001.
- [156] Heloise Fernandes, C. Cesar, and Maria Barjas-Castro. “Electrical properties of the red blood cell membrane and immunohematological investigation”. In: *Revista brasileira de hematologia e hemoterapia* 33 (Mar. 2011), pp. 297–301.

## References

- [157] Igor V Pivkin and George Em Karniadakis. “Accurate coarse-grained modeling of red blood cells”. eng. In: *Physical review letters* 101.11 (2008), pp. 118105–118105.
- [158] Dmitry A Fedosov, Bruce Caswell, and George Em Karniadakis. “A Multiscale Red Blood Cell Model with Accurate Mechanics, Rheology, and Dynamics”. eng. In: *Biophysical journal* 98.10 (2010), pp. 2215–2225.
- [159] G Závodszky, B van Rooij, V Azizi, and A Hoekstra. “Cellular Level In-silico Modeling of Blood Rheology with An Improved Material Model for Red Blood Cells”. eng. In: *Frontiers in physiology* 8 (2017), pp. 563–563.
- [160] Gábor Zavodszky, Britt van Rooij, Victor Azizi, Saad Alowayyed, and Alfons Hoekstra. “Hemocell: a high-performance microscopic cellular library”. eng. In: *Procedia computer science* 108 (2017), pp. 159–165.
- [161] R Skalak, A Tozeren, R.P Zarda, and S Chien. “Strain Energy Function of Red Blood Cell Membranes”. eng. In: *Biophysical journal* 13.3 (1973), pp. 245–264.
- [162] O. Yeoh. “Some Forms of the Strain Energy Function for Rubber”. In: *Rubber Chemistry and Technology* 66 (Nov. 1993), pp. 754–771.
- [163] S Ramanujan and C Pozrikidis. “Deformation of liquid capsules enclosed by elastic membranes in simple shear flow: large deformations and the effect of fluid viscosities”. eng. In: *Journal of fluid mechanics* 361 (1998), pp. 117–143.
- [164] Robert M Macmeccan, J. R Clausen, G. P Neitzel, and C. K Aidun. “Simulating deformable particle suspensions using a coupled lattice-Boltzmann and finite-element method”. eng. In: *Journal of fluid mechanics* 618 (2009), pp. 13–39.
- [165] É Foessel, J Walter, A.-V Salsac, and D Barthes-Biesel. “Influence of internal viscosity on the large deformation and buckling of a spherical capsule in a simple shear flow”. eng. In: *Journal of fluid mechanics* 672 (2011), pp. 477–486.
- [166] J WALTER, A.-V SALSAC, and D BARTHÈS-BIESEL. “Ellipsoidal capsules in simple shear flow: prolate versus oblate initial shapes”. eng. In: *Journal of fluid mechanics* 676 (2011), pp. 318–347.
- [167] Toshihiro Omori, Haruki Hosaka, Yohsuke Imai, Takami Yamaguchi, and Takuji Ishikawa. “Numerical analysis of a red blood cell flowing through a thin micropore”. eng. In: *Physical review. E, Statistical, nonlinear, and soft matter physics* 89.1 (2014), pp. 013008–013008.
- [168] J.M Lyu, Paul G Chen, G Boedec, M Leonetti, and M Jaeger. “An isogeometric boundary element method for soft particles flowing in microfluidic channels”. eng. In: *Computers & fluids* 214 (2021), pp. 104786–.
- [169] Charles Samuel Peskin. *Flow patterns around heart valves: a digital computer method for solving the equations of motion*. eng. 1972.
- [170] Charles S Peskin. “The immersed boundary method”. eng. In: *Acta numerica* 11 (2002), pp. 479–517.
- [171] Christos Kotsalos, Jonas Latt, and Bastien Chopard. “Bridging the computational gap between mesoscopic and continuum modeling of red blood cells for fully resolved blood flow”. eng. In: *Journal of computational physics* 398 (2019), pp. 108905–.



## References

- [172] Xiaoyi He, Shiyi Chen, and Gary D. Doolen. “A Novel Thermal Model for the Lattice Boltzmann Method in Incompressible Limit”. In: *Journal of Computational Physics* 146.1 (1998), pp. 282–300. URL: <https://www.sciencedirect.com/science/article/pii/S0021999198960570>.
- [173] I Halliday, S V Lishchuk, T J Spencer, G Pontrelli, and C M Care. “Multiple-component lattice Boltzmann equation for fluid-filled vesicles in flow”. eng. In: *Physical review. E, Statistical, nonlinear, and soft matter physics* 87.2 (2013), pp. 023307–023307.
- [174] Joseph D. Bronzino. *The biomedical engineering handbook*. eng. Second edition. The electrical engineering handbook series. Boca Raton, Fla: CRC Press.
- [175] Stefano Guido and Giovanna Tomaiuolo. “Microconfined flow behavior of red blood cells in vitro”. In: *Comptes Rendus Physique* 10.8 (2009). Complex and biofluids, pp. 751–763. URL: <https://www.sciencedirect.com/science/article/pii/S1631070509001480>.
- [176] Alfred Gray, Elsa Abbena, and Simon Salamon. *Modern Differential Geometry of Curves and Surfaces with Mathematica, Third Edition (Studies in Advanced Mathematics)*. Chapman & Hall/CRC, 2006.
- [177] “Modern differential geometry of curves and surfaces with mathematica (second edition)”. eng. In: *Computers & mathematics with applications (1987)* 36.8 (1998), pp. 121–.
- [178] P.B. Canham. “The minimum energy of bending as a possible explanation of the biconcave shape of the human red blood cell”. In: *Journal of Theoretical Biology* 26.1 (1970), pp. 61–81. URL: <https://www.sciencedirect.com/science/article/pii/S0022519370800327>.
- [179] W. Helfrich. “Elastic Properties of Lipid Bilayers: Theory and Possible Experiments”. In: *Z. Naturforsch. C* 28 (Dec. 1973).
- [180] E.A Evans. “Bending Resistance and Chemically Induced Moments in Membrane Bilayers”. eng. In: *Biophysical journal* 14.12 (1974), pp. 923–931.
- [181] Udo Seifert. “Configurations of fluid membranes and vesicles”. In: *Advances in Physics* 46.1 (1997), pp. 13–137. eprint: <https://doi.org/10.1080/00018739700101488>. URL: <https://doi.org/10.1080/00018739700101488>.
- [182] James J. Callahan. *Advanced Calculus: A Geometric View*. Springer-Verlag New York, 2010.
- [183] E Evans and YC Fung. “Improved measurements of the erythrocyte geometry”. In: *Microvascular research* 4.4 (1972).
- [184] Timothy Spencer, Ian Halliday, and Chris Care. “A local lattice Boltzmann method for multiple immiscible fluids and dense suspensions of drops”. In: *Philosophical transactions. Series A, Mathematical, physical, and engineering sciences* 369 (June 2011), pp. 2255–63.
- [185] Udo Seifert. “Vesicles of toroidal topology”. In: *Phys. Rev. Lett.* 66 (18 May 1991), pp. 2404–2407. URL: <https://link.aps.org/doi/10.1103/PhysRevLett.66.2404>.
- [186] David Boal. *Mechanics of the Cell*. 2nd ed. Cambridge University Press, 2012.

## References

- [187] M. Mutz and D. Bensimon. “Observation of toroidal vesicles”. In: *Phys. Rev. A* 43 (8 Apr. 1991), pp. 4525–4527. URL: <https://link.aps.org/doi/10.1103/PhysRevA.43.4525>.
- [188] Verena C. Wimmer, Heinz Horstmann, Alexander Groh, and Thomas Kuner. “Donut-Like Topology of Synaptic Vesicles with a Central Cluster of Mitochondria Wrapped into Membrane Protrusions: A Novel Structure–Function Module of the Adult Calyx of Held”. In: *Journal of Neuroscience* 26.1 (2006), pp. 109–116. eprint: <https://www.jneurosci.org/content/26/1/109.full.pdf>. URL: <https://www.jneurosci.org/content/26/1/109>.
- [189] W. Wintz, H. -G. Döbereiner, and U. Seifert. “Starfish vesicles”. In: *EPL (Europhysics Letters)* 33.5 (Feb. 1996), pp. 403–408.
- [190] Xavier Michalet. “Equilibrium shape degeneracy in starfish vesicles”. In: *Physical review. E, Statistical, nonlinear, and soft matter physics* 76 (Sept. 2007), p. 021914.
- [191] John B. Kogut. “Chapter 12 - Curvature, Strong Gravity, and Gravitational Waves”. eng. In: *Special Relativity, Electrodynamics, and General Relativity*. Second Edition. Elsevier Inc, 2018, pp. 241–341.
- [192] P J Roache. “Perspective: A method for uniform reporting of grid refinement studies”. In: *Journal of Fluids Engineering; (United States)* 116:3 (Sept. 1994). URL: <https://www.osti.gov/biblio/6817347>.
- [193] Ismail Celik, U Ghia, P.J. Roache, Chris Freitas, H Coloman, and Peter Raad. “Procedure of Estimation and Reporting of Uncertainty Due to Discretization in CFD Applications”. In: *J. Fluids Eng.* 130 (July 2008), p. 078001.
- [194] Dominique P. Chevallier and Jean Lerbet. “7 - Dynamics”. eng. In: *Multi-Body Kinematics and Dynamics with Lie Groups*. Elsevier Ltd, 2018, pp. 235–267.
- [195] W Yao, Z Wen, Z Yan, D Sun, W Ka, L Xie, and S Chien. “Low viscosity Ektacytometry and its validation tested by flow chamber”. In: *Journal of biomechanics* 34.11 (Nov. 2001), pp. 1501–1509. URL: [https://doi.org/10.1016/s0021-9290\(01\)00109-9](https://doi.org/10.1016/s0021-9290(01)00109-9).
- [196] Johnson Chris R and Hansen Charles D. “ParaView: An End-User Tool for Large-Data Visualization”. eng. In: *Visualization Handbook*. Elsevier, 2005, pp. 1–1.
- [197] L Dean. *Blood Groups and Red Cell Antigens*. National Center for Biotechnology Information, 2005.
- [198] Michael A. Seaton, Richard L. Anderson, Sebastian Metz, and William Smith. “DL\_MESO: highly scalable mesoscale simulations”. In: *Molecular Simulation* 39.10 (2013), pp. 796–821. eprint: <https://doi.org/10.1080/08927022.2013.772297>. URL: <https://doi.org/10.1080/08927022.2013.772297>.
- [199] Benjamin Owen and Timm Krüger. *Numerical investigation of the formation and stability of homogeneous pairs of soft particles in inertial microfluidics*. 2021. arXiv: 2108.05277 [physics.flu-dyn].
- [200] Ting Ye, Nhan Phan-Thien, Boo Cheong Khoo, and Chwee Teck Lim. “Stretching and Relaxation of Malaria-Infected Red Blood Cells”. eng. In: *Biophysical journal* 105.5 (2013), pp. 1103–1109.

## References

- [201] George B. Arfken, Hans J. Weber, and Frank E. Harris. “Chapter 8 - Sturm-Liouville Theory”. In: *Mathematical Methods for Physicists (Seventh Edition)*. Ed. by George B. Arfken, Hans J. Weber, and Frank E. Harris. Seventh Edition. Boston: Academic Press, 2013, pp. 381–399. URL: <http://www.sciencedirect.com/science/article/pii/B9780123846549000086>.